



# Robust regional moment tensor determination in complex geological settings: Quantifying uncertainties and exploring Bayesian approaches

Zur Erlangung des akademischen Grades eines  
Doktors der Naturwissenschaften (Dr. rer. nat.)

von der KIT-Fakultät für Physik  
des Karlsruher Instituts für Technologie (KIT)  
genehmigte

Dissertation

von

**M.Sc. Mike Simon Lindner**  
aus Langenbrand bei Schömberg

Tag der mündlichen Prüfung:

21.07.2023

Referent: Prof. Dr. Andreas Rietbrock  
Korreferent: apl. Prof. Dr. Frank Krüger





*“All Things Must Pass”*

– George Harrison, M.B.E. –



# Abstract

Earthquakes are transient failures of the natural state of the Earth, generated by a sudden release of accumulated stress. They manifest themselves on the Earth's surface as ground motions that may result in significant damage to the socio-economic landscape. We use seismometers to record these ground motions and analyse them with physical and mathematical methods in modern high-performance-computations. Derived models give us a valuable insight into the Earth's structure and the physical processes that lead to earthquakes. Understanding its source mechanism is crucial to quantify the potential geological hazard of a region and the local stress regime.

The main goal of this study is the quantitative description of the earthquake source mechanism in a moment tensor (MT) representation. The underlying point source approximation of the earthquake is a robust standard approach in seismology. The equivalent forces fully describe the generated wavefield that interacts with the Earth's structure and causes motions at its surface. State-of-the-art MT modeling now often incorporates a Bayesian formulation of associated errors in the data and model assumptions. For this thesis, I created a new python-based MT inversion routine "AmΦB - uniXtree" that uses a Bayesian error formulation to mitigate the effects of uncertainties due to different sources of errors.

My area of interest is the Lesser Antilles Arc (LAA) subduction zone in the eastern Caribbean Sea, where I use data recorded on ocean bottom seismometers (OBS). OBS data are affected by strong seismic noise and issues related to the sensor installation, notably mostly affecting the horizontal recordings. Waveform data have so far been often discarded or limited for source modeling. In this thesis, the complete three components of the recorded waveforms are used for the first time in an application for MT inversion. With the newly derived source mechanisms, the regional MT database could be expanded significantly and a detailed analysis of the stress regime could be given.

Additionally, based on this data, this study shed light on the 2007 intermediate-depth  $M_w 7.4$  Martinique earthquake in the central parts of the LAA, which is hinted to have had a complex source process in all existing MT solutions. Furthermore, the location and size of this earthquake are not only unusual within the LAA but also in comparison to the global seismic intermediate-depth range (70-300 km).

I conducted several additional studies in collaboration. Two of them are featured in this thesis and used to benchmark my inversion code and examine further prominent error sources of MT solutions. For the 2020 Monte Christo Range earthquake in Nevada, USA, I extended my inversion routine to incorporate two individual faults. For an induced earthquake sequence near Blackpool, UK, I added a restricted cross-correlation time update to counter arrival time uncertainties between modeled and observed data.

My study demonstrates that we can use valuable OBS data for MT source modeling if we quantify prominent error sources in a Bayesian approach to mitigate potential effects on the source solution. The newly collected source mechanism data in the LAA offered a detailed insight into the tectonic setting and highlighted the source complexity of the Martinique earthquake, which I interpret as a source doublet consisting of two different faulting styles on an ancient subducted mid-oceanic ridge transform structure.



# List of Figures

1.1	Geophysical setting: Subduction zone . . . . .	4
1.2	Target area in the Lesser Antilles Arc. . . . .	7
2.1	Schematic plot of the representation theorem. . . . .	13
2.2	System of force couples. . . . .	17
2.3	Geometric setting of an earthquake fault. . . . .	18
2.4	Radiation pattern of prominent source mechanisms. . . . .	20
2.5	Moment tensor decomposition. . . . .	22
2.6	Example: Principal axis of a strike-slip. . . . .	24
2.7	Overview of source type plots. . . . .	27
3.1	Fundamental moment tensor solutions. . . . .	30
3.2	Data example and covariance matrices. . . . .	34
3.3	Uniform parameter space. . . . .	36
3.4	Tree sampling in 2D. . . . .	37
4.1	Plate reconstructions of the Caribbean Sea. . . . .	42
4.2	Modern Lesser Antilles Arc. . . . .	44
5.1	Bathymetric map of the Lesser Antilles subduction zone. . . . .	47
5.2	Probabilistic power spectral density. . . . .	48
5.3	Example: Influence of false station alignment on the waveform. . . . .	51
5.4	Example: Influence of station alignments on a strike-slip. . . . .	55
5.5	Example: Performance of a L2 v.s. a Bayesian error formulation. . . . .	55
5.6	Synthetic test: High horizontal noise. . . . .	56
5.7	Synthetic test: Alignment uncertainty. . . . .	58
5.8	Synthetic test: Influence of vertical data v.s. three component data. . . . .	59
5.9	Focal mechanism classification (FMC) diagram. . . . .	61
5.10	Moment tensor map. . . . .	62
5.11	Cross-section plot. . . . .	63
5.12	Stress inversion. . . . .	66
5.13	3D sketch of the Lesser Antilles subduction zone. . . . .	69
6.1	Global statistics of intermediate-depth (70-300 km) earthquakes since 2000. . . . .	73
6.2	Bathymetric map of the Lesser Antilles subduction zone. . . . .	75
6.3	Cross-correlation clustering of the fore- and aftershock seismicity associated to the 2007 $M_w$ 7.4 Martinique earthquake. . . . .	76
6.4	Regional 3D full waveform inversion. . . . .	78
6.5	3D sketch and depth cross-sections of the slab segment between Dominica and Martinique. . . . .	81
7.1	Overview map. . . . .	88
7.2	Background noise recorded at different stations during the analysis. . . . .	89

7.3	Template waveforms recorded at station AQ04. . . . .	92
7.4	Spectral components. . . . .	93
7.5	Cumulative number of detections for each template in 20-80 Hz frequency band. . . . .	95
7.6	Results of template matching as station AQ04. . . . .	96
7.7	Clustering the detected events in AQ04. . . . .	97
7.8	Multi stations event association. . . . .	97
7.9	Inversion results for event T4. . . . .	98
7.10	Inversion results for event T5. . . . .	99
7.11	Relative location of 34 events using HypoDD. . . . .	100
7.12	Location of the events in cluster C2, C3 and C5. . . . .	102
7.13	Locations of selected events. . . . .	103
8.1	Setting and data. . . . .	108
8.2	Nevada rupture history. . . . .	112
A.1	Upper/Lower hemisphere projection. . . . .	147
A.2	Profls used in CAP. . . . .	149
A.3	Uniform and non-uniform sampling in a FMC - focal mechanism diagram. . . . .	150
B.1	Example: Waveform fit with covariance matrix. . . . .	158
C.1	Waveform fit . . . . .	161
C.2	Hypocenter shift and origin time delay. . . . .	162
C.3	Information content of the 3D cartoon. . . . .	163
C.4	Cross-Section subplot with beachballs. . . . .	163
C.5	Doublet location grid with cross-section at 61.25°W. . . . .	164
C.6	Location Grid. . . . .	167
D.1	InSAR images. . . . .	169
D.2	InSAR modeling. . . . .	171

# List of Tables

2.1	Important recurring parameters: Seismic point source . . . . .	11
2.2	Important recurring parameters: Moment tensor . . . . .	16
2.3	Isotropic components of a moment tensor. . . . .	23
2.4	Selected prominent double-couple solutions. . . . .	25
2.5	Selected prominent CLVD solutions. . . . .	26
3.1	Important recurring parameters: Moment tensor inversion . . . . .	29
5.1	Reference events. . . . .	54
5.2	Stress inversion. . . . .	64
7.1	Information of the 6 largest events. . . . .	88
7.2	Values of the cross channel correlation. . . . .	91
7.3	Results of template matching. . . . .	94
7.4	Results of moment tensor inversion. . . . .	98
8.1	SAR image information. . . . .	109
8.2	Regional seismic network. . . . .	110
8.3	Comparison with other studies. . . . .	113
A.1	Fundamental mechanism for CAP. . . . .	148
B.1	Inversion results. . . . .	151
B.2	Overview of 151 local moment tensor solutions. . . . .	154
C.1	Table of moment tensor modelling. . . . .	160
C.2	Table of moment tensor solutions. . . . .	164
C.3	Seismic activity associated to the Martinique event. . . . .	165
C.4	Regional seismic network of 2007. . . . .	166
D.1	InSAR modeling. . . . .	170





# Contents

<b>List of Figures</b>	<b>v</b>
<b>List of Tables</b>	<b>vii</b>
<b>I Introduction, theory and method</b>	<b>1</b>
<b>1 Introduction</b>	<b>3</b>
1.1 Motivation . . . . .	8
1.2 Outline . . . . .	9
<b>2 Theory on moment tensor</b>	<b>11</b>
2.1 Seismic point source . . . . .	11
2.1.1 Equation of motion in a continuum . . . . .	11
2.1.2 The representation theorem . . . . .	13
2.2 Moment tensor . . . . .	16
2.2.1 Coordinate system . . . . .	17
2.2.2 Principal axes . . . . .	18
2.2.3 Moment tensor decomposition . . . . .	21
<b>3 Moment tensor inversion</b>	<b>29</b>
3.1 Inversion strategies . . . . .	29
3.1.1 First motion polarity . . . . .	29
3.1.2 Full waveform . . . . .	30
3.1.3 Further inversion codes and strategies . . . . .	31
3.2 AmΦB - uniXtree . . . . .	32
3.2.1 Bayesian error formulation . . . . .	33
3.2.2 Uniform X-dimensional tree-sampling - uniXtree . . . . .	34
3.2.3 Inversion application . . . . .	37
<b>II Moment tensor inversion in the Lesser Antilles</b>	<b>39</b>
<b>4 Geology of the Lesser Antilles</b>	<b>41</b>
<b>5 Bayesian regional moment tensor from ocean bottom seismograms recorded in the Lesser Antilles: Implications for regional stress field</b>	<b>45</b>
5.1 Abstract . . . . .	45
5.2 Introduction . . . . .	46
5.3 Method AmΦB - full waveform RMT inversion routine . . . . .	49
5.3.1 Ambient noise . . . . .	50
5.3.2 Station alignment . . . . .	50
5.3.3 uniXtree - uniform X-dimensional tree-importance sampling . . . . .	51

5.4	Data . . . . .	52
5.4.1	VoiLA OBS deployment . . . . .	53
5.4.2	Data selection . . . . .	53
5.5	Synthetic tests . . . . .	54
5.5.1	Influence of station alignment . . . . .	54
5.5.2	The influence of ocean noise . . . . .	54
5.5.3	Influence of the VoiLA network geometry . . . . .	56
5.6	Results . . . . .	59
5.6.1	Reference event set . . . . .	59
5.6.2	Combined MT catalog for northern LA subduction zone . . . . .	60
5.6.3	Stress inversion . . . . .	64
5.7	Tectonic implications . . . . .	65
5.8	Conclusions . . . . .	68
<b>6</b>	<b>Complex Martinique intermediate-depth quake reactivates early Atlantic break-up structures</b>	<b>71</b>
6.1	Abstract . . . . .	71
6.2	Introduction . . . . .	71
6.3	The 2007 $M_w$ 7.4 Martinique earthquake . . . . .	72
6.4	Data . . . . .	72
6.4.1	Source location update . . . . .	74
6.4.2	Aftershocks . . . . .	74
6.5	Source modelling . . . . .	76
6.5.1	Data selection . . . . .	76
6.5.2	Full waveform modeling for Green's function based on 3D velocity model . . . . .	77
6.5.3	Inversion strategy . . . . .	77
6.6	Discussion . . . . .	79
6.7	Conclusion . . . . .	80
<b>III</b>	<b>Moment tensor inversion outside the Lesser Antilles</b>	<b>83</b>
<b>7</b>	<b>Induced seismicity due to hydraulic fracturing near Blackpool, UK: Source modeling and event detection</b>	<b>85</b>
7.1	Abstract . . . . .	85
7.2	Introduction . . . . .	86
7.3	Data and data quality . . . . .	87
7.4	Processing method . . . . .	89
7.5	Application and results . . . . .	90
7.5.1	Event detection . . . . .	90
7.5.2	Source modelling . . . . .	97
7.5.3	Event relocation . . . . .	99
7.5.4	Interpretation and discussion . . . . .	100
7.5.5	Conclusion . . . . .	104
<b>8</b>	<b>Unfolding a horse tail structure: Analysis of the 2020 <math>M_w</math>6.5 Monte Christo Range, Nevada earthquake sequence</b>	<b>107</b>
8.1	Abstract . . . . .	107
8.2	Introduction . . . . .	107
8.3	Data . . . . .	109
8.3.1	Geodetic data . . . . .	109
8.3.2	Seismic data . . . . .	109
8.4	Source inversion . . . . .	110

---

8.4.1	Geodetic inversion . . . . .	110
8.4.2	Probabilistic moment tensor . . . . .	110
8.4.3	Stress inversion . . . . .	111
8.5	Comparison with other studies . . . . .	111
8.6	Conclusion . . . . .	113
<b>IV</b>	<b>Conclusion and outlook</b>	<b>115</b>
<b>9</b>	<b>Conclusion and outlook</b>	<b>117</b>
9.1	Conclusion . . . . .	118
9.2	Outlook . . . . .	121
<b>V</b>	<b>Appendix</b>	<b>145</b>
<b>A</b>	<b>Chapter 3</b>	<b>147</b>
<b>B</b>	<b>Chapter 5</b>	<b>151</b>
<b>C</b>	<b>Chapter 6</b>	<b>159</b>
<b>D</b>	<b>Chapter 8</b>	<b>169</b>



# Publications

**Publications related to this thesis:** Several chapters of this thesis have already been published in peer-reviewed scientific journals:

- **Lindner, M.**, Rietbrock, A., Bie, L., Goes, S., Collier, J., Rychert, C., Harmon, N., Hicks, S. P., Henstock, T., and the VOILA working group (2022). “Bayesian regional moment tensor from ocean bottom seismograms recorded in the Lesser Antilles: implications for regional stress field”. *Geophysical Journal International* 233.2, pp. 1036–1054. doi: 10.1093/gji/ggac494.
- Karamzadeh, N., **Lindner, M.**, Edwards, B., Gaucher, E., and Rietbrock, A. (2021). “Induced seismicity due to hydraulic fracturing near Blackpool, UK: source modeling and event detection”. *Journal of Seismology* 25, pp. 1385–1406. doi: 10.1007/s10950-021-10054-9.
- **Lindner, M.**, Rietbrock, A., Bie, L., Goes, S., and Gao, Y.-J. (2023). “Complex Martinique intermediate-depth earthquake reactivates early Atlantic break-up structures”. Submitted to *Geophysical Research Letters*.

**Presentations:** Results of this thesis have already been presented at scientific national and international conferences:

- **Mike Lindner** and Andreas Rietbrock. The influence of 3D velocity model on regional moment tensors in a subduction zone setting. In *EGU General Assembly Conference Abstracts*, EGU General Assembly Conference Abstracts, page 12824, April 2018.
- **Mike Lindner**, Andreas Rietbrock, and Miachael Fritsch. Did the 2007  $M_w 7.4$  intermediate-depth Martinique earthquake rupture on two orthogonal faults? Evidence of a reactivated subducted ridge-parallel transform fault. In *AG Seismologie*, 45. Sitzung der AG Seismologie, September 2019.
- **M. Lindner**, A. Rietbrock, L. Bie, V. Clouard, J. Collier, S. D. B. Goes, N. Harmon, T. Henstock, S. P. Hicks, R. E. A. Robertson, C. Rychert, and D. Schlaphorst. Re-evaluation of the 2007  $M_w 7.4$  intermediate-depth Martinique earthquake: evidence for rupture on orthogonal faults. In *AGU Fall Meeting Abstracts*, volume 2019, pages T31D–0277, December 2019.
- **Mike Lindner**, Andreas Rietbrock, Lidong Bie, Valerie Clouard, Jenny Collier, Saskia Goes, Nicholas Harmon, Timothy Henstock, Stephen Hicks, Richard Robertson, Catherine Rychert, and David Schlaphorst. A Bayesian approach for regional moment tensor inversion using ocean bottom seismograms in the Lesser Antilles and the implications for regional stress field. In *AGU Fall Meeting Abstracts*, volume 2021, pages T25A–0162, December 2021.
- **Mike Lindner**, Andreas Rietbrock, Lidong Bie, and the VoiLa working group. A Bayesian approach for regional moment tensor inversion using ocean bottom seismograms in the Lesser Antilles and the implications for regional stress field. In *Haiti Geosciences 2021 Conference*, CARIBACT International Joint Laboratory and its partners URGeo (Faculty of Sciences of the State University of Haiti) and ERC2 (Quisqueya University), 2022.
- **Mike Lindner**, Andreas Rietbrock, Lidong Bie, Saskia Goes, Jenny Collier, Catherine Rychert, Nicholas Harmon, Stephen P Hicks, Tim Henstock, and the VoiLA working group. From Small to Large: Tectonic Stresses and Seismic Activity in the Lesser Antilles Subduction Zone. In *AG Seismologie*, 48. Sitzung der AG Seismologie, September 2022.

**Publications not related to this thesis:**

- Iraklis Klampanos, Athanasios Davvetas, Andre Gemund, Malcolm Atkinson, Antonios Koukourikos, Rosa Filgueira, Amrey Krause, Alessandro Spinuso, Angelos Charalambidis, Federica Magnoni, Emanuele Casarotti, Christian Page, **Mike Lindner**, Andreas Ikononopoulos, and Vangelis Karkaletsis. Dare: A reflective platform designed to enable agile data-driven research on the cloud. In: 2019 15th International Conference on eScience (eScience), pp. 578–585. doi: 10.1109/eScience.2019.00079.
- Kufner, S.-K., Bie, L., Gao, Y., **Lindner, M.**, Waizy, H., Kakar, N., and Rietbrock, A. (2023). “The Devastating 2022 M6.2 Afghanistan Earthquake: Challenges, Processes, and Implications”. *Geophysical Research Letters* 50.11. doi: 10.1029/2022GL102176.

**Presentations not related to this thesis:**

- **Mike Lindner**, Thomas Forbriger, Malte Westerhaus, Michael Mayer, Andreas Rietbrock, and Hansjörg Kutterer. Skill-building in Seismo-Geodesy observatory practice at Black Forest Observatory (BFO). In Herbsttagung 2021, Arbeitskreis Geodäsie/Geophysik, 2021.
- Katrin Heß, Yvonne Kemm, **Mike Lindner**, Michael Mayer, Luisa Schneider, Gunar Sturm, and Katrin Sturm-Richter. Nachhaltige und partizipative transformationsprozesse in der (online-)lehre – das beispiel des programms research infrastructures in research-oriented teaching“. Vortrag gehalten auf 50. dghd-Jahrestagung Transformationen. Perspektiven auf eine postdigitale Hochschullehre“ (2022), Paderborn, Deutschland, 6.–9. September 2022, 2022.

## Part I

# Introduction, theory and method





# Chapter 1

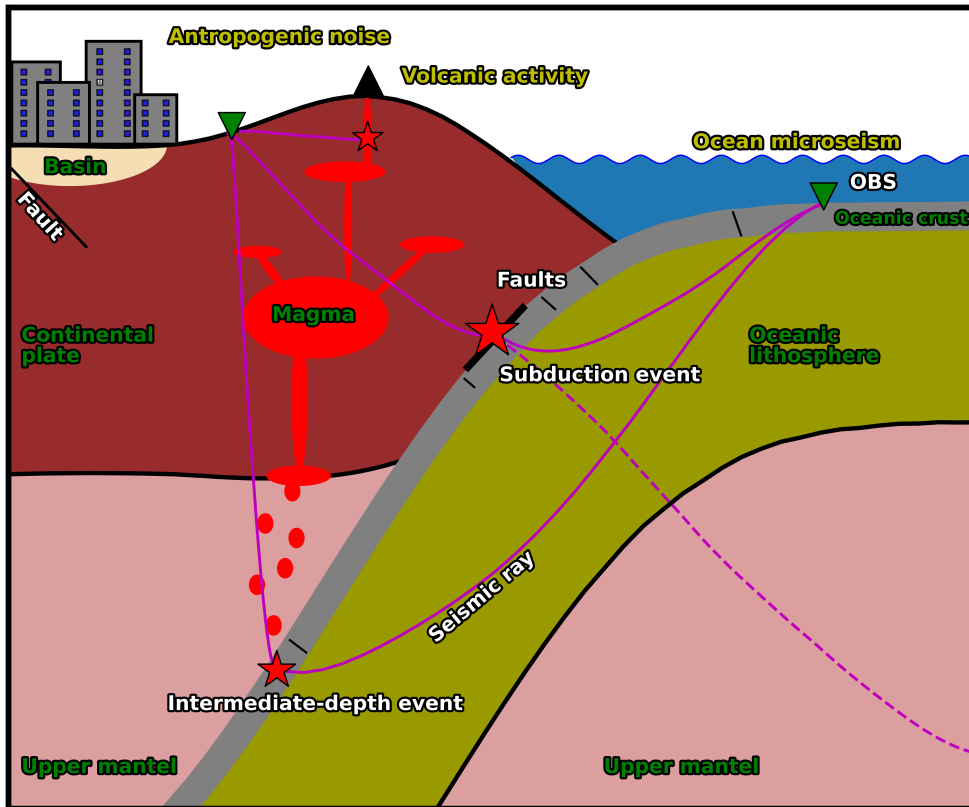
## Introduction

In 1906, near Point Reyes just north of the city of San Francisco, the US geologist G.K. Gilbert took one of the most iconic pictures in his field of science. It depicts two wooden fences, offset by about 2.5 meters with a scar in the ground passing perpendicular through them. These fences were not built intentionally this way, as the scar is related to the devastating  $M7.8$  San Francisco earthquake that struck the city in the early morning on April, 18, 1906. This event can be associated with the San Andreas Fault, a continental transform fault with a relative southeastward motion of the North American and a northwestward motion of the Pacific Plate – a strike-slip mechanism. This earthquake triggered modern geophysical research and brought upon a re-thinking of the physical processes in the Earth’s interior (Agnew, 2002). Since then new mathematical and physical models combined with powerful modern computational techniques brought forward the interpretation of earthquake source mechanism, even if it is not visible at the surface. We can conduct detailed studies of the source process and describe complex events of different sizes in different settings. This, however, relies on a good understanding of the geological structure, the physical processes in the Earth’s interior, and the geophysical characterization of the source itself.

Figure 1.1 depicts the schematic setup of a convergent plate boundary – a subduction zone – where dense and cold oceanic lithosphere sinks beneath a less dense plate (e.g., continental lithosphere) into the mantle. This process is accompanied by strong seismic activity that originates at different locations due to different physical processes. Each earthquake produces characteristic signals that depend on the underlying source mechanisms. The excited signal travels as a seismic wavefield through the Earth’s interior and interacts (Earth’s response) with its structure (e.g., subducted slab, continental crust with heterogeneities like magmatic chambers, basins) until it’s recorded at an observation point (e.g., seismometer) at the surface. The signal now contains information about the source, the Earth, and the seismometer, which we seek to separate into their respective contributions. The general mathematical approach to describe this process is the convolution model (Gilbert et al., 1975). However, the separation is not straightforward as the complexities of the source process and the Earth’s structure introduces ambiguities into the recorded data that we cannot simply resolve in a single step. The study of one (i.e., source mechanism) requires a profound knowledge of the other two.

The scope of this thesis is the characterization of the seismic source process. Seismic sources, be they of natural origin or from anthropogenic activities, induce a directed force into the Earth. I focus on naturally occurring sources, i.e., tectonic earthquakes, which do not occur arbitrarily but follow physical laws in time (Gutenberg et al., 1944) and space (e.g., Wadati, 1928; Frohlich, 1987). They are connected to pre-existing weakening structures in the Earth, so-called faults, that can be observed at the continental crust, oceanic crust, at plate boundaries and can reach deep into the mantle.

The driving force, that leads to the breaking of these structures, is the plate motions that slowly



**Figure 1.1:** Geophysical setting in a subduction zone (cartoon). Labels in yellow represent potential noise sources, green describes the Earth's structure. Earthquake events (red stars) can yield from different processes; e.g., subduction of the oceanic lithosphere (thrust events at the plate interface), bending faults in the subducted crust (Ranero et al., 2005), dehydration embrittlement of the oceanic crust at intermediate depths (Kirby et al., 1990), volcanic/magmatic processes (Nishimura, 2011) or from continental fault systems. A well-arranged and dense seismic network (green triangles) helps to record, locate, classify, and model these events. Ocean bottom seismometer (OBS) stations increase the station coverage to offshore regions. The complex geometry of the zone strongly affects the travel paths (magenta lines: solid for local paths and dotted for teleseismic paths) of the seismic waves between the sources and the receivers. Furthermore, local noise sources (e.g., cities, ocean, weather) affect the recordings.

build up tectonic stresses which are then released during an earthquake when the internal rigidity of the rocks is exceeded. Reid (1910) formulated this process in the elastic rebound theory after examining the changes of predefined survey lines before and after the 1906 San Francisco earthquake (e.g., Shearer, 2009). He showed that the stored strain energy gets released in a sudden relative movement (shear) offsetting two adjunct Earth's volumes, i.e. G.K. Gilbert's picture of the two offset fences. Some of the prominent large-scale structures include the opening of graben and rift systems, e.g., Rhine Graben (Bonjer, 1997), the East African Rift (Barth, 2007), mountain building, e.g., Alps (Petersen et al., 2021), shear-movements, e.g., San Andreas Fault, fracture zones, or most prominently subduction processes, e.g., Pacific Ring of Fire, Hellenic Arc, South Sandwich, Lesser Antilles.

Earthquakes can be devastating strong events – megathrusts – with highly complex rupture histories along several hundreds-of-kilometer-long segments (e.g., the 2004  $M_w$ 9.1 – 9.3 Sumatra earthquake, the 2011  $M_w$ 9.0 – 9.1 Tohoku earthquake) or on a network of fault structures incorporating different source styles, e.g., the 2007  $M_w$ 7.4 Martinique doublet (Lindner et al., 2023), the 2011  $M_w$ 7.1 Araucania doublet (Hicks et al., 2015), the 2012  $M_w$ 8.6 Wharton Basin sequence (Hill et al., 2015), the 2019  $M_w$ 6.4 and  $M_w$ 7.1 Ridgecrest sequence (Wang et al., 2020), or the recent 2023  $M_w$ 7.8 and

$M_w$ 7.6 Turkey–Syria earthquake doublet (Dal Zilio et al., 2023). They are evaluated as extreme scenarios that can have far-reaching indirect effects on the society and economy. For instance, the 2004 Sumatra event, with the triggered tsunami, is the most destructive event in terms of fatalities in recent history (Satake, 2014) while the 2011 Tohoku event is the costliest natural disaster on record (Kajitani et al., 2013). Such events are usually well studied and cross-validated using different techniques, e.g., InSAR (Kwong et al., 2019), High-Rate GPS (Tsang et al., 2019) or geological observations (Kufner et al., 2023). They offer the opportunity for discoveries, e.g., Inge Lehmann’s description of the inner solid core following the 1929 Murchison earthquake in New Zealand. These mega-events are generally rare in their occurrence with re-occurrence times of hundreds to thousands of years depending on their size and location.

Much more frequently occurring intermediate-sized events ( $M_w \leq 6.5$ ) can have a much larger influence on the citizens within a limited region, e.g., the 2016  $M_w$ 6.5 Norica event (Scognamiglio et al., 2018) or the 2019  $M_w$ 6.3 Durres event (Govorčin et al., 2020). The most recent 2022  $M_w$ 6.2 Afghanistan earthquake ruptured a so-far unknown fault segment and resulted in the largest humanitarian loss in 2022 (Kufner et al., 2023). It is therefore crucial to study earthquakes of different sizes at different locations to qualitatively assess their influence on human society.

If we want to study the rupture process of an earthquake, profound knowledge of the Earth’s interior is crucial. Complex geological structures and local heterogeneity (e.g., soft soil basins, magma chamber) influence the traveling wavefront, causing reflections, conversions, scattering, or other effects on the waveforms. The Earth’s structure can be represented by a velocity models that vary in complexity and resolution. 1D models are the most basic structural models and represent a stratified Earth, described by a set of physical parameters (e.g., P-wave velocity, S-wave velocity, density, quality factor). Widely used global spherical average reference models include PREM<sup>1</sup> (Dziewonski et al., 1981), IASP91 (Kennett et al., 1991), or AK135 (Kennett et al., 1995). Regional variations are considered in the global crustal models, e.g., crust2.0 (Bassin et al., 2000) or crust1.0 (Laske et al., 2013) or come from local studies (e.g., Bie et al., 2020; Leon-Rios et al., 2019). These models have their limitations as they cannot image non-horizontal structures (e.g., subducting plates) or localized high/low-velocity zones. Especially the travel times that depend solely on the structure can be separated from the source mechanism (Gilbert et al., 1975). More sophisticated but also much more complicated in their creation are 3D models. These models do exist on a global (e.g., Simmons et al., 2012; Debayle et al., 2016; Simmons et al., 2021) or regional scale (e.g., Blom et al., 2020; Braszus et al., 2021; Lloyd et al., 2020; Leon-Rios et al., 2021; Gao et al., 2022) in varying resolutions<sup>2</sup>.

The impact of an earthquake can be felt on the Earth’s surface and requires adequate sensory to measure the induced relative movements. A seismologist hereby depends on seismograms as data basis – time series recorded on a seismometer representing the ground motion (e.g., particle velocity in m/s) at the geographical location of the installment. The influence of the sensory setup (seismometer and data logger) on the waveforms is generally well-known and physically fully describable (Scherbaum, 2013). The recorded data represent motions along a principal axis of a Cartesian coordinate system and hence depend on the alignment of the sensor relative to north and the gravitational axis. A good installation also includes the shielding from environmental influences i.e., seismic noise, thermal or hydrostatic fluctuations (e.g., Forbriger, 2012; Bormann et al., 2013). However, satisfying all conditions is not guaranteed and arising effects might influence the geophysical analysis.

To study the earthquake source, we need to quantify and mitigate these effects. Especially seismic noise, be it of anthropogenic (e.g., cities, streets, industrial sites) or natural (e.g., weather or waves at the coast) origin, has large influences on the recordings due to its broad-band characteristics (e.g., Bormann et al., 2013). The influence of such signals depends on the amplitudes in the relevant

<sup>1</sup>Preliminary Reference Earth Model

<sup>2</sup>For an overview of different models see the SAGE data service by IRIS<sup>3</sup> (IRIS-SAGE, 2023).

frequency bands of an earthquake. Especially susceptible are small-magnitude events that may disappear in the noise. Using the pre-event noise is a basic approach to selecting and rating the data used for scientific applications and strongly influences the uncertainty range of the source solution.

Of interest for this study are uncertainties associated with seismograms of ocean bottom seismometer (OBS). I identified three main sources of errors that may affect the effective incorporation of OBS data in earthquake source modeling. The first one is ocean microseism which differs in its nature from the noise measured on land (Schmidt-Aursch et al., 2022) and holds dominant frequencies in the preferred range for source modeling (Yang et al., 2012). The second one is the uncertainty in station locations, and alignments of the sensors. The third one is the complex and insufficient study of the velocity structure of the oceanic crust and the geometry of the subduction zone beneath OBS locations.

Research projects investigating the physical properties of subduction zones now often incorporate OBS (e.g., Romanowicz et al., 1998; Ruiz et al., 2013; Cabieces et al., 2020; Leon-Rios et al., 2021). However, the recorded data often provide only a limited source of information for earthquake source modeling. Especially restricted in the land station coverage are island arcs like the Lesser Antilles Arc on the eastern Caribbean Sea. The arc is part of a comparably small but highly complex subduction zone along which subduction is largely driven by the westward motion of the American continents (Braszus et al., 2021). Between March 2016 to May 2017, a regional OBS network was installed as part of the NERC-funded<sup>4</sup> international multidisciplinary consortium project – VoiLA – to study the Volatiles in the Lesser Antilles Island Arc (Goes et al., 2019). The network consisted of 34 broad-band sensors deployed in the forearc and the backarc area (Collier, 2015) along the arc with a focus on the northern parts (Figure 1.2). During its operation, 381 seismic events were located with high accuracy and assigned with local magnitudes (Bie et al., 2020). This unprecedented database offered the opportunity to conduct a regional study on earthquake source mechanism.

A robust and widely used approach is the point-source approximation of a seismic source in a moment tensor (MT) representation (Burridge et al., 1964). It is based on the assumption that the source dimension is neglectable compared to the source-receiver distance (e.g., large events in teleseismic or small events in a regional setting). The radiated wavefield displays symmetric characteristics (Nakano, 1923) for oblique shear movement at the fault (e.g., relative motion of the adjunct plates at the San Andreas Fault or over-/underriding plate motion in a subduction process). However, we often recognize deviations between the model and the observed data, introducing movements that cannot be explained by a simple shear motion on one fault plane i.e., volumetric changes or complex geometries (Foulger et al., 2014). An important measure for such aberrations is a Compensated Linear-Vector Dipole (CLVD, Knopoff et al., 1970). In itself it holds no physical meaning, however, its occurrence may hint at a physical cause.

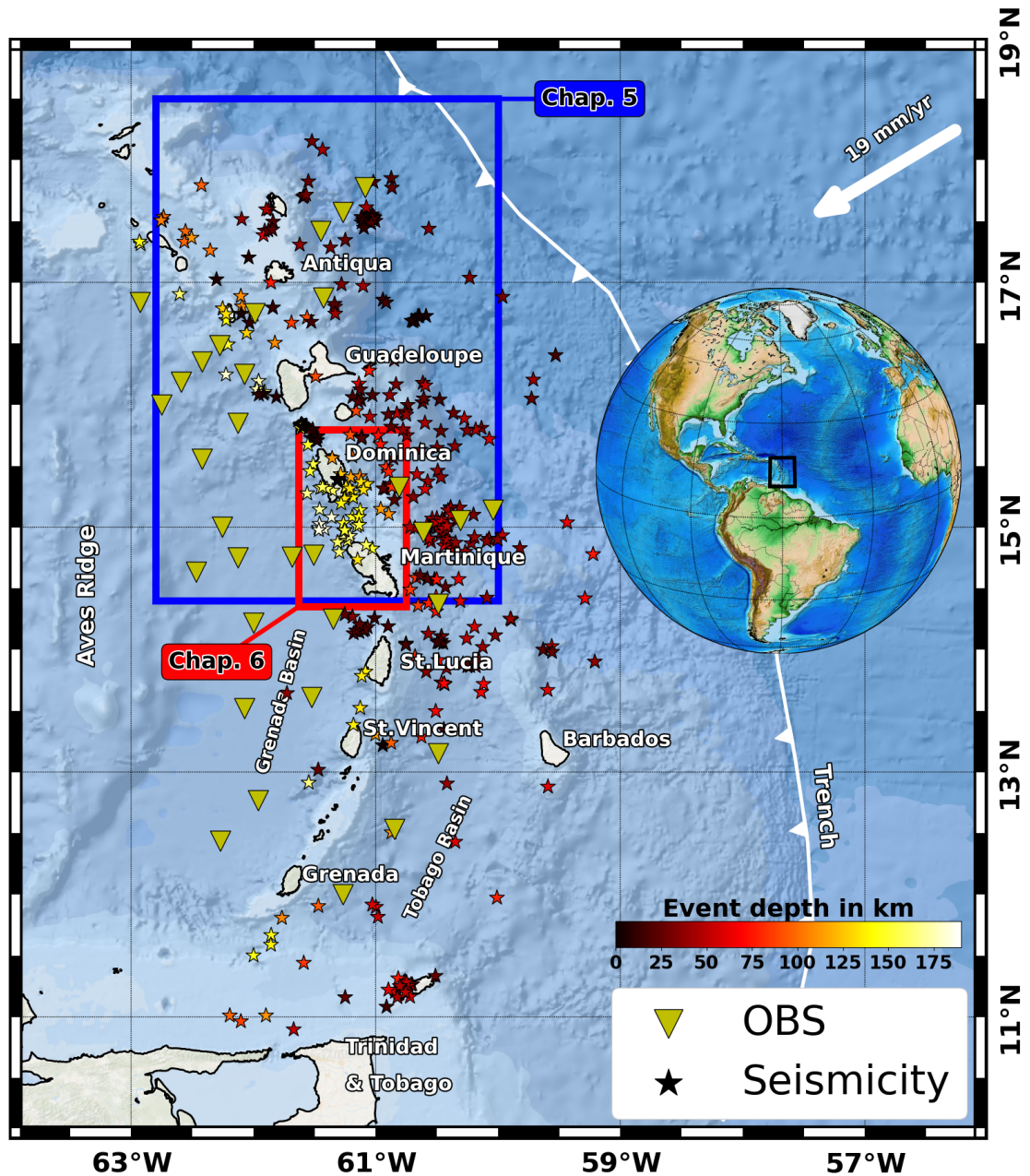
If we aim to study the faulting activity and the prevalent stress regime in a specific region for all its complexities (e.g., to understand the occurring CLVDs) we need to resort back to multiple source solutions. With ongoing advancements in computational infrastructures for automatic inversion routines, various earthquake agencies have compiled large and continuously growing global and regional moment tensor databases of different quality. Global catalogs include the GCMT<sup>5</sup> catalog which claims to be complete for events with  $M \geq 5.0$  between 2004 to 2010 (Ekström et al., 2012), the GEOFON program of the GFZ<sup>6</sup> in Potsdam with the completeness of  $M_w \geq 5$  globally and about  $M_w \geq 4$  for events within Europe (Saul et al., 2011) and the USGS<sup>7</sup> moment tensor database which features global solutions with a focus on the US territories. Purely regional catalogs include

<sup>4</sup>Natural Environment Research Council

<sup>5</sup>Global Centroid Moment Tensor

<sup>6</sup>Geoforschungszentrum

<sup>7</sup>United States Geological Survey



**Figure 1.2:** The Lesser Antilles Arc is located at the eastern end of the Caribbean Sea, where the joint Atlantic oceanic lithosphere is subducted by an average rate of  $\sim 1.9$  cm/year relative to South America (Demets et al., 2010). As part of the VoiLa project (Goes et al., 2019), 34 OBS stations were deployed around the arc and allowed to locate 381 local seismic events (Bie et al., 2020). Findings of this thesis within the blue boxed area are in Chapter 5 and a focus study of the activity within the red box is done in Chapter 6.

the European-Mediterranean RCMT<sup>8</sup> database of the INGV<sup>9</sup> in Italy (Pondrelli, 2002) with the completeness of  $M_w 4.5$  since 1997 (e.g., Pondrelli et al., 2011) or the NIED<sup>10</sup> seismic moment tensor catalog for regional earthquakes around Japan (Fukuyama et al., 1998) that claims to provide reliable MT solutions down to  $M_w 3.5$  (Kubo et al., 2002). But even these regional catalogs are missing out on the majority of small events. Here we depend on temporal local studies that can go to much lower magnitudes and feature more reliable solutions, e.g., the West Bohemia catalog from 2008 to 2018 with events between  $M_L 0.5$  and  $M_L 4.4$  (Vavryčuk et al., 2022) or the database for Western Greece spanning 10 years for magnitudes between 2.8 and 6.8 (Serpetsidaki et al., 2016). Small seismic events might not inflict critical damage on the local infrastructure but give valuable insight into the seismic activity within their respective regions. Using the source solutions we are able to infer the prevailing stress regime (Hardebeck, 2015; Uchide, 2020) and can identify seismic active areas and their radiation pattern for potential damaging events. Such studies depend on a high quality observation network and are especially difficult for off-shore events, e.g., subduction zones. Studies in such environments strongly benefit from the usage of OBS deployments.

I follow a Bayesian approach (e.g., Tarantola, 2004) to quantify the effects of noise and the sensor alignment uncertainties on the moment tensor solution. While noise is frequently considered in modern inversion approaches (e.g., Duputel et al., 2012; Vackář et al., 2017; Pugh et al., 2016; Vasyura-Bathke et al., 2020), the alignment uncertainty is so far neglected if the observation network is large enough and well distributed around the source location. However, actual effects on the source solution have never been quantified and a well-positioned source-receiver arrangement is hardly achieved in reality. Timing issues are considered by a restricted cross-correlation shift in the Cut-and-Paste (CAP) approach (Zhao et al., 1994) which allows me to cut and shift relative phase information to compare observed with synthetic data.

## 1.1 Motivation

The main goal of this thesis is earthquake source modeling using full waveform OBS data acquired during the VoiLA deployment in the Lesser Antilles subduction zone. Previous outputs of the VoiLA project were, among other things, a seismic database with well-located hypocenters and a local 1D velocity model. Both products presented a high-quality data set that reduced respective uncertainties in the source inversion. Full waveform source modeling using only OBS data is challenging due to large noise amplitudes on the horizontal components (high horizontal noise) and station misalignments which limited former studies in their usage. I tackle this issue by formulating these uncertainties in a Bayesian context. I created the Python program “AmΦB – Amphibious Bayesian” that allows me to consider them in my original uniXtree importance sampling algorithm, which efficiently samples in an X-dimensional parameter space following a uniform tree structure. The newly acquired moment tensor solutions largely increased the local database and allow a detailed study of the seismotectonic setting. Notable is hereby the highly active seismic cluster in intermediate depths near Martinique. The source process of earthquakes at intermediate depths is still debated and only resolved in a limited fashion. I focus on the following three key questions:

1. Can three-component OBS data be successfully used for full-waveform moment tensor inversion?
2. What can we learn about the seismotectonic setting of the Lesser Antilles Arc?
3. Can CLVD information be connected to a physical cause?

To explore the third question, I further tested the versatility of my code in different settings outside

---

<sup>8</sup>Regional Centroid-Moment Tensors

<sup>9</sup>Istituto nazionale di geofisica e vulcanologia

<sup>10</sup>National Research Institute for Earth Science and Disaster Resilience

the Lesser Antilles with various underlying complexities in the modeling process. Two of these applications are also presented here.

## 1.2 Outline

In the following, I will give a brief overview of the structure of this thesis. Following this general introduction, I introduce the *Theory and Methods*. In Chapter 2, I outline the physical definition of the moment tensor and its mathematical formulation. I discuss the equation of motion in a continuum and the representation theorem for a point source. This is followed by a general decomposition approach of the moment tensor into its physical components (Section 2.2). Chapter 3 gives an overview of different strategies for moment tensor inversion (Section 3.1) and introduces my new routine AmΦB – uniXtree (Section 3.2). I tested my inversion routine in different *Applications* using OBS and land recordings. The application in this thesis is focused on the Lesser Antilles Arc. Chapter 4 gives an overview of the geological history of the Caribbean Sea and the modern arc. In Chapter 5, I describe the modeling of moment tensors using the VoiLA OBS data set and the subsequent seismotectonic interpretations (Section 5.6) of the subduction zone. This chapter also includes different synthetic tests (Section 5.5) examining the influence of OBS-associated uncertainties and the performance of my Bayesian error formulation. The content of this chapter is published in the peer-reviewed journal *Geophysical Journal International* as Lindner et al. (2022). This work is followed by my focus study on the 2007  $M_w7.4$  intermediate-depth Martinique earthquake doublet in Chapter 6. This event is globally unique and gives valuable insight into the historical evolution of the Caribbean Sea toward the current seismotectonic settings of the arc. The content of this study is submitted to *Geophysical Research Letters*. Applications outside the Lesser Antilles originate from different collaboration works and provided valuable benchmark tests for my inversion routine on additional sources of uncertainties. Chapter 7 features my contributions on induced earthquakes by hydraulic fracturing near Blackpool, England. Using small-magnitude events I examined the performance of my code in high-frequency bands (up to 3 Hz) and with imprecise time information. This work was published in the peer-reviewed journal *Geophysical Journal International* (Karamzadeh et al., 2021). Chapter 8 features my unpublished work on the 2020  $M_w6.5$  Monte Christo Range, Nevada earthquake sequence. The complexity of the rupture history led to my development of the doublet inversion routine, that was used for the Martinique earthquake in Chapter 6. A *Summary* of my thesis and conclusions regarding the key questions posed in Section 1.1 are given in Chapter 9 which ends with a brief outlook on possible future extensions.





## Chapter 2

# Theory on moment tensor

In this chapter, I summarize the theoretical background of a seismic source in the formulation of a moment tensor following a point source approximation. The physical model of the forward formulation and descriptive equations are introduced and constructing elements of the general seismological source are discussed. All equations and physical principles in this chapter were, if not noted otherwise, derived and discussed in detail in, e.g., Kennett (2009), Dahlen et al. (1998), Kennett (2001), Aki et al. (2002), and Stein et al. (2009). In the second part I will introduce the general eigenvalue decomposition approach of a moment tensor, e.g., Jost et al. (1989) and Dahm et al. (2014).

### 2.1 Seismic point source

Important and recurring parameters introduced in this section are listed in Table 8.3.

*Table 2.1: Important recurring parameters.*

Symbol	Parameter
$\lambda, \mu$	Lamé parameter
$\vec{u}, \vec{d}$	displacement
$\vec{f}, \vec{e}$	body force
$\vec{\tau}_{ij}, \sigma_{ij}, \Gamma_{ij}$	model/true stress, stress glut
$\vec{n}$	fault normal
$\Sigma, \vec{\xi}$	fault area, coordinate
$G_{kp}, \mathbf{G}$	Green's function/matrix
$\vec{T}$	traction
$\mathbf{M}, m$	moment tensor, moment tensor density
$s(t)$	source time function

#### 2.1.1 Equation of motion in a continuum

A seismic event can be observed as a suddenly occurring local and transient change in the natural state of the Earth (e.g., ground motion). Such events can be of anthropogenic (e.g., running machinery, walking humans or animals, explosions) or natural (e.g., earthquakes, volcanic eruptions, landslides, meteor impact, meteorological occurrences) cause. While former sources might differ in their complexity (e.g., defined movements of machines or arbitrary sequence of steps of a crowd) they are of no interest to this study and occur primarily as undesired noise signals in the data. As for the latter source, the scope of this study is focused on the description of earthquakes, however, the introduced theory holds for all aforementioned types of sources.

An earthquake can be defined as a dislocation problem occurring in the Earth's interior. Such dislocations generally occur on pre-existing weakening structures – faults – and display a finite geometry. Seismic activity on these structures depends on the prevailing local stress regime  $\sigma_{ij}$ . The occurrence of an earthquake poses as a finite nonlinear failure of the physical equilibrium (natural state) that needs to be corrected. Using the equation of motion in a continuum we can describe a displacement  $\vec{u}$  in an elastic medium induced by an acting body force  $f_j$  and an “extra” body force  $e_j$  (Kennett, 2009) as

$$\rho \partial_{tt} u_j = \partial_i \tau_{ij} + f_j + e_j \quad (2.1)$$

with material density  $\rho$ , spatial derivative  $\partial_i$  in  $i$ -direction and second time derivative  $\partial_{tt}$ . Body force  $f_j$  is mainly contributed by self-gravitational effects, which we can assume as stationary in time for our purposs. Extra body force  $e_j$  is introduced in the literature as “equivalent force distribution” and yields from the earthquake, hence is only non-zero at the fault.  $\tau_{ij}$  is the theoretical stress, as the true stress  $\sigma_{ij}$  is not known, and is contributed by both body forces (stress is defined as the force per unit area  $\sigma = F/A$ ). It deviates from the true physical stress and defines the extra force  $e_j$  with

$$e_j = \partial_i \sigma_{ij} - \partial_i \tau_{ij} \quad \text{and} \quad e_j^S = n_i \sigma_{ij} - n_i \tau_{ij} \quad (2.2)$$

at its surface as a traction force parallel to the outward-pointing surface normal  $\vec{n}$ .

Using the generalized Hooke's Law, we can model the theoretical stress as

$$\tau_{ij} = c_{ijpq} \varepsilon_{pq} \quad \text{with strain tensor} \quad \varepsilon_{pq} = \frac{1}{2} (u_{p,q} + u_{q,p}). \quad (2.3)$$

Here,  $u_{p,q}$  and  $u_{q,p}$  describe the derivatives of the displacement in  $q$ -direction and  $p$ -direction, respectively. The relation between stress and strain is proportional until its reaching the initiation point of plastic deformation (yield point). We only focus on the proportionality range and describe with the elasticity tensor  $c_{ijpq}$ . This tensor contains 81 components ( $3^4$ ) that can be reduced to 21 components (symmetric  $6 \times 6$  matrix) due to symmetric characteristics of the stress ( $\tau_{ij} = \tau_{ji} \Rightarrow c_{ijpq} = c_{jipq}$ , balance of the angular momentum) and strain ( $\varepsilon_{pq} = \varepsilon_{qp} \Rightarrow c_{ijpq} = c_{ijqp}$ , assuming small excitations that can be treated as linear) tensor and energetic ( $c_{ijpq} = c_{pqij}$ , hyperelasticity<sup>1</sup>) assumptions. Written as matrix we have,

$$\tau_{ij} = \begin{pmatrix} \tau_{11} & \tau_{12} & \tau_{13} \\ \tau_{21} & \tau_{22} & \tau_{23} \\ \tau_{31} & \tau_{32} & \tau_{33} \end{pmatrix}, \quad \varepsilon_{pq} = \begin{pmatrix} \varepsilon_{11} & \varepsilon_{12} & \varepsilon_{13} \\ \varepsilon_{21} & \varepsilon_{22} & \varepsilon_{23} \\ \varepsilon_{31} & \varepsilon_{32} & \varepsilon_{33} \end{pmatrix} \quad (2.4)$$

and the elasticity tensor in the convention of Voigt (1928) as

$$C_{mn} = \begin{pmatrix} c_{1111} & c_{1122} & c_{1133} & c_{1123} & c_{1113} & c_{1112} \\ c_{2211} & c_{2222} & c_{2233} & c_{2223} & c_{2213} & c_{2212} \\ c_{3311} & c_{3322} & c_{3333} & c_{3323} & c_{3313} & c_{3312} \\ c_{2311} & c_{3222} & c_{2333} & c_{2323} & c_{2313} & c_{2312} \\ c_{1311} & c_{1322} & c_{1333} & c_{1323} & c_{1313} & c_{1312} \\ c_{1211} & c_{1222} & c_{1233} & c_{1223} & c_{1213} & c_{1212} \end{pmatrix} = \begin{pmatrix} C_{11} & C_{12} & C_{13} & C_{14} & C_{15} & C_{16} \\ C_{21} & C_{22} & C_{23} & C_{24} & C_{25} & C_{26} \\ C_{31} & C_{32} & C_{33} & C_{34} & C_{35} & C_{36} \\ C_{41} & C_{42} & C_{43} & C_{44} & C_{45} & C_{46} \\ C_{51} & C_{52} & C_{53} & C_{54} & C_{55} & C_{56} \\ C_{61} & C_{62} & C_{63} & C_{64} & C_{65} & C_{66} \end{pmatrix}. \quad (2.5)$$

The matrix equation is then

$$\vec{\tau} = \mathbf{C} \cdot \vec{\varepsilon} \quad \Leftrightarrow \quad c_{ijpq} = \frac{\tau_{ij}}{\varepsilon_{pq}} = \text{constant}, \quad (2.6)$$

with the six independent elements of stress and strain in vector form

$$\vec{\tau} = [\tau_{11}, \tau_{22}, \tau_{33}, \tau_{23}, \tau_{13}, \tau_{12}]^T$$

and  $\vec{\varepsilon} = [\varepsilon_{11}, \varepsilon_{22}, \varepsilon_{33}, \varepsilon_{23}, \varepsilon_{13}, \varepsilon_{12}]^T.$

<sup>1</sup>Hyperelastic materials return to their initial form if the induced force is released, e.g., rubber band.

With isotropic assumptions, we can further reduce it to two parameters – Lamé parameters – which form an elastic fourth-order tensor with

$$c_{ijpq} = \mu(\delta_{ip}\delta_{jq} + \delta_{iq}\delta_{jp}) + \lambda\delta_{ij}\delta_{pq}. \quad (2.7)$$

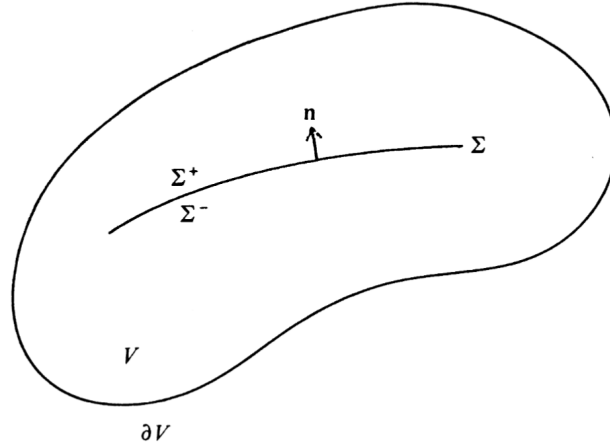
The elastic matrix is then

$$C_{mn} = \begin{pmatrix} 2\mu + \lambda & \lambda & \lambda & 0 & 0 & 0 \\ \lambda & 2\mu + \lambda & \lambda & 0 & 0 & 0 \\ \lambda & \lambda & 2\mu + \lambda & 0 & 0 & 0 \\ 0 & 0 & 0 & \mu & 0 & 0 \\ 0 & 0 & 0 & 0 & \mu & 0 \\ 0 & 0 & 0 & 0 & 0 & \mu \end{pmatrix}. \quad (2.8)$$

The first Lamé parameter  $\lambda$  describes an elastic modulus (elastic properties of materials) and the second Lamé parameter  $\mu$  is equivalent to the shear modulus or rigidity (ratio of shear stress to shear strain).

### 2.1.2 The representation theorem

Let us assume a finite elastic body with volume  $V$  and surface  $S$  (Figure 2.1). In its interior, located at  $\vec{\eta}$ , is a discontinuity (i.e., fault) with surface area  $\Sigma$ . At time  $t'$ , a displacement  $\vec{u}(\vec{\xi}, t')$  at  $\vec{\xi} \in \Sigma$  is generated, which is orientated parallel to the surface normal  $\vec{n}$  of  $\Sigma$  and introduces traction  $[\vec{T}]$  from  $\Sigma^-$  to  $\Sigma^+$ . This motion on the fault results in a displacement  $u_k(\vec{x}, t)$  in  $k$ -direction at an observation point  $\vec{x} \in S$  at time  $t$ .



**Figure 2.1:** Schematic plot of the representation theorem. Here,  $\partial V$  is surface  $S$ . Figure by Kennett (2009).

Using the equation of motion (Equation 2.2), Burridge et al. (1964) derived the elastodynamic *representation theorem* to relate the displacement at the source to a displacement at the surface  $S$ :

$$u_k(\vec{x}, t) = \int_{-\infty}^{\infty} dt' \int_V f_p(\vec{\eta}, t') G_{kp}(\vec{x}, t - t'; \vec{\eta}, 0) dV \\ + \int_{-\infty}^{\infty} dt' \int_{\Sigma} \{ [u_i] c_{ijpq} n_j G_{kp,q}(\vec{x}, t - t'; \vec{\xi}, 0) - [T_p] G_{kp}(\vec{x}, t - t'; \vec{\xi}, 0) \} d\Sigma \quad (2.9)$$

The first expression on the right-hand side represents an integral over the full volume of the body with an acting body force  $\vec{f} = \vec{f}(\vec{\eta}, t')$  throughout  $V$ , generated at a general position  $\vec{\eta}$  at time  $t'$ . This force primarily originates from the gravitational potential and is for this study of lesser interest. The second expression represents the contribution from the activity on  $\Sigma$ . Parameters written in square brackets (e.g.,  $[\vec{u}]$  or  $[\vec{T}]$ ) refer to the discontinuity from  $\Sigma^-$  to  $\Sigma^+$  hence describe the

differences between both sides of the fault (e.g.,  $[\vec{u}] = \vec{u}|_{\Sigma^+} - \vec{u}|_{\Sigma^-}$ ).  $[\vec{u}]$  describes the displacement discontinuity  $\vec{u} = \vec{u}(\vec{\xi}, t')$  on  $\Sigma$ ,  $\vec{\xi}$  being a general position on  $\Sigma$ , in direction of  $\vec{n}$  and is effectively the equivalent body force at the fault. The second part is governed by the traction discontinuity  $\vec{T} = \vec{T}(\vec{u}(\vec{\xi}, t'), \vec{n})$  which describes the traction on  $\Sigma$  that measures the force acting per unit area across the internal surface pointing from  $\Sigma^-$  as pressure  $-\vec{n}\vec{T}$  to  $\Sigma^+$  as pulling force  $\vec{n}\vec{T}$ . In other words, it quantifies the contact force between particles at both sides of the surface and is related to the stress field  $\tau_{ij}$  (compare Equation 2.3)

$$[\vec{T}] = [\tau_{ij}] = [u_{p,q}]c_{ijpq}. \quad (2.10)$$

Notable in Equation 2.9 is a missing surface integral over  $S$ . While it is still involved in the derivation of the representation theorem, it vanishes if homogeneous boundary conditions (Dirichlet and Neumann) on  $S$  (free surface condition in the assumption of transition between the solid Earth to vacuum) for  $u_i$  and  $G_{kp}$  are applied (Burridge et al., 1964). This assumption allows a reciprocal examination (Betti's theorem) of the source-receiver ( $\vec{\xi}$  to  $\vec{x}$ ) geometry if the source is treated as a point in space (point source approximation). Propagating effects between both points due to the structural components in the body volume  $V$  are described by Green's tensor  $\mathbf{G}$ . The tensor is defined as a solution of the wave equation

$$\rho \frac{\partial^2 G_{in}}{\partial t^2} - \frac{\partial}{\partial x_j} \left( c_{ijpq} \frac{\partial G_{pn}}{\partial x_q} \right) = \delta_{in} \delta(\vec{x} - \vec{\xi}) \delta(t - t') \quad (2.11)$$

excited by a delta impulse in time and space. The delta impulse in space allows this approximation of the source as a single point in space. This is useful and well-chosen if the studied source is small compared to the receiver distance and allows to further simplify Equation 2.9. By applying all the aforementioned relations, Equation 2.9 can be expressed as

$$u_k(\vec{x}, t) = \int_{-\infty}^{\infty} dt' \int_{\Sigma} G_{kp}(\vec{x}, t - t'; \vec{\xi}, 0) e_p(\vec{\xi}, t') d\Sigma. \quad (2.12)$$

This equation describes the ground displacement in  $k$ -direction as a time and volume integration of  $\Sigma$  over a linear combination of the structural Green's tensor between source  $\vec{\xi}$  and observation  $\vec{x}$  point and the body force  $\vec{e} = \vec{e}(\vec{\xi}, t')$ . The body force is then composed of the displacement

$$\vec{e}^{[\vec{u}]}(\vec{\xi}, t') = \int_{\Sigma} [u_i] c_{ijpq} n_j \frac{\partial}{\partial \xi_q} \delta(\xi) d\Sigma \quad (2.13)$$

and the traction discontinuity

$$\vec{e}^{[\vec{T}]}(\vec{\xi}, t') = \int_{\Sigma} [\vec{T}] \delta(\xi) d\Sigma \quad (2.14)$$

following the approximation of a point source with  $[\vec{T}] \approx [\vec{T}] \delta(\xi) d\Sigma$  at the fault surface.  $\Sigma$  acts as a boundary in the solid media (Gaussian pill box model) and has to satisfy certain conditions. The integral in  $\vec{e}^{[\vec{T}]}$  becomes negligible if the source volume is restricted to a surface (thickness approaches zero). This leads to the same contribution of traction on the top and bottom side of  $\Sigma$  with inverse sign because the unit normals are pointing in the opposite directions  $\vec{T}^+ + \vec{T}^- = 0$ . This assumption is further contributed by the model of a spontaneous rupture ( $\delta$ -function) which results in continuous traction on the fault. Traction becomes important for more complex extended dynamic source models where friction across the fault plane varies (e.g., Madariaga et al., 2002; Ramos et al., 2022) but then introduces more uncertainties into the modeling. This leaves only the body force contribution of displacement discontinuity.

Backus et al. (1976a,b) introduced the moment tensor density  $m_{pq}$

$$m_{pq} = [u_i] n_j c_{ijpq} \quad (2.15)$$

to describe the equivalent force distribution of  $e_p^{[\vec{u}]}$  across the source region. With  $c_{ijpq}$  assumed to be isotropic (see Equation 2.7), we can write

$$m_{pq} = \mu([u_p]n_q + [u_q]n_p) + \lambda[u_i]n_i\delta_{pq}. \quad (2.16)$$

Equation 2.3 and Equation 2.2 shows that the moment tensor density directly relates to the stress changes induced by the source. Backus et al. (1976a,b) introduced the quantity *stress glut*  $\Gamma_{ij}$  to describe the difference between natural stress-field  $\sigma_{ij}$  and the theoretical stress-field  $\tau_{ij}$  as

$$\Gamma_{ij} = \sigma_{ij} - \tau_{ij} = m_{ij}. \quad (2.17)$$

Here,  $m_{ij}$  is symmetric as the summed force (net force) exerted by the equivalent force  $\vec{e}^{[\vec{u}]}$  must vanish.  $\Gamma_{ij}$  is only non-zero within the source volume, indicating that the modeled stress changes with the source volume while the true stress remains unchanged.

This assumption further simplifies Equation 2.12 to

$$u_k(\vec{x}, t) = \int_{-\infty}^{\infty} dt' \int_{\Sigma} G_{kp}(\vec{x}, t - t'; \vec{\xi}, 0) e_p^{[\vec{u}]}(\vec{\xi}, t') d\Sigma \quad (2.18)$$

which is the general form of the representation theorem used in different publications (e.g., Stump et al., 1977; Nabelek, 1984; Jost et al., 1989; Dahm, 1993; Foulger et al., 2014). However, this expression is not practicable and includes higher-order contributions in the body force term and the Green's tensor which are negligible. Stump et al. (1977) used a Taylor expansion around the point source location  $\vec{\xi}$  to get

$$G_{kp}(\vec{x}, t - t'; \vec{\xi}, 0) = \sum_{n=0}^{\infty} \frac{1}{n!} \xi_{j1} \dots \xi_{jn} G_{kp,j1\dots jn}(\vec{x}, t - t'; \vec{\xi}, 0) \quad (2.19)$$

with  $n$  being the index of the  $n$ -th partial derivative to  $j$ . Likewise, the equivalent body force can be extended with

$$M_{pq1\dots qn}(t) = \int_{\Sigma} (\xi_0 - \xi_{q1})(\xi_0 - \xi_{q2}) \dots (\xi_0 - \xi_{qn}) e_p^{[u]}(\vec{\xi}, t') d\Sigma \quad (2.20)$$

defining the *seismic moment tensor* in  $n$ -th degree of a point source.

Combining both extensions, Equation 2.18 leads to

$$\begin{aligned} u_k(\vec{x}, t) &= \sum_{n=0}^{\infty} \frac{1}{n!} G_{kp,j1\dots jn}(\vec{x}, t - t'; \vec{\xi}, 0) * M_{pq1\dots qn}(t) \\ &= G_{kp}(\vec{x}, t - t'; \vec{\xi}, 0) * M_p(t) + \frac{\partial}{\partial \xi_q} G_{kp}(\vec{x}, t - t'; \vec{\xi}, 0)|_{\vec{\xi}_0} * M_{pq1} + \dots \end{aligned} \quad (2.21)$$

describing the summation of the terms in  $n$ -degrees with the time integral replaced by a convolution (operator  $*$ ) of Green's tensor and the moment tensor. The zeroth-degree ( $n = 0$ ) moment tensor  $M_p(t)$  describes the vectorial sum of the net force that, following Newton's 3rd Law, is zero if effects of gravitation and mass advection are omitted (Dahm, 1993; Donner, 2021). The first-degree ( $n = 1$ ) term represents the commonly used second-order moment tensor for the seismic point source approximation at low frequencies below the corner frequency of the studied event (Doornbos, 1982; Donner, 2021). In this approximation we can represent fault size, source-time function and the rupture velocity of the earthquake (Stump et al., 1982). Moments of higher order ( $n > 1$ , usually up to  $n = 3$ ) can give information about the finiteness of a propagating fault (Backus, 1977b,a), whereas each higher-degree contribution introduces new unique variables. Few studies have been conducted using these higher-degree contributions, e.g., for the 1994 Bolivia deep earthquake to constrain the kinematic rupture geometry (Dahm et al., 1999), the 1999 Izmit earthquake to describe the spatiotemporal source behavior (Clévéde et al., 2004) or in applications for teleseismic

settings to resolve the fault plane ambiguity (McGuire et al., 2001). I will follow the first-degree approximation as Backus et al. (1976a) showed that terms of higher-degree have no significant influences on small sources or large wavelengths and would highly complicate the description of the source. These assumptions lead to the point-source formulation of the moment tensor problem

$$u_k(\vec{x}, t) = M_{pq}(t) * \frac{\partial}{\partial \xi_q} G_{kp}(\vec{x}, t - t'; \vec{\xi}, 0)|_{\xi_0}. \quad (2.22)$$

The moment tensor can be treated as time independent, if all of its elements have the same known time dependency. This can be achieved by introducing a source time function (STF)  $s(t)$  to the Green's tensor which introduces a rupture history to the earthquake. STFs can become arbitrarily complex and reflect frequency-dependent processes on an extended fault. Using a delta function as SFT can be a good approximation for narrow bandpass-filtered waveforms within the lower frequency range of an earthquake. Equation 2.22 then becomes

$$u_k(\vec{x}, t) = [G_{kp,q}(\vec{x}, t - t'; \vec{\xi}, 0) * s(t)] M_{pq}, \quad (2.23)$$

with  $M_{pq}$  representing the components of the final second-order moment tensor  $\mathbf{M}$ . Mathematically, a moment tensor describes a  $3 \times 3$  matrix of 9 scalar elements. This number is reduced to six independent elements following the symmetry of the underlying moment tensor density  $m_{pq}$  (Equation 2.17). Subsequently, I will only refer to the matrix formulation

$$\mathbf{U} = \mathbf{G}\mathbf{M} \quad \text{or} \quad \vec{d} = \mathbf{G}\vec{m} \quad (2.24)$$

with  $\mathbf{G}$  being the Green's function matrix including the STF  $s(t)$ ,  $\mathbf{U} \rightarrow \vec{d}$  the displacement time series representing the observed data and  $\mathbf{M} \rightarrow \vec{m}$  as moment tensor or model vector.

## 2.2 Moment tensor

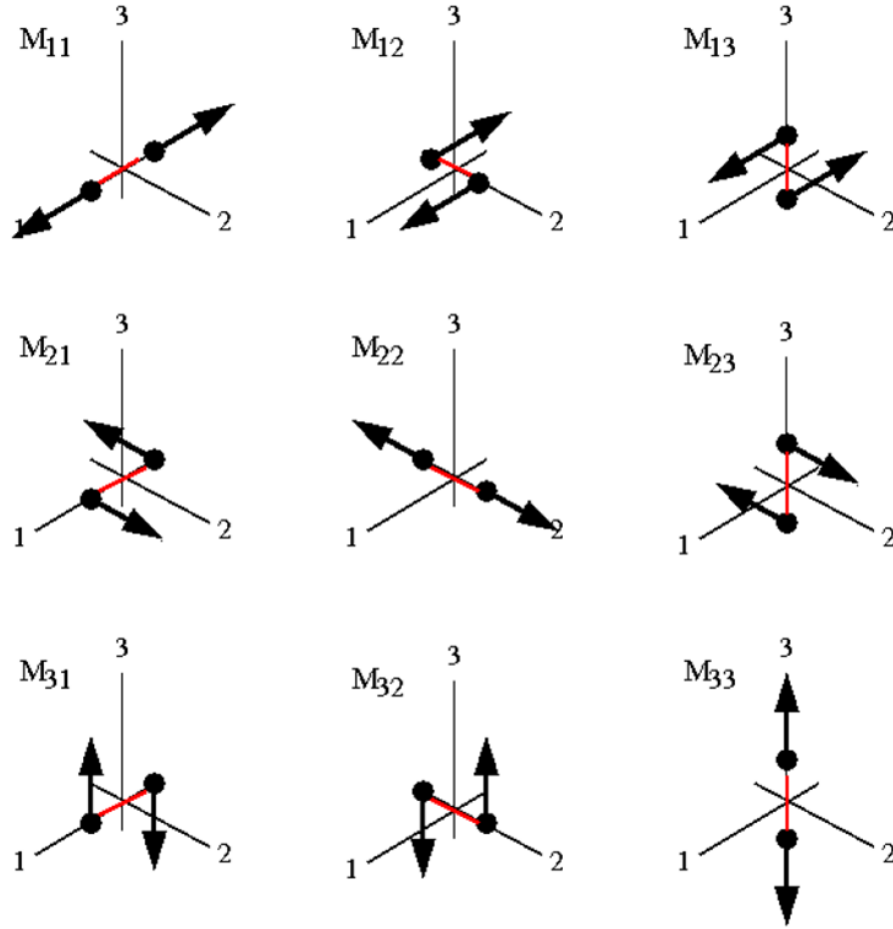
Representing source activity in a moment tensor formulation has versatile applications to different types of sources. However, in order to quantify them, an approach is needed to extract these information out of the  $3 \times 3$  tensor. I showed in Section 2.1.2 that the moment tensor  $\mathbf{M}$  is related to an equivalent body force which is described by several individual forces acting on a body. The individual forces are known as generalized force couples and have equal magnitudes in opposite directions at different lines of action. The vector sum of a couple is always zero. To describe an arbitrary source, only six elements are needed due to the symmetric features of the moment tensor. Elements on the main diagonal are linear vector dipoles (LVD) pointing parallel to a respected coordinate axis at an offset to its origin point. The off diagonal elements are force couples conserving the torque and are called double-couples. Important and recurring parameters introduced in this section are listed in Table 2.2.

**Table 2.2:** Important recurring parameters.

Symbol	Parameter
$x, y, z$	cartesian coordinates
$r, \Theta, \phi$	spherical coordinates
$\psi, \delta, \lambda$	strike, dip, rake
$\mu, \lambda_L$	Lamé parameter
$D_N/D_S, A$	tensile/shear displacement, fault area
$\Upsilon/v, \vec{e}$	eigenvalue, eigenvector
$a, b$	isotropic, deviatoric
$M_w, M_0$	moment magnitude, scalar moment
T/B/P	tension/null/pressure

### 2.2.1 Coordinate system

Figure 2.2 depicts the force couples in a Cartesian coordinate system at a possible  $3 \times 3$  matrix arrangement.



**Figure 2.2:** System of force couples. Figure by Dahm et al. (2014).

The force couples are reflected in their postings in the moment tensor

$$M_{pq} = \begin{pmatrix} M_{11} & M_{12} & M_{13} \\ M_{21} & M_{22} & M_{23} \\ M_{31} & M_{32} & M_{33} \end{pmatrix} \quad (2.25)$$

with symmetric elements

$$M_{12} = M_{21}, \quad M_{13} = M_{31}, \quad \text{and} \quad M_{23} = M_{32}. \quad (2.26)$$

This arrangement of the elements is not unique and depends on the chosen coordinate system. Over time two prominent systems have been proposed which hold specific advantages for different application:

1. Cartesian coordinate system: This system holds advantages for regional applications where the curvature of the Earth does not need to be considered. The definition of the coordinate axes, and hence the order of the elements in the moment tensor, may differ in the literature and thereupon build forward modelling or inversion codes (see Dahm et al. (2014) for an overview). The two most commonly used are the NED-system with  $x$  pointing north (N),  $y$  eastwards (E) and  $z$  downwards (D) hence on the main diagonal  $[M_{xx}, M_{yy}, M_{zz}]$  and the USE-system with  $z$  pointing upwards (U),  $x$  southwards (S) and  $y$  eastwards (E), hence on the main diagonal  $[M_{zz}, M_{xx}, M_{yy}]$ .



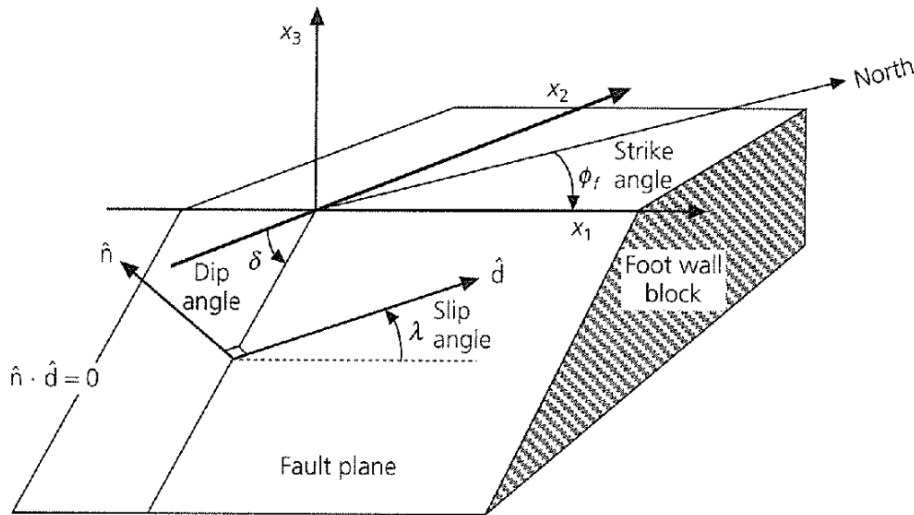
2. Spherical coordinate system: Gilbert et al. (1975) proposed to describe the full wavefield using a summation of normal modes of the Earth. They assumed a non-rotating spherically symmetric Earth that is excited by two distinct kinds of oscillation, which describe the surface displacement  $\vec{u} = (u_r, u_\Theta, u_\phi)$ . Toroidal or torsional oscillations can be separated into P-SV and SH motions and contribute to  $u_\Theta$  and  $u_\phi$ . A poloidal or spheroidal oscillation relates to P-SV motions which combines radial and transverse motions and contributes to the full displacement field  $\vec{u}$ . The wave motion is represented in the Green's function and therefore independent of the moment tensor formulation. The relation remains but alters order and direction of the moment tensor elements. The spherical coordinate representation follows the  $r - \Theta - \phi$ -system where  $r$  is pointing upward,  $\Theta$  southward and  $\phi$  westward. This system is used in the Global Centroid Moment tensors (GCMT) catalogue (Dziewonski et al., 1981) and in prominent waveform simulation codes such as SPECFEM3D global (Komatitsch et al., 1999) and SALVUS (Afanasiev et al., 2019).

I will follow the USE (Up-South-East) system which has common features to the  $r - \Theta - \phi$ -system and is used in the python framework *obspy* (Beyreuther et al., 2010). The conversion between the Cartesian and the Spherical coordinate system is

$$\mathbf{M} = \begin{pmatrix} M_{rr} & M_{r\Theta} & M_{r\phi} \\ M_{\Theta r} & M_{\Theta\Theta} & M_{\Theta\phi} \\ M_{\phi r} & M_{\phi\Theta} & M_{\phi\phi} \end{pmatrix} = \begin{pmatrix} M_{zz} & M_{zx} & -M_{zy} \\ M_{xz} & M_{xx} & -M_{xy} \\ -M_{yz} & -M_{yx} & M_{yy} \end{pmatrix} \quad (2.27)$$

## 2.2.2 Principal axes

In Section 2.1.2, I introduced a seismic fault as arbitrary surface area  $\Sigma$  which is composed of two adjunct parts ( $\Sigma^-$  and  $\Sigma^+$ ) being displaced relative to each other. Taking it into a more geometrical framework (Figure 2.3), fault surface  $\Sigma$  can be described as a finite, rectangular plane with its top boundary line rotated clockwise relative to geographic North (fault strike  $\psi$ ) and dipping relative to the Earth surface (fault dip  $\delta$ ). This model is generally known as a single fault model.



**Figure 2.3:** Geometric setting of an earthquake fault. Figure by Stein et al. (2009).

The geometric range is restricted by the relative orientation to north between  $0^\circ$  to  $360^\circ$  and possible fault dip angles from  $0^\circ$  (parallel to Earth's surface) to  $90^\circ$  (perpendicular to Earth's surface). Using these parameters it is possible to describe the static fault but not its dynamic range. The foot wall block represents one adjunct part of the structure, the second moving relative to it by the fault rake angle  $\lambda$  in the range  $-180^\circ$  to  $180^\circ$ . The fault rake defines the angle between the fault

strike and the fault slip-direction. Rake angles with positive sign describe downward, negative sign upward,  $\lambda = 0^\circ$  movements parallel and in striking direction and  $-180^\circ = 180^\circ$  movements parallel and opposite the striking direction. The orientation and slip-direction can then be described using the fault plane normal vector

$$\vec{n} = \begin{pmatrix} -\sin(\delta)\sin(\psi) \\ -\sin(\delta)\cos(\psi) \\ \cos(\delta) \end{pmatrix} \quad \text{and} \quad \vec{u} = \bar{u} \begin{pmatrix} \cos(\lambda)\cos(\psi) + \cos(\delta)\sin(\lambda)\sin(\psi) \\ -\cos(\lambda)\sin(\psi) + \sin(\delta)\cos(\lambda)\cos(\psi) \\ \sin(\delta)\sin(\lambda) \end{pmatrix} \quad (2.28)$$

giving the unit vector in slip-direction with average displacement  $\bar{u}$ . Following Equation 2.16, the moment tensor of a general dislocation source can be expressed by

$$M_{pq} = \mu \Sigma (n_p u_p + n_q u_q) + \lambda_L \Sigma n_i u_i \delta_{pq} \quad (2.29)$$

using the Lamé constants  $\lambda_L$  and  $\mu$  and displacement at the fault  $\vec{u}$ . The first part on the right-handed side describes a pure shear movement with results in a displacement between the two adjacent planes  $\Sigma^-$  and  $\Sigma^+$ . The second term introduces a dislocation of a tensile crack describing the opening of the fault planes parallel to  $\vec{n}$  between  $\Sigma^-$  and  $\Sigma^+$ . Tensile cracks are complex mechanisms that involve a mixture of different processes<sup>2</sup>. The relation between Equation 2.29 and the general dislocation fault model can be derived from the eigenvalue decomposition of  $\mathbf{M}$ . It allows to rotate a given tensor into a Cartesian coordinate system spanned by its principal axes  $\vec{e}^i$  ( $i \in [P, T, B]$ ) with

$$\mathbf{M} \vec{e}^i = \Upsilon \vec{e}^i. \quad (2.30)$$

This expression follows the definition of  $\mathbf{M}$  using the matrix multiplication

$$\mathbf{M} = \vec{e}^i \Upsilon (\vec{e}^i)^\top = \begin{pmatrix} \vec{e}_x^P & \vec{e}_x^B & \vec{e}_x^T \\ \vec{e}_y^P & \vec{e}_y^B & \vec{e}_y^T \\ \vec{e}_z^P & \vec{e}_z^B & \vec{e}_z^T \end{pmatrix} \cdot \begin{pmatrix} v^P & 0 & 0 \\ 0 & v^B & 0 \\ 0 & 0 & v^T \end{pmatrix} \cdot \begin{pmatrix} \vec{e}_x^P & \vec{e}_y^P & \vec{e}_z^P \\ \vec{e}_x^B & \vec{e}_y^B & \vec{e}_z^B \\ \vec{e}_x^T & \vec{e}_y^T & \vec{e}_z^T \end{pmatrix} \quad (2.31)$$

with  $\vec{e}^P$  representing the pressure or P-axis,  $\vec{e}^T$  representing the tension or T-axis,  $\vec{e}^B$  the null or B-axis and  $\Upsilon$  with  $v^T \geq v^B \geq v^P$  the eigenvalues as real numbers (e.g., Stein et al., 2009). The orthogonal eigenvectors describe the radiated force relative to the pressure or tension axis. However, the direction of both axes do not need to coincide with the maximal tectonic stress (McKenzie, 1969) as e.g., new faults tend to occur  $25^\circ$ - $30^\circ$  to the principal stresses instead of  $45^\circ$  (see angle between T-axis and active fault plane Figure 2.6, or in Barth, 2007). The relation between these axis, the fault normal and slip direction is given with

$$\vec{e}^T = \frac{1}{\sqrt{2}}(\vec{n} + \vec{u}), \quad \vec{e}^P = \frac{1}{\sqrt{2}}(\vec{n} - \vec{u}) \quad \text{and} \quad \vec{e}^B = \vec{n} \times \vec{u} \quad (2.32)$$

or in the inverse formulation

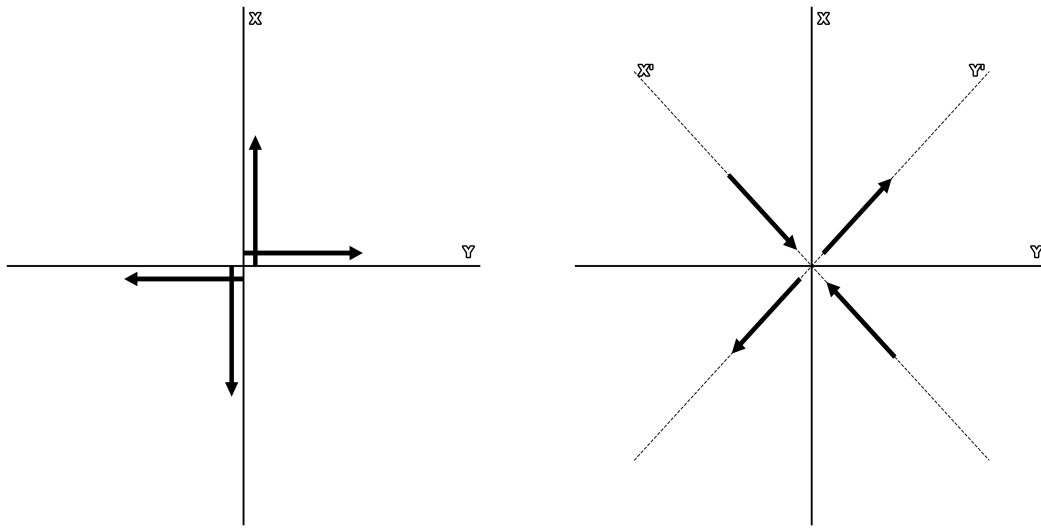
$$\vec{u} = \frac{1}{\sqrt{2}}(\vec{e}^T + \vec{e}^P) \quad \text{and} \quad \vec{n} = \frac{1}{\sqrt{2}}(\vec{e}^T - \vec{e}^P) \quad (2.33)$$

representing the 1st nodal plane and

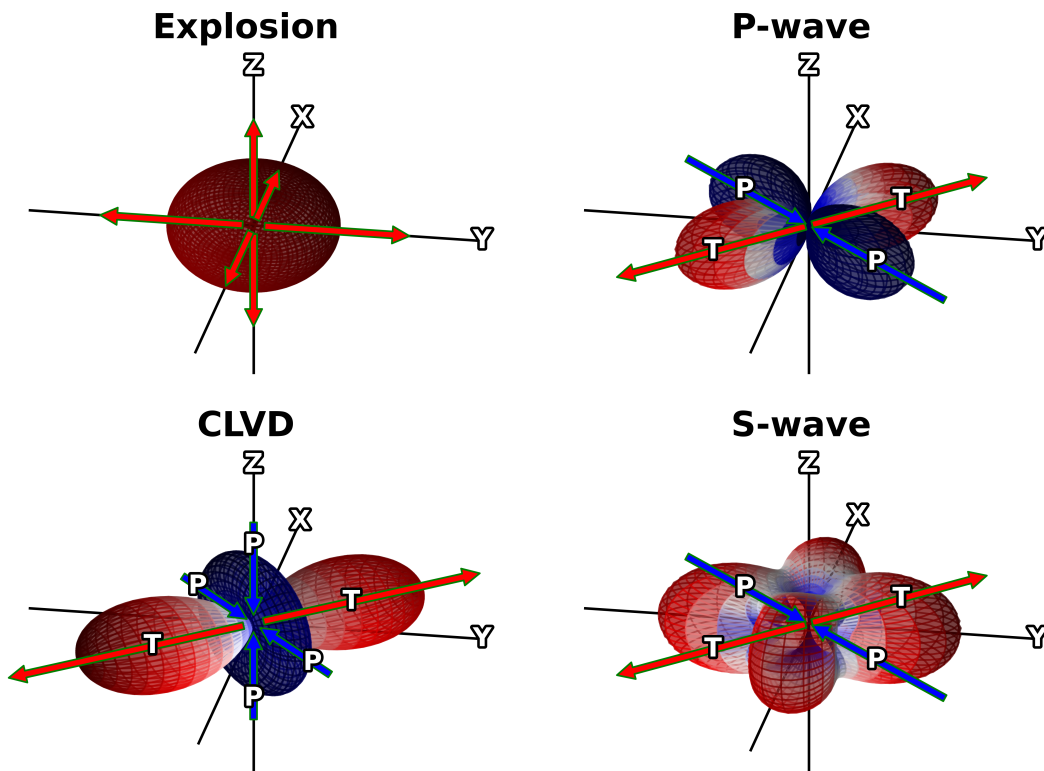
$$\vec{u} = \frac{1}{\sqrt{2}}(\vec{e}^T - \vec{e}^P) \quad \text{and} \quad \vec{n} = \frac{1}{\sqrt{2}}(\vec{e}^T + \vec{e}^P) \quad (2.34)$$

representing the 2nd nodal plane. Parallel to the intersection of the planes is the B-axis. Figure 2.4a displays this relation between the two coordinate representations. The graph on the left represents a force couple (e.g.,  $M_{12} = M_{21}$  in Figure 2.2) within a Cartesian coordinate system. It is given by the first part of Equation 2.29 and describes a double-couple in terms of the fault normal  $\vec{n}$  and slip direction  $\vec{u}$ . Using the eigenvalue transformation the force couple is rotated by  $45^\circ$  ( $[X, Y] \rightarrow [X', Y']$ )

<sup>2</sup>As I will not focus on these types of source mechanisms, interested readers may resort to Dahm et al. (e.g., 2014).



(a) Coordinate transformation.



(b) Radiation pattern. The B-axis of the CLVD, P-wave and S-wave radiation are oriented parallel to the Z-axis.

**Figure 2.4:** Coordinate transformation and general radiation pattern of prominent source mechanisms.

and results in the graph to the right with the vectors pointing parallel to the pressure (P) and tension (T) axis of the source mechanism. From Equations 2.33 and 2.34 follows

$$n_p u_p + n_q u_q = \vec{e}^T \vec{e}^T - \vec{e}^P \vec{e}^P \quad (2.35)$$

with  $\vec{e}^i \vec{e}^i$  being a dyadic second rank matrix (e.g., Ben-Menahem et al., 1981; Jost et al., 1989). This highlights both strength and limitation of the moment tensor source model.  $\vec{u}$  and  $\vec{n}$  are interchangeable, following the symmetric behaviour of  $\mathbf{M}$ , without affecting the displacement field. This simplifies the source modelling, however, introduces ambiguities into the interpretation of the fault geometry (active plane versus auxiliary plane). It is therefore not possible to definitely identify which of the two nodal planes represents the actual geological fault by simply using the moment tensor solution. Possible additional indicators include the historical seismicity, rupture directivity modelling or geological observations at the surface (e.g., surface rupture).

The sum of the eigenvalues  $\Upsilon$  describe the volumetric changes (see Section 2.2.3) during the source process. General case for tectonic earthquakes is a sum of zero which represents a deviatoric source mechanism (see Section 2.2.3). Regarding the eigenvalues two general cases become need to be distinguished: (a) The first case is that one eigenvalue equals zero (corresponding to the B-axis), one equals 1 (T-axis) and the remaining one equals  $-1$  (P-axis). This state describes a pure double-couple (see Section 2.2.3) source mechanism which can be full described by three angles ( $\psi$ ,  $\delta$  and  $\lambda$ ) and a scalar value (see section 2.2.3). (b) However, if non of the eigenvalues is zero but the sum is, the moment tensor is composed of contribution that are not of volumetric origin and do not fulfill the single source assumption. Possible explanations are much more complex source settings consisting of e.g., a major and minor double-couple or a double-couple and a CLVD, short for Compensated Linear Vector Dipol (see Section 2.2.3). Figure 2.4b displays the radiation pattern of aforementioned sources. Explosions and CLVD are special cases and will be discussed in Section 2.2.3. The radiation pattern of the P- and S-wave describe different wave-types of the same double-couple mechanism displayed in Figure 2.4a - a strike-slip mechanism (see Section 2.2.3). The orbitals of pressure and tension are parallel to the respected principal axis (P-wave) or in a given angular relation to them (e.g., S-wave is rotated by  $45^\circ$ ).

Considering the relations in Equations 2.28 to 2.32, we can now define the moment tensor elements of a shear dislocation using the geometric parameters and the fault displacement  $\vec{U}^3$ :

$$\begin{aligned} M_{zz} &= M_0 \cdot [\sin(2\delta)\sin(\lambda)] \\ M_{xx} &= -M_0 \cdot [\sin(\delta)\cos(\lambda)\sin(2\phi) + \sin(2\delta)\sin(\lambda)\sin^2(\phi)] \\ M_{yy} &= M_0 \cdot [\sin(\delta)\cos(\lambda)\sin(2\phi) - \sin(2\delta)\sin(\lambda)\cos^2(\phi)] \\ M_{xz} &= -M_0 \cdot [\cos(\delta)\cos(\lambda)\cos(\phi) + \cos(2\delta)\sin(\lambda)\sin(\phi)] \\ M_{yz} &= -M_0 \cdot [\cos(\delta)\cos(\lambda)\sin(\phi) - \cos(2\delta)\sin(\lambda)\cos(\phi)] \\ M_{xy} &= M_0 \cdot [\sin(\delta)\cos(\lambda)\cos(2\phi) + 0.5\sin(2\delta)\sin(\lambda)\sin(2\phi)] \end{aligned} \quad (2.36)$$

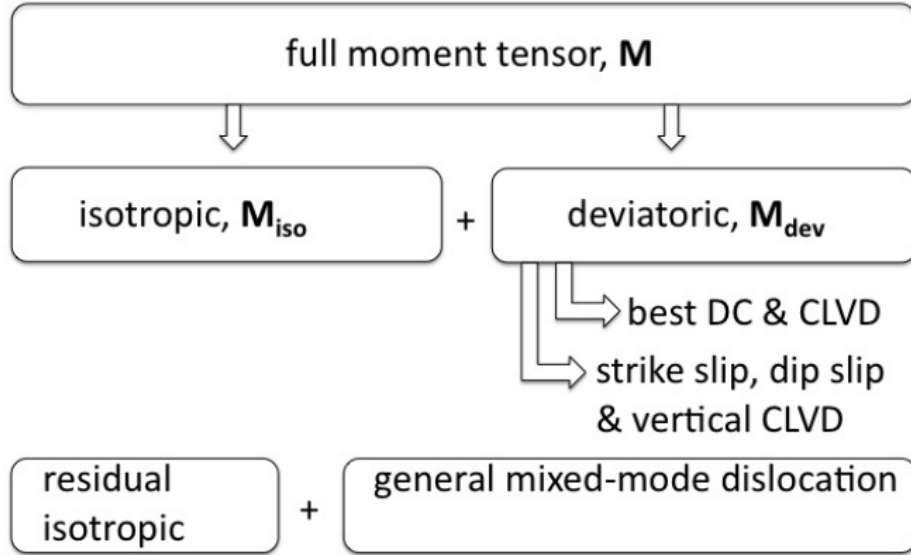
Shown element-wise relation combines dislocations due to a shear movement and dislocation generated by a tensile crack. Later source process is of non-deviatoric nature and is contributed of a mixture of isotropic and CLVD contributions.

### 2.2.3 Moment tensor decomposition

In Section 2.2.2 I introduced the eigenvalue transformation of the general Cartesian coordinate system (see Section 2.2.1) to a source specific system aligning with the principal stresses of a shear mechanism. In order to interpret a moment tensor we need to decompose it into its different contributions. Figure 2.5 depicts the general decomposition strategy.

---

<sup>3</sup>see, e.g., Dahm et al. (2014) for tensile crack contributions.



**Figure 2.5:** Moment tensor decomposition. Figure by Dahm et al. (2014).

The full moment tensor  $\mathbf{M}$  is, in a first step, separated into isotropic and deviatoric contributions

$$\mathbf{M} = \mathbf{M}_{\text{iso}} + \mathbf{M}_{\text{dev}} \quad (2.37)$$

whereas the deviatoric part can be further decomposed into different parts (e.g., double-couple, CLVD) depending on the complexity of the actual source mechanism. This decomposition can be described using scalar portion parameters (e.g.,  $a$  and  $b$ , Zhu et al., 2013) relative to the tensor  $\|\mathbf{M}_x\| = \frac{\mathbf{M}_x}{M_0}$  normalized by the seismic moment  $M_0$

$$\|\mathbf{M}\| = a\|\mathbf{M}_{\text{iso}}\| + \sqrt{1 - a^2}(\sqrt{1 - b^2}\|\mathbf{M}_{\text{DC}}\| + b\|\mathbf{M}_{\text{CLVD}}\|) \quad (2.38)$$

with  $a \in [-1, 1]$  representing the isotropic to deviatoric portion of the tensor and  $b \in [-1, 1]$  representing the double-couple to CLVD portion part of the full moment tensor.

### Seismic moment

The strength of a source is described by the seismic moment (Aki, 1966)

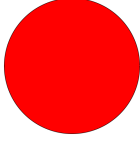
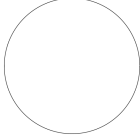
$$M_0 = \frac{1}{\sqrt{2}} \sqrt{M_{ij}^2} = \mu A \bar{u}, \quad (2.39)$$

a scalar quantity with the physical SI unit  $[M_0] = \text{Nm}$  (e.g., used in the USGS catalogue) or in CGS with  $[M_0] = \text{dyne-cm} = 10^{-7} \text{Nm}$  (e.g., used in the GCMT catalogue) which both represent torque. It is also possible to relate the seismic moment to the source setting by using a shear modulus  $[\mu] = \frac{\text{N}}{\text{m}^2}$ , surface area of the fault  $A = \text{m}^2$  and the average displacement discontinuity (slip)  $[\bar{u}] = \text{m}$ .  $M_0 = M_0(t)$  is time dependent (compare STF) as slip and the fault area are construct over the rupture period which can last up to several minutes for large earthquakes (e.g., 2011 M9.0 Tohoku event with a half duration of  $t_{\text{half}} = 70$  seconds according to the GCMT solution). The final moment is computed on the average slip and the full fault area. Notable for later application is the linear relation of the seismic moment to the signal amplitude. The relative amplification of the amplitude can be used to re-scale  $M_0$ . Using this definition of the seismic moment, (Hanks et al., 1979) defined the the moment magnitude scale

$$M_w = \frac{2}{3} (\log_{10} M_0 - 16.1). \quad (2.40)$$

Using quantities  $M_0$  and  $M_w$ , it is possible to express the strength of a seismic source but not it's underlying mechanism.

**Table 2.3:** *Isotropic components of a moment tensor.*

Mechanism	MT	$tr(\mathbf{M})$	Beachball
Explosion	$\frac{1}{\sqrt{3}} \begin{pmatrix} 1 & 0 & 0 \\ 0 & 1 & 0 \\ 0 & 0 & 1 \end{pmatrix}$	$> 0$	
Implosion	$-\frac{1}{\sqrt{3}} \begin{pmatrix} 1 & 0 & 0 \\ 0 & 1 & 0 \\ 0 & 0 & 1 \end{pmatrix}$	$< 0$	

### Isotropic source

The most basic source model is that of isotropic radiation. Exited force couples are only non-zero on the main diagonal and share a uniform magnitude in all directions. For the moment tensor these contributions are referred to as the trace

$$tr(\mathbf{M}) = \sum_i^3 M_{ii} \quad (2.41)$$

of the matrix. If  $tr(\mathbf{M}) > 0$ , then the isotropic component describes a positive volume change (i.e., explosion), if  $tr(\mathbf{M}) < 0$  a negative volume change (i.e., implosion) and if  $tr(\mathbf{M}) = 0$  no changes in the volume (see Table 2.3). These volumetric changes can occur within the Earth, e.g., volcanic (Thurin et al., 2022) or mining activities (Lizurek, 2017; Caputa et al., 2021), near or on its surface (e.g., nuclear test explosions, Gaebler et al., 2019) or above it (e.g., meteor explosion). The isotropic component is of minor interest for tectonic earthquake events as it is assumed that volume changes cannot occur at considerable depths due to the lithostatic pressure (Cassinis, 2013). The isotropic moment tensor is then

$$\mathbf{M}_{iso} = \frac{1}{3} tr(\mathbf{M}) \mathbf{I} \quad (2.42)$$

with normalization factor  $\frac{1}{3}$  and unit matrix  $\mathbf{I}$ .

### Deviatoric source

The deviatoric moment tensor  $\mathbf{M}_{dev}$  describes a system of three unequal principal stresses and is defined solely by vector dipoles. Its properties are derived from the isotropic part, after its removal from the full tensor:

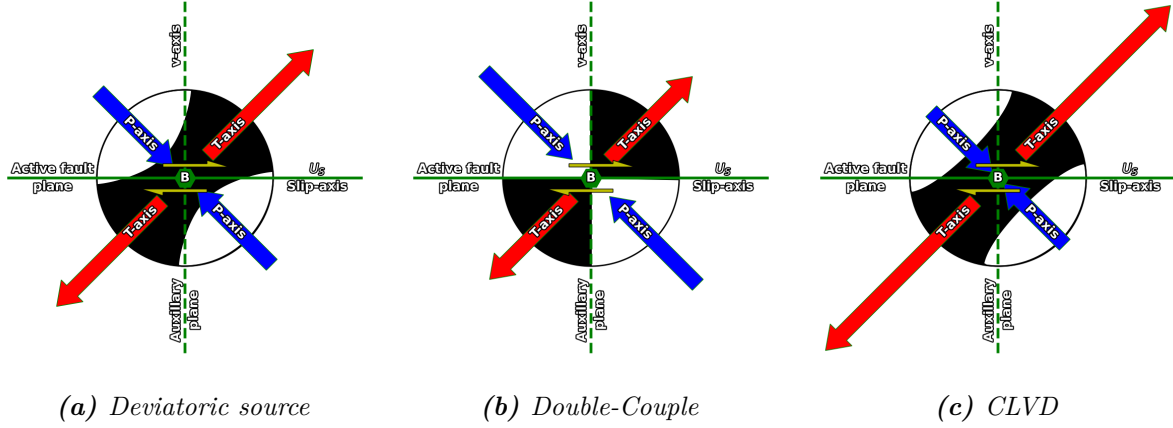
$$\mathbf{M}_{dev} = \mathbf{M} - \mathbf{M}_{iso} \quad (2.43)$$

It is related to shear faulting which includes no net volume change, hence the trace of  $\mathbf{M}$  is zero (Ammon et al., 2020). Shear movements change the form of a body but conserved the volume. On the other hand, this also means that a pure isotropic source changes the volume of a body, but not its shape. The three vector dipoles of a deviatoric source are

$$\bar{m}_1 = \begin{pmatrix} m_1^* & 0 & 0 \\ 0 & 0 & 0 \\ 0 & 0 & 0 \end{pmatrix}, \bar{m}_2 = \begin{pmatrix} 0 & 0 & 0 \\ 0 & m_2^* & 0 \\ 0 & 0 & 0 \end{pmatrix}, \bar{m}_3 = \begin{pmatrix} 0 & 0 & 0 \\ 0 & 0 & 0 \\ 0 & 0 & m_3^* \end{pmatrix}$$

and act in a linear combination to constructed the tensor based on the orthonormal basis of eigenvectors (e.g., Jost et al., 1989; Vavryčuk, 2015)

$$\mathbf{M}_{dev} = m_1^* \vec{e}^i \vec{e}^i + m_2^* \vec{e}^j \vec{e}^j + m_3^* \vec{e}^k \vec{e}^k. \quad (2.44)$$



**Figure 2.6:** Example of the principal axis for a) a deviatoric source composed of a strike-slip with 50% CLVD b) pure strike-slip and c) a pure CLVD. The T-axis corresponds to the positive eigenvalue and the direction of tension. The P-axis corresponds to the negative eigenvalue and the direction of pressure. The B-axis is pointing outwards the paper plane at the intersection between the two nodal planes. P and T axis do not have to be identical to the axis of maximal tectonic stress. Slip with displacement  $U_S$  occurred on the active plane along the green arrows.

with  $i, j, k \in [T, B, P]$  and  $i \neq j \neq k$  and  $m_i^*$  being a diagonal matrix representing the deviatoric stress. Equation 2.44 describes the orientation of the three vector dipoles in the direction of the principal stresses. A deviatoric moment tensor can be further decomposed into different contributions.

**Double-couple** A double-couple force system is equivalent to two orthogonal force dipoles. Then Equation 2.29 solely depends on the first right-handed expression, fault slip  $U_S$  is parallel to fault surface  $\Sigma$  and no tensile cracks are involved ( $D_N = 0$ ). The two forces are in balance (net force is zero) and the principal stress parallel to the B-axis is zero. The eigenvalues of the B-axis must be zero since the fault normal, the slip vector, the P and T axes all lie in a single plane (e.g., Figure 2.4b, P/S-wave Ammon et al., 2020). A double-couple source mechanism represent the classical shear displacement on a single fault plane (Figure 2.3) which describes the general model of a tectonic earthquake (e.g., Table 2.4). From Equation 2.44 follows the eigenvector representation of a double-couple

$$\mathbf{M}_{DC} = \frac{1}{2}(m_i - m_j)(\vec{e}^i \vec{e}^i - \vec{e}^j \vec{e}^j) \quad (2.45)$$

with two vector dipoles pointing orthogonal to each other.

Table 2.4 lists the four basic double-couple mechanism. Each mechanism is defined by its active plane  $(\psi_1, \delta_1, \lambda_1)$  but will result in the same representation by using the auxiliary plane  $(\psi_2, \delta_2, \lambda_2)$ . All displayed mechanism follow their exemplary definition (e.g., pure normal fault) with a fault strike in  $0^\circ N$  and  $\pm 45^\circ N$  to introduce a second example to highlight changes in the tensor. Note that the rotation is around the z-axis and does not influence element  $M_{zz}$ . General identifications of the pure mechanisms are as followed:

- A pure strike-slip mechanism (e.g., MT1 and Beach1) describes a slip in direction of the fault strike (e.g.,  $\psi = 0^\circ$ ) which is dipping  $\delta = 90^\circ$  relative to the surface. Figure 2.6b shows the same mechanism as Beach1 and highlights the orientations of the principal axis. In this case, moment tensor element  $M_{xy} = -1$  gives the principle stress in xy-direction and represents a vector dipole. If the strike is rotated clockwise by  $45^\circ$  (Beach2) resulting moment tensor (MT2) consists of two single forces  $M_{xx} = -1$  and  $M_{yy} = 1$  as the principle stresses are now parallel to the x-direction and y-direction.

**Table 2.4:** Selected prominent double-couple solutions. The beachballs are plotted in the lower hemisphere projection (see Chapter A). The moment tensors (MT1 and MT2) are normalized by  $\frac{1}{\sqrt{2}}$  to conserve the seismic moment for all mechanisms.

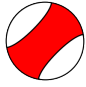
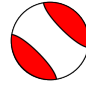

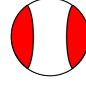
Mechanism ( $\psi_1, \delta_1, \lambda_1$ )/ ( $\psi_2, \delta_2, \lambda_2$ )	MT1	Beach1	MT2 ( $\psi_i \pm 45^\circ$ )	Beach2
Strike-Slip ( $0^\circ, 90^\circ, 0^\circ$ )/ ( $270^\circ, 90^\circ, -180^\circ$ )	$\frac{1}{\sqrt{2}} \begin{pmatrix} 0 & 0 & 0 \\ 0 & 0 & -1 \\ 0 & -1 & 0 \end{pmatrix}$		$\frac{1}{\sqrt{2}} \begin{pmatrix} 0 & 0 & 0 \\ 0 & -1 & 0 \\ 0 & 0 & 1 \end{pmatrix}$	
Normal Fault ( $0^\circ, 45^\circ, -90^\circ$ )/ ( $180^\circ, 45^\circ, -90^\circ$ )	$\frac{1}{\sqrt{2}} \begin{pmatrix} -1 & 0 & 0 \\ 0 & 0 & 0 \\ 0 & 0 & 1 \end{pmatrix}$		$\frac{1}{\sqrt{2}} \begin{pmatrix} -1 & 0 & 0 \\ 0 & 0.5 & 0.5 \\ 0 & 0.5 & 0.5 \end{pmatrix}$	
Thrust Fault ( $0^\circ, 45^\circ, 90^\circ$ )	$\frac{1}{\sqrt{2}} \begin{pmatrix} 1 & 0 & 0 \\ 0 & 0 & 0 \\ 0 & 0 & -1 \end{pmatrix}$		$\frac{1}{\sqrt{2}} \begin{pmatrix} 1 & 0 & 0 \\ 0 & 0.5 & -0.5 \\ 0 & -0.5 & 0.5 \end{pmatrix}$	
Dip-Slip ( $0^\circ, 90^\circ, 90^\circ$ )/ ( $225^\circ, 0^\circ, 135^\circ$ )	$\frac{1}{\sqrt{2}} \begin{pmatrix} 0 & 0 & 1 \\ 0 & 0 & 0 \\ 1 & 0 & 0 \end{pmatrix}$		$\frac{1}{\sqrt{2}} \begin{pmatrix} 0 & \frac{\sqrt{2}}{2} & \frac{\sqrt{2}}{2} \\ \frac{\sqrt{2}}{2} & 0 & 0 \\ \frac{\sqrt{2}}{2} & 0 & 0 \end{pmatrix}$	

- A normal fault describes downward slip on a  $45^\circ$  dipping fault plane. Example MT1/Beach1 is described by  $M_{zz} = -1$  along the direction of the P-axis and  $M_{yy} = 1$  in direction of the T-axis. Rotated by  $45^\circ$  does not change element  $M_{zz}$  but the direction of the T-axis in xy-direction.
- A thrust fault or reverse fault is the opposite mechanism of a normal fault. By keeping the geometry constant (fixing strike and dip of the fault plane) the fault rake is now  $90^\circ$  and the fault slip upwards orientated. Differences in the moment tensor are described, similar to an explosion to implosion, by changing the sign of  $\mathbf{M}$ . Rotated by  $-45^\circ$  the moment tensor behaves the same (but times the factor  $-1$ ) as a normal fault. However, the sign of the off-diagonal element  $M_{xy} = -1$  changes as the principal axis in the xy-plane is now pointing into a different quadrant. Here is to be noted, that due to the LH projection the positive and negative quadrants in the Cartesian system become interchanged. This is why the clockwise rotation of the normal fault brings the T-axis in the positive quadrant and not the negative one, as inferred by the beachball. This results in the negative elements in xy direction for the rotated thrust fault and the positive ones for the rotated normal fault.
- A dip-slip mechanism represents a slip moving in dipping direction. Element  $M_{yz} = 1$  describes the principal axis oriented parallel to y-axis pointing  $45^\circ$  up/downwards relative to z-direction, hence parallel to zy-direction. Rotated by  $45^\circ$  around the z-direction is equal a rotation matrix with  $\sin(45^\circ) = \cos(45^\circ) = \frac{\sqrt{2}}{2}$  in zy-direction and zx-direction, hence  $M_{zx} = M_{zy} = \frac{\sqrt{2}}{2}$ . The auxiliary solution of a dip-slip represents slip parallel to the surface hence orthogonal to the gravity axis.

**Compensated Linear Vector Dipole - CLVD** A CLVD holds no direct physical meaning and is introduced to mathematically complete the moment tensor decomposition (Vavryčuk, 2015). It represents a directed force that aligns along the axis with the largest deviatoric eigenvalue and compensates excessive or deficient wave energy. The sum of its eigenvalues is zero, which defines a



**Table 2.5:** Selected prominent CLVD solutions. The moment tensors (MT1 and MT2) are normalized by  $\frac{1}{\sqrt{6}}$  to conserve the seismic moment for all mechanisms.

Mechanism ( $\psi_1, \delta_1, \lambda_1$ )/ ( $\psi_2, \delta_2, \lambda_2$ )	MT1 (positive)	Beach1	MT2 (negative)	Beach2
Strike-Slip ( $0^\circ, 90^\circ, 0^\circ$ )/ ( $270^\circ, 90^\circ, -180^\circ$ )	$\frac{1}{\sqrt{6}} \begin{pmatrix} 0.6 & 0 & 0 \\ 0 & -0.3 & -1 \\ 0 & -1 & -0.3 \end{pmatrix}$		$\frac{1}{\sqrt{6}} \begin{pmatrix} -0.6 & 0 & 0 \\ 0 & 0.3 & -1 \\ 0 & -1 & 0.3 \end{pmatrix}$	
Normal Fault ( $0^\circ, 45^\circ, -90^\circ$ )/ ( $180^\circ, 45^\circ, -90^\circ$ )	$\frac{1}{\sqrt{6}} \begin{pmatrix} -1.2 & 0 & 0 \\ 0 & 0.6 & 0 \\ 0 & 0 & 0.6 \end{pmatrix}$		$\frac{1}{\sqrt{6}} \begin{pmatrix} -0.6 & 0 & 0 \\ 0 & -0.6 & 0 \\ 0 & 0 & 1.2 \end{pmatrix}$	

CLVD as a deviatoric mechanism, however the individual values do not behave like a double-couple. All are non-zero whereas two have the same and one with the opposite sign. Consequently, the additional force has the ratio 2:1 along one axis and 1:2 along the remaining two but with sign reversal so that the net force becomes zero. Figure 2.4b displays the P-wave radiation corresponding to the CLVD in Figure 2.6c. Both CLVD representations were computed based on a strike-slip (Figure 2.6b) and align with its P and T axes. Table 2.5 gives an overview of selected CLVD mechanisms. Each is based on an underlying double-couple mechanism to define the principal coordinate system. MT1 and corresponding beachball Beach1 shows a pure positive CLVD while MT2 and Beach2 a pure negative CLVD. The beachball representation of a pure CLVD resembles in its color pattern to a billiard bowl (number 9 to 15). The curvature of the nodal lines becomes lesser with increasing absolute CLVD percentage (Equation 2.38;  $a = 0$  and  $b \rightarrow 1$ ) while one color coverage increases in area while the other decreases.

From Equation 2.44 follows the eigenvector representation of a CLVD

$$\mathbf{M}_{\text{CLVD}} = \frac{1}{3} m_i (2\vec{e}^i \vec{e}^i - \vec{e}^j \vec{e}^j - \vec{e}^k \vec{e}^k) \quad (2.46)$$

which is equivalent to two double-couples

$$2\vec{e}^i \vec{e}^i - \vec{e}^j \vec{e}^j - \vec{e}^k \vec{e}^k = (\vec{e}^i \vec{e}^i - \vec{e}^j \vec{e}^j) + (\vec{e}^i \vec{e}^i - \vec{e}^k \vec{e}^k) \quad (2.47)$$

with  $i, j, k \in [\text{T}, \text{B}, \text{P}]$  and  $i \neq j \neq k$  representing the orthogonal eigenvectors.

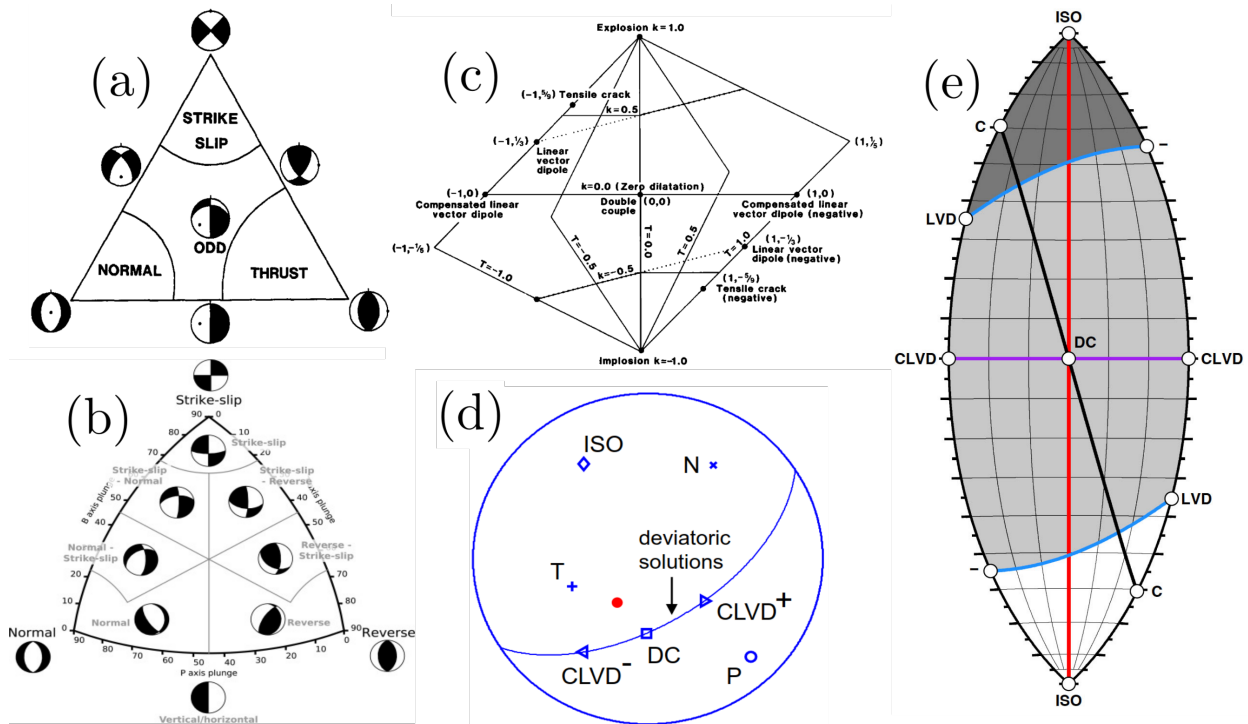
### Mixed models and their classification

Decomposition may not be as straight forward in real data application. Figure 2.5 shows at the bottom a mixed combination of differently weighed contributions. A deviatoric source can be composed of three double-couples (Equation 2.45) or three CLVD sources (Equation 2.46, Ben-Menahem et al., 1981; Jost et al., 1989). A popular decomposition is that of a double-couple and a CLVD. Figure 2.6a shows a deviatoric source solution constructed in an evenly weighted summation ( $b = 0.5$ , Equation 2.38) a pure strike-slip (Figure 2.6b) and a pure CLVD source (Figure 2.6c). Another decomposition would be a major and minor couple. The normal fault based CLVD in Table 2.5 can be deconstructed into two evenly weighted perpendicular normal faults while the strike-slip based CLVD might be composed of a weighted summation between a strike-slip and a normal fault. The first mechanism can be observed at volcanic sides and might represent a ring fault of a collapsing caldera (Ekström, 1994), while the second example is observed at oceanic ridge-transform intersections (Frohlich, 1995). However, a CLVD does not need to be related to a

physical interpretation of the source process and can hint to artifacts of the inversion, especially for small earthquakes (Rösler et al., 2022). The reliability of the CLVD component to represent a real source process is therefore important to be validated if used in complex interpretations. Using a statistical analysis of historical MT solutions of different catalogues, (Rösler et al., 2023) showed that large non-double-couple contributions are more likely to be related to the source itself, especially for large events. Furthermore, restrictions in the isotropic contribution (e.g., for assumptions of purely deviatoric tectonic events) showed to effect the CLVD (Vavryčuk, 2011).

Much more complex mixed mechanisms are tensile cracks which represent an opening movement (in  $v$ -direction relative of  $\Sigma$ ) of the adjacent fault planes (second part of Equation 2.29). A pure tensile or compressive faulting involves isotropic and CLVD contributions but no shear movements. Shear-tensile dislocations are the most complex sources and involve all of aforementioned moment tensor contributions.

The classification of such mechanism depends on correct decomposition and the display of common features within an adequate coordinate systems. Several have been proposed to display different properties of the moment tensor (Figure 2.7). Ternary diagrams (Frohlich, 1992) and in a newer modification the Focal-Mechanism-Diagrams (FMC, e.g., Álvarez-Gómez, 2019) are useful to represent double-couples relative to the plunge of the principal axes. Non-double-couples need a more sophisticated system. Prominent representations are Hudson plots (Hudson et al., 1989) in different realizations of the diamond shape and Riedesel-Jordan plots (Riedesel et al., 1989) and thereupon build modifications with the most notable one, the lune plot (Tape et al., 2012). Mentioned coordinate systems try to differentiate between positive or negative changes in the CLVD and isotropic parts. They allow to represent mixture forms like tensile cracks or LVDs and have at their coordinate origin point a double-couple solution spanning the unit vectors. The source mechanism then becomes more complex and the principal axis alter with increasing distance to this origin point towards a pure isotropic or CLVD mechanism.



**Figure 2.7:** Overview of source type plots. a) Ternary – Figure by Frohlich (1992) b) FMC – Figure by Álvarez-Gómez (2019) c) Hudson – Figure by Hudson et al. (1989) d) Riedesel-Jordan – Figure by Vavryčuk (2015) e) Lune – Figure by Tape et al. (2012), supplementary.



## Chapter 3

# Moment tensor inversion

In this chapter I give an overview of different inversion methods and introduce my new approach “AmΦB - uniXtree”. Important and recurring parameters introduced in this chapter are listed in Table 3.1. A moment tensor is a useful model to describe the source process of a seismic event. In order to derive this tensor from observable data, we need to conduct an inversion. Equation 2.24 describes the forward formulation outgoing from the hypocenter location with moment tensor  $\mathbf{M}$  representing the source mechanism. Effects of the source are observed at an arbitrary surface location which results in data  $d$ . These observations depend on the path effects throughout the Earth’s subsurface which are described as a physical model with Green’s function matrix  $\mathbf{G}$ .

*Table 3.1: Important recurring parameters.*

Symbol	Parameter
$W/Q/V$	Green’s functions in Z/R/T
$\theta_j$	station azimuth
$\mathbf{E}$	kernel
$\vec{a}$	Moment tensor weight
$\vec{s}_{Fj}$	fundamental synthetics

### 3.1 Inversion strategies

In the following I will introduce different approaches for source inversion using first motion polarities and waveform information in the time-domain.

#### 3.1.1 First motion polarity

The simplest and most cost-efficient approach is the use of first-motion polarities (FMP). This method traces back to the earliest descriptions of the source (Agnew, 2002) where seismologists recognized symmetric patterns when they mapped the polarities of P-waves. In a first step the source and receiver arrangement is plotted onto a polar diagram (Schmidt net). The back-azimuths between each source-receiver pairing defines the azimuth in the diagram and the radius is given by the incident angle of the incoming P-wave. Data are the first motion polarity (up, down or undefinable) of P- and S-waves on the corresponding components and possibly amplitude ratios between them. The inversion itself is conducted as a grid search over the focal sphere using different bootstrap approaches to simulate uncertainties, e.g., HASH (Hardebeck et al., 2002) or FocMec (Snoke, 2003), or a Bayesian formulation, e.g., MTFit (Pugh, 2015), which allows for full deviatoric inversions.

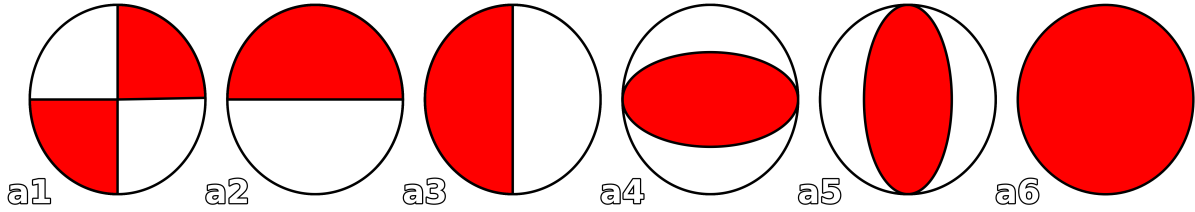
### 3.1.2 Full waveform

Cut-and-Paste (CAP, Zhao et al., 1994; Chen et al., 2015) is based on the mathematical decomposition of pure double-couple sources into three, differently weighted, fundamental mechanisms (see Table A.1). The method takes advantage of the point symmetric radiation characteristics in a 1D velocity model. The combined weighted waveforms for an arbitrary pure double-couple mechanism in an arbitrary azimuth direction depend only on the Green's functions in receiver distance and assumed source depth. “Cut” refers to the identification of seismic phases by cutting relevant signal windows out of the full signal, filtered in a narrow bandpass. “Paste” allows to do a weighted summation of the Green's functions ( $W_i, Q_i, V_i$ ) computed for the three fundamental mechanisms in specific azimuthal directions. The mathematical description of the composed waveform at station  $j$  in distance  $n$  and azimuth  $\theta_j$  for a given source mechanism is:

$$\begin{aligned} u_{Z,j}(t) &= s(t) * \sum_i W_{i,n}(t) A_i(\Theta, \lambda, \delta) \\ u_{R,j}(t) &= s(t) * \sum_i Q_{i,n}(t) A_i(\Theta, \lambda, \delta) \\ u_{T,j}(t) &= s(t) * \sum_i V_{i,n}(t) A_{i+3}(\Theta, \lambda, \delta) \end{aligned} \quad (3.1)$$

with  $\Theta = \theta_j + \psi$  and  $*$  describing a convolution with source time function  $s(t)$ . Weight  $A_i$  is a function of the fault parameters strike  $\psi$ , dip  $\delta$  and rake  $\lambda$  (see Table A.1).

A more sophisticated approach to describe the full moment tensor involves six fundamental solutions and can be applied for 3D velocity models. Krizova et al. (2013) proposed a weighed combination of five double-couples and one isotropic source (Figure 3.1). However, the choice of these five double-couples is not restricted to only these (e.g., Kikuchi et al., 1991).



**Figure 3.1:** Fundamental moment tensor solutions.

Compared to CAP, which uses fundamentals in a specific azimuth and distance to model the signals at arbitrary station locations, this approach depends on the fundamental waveform information at the exact station location. The displacement time signal  $\vec{u}(t)$  along component  $i$  is

$$u_i(t) = \sum_{j=1}^6 a_j \underbrace{\left( \sum_p \sum_q M_{pq}^j * G_{ip,q} \right)}_{\text{kernel}} = \sum_{j=1}^6 a_j E_i^j(t) \quad (3.2)$$

with kernel function  $E_i^j(t)$  describing the seismogram of the  $j$ th fundamental solution at the observation point. Unitless weight  $a = [a_1, a_2, a_3, a_4, a_5, a_6]$  then relates to the six moment tensor elements, thus re-scaling them relative to a fixed, known moment  $M_0$  in  $M_{pq}^j$ . The relation between the synthetic amplitudes at known magnitude and the observable at unknown magnitude behaves linear to the excited moment. The moment tensor can then be constructed using weight vector  $\vec{a}$  as

$$\mathbf{M} = \begin{pmatrix} a_4 + a_5 + a_6 & a_2 & a_3 \\ a_2 & -a_4 + a_6 & -a_1 \\ a_3 & -a_1 & -a_5 + a_6 \end{pmatrix} \quad (3.3)$$

where i.e., weight  $a_1$  represents the MT solution for a strike-slip in the USE-notation. In matrix formulation, Equation 3.2 becomes

$$\begin{aligned} \vec{u} &= \mathbf{E}\vec{a} \\ \text{with } \mathbf{E} &= \begin{bmatrix} \vec{s}_{F1}, & \vec{s}_{F2}, & \vec{s}_{F3}, & \vec{s}_{F4}, & \vec{s}_{F5}, & \vec{s}_{F6} \end{bmatrix} \\ \text{and } \vec{s}_{Fj} &= \begin{bmatrix} s_1, & s_2 & \dots & s_{N-1} & s_N \end{bmatrix}^\top \end{aligned} \quad (3.4)$$

representing a synthetic data vector consisting of  $N$  samples. Matrix  $\mathbf{E}$  then has the dimension  $N \times 6$ . To retrieve the inverse formulation of the forward problem we perform a mathematical transformation by multiplying both sides with the transposed matrix  $\mathbf{E}^\top$

$$\mathbf{E}^\top \vec{u} = \mathbf{E}^\top \mathbf{E} \vec{a}. \quad (3.5)$$

$\mathbf{E}^\top \mathbf{E}$  is a square matrix for which an inverse exist. The inverse formulation is then

$$\vec{a} = \underbrace{(\mathbf{E}^\top \mathbf{E})^{-1} \mathbf{E}^\top}_{\mathbf{E}^*} \vec{u} = \mathbf{E}^* \vec{u} \quad (3.6)$$

whereas matrix  $\mathbf{E}^*$  is of size  $(6 \times N) \cdot (N \times 6) \cdot (6 \times N) = 6 \times N$ .

### 3.1.3 Further inversion codes and strategies

Different methods and inversion codes for moment tensor modelling have been proposed and developed. Each method has its own specific application or includes certain assumptions. Commonly used are time-domain approaches where bandpass-filtered observed data are compared with synthetically computed time-series.

The most widely applied inversion procedure is Time Domain Seismic Moment Tensor INVersion (TDMT\_INV, Dreger et al., 1993; Dreger, 2003), which is used by different universities and national agencies (e.g., NIED in Japan or INGV in Italy). It resorts to pre-computed Green's functions for fast computation of specific source-receiver configurations to fit the constructed synthetics to the observables in a grid search of strike, dip and rake.

The inversion scheme discussed by Krizova et al. (2013) is used in ISOLA (Sokos et al., 2008; Sokos et al., 2013). It offers a handy graphical user interface (GUI) that gives its user different options for 1D waveform simulation, data pre-processing, plotting and, e.g., multiple-point source models. An example for applications with 3D waveforms synthetics is gCAP3D (Zhu et al., 2016) which was developed on the basis of CAP and uses its ‘‘Cut’’ feature to extract selected wave phases (see Section 3.1.2).

More sophisticated is cmt3d (Liu et al., 2004) or its Python version pycmt3D (Lei, 2017). This method considers uncertainties in the moment tensor elements and the hypocenter location relative to an initial solution (e.g., from less sophisticated 1D inversions). It uses perturbed waveforms, hence element wise simulated force couples at a given relative magnitude, at the best hypocenter location to update the moment tensor itself. An update in the hypocenter location depends on simulations of the starting solution at a spatial offset (in latitude, longitude and depth) relative to the initial location.

Moment tensor inversion in the frequency domain can be achieved in a similar mathematical approach as in the time domain following the inverse formulation between data, Green's tensor and model parameters (Stump et al., 1977). Free software packages include VOLPIS (Cesca et al., 2008) for applications on volcanic signals and RAPIDINV (Cesca et al., 2010) with different applications in regional and teleseismic distance. Further case studies use non-commercial codes to perform MT inversion of small seismic events in near-source observations (e.g., Yang et al., 2018) or for large ( $M > 7$ ) events in a regional (nation-wide) scale (e.g., Nakano et al., 2008). Frequency

information is usually used in a joint inversion with polarities (e.g., Cesca et al., 2006) or time domain information (e.g., Vavryčuk et al., 2012; Sen et al., 2013). For an overview of different techniques and applications see Dahm et al. (e.g., 2014) and D’Amico (2018).

Increasingly popular are Bayesian applications to quantify specific sources of errors as a prior in a co-variance matrix. These errors are generally distinguished between measurement errors of the observed data (e.g., ambient noise) and theoretical errors in the synthetic time series (e.g., faulty model assumptions, inversion artifacts). The description of these errors is not straightforward and different approaches have been proposed to tackle specific settings.

Ambient noise is the most commonly identified source of errors and can be highly frequency-dependent (Peterson, 1993; Bormann et al., 2013). It is usually described as a stationary and uncorrelated Gaussian process, i.e., white noise, with zero mean and a time-invariant infinite standard deviation relative to the observed amplitudes. This basic assumption is used in, e.g., Bayesian ISOLA, an enhancement of the ISOLA software (Vackář et al., 2017). More sophisticated are models with serially correlated and non-stationary noise assumptions (e.g., Tarantola et al., 1982; Dettmer et al., 2007; Yagi et al., 2011; Duputel et al., 2012) and discussed in Vasyura-Bathke et al. (2021). The individual samples of serially correlated noise are not random but display a dependency on the preceding ones, i.e., trends, while non-stationary indicates a time-dependent behavior of the signal, i.e., prominent transient noise sources (e.g., bypassing cars on a quiet road).

Poorly known velocity models can have a major influence on the source solutions (Vasyura-Bathke et al., 2021) as the model defines the shape and traveltimes of the seismic phases. Different approaches have been proposed to mitigate these effects in a Bayesian formulation like diffMT (Jia et al., 2022) which uses amplitude ratios of common selected phases of relative measurements for clustered seismic event pairs to remove the path and site effects. Recent applications by Gu et al. (2017) and Scarinci et al. (2023) used a Bayesian formulation to assess the uncertainties in the velocity model and location for small induced seismicity in an oil/gas field and could mitigate the effects of the non-double-couple component of the recovered mechanisms.

But also effects of the source assumption itself are frequently considered. Duputel et al. (2012) considered, besides increased noise as a data error, the uncertainty in the hypocenter location as an error in the model assumptions. The Bayesian Earthquake Analysis Tool (BEAT, Vasyura-Bathke et al., 2020), a pyrocko (Heimann et al., 2017) extension for MT inversion using 1D velocity models, considers uncertainties of multiple source parameters in a Markov chain Monte Carlo sampling for different source assumptions including the full moment tensor, rectangular, static or kinematic finite faults jointly using seismic and geodetic data. The variety of Bayesian and non-Bayesian MT inversion routines is large but mostly focused on a certain application. My aim in this thesis is the qualitative and robust MT inversion using ocean bottom seismometers (OBS). To work with such data, we have to introduce a completely new cause of errors, the sensor alignment, which none of the existing codes considers so far.

## 3.2 AmΦB - uniXtree

In the following I will introduce my new moment tensor inversion procedure AmΦB – “Amphibious Bayesian”. My aim is not to replace inversion schemes but to provide a new framework which allows to consider sensor misalignment in a Bayesian formulation. It enables the usage of data from OBSs but may also find application for land stations as misalignments are common in all seismic networks. Potential effects are often neglected if the station coverage is evenly distributed and large enough to cancel out these effects in the average solution. General effects have not been quantified and misalignment up to  $10^\circ$  relative to the north direction are accepted as a rule of thumb. Further effects contributing to the uncertainties in the source solution are high noise or incorrect time information like station delay or uncertain origin time. Strategies handling the alignment issues of OBS traces and potential effects on the MT solution are discussed in chapter 5 of this thesis.

### 3.2.1 Bayesian error formulation

Equation 2.24 implies a perfect knowledge of the Earth's subsurface, an exact description of the forces in the moment tensor formulation and the absence of external noise sources. Naturally, this is not possible. Green's function matrix  $\mathbf{G}$  represents the Earth under special physical assumptions with limited geometrical resolution and may only be representative for restricted frequency bands. Deviations between the true Earth and the Earth's model can be expressed as the difference between the observed and the synthetic waveforms:

$$\vec{e} = \vec{d}^{\text{obs}} - \mathbf{G}\vec{m} \quad (3.7)$$

$$\rightarrow \vec{d}^{\text{obs}} = \mathbf{G}\vec{m} + \vec{e}. \quad (3.8)$$

The error  $\vec{e}$  is the residuum time series and includes different types of errors such as anthropogenic noise, limitations/misrepresentations in the Earth's model and the source representation, or issues in the measurement (e.g., sensor installation). Considering these uncertainties in the moment tensor inversion problem, Equation 3.8 can be expressed in an ordinary least squares formulation (e.g., Yagi et al., 2008):

$$(\mathbf{G}\vec{m} - \vec{d}^{\text{obs}})^T \mathbf{C}_D^{-1} (\mathbf{G}\vec{m} - \vec{d}^{\text{obs}}) \rightarrow \min \quad (3.9)$$

This formulation represents the error kernel of my inversion method. To statistically quantify the errors, I introduce a Gaussian distributed probability density. Constructing the probability density function (PDF) as stochastic information of the model space, we can write

$$Q(\vec{m}) = k e^{-0.5[(\mathbf{G}\vec{m} - \vec{d}^{\text{obs}})^T \mathbf{C}_D^{-1} (\mathbf{G}\vec{m} - \vec{d}^{\text{obs}})]} \quad (3.10)$$

where  $k$  is a normalization factor satisfying  $\sum Q(\vec{m}) = 1$ . Here,  $\mathbf{C}_D$  represents the covariance matrix of error  $\vec{e}$ . Likewise, this matrix can be decomposed into the underlying error sources following the error propagation rule,

$$\mathbf{C}_D = \mathbf{C}_d + \mathbf{C}_T. \quad (3.11)$$

In this work I focus on two different sources of uncertainty: high noise amplitudes and false sensor alignments relative to North (see Figure 3.2).

The noise level before a transient event is assumed to be constant during and after it. Noise interferes with the earthquake and alters the signal by constructive or destructive interference with the amplitude. A measure for this is the signal-to-noise ratio (SNR), a scalar value computed between a relative value of the noise amplitude (e.g., absolute mean or peak) and the interested signal part (which is also affected by noise). The simplest Bayesian model for noise is that of a constant value multiplied with the unit matrix in size of the signal length:  $\mathbf{C}_{dn} = \sigma_n^2 \mathbf{I}$ . Duputel et al. (2012) noted that this formulation might underrepresent the actual influence of the noise and additionally considered the signal sampling

$$(C_d^{ij})_n = \sigma_n^2 e^{-|\Delta t^{ij}|/t_0} \quad (3.12)$$

with  $t_0 = 1/f_{\min}$ ,  $f_{\min}$  being the lower frequency corner of the bandpass filtered data, and  $\Delta t^{ij}$  representing the time difference between sample  $i$  and  $j$ .

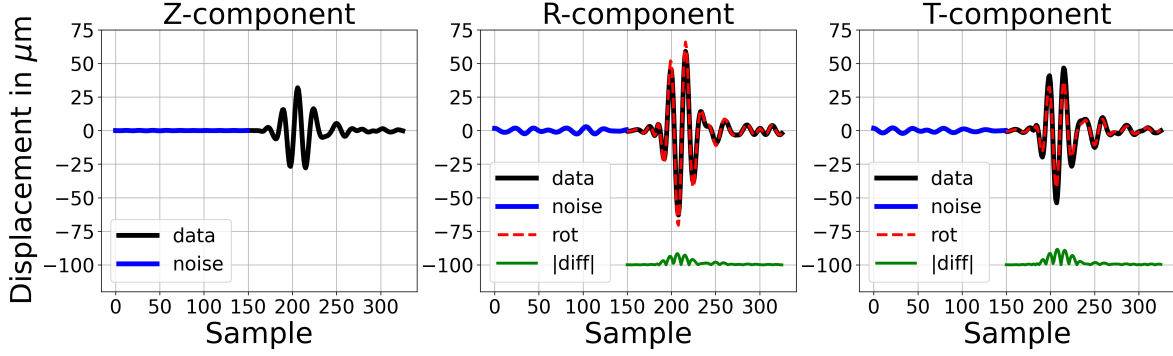
Nothing a seismometer during its installation is an important basic step to ensure consistent data handling over a broad network. While this is usually done by a skilled field technician or trained seismologist for land stations with a magnetic compass or gyro-compass (this may ensure a high-quality installment but will not be free of errors), the orientations of OBS stations are random and have to be corrected after the deployment. The effect on the waveforms can be interpreted as a linear energy redistribution between the horizontal components R and T scaled by angle  $\Phi_n$  at small deviating alignments. I follow the model by Duputel et al. (2012) who described the uncertainty on the source attributed by the hypocenter uncertainty. It was modeled using a linear



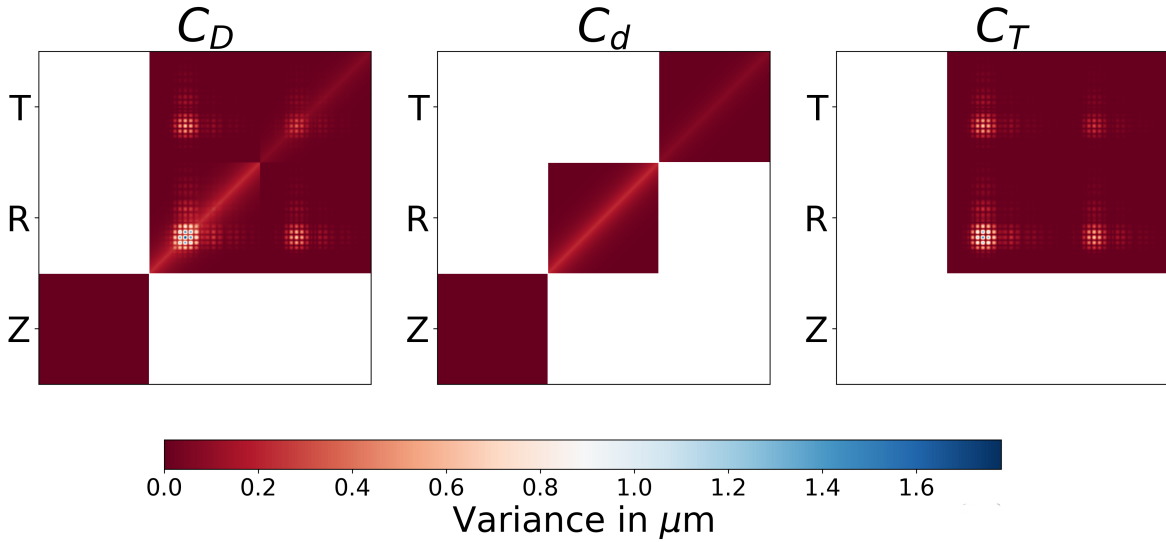
gradient of the spatial offset instead of performing a Monte-Carlo simulation within the assumed error range. The covariance matrix is then

$$\mathbf{C}_T = [\nabla \vec{d}(\overline{\Phi}_n)] \mathbf{C}_{d\Phi_n} [\nabla \vec{d}(\overline{\Phi}_n)]^\top \quad (3.13)$$

with  $\mathbf{C}_{d\Phi_n}$  being the variance of  $d\Phi$  and alignment gradient  $\nabla \vec{d}(\overline{\Phi}_n)$  following the rotation matrix along the vertical axis.



(a) *Data for covariance matrices.* The term *rot* (red dotted line) represents a clockwise horizontal rotation of  $10^\circ$ . The label *|diff|* is the difference between initial and rotated data.



(b) *Covariance matrices.*

**Figure 3.2:** Data example and covariance matrices.

### 3.2.2 Uniform X-dimensional tree-sampling - uniXtree

#### Uniform parameterization

Uniform sampling of the source parameters in an evenly spaced Cartesian coordinate system, be it a direct sampling of 6-moment tensor elements (e.g., Staehler et al., 2014) or a parameterization of five source parameters and seismic moment  $M_0$ , does not result in a uniform distribution of moment tensor solutions (Tape et al., 2016). Likely effects are under- or oversampling of relevant or irrelevant solutions that can cause an increase of the computation time, large sampling-based uncertainties, or even overestimation of local minima.

The eigenvalue decomposition (see Section 2.2.2) yields a Cartesian coordinate system spanned by the principal axis of the dominant double-couple source mechanism. This is not useful for large non-double-couple contributions in the source. (Tape et al., 2013) introduced the *uvw*-coordinate

system which is based on the eigenvalue space  $\Upsilon$ . The basis vectors are chosen to represent the three fundamental contributions of the full moment tensor using the eigenvalues of respected pure solution

$$\begin{aligned}\vec{\Upsilon}^{\text{DC}} &= \frac{1}{\sqrt{2}}(1, 0, -1), & (\text{see Equation 2.45}), \\ \vec{\Upsilon}^{\text{CLVD}} &= \frac{1}{\sqrt{6}}(-1, 2, -1), & (\text{see Equation 2.46}), \\ \text{and } \vec{\Upsilon}^{\text{ISO}} &= \frac{1}{\sqrt{3}}(1, 1, 1), & (\text{see Equation 2.42}).\end{aligned}$$

They define a matrix for the basis with

$$V = \frac{1}{\sqrt{6}} \begin{pmatrix} \sqrt{3} & 0 & -\sqrt{3} \\ -1 & 2 & -1 \\ \sqrt{2} & \sqrt{2} & -\sqrt{2} \end{pmatrix} \quad (3.14)$$

which has the eigenvalues related to the new coordinate system with

$$\begin{aligned}\sqrt{2}u &= v_1 - v_2, & \sqrt{6}v &= -v_1 + 2v_2 - v_3 & \text{and} & \sqrt{3}w &= v_1 + v_2 + v_3 \\ \text{or as a matrix} & \quad \Upsilon &= V^{-1} \cdot (u, v, w)\end{aligned}$$

whereas  $v \in \Upsilon$ . Following the Riedesel-Jordan representation (Riedesel et al., 1989, Figure 2.7, d) of different source types on a sphere, Tape et al. (2012) proposed to locate the non-double-couple contributions on a fixed fundamental lune (e.g., Tape et al., 2018) of the unit sphere (Figure 2.7, e). The spherical coordinate system is given by

$$\begin{pmatrix} u \\ v \\ w \end{pmatrix} = \begin{pmatrix} \rho \sin(\beta) \cos(\gamma) \\ \rho \sin(\beta) \sin(\gamma) \\ \rho \cos(\beta) \end{pmatrix}, \quad (3.15)$$

where longitude  $|\gamma| \leq \frac{\pi}{6}$  and colatitude  $0 \leq \beta \leq \pi$  span the lune on the sphere. Its central location ( $\gamma = \beta = 0$ ) coincides with the piercing point of the  $u$ -axis which represents a pure double-couple solution, hence non-zero values of the two angles describe non-double-couple contributions in the moment tensor. The strength of the individual parts are given by (e.g., Tape et al., 2018)

$$\vec{\Upsilon}(\beta, \gamma) = u\vec{\Upsilon}^{\text{DC}} + v\vec{\Upsilon}^{\text{CLVD}} + w\vec{\Upsilon}^{\text{ISO}} \quad (3.16)$$

while Euclidean norm  $\frac{\|\vec{\Upsilon}\|}{\sqrt{2}} = \frac{\rho}{\sqrt{2}} = M_0$  defines the seismic moment. The representation of double-couple solutions is achieved by a rotation of the eigenvalues  $\vec{\Upsilon}$ ,

$$\mathbf{M} = [\vec{\Upsilon}]_{\mathbf{U}} = \mathbf{U}[\vec{\Upsilon}]\mathbf{U}^{-1} \quad (3.17)$$

with rotation matrix  $\mathbf{U} = \mathbf{U}(\psi, \lambda, \theta)$  relative to the  $xyz$ -axes. Inserting Equation 3.16 into Equation 3.17 yields the conversion operator  $G$  of the eigenvalues describing the full moment tensor to the  $uvw$ -system including the lune representation (Figure 3.3)

$$G(u, v, \psi, \lambda, h) \stackrel{\text{Figure 3.3}}{=} G(u, v, \kappa, \sigma, h) = [\vec{\Upsilon}(\beta(u), \gamma(v))]_{\mathbf{U}(\kappa, \sigma, \theta(h))} = [\vec{\Upsilon}]_{\mathbf{U}} \quad (3.18)$$

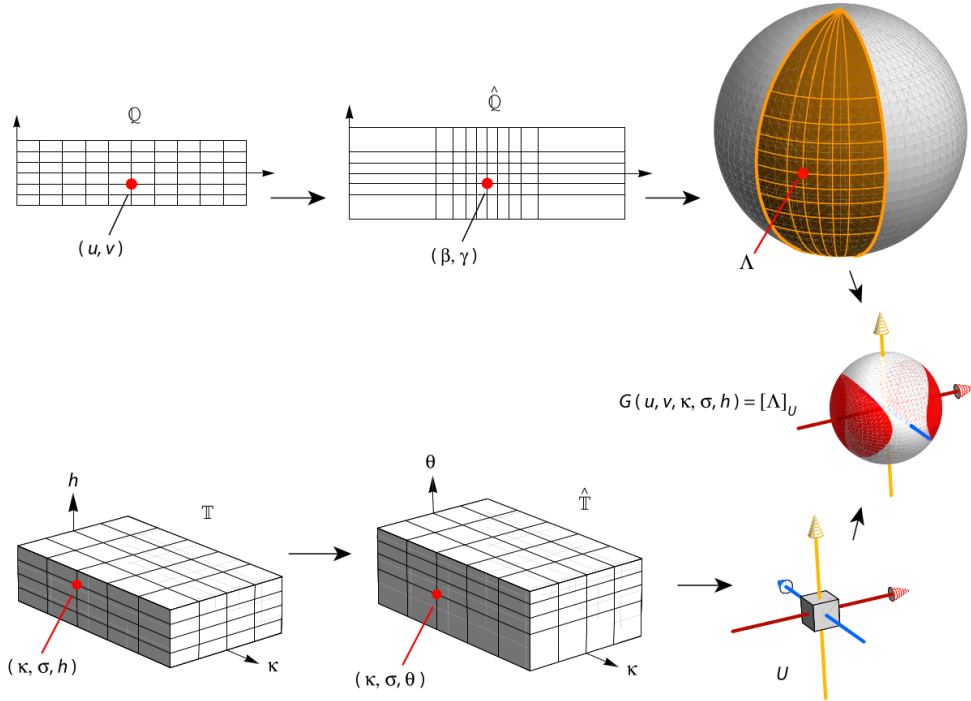
Uniform sampling is then achieved using uniform coordinates for the eigenvalue triples on the lune and uniform orientations of the double-couple (Tape et al., 2015, Tape representation):

- Strike with  $\psi \in [0, 2\pi)$
- Dip with  $\theta \in [0, \frac{\pi}{2}]$  and in the uniform Tape representation:  $h = \cos(\theta)$  and its inverse with  $\theta(h) = \arccos(h)$  with  $h \in [0, 1]$

- Rake with  $\lambda \in [-\pi, \pi)$
- CLVD  $\in [-100\%, 100\%]$  and in the uniform Tape representation:  $v = \frac{1}{3}\sin(3\gamma)$  with  $\gamma \in [-\frac{\pi}{6}, \frac{\pi}{6}]$  and its inverse with  $\gamma(v) = \frac{1}{3}\arcsin(3v)$  with  $v \in [-\frac{1}{3}, \frac{1}{3}]$ . Conversion between classical CLVD parameter to uniform parameterization  $\gamma$  is done by multiplying by 30/100 and back with 100/30 to convert  $\gamma$  in degree and then to radian.
- ISO  $\in [-100\%, 100\%]$  and in the uniform Tape representation:  $u = \frac{3}{4}\beta - \frac{1}{2}\sin(2\beta) + \frac{1}{16}\sin(4\beta)$  with  $\beta \in [0, \pi]$ . Its inverse  $\beta(u)$  may be calculated numerically. Conversion between classical ISO parameter to uniform parameterization  $\beta$  is done by multiplying by 90/100 and back with 100/90 to convert  $\beta$  in degree and then to radian.

Throughout my work I will only focus on deviatoric parameters, hence a general tectonic shear mechanism without volume changes. This restriction results in a 4D parameter space spanned by  $\psi$ ,  $h$ ,  $\lambda$ , and  $\gamma$ . Probability  $P_i$  of a source solution is then defined by Equation 3.10 with the PDF  $Q(\vec{m})$  and weighted by the corresponding sub-volume  $V_i$  with:

$$P_i = V_i \cdot Q(\vec{m}) \quad (3.19)$$



**Figure 3.3:** Uniform parameter space. Here,  $\kappa$  is strike  $\psi$ ,  $\sigma$  is rake  $\lambda$  and eigenvalue space  $\Lambda$  is  $\Upsilon$ . Figure by Tape et al. (2015)

### Efficient sampling

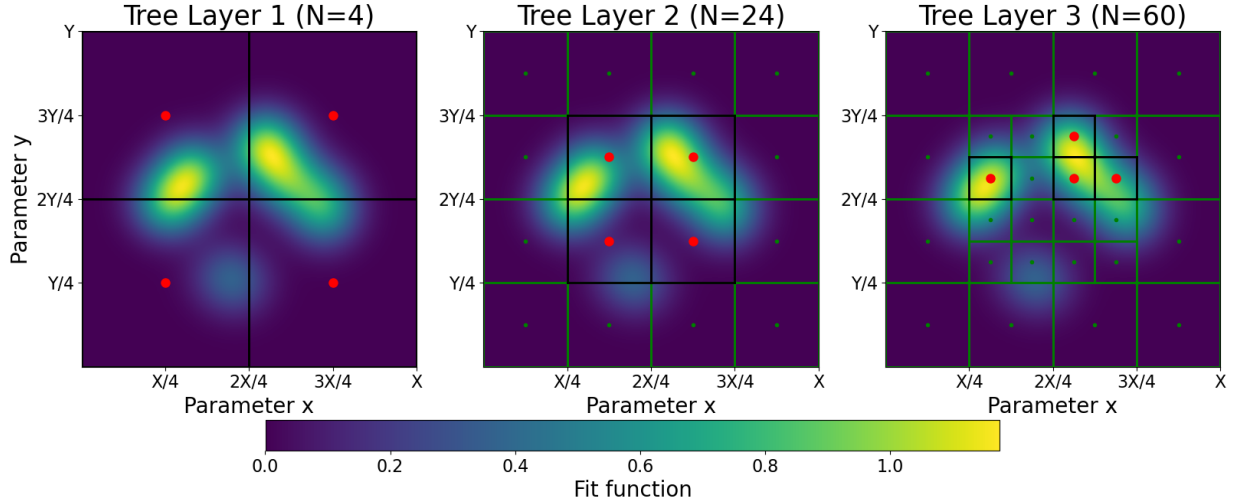
Using a direct sampling approach of the Tape parameters, I explored the tree-importance sampling algorithm that is extensively used for different computational problems, e.g., 3D visualizations (Meagher, 1982; Fujimura et al., 1984) or in more modern applications together with e.g., neural networks (Wang et al., 2017a). The application to geophysical problems was first applied by Lomax et al. (2001) for an octant sampling of the 3D hypocenter location and is applied in recent studies for geophysical imaging, e.g., Hawkins et al. (2015). Compared to generally used techniques such as the Monte Carlo or Metropolis-algorithm, it has been shown that an oct-tree algorithm is more global and complete while only depending on a few parameters (Lomax et al., 2001).

Tree sampling represents an interval halving of a fixed parameter space, e.g.,  $\psi \in [0^\circ, 360^\circ)$ , and can be defined by its boundary values or the central  $c_L$  point and the half-width  $dc$ . The

central point acts as representative coordinate of the spanned parameter space (e.g., range, area or volume in Equation 3.19) and solves the forward problem (Equation 3.10). Further subdivision of this parameter space is then represented by a new set of central coordinates

$$c_{L+1} = c_L \pm \frac{dc}{2^L} \quad (3.20)$$

with  $L \in \mathbb{N}_0$  giving the number of subdivisions (layers).



**Figure 3.4:** Tree sampling in 2D. Each area is represented by its central point with parameter  $c_L = [x_i, y_j]$  relative to  $c_0 = [\frac{X}{2}, \frac{Y}{2}]$  and  $dc = [\frac{X}{2}, \frac{Y}{2}]$ . Red dots are the top four points, green ones all other pairs examined with lesser importance. Black lines encircle the most probabilistic area, while green ones are of lesser importance.

To explore the strength of this sampling approach, let us consider an arbitrary two dimensional  $X \times Y$  parameter space with two local maxima (compare Figure 3.4). Each maximum, with only one being the global one, can represent different information of the examined problem which we ideally should know both. Displayed in the background as a colormap is the full probability density map  $Q(\vec{m})$  of all models  $m(X_i, Y_j)$ . In the initial step the full parameter space is subdivided into  $2^2 = 4$  sub-volumes outlined with black lines and parameterized by their central coordinates ( $c_L$ , red dots). After ranking the computed probabilities  $P_i$  with  $i \in [1, 2, 3, 4]$  the tree assembles an importance list of the four sub volumes (second layer  $L$  with central coordinate  $c_2$ ). Here I introduce parameter  $I_{\text{top}} = 4$  that sets the number of sub volumes that are further examined. In the second step the subdivision leads to  $(2^2)I_{\text{top}}$  new cells to be examined and ranked accordingly. Now, outlines in black are the top four cells with the highest probability, green cells with a lower one. As before in the third ( $c_3$ ) and subsequent steps these cells are further subdivided and ranked accordingly until a termination criterion is met. The strong point of the procedure is the potential re-evaluation of previous larger cells if their probability compared to the current region becomes relevant again. This feature allows the examination of multiple solutions, be it in case of the source sampling, the auxiliary plane or even a minor couple. In this setting I am able to specialize the inversion process by restricting the parameter space or entirely fixing one to a constant value. This allows me to include external information from, e.g., InSAR, historical solutions, or information from field geologists about the approximated fault orientation.

### 3.2.3 Inversion application

Data vector  $\vec{d}$  and data covariance matrix  $\mathbf{C}_d$  are treated as constant during the inversion. The synthetic model and the model covariance matrix  $\mathbf{C}_T$  are sampled using the uniXtree algorithm. The synthetics are computed for the given coordinates  $(\psi, \theta, \lambda, \gamma, \beta)$  with the kernel of Equation 3.2.

I use, depending on the available velocity model, different approaches to construct the kernel. For 1D media I can use the CAP approach and compile a synthetic Green’s function database (compare Table A.1). I then simulate for any given source-receiver geometry the fundamental mechanisms needed in Equation 3.2. This way I am able to reduce the computational cost for the Green’s function calculation and create a database for an arbitrary source-receiver geometry. A possible simulation code for the CAP fundamentals is SPECFEM3D (Komatitsch et al., 1999). Another approach is the “fomosto” tool of “pyrocko”. Using the large pre-computed Green’s function store, I can quickly simulate the fundamental mechanisms for any given region. Fomosto uses different backends such as QSEIS (Wang, 1999, using propagator theory) or QSSP (Wang et al., 2017b, using normal mode theory) to create a database of chosen dimension. Aforementioned approaches are limited to 1D velocity information. Using 3D data with, e.g., SPECFEM3D (Komatitsch et al., 1999) or SALVUS (Afanasyev et al., 2019), I can simulate the element-wise synthetics at the given source-receiver arrangement. Based on these synthetics I then construct the needed fundamentals for the kernel.

## Part II

# Moment tensor inversion in the Lesser Antilles



## Chapter 4

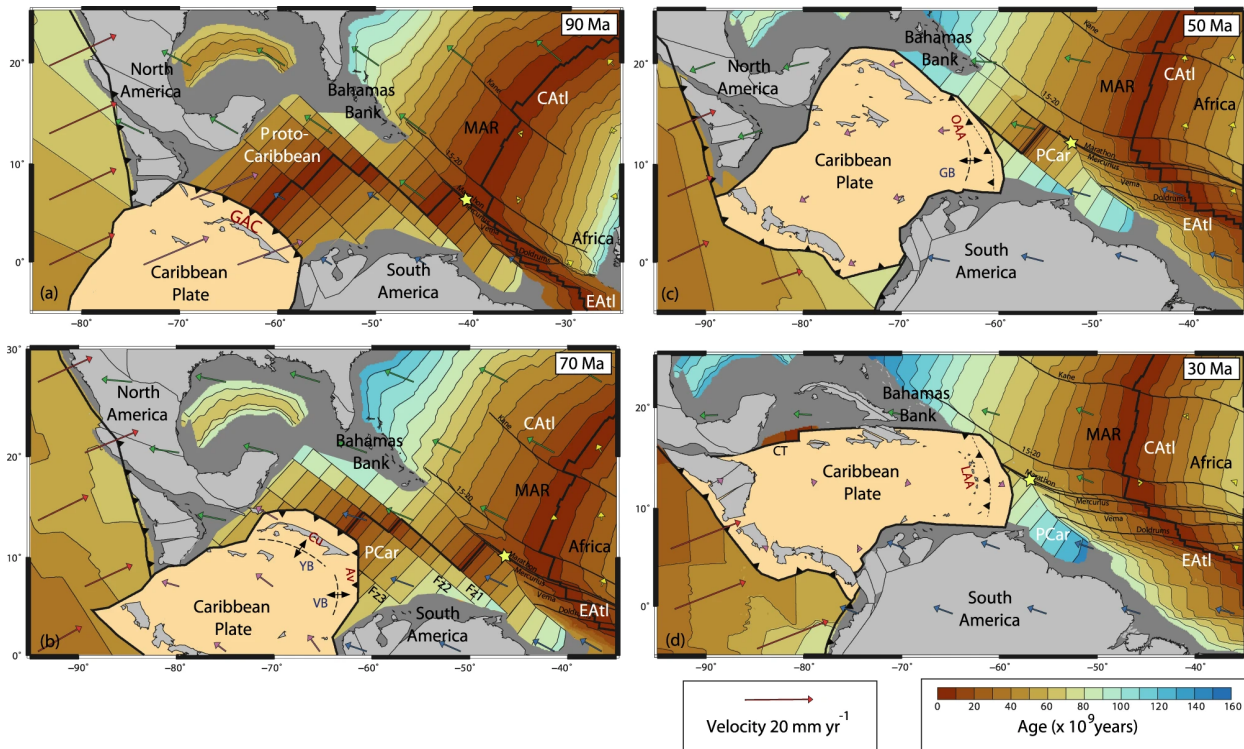
# Geology of the Lesser Antilles

With the break-up of the supercontinent Pangea at the end of the Triassic to the early Jurassic period ( $\sim 200$  Ma, e.g., Rogers et al., 2004), the continents of Laurasia (modern North America and Eurasia) and Gondwanaland (modern South America, Africa, Antarctica, Australia, and India) started to emerge north and south of the equator. This initiated the opening of the Central Atlantic (CA<sub>tl</sub>) at the Mid-Atlantic Ridge (MAR) and the Proto-Caribbean (PCar) Seaway between the North American and the still-conjoined South-American/African continent. During the Late Jurassic and Early Cretaceous ( $\sim 145$  Ma) Earth age (Boschman et al., 2014), the formation of the Caribbean oceanic plate in the area of the modern Eastern Pacific Ocean initiated as the Caribbean Large Igneous Province (CLIP, Serrano et al., 2011). It consisted of a large accumulation of igneous/magmatic rocks (e.g., basalt) and is assumed to be linked in its origin to the Galapagos mantle plume (Buchs et al., 2016). The CLIP mitigated to the east relative to the American plates, pushing and separating the north-south American land bridge towards northeast (Harris et al., 2018). Parts of this land bridge will later form the Greater Antilles consisting of Cuba, Hispaniola, Puerto Rico, Jamaica, and the Cayman Islands (Pindell, 1994).

The subduction of the Proto-Caribbean plate beneath the Great Arc of the Caribbean (GAC) began about 90 Ma ago with the opening of the Equatorial Atlantic (EA<sub>tl</sub>), see Figure 4.1, a), by Braszus et al. (2021). This resulted in a mid-oceanic triple junction (marked with a yellow star in Figure 4.1) between the modern North/South American continent and the African continent (Müller et al., 2019). Towards the end of the Cretaceous period in the Maastrichtian age ( $\sim 72$  Ma, see Figure 4.1, b), the growth in the inter-American gap came to a halt, closing the boundary between north and south, breaking apart the triple junction between the Proto-Caribbean ridge and the Mid-Atlantic ridge (Pindell et al., 2005). After colliding with the Bahamas Bank in the Early Eocene ( $\sim 55$  Ma), inter-plate convergence shifted from northeast-southwest to east-west leading to its current orientation (Boschman et al., 2014). Regional magmatism in the Greater Antilles ceased and the formation of the Lesser Antilles Arc (LAA) was initiated.

The modern Caribbean plate is for the most part surrounded by the conjoined North and South American plates, which induce shear movements along the borders (Boschman et al., 2014). Triggered by slab roll-back ca. 59 Ma ago (Allen et al., 2019), volcanic activity in the remnant Aves Ridge in the Outer Antillean Arc (OAA) ceased and the Grenada Basin (GB) opened (see Figure 4.1, c), caused by a north-south-striking ridge as a result of the retreating Caribbean-Atlantic trench (Harris et al., 2018). The recent arc is proposed (e.g., Christeson et al., 2008) to have been formed since the Neogene ( $\sim 23$  Ma) and consists of the outer Limestone Caribbeans Arc (LCA) with islands in the north up until the eastern part of Guadeloupe and the younger modern inner Lesser Antilles Arc (iLAA) south of it (see Figure 4.2). Separating Lesser from the Greater Antilles is the Anegada Passage ( $\sim 18.25^\circ\text{N}$ ,  $\sim 63.50^\circ\text{E}$ ), a Neogene graben complex (e.g., Bouysse et al., 1990; Laurencin et al., 2017). The backarc region is dominated by the Grenada Basin and exhibits an unusually thick crustal structure ( $> 30$  km) with an oceanic-type lower layer, similar to the





**Figure 4.1:** Plate reconstructions of the Caribbean Sea by Müller et al. (2019) and modified by Braszus et al. (2021). The figure features four times in the reconstruction history of the Caribbean Sea. a) 90 Ma ago in the Early Jurassic. b) 70 Ma ago during the late Cretaceous. c) 50 Ma ago during the Early Eocene. d) 30 Ma ago during the Early Oligocene. Original figure by Braszus et al. (2021).

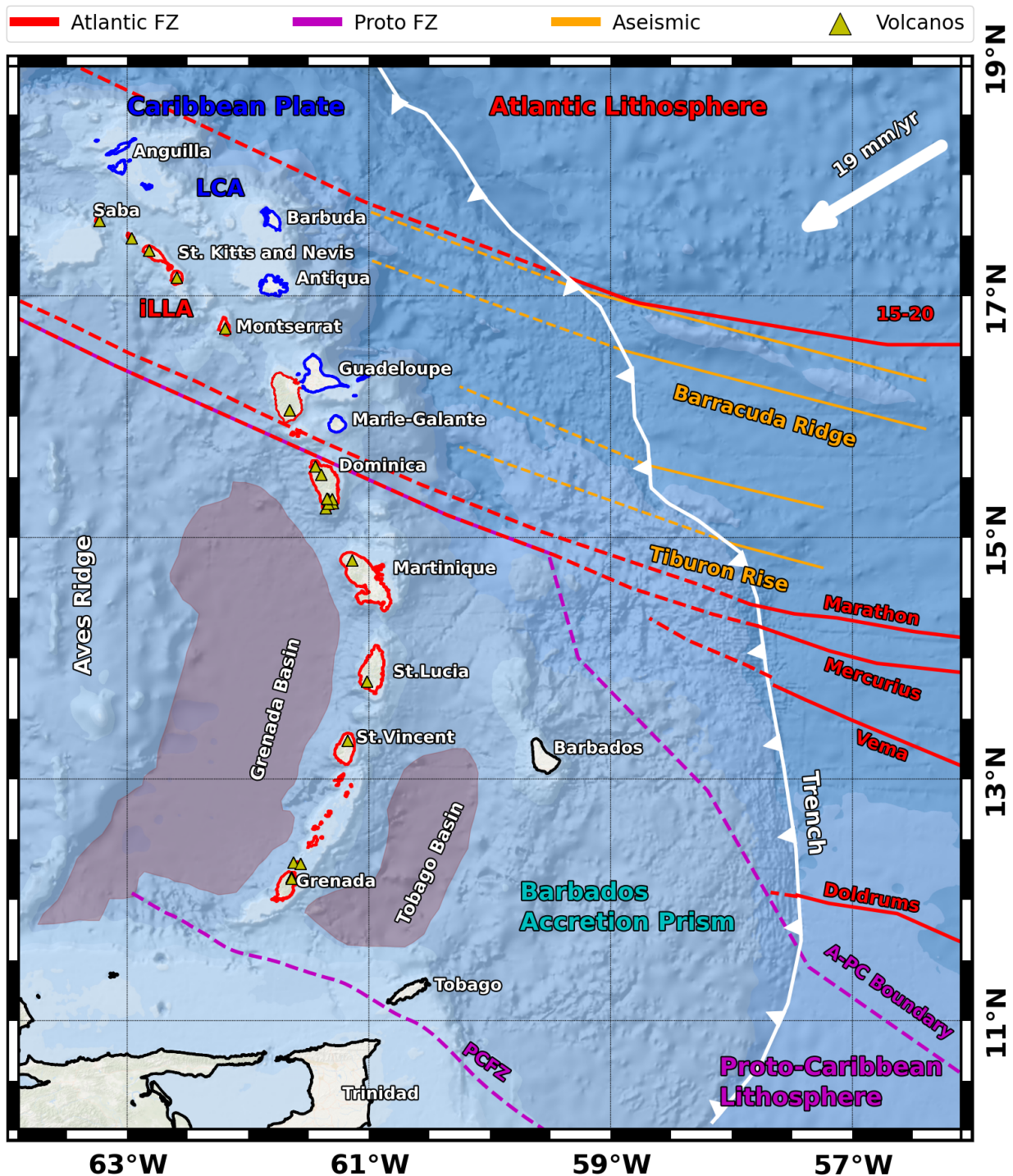
Venezuela Basin (VB, see Figure 4.1, c) west to the Aves Ridge, and a stratified sedimentary upper layer coming from the arc (Westbrook et al., 1984). A recent study of the outer rise region by Allen et al. (2022) found a clear decrease of the velocity in the lower crust and upper mantle of the incoming Atlantic oceanic plate. They interpreted this with bending-related hydration of the subducted slab, which is carried into the mantle. Volatiles, especially water, strongly affects the production of magma and earthquakes (Cooper et al., 2020).

The forearc region exhibits a much more complex morphology like the large Barbados Accretion Prism in the south, which is formed by off-scraping of sediment during the subduction process and turbidites from the Orinoco river in Venezuela (Yannick et al., 2010). The northern part ( $> 15^\circ\text{N}$ ) is marked by complex graben, rifts, and valley structures (e.g., Westbrook et al., 1984; Feuillet et al., 2002; Gonzalez et al., 2017). The arc also features three young ( $< 2\text{ Ma}$ ) volcanic centers which pose a volcanic hazard to the locals (Lindsay et al., 2018): from Saba to Montserrat in the north, between St. Lucia to Grenada in the south and the most active one between Guadeloupe to Martinique in the center (Wadge et al., 1984) with increased activity around Dominica in the last 100 ka (Wadge, 1984) which can be related to lithospheric mantle deserpentinization and the projected water release in a depth of 150-160 km (Paulatto et al., 2017; Bie et al., 2022). The volcanic activity is fueled by the subduction process of the joint Atlantic oceanic crust, which is assumed to be stable since the last 20 Ma, and shows an average rate of  $\sim 1.9\text{ cm/year}$  relative to South America (Demets et al., 2010).

In its current condition, the plate boundary zone between the American plates is still a subject of debate. The oceanic crust is plunged in an east-west orientation, featuring five major fracture zones which can be traced back to the Mid-Atlantic Ridge (Schlaphorst et al., 2016). Different publications set the plate boundary between  $13.5^\circ\text{N}$  and  $17^\circ\text{N}$  within the Mercurius and Fifteen-Twenty fracture zone (e.g., Wadge et al., 1984; Gonzalez et al., 2017; Harris et al., 2018). The domain boundary

between the conjoined Atlantic and the Proto-Caribbean oceanic plate is assumed to progress from the southern parts of the arc east to the trench and indistinguishable merges with the outline of the Mercurius fracture zone after its subduction (Braszus et al., 2021). The subducted slab exhibits a curved outline (spoon-shaped) along the north-south axis (Harris et al., 2018). In the southern region, bordering the Venezuelan continental shelf, the slab has a nearly vertical dip, which to the north is reduced to a more gentle dip of  $30^\circ$  (Bie et al., 2020) to  $45^\circ$  (Wadge et al., 1984) in the central part near Martinique and steepens back to a nearly vertical dip in the Greater Antilles near eastern Hispaniola.

Coupling between the subducted and the overriding plate is particularly weak in a global comparison (Astiz et al., 1988) and the morphology of the subducted plate, especially the progressing fracture zones, is barely known (Bouysse et al., 1990). Of particular interest is the central part between Martinique and Guadeloupe ( $14.5^\circ$  to  $16^\circ$ ). This region acts as the borderline between increased seismicity, especially for larger events ( $M > 7$ ), in the northern part and the less active part in the south (e.g., Dorel, 1981; Russo et al., 1992), whereas the curvature of the slab in depth has here its reversal point (e.g., Wadge et al., 1984; Harris et al., 2018). The seismic hazard in Guadeloupe and Martinique, based on historical catalogs of felt strong motion events since 1530 a.D., is estimated to exhibit intensities of IX every century with the remaining possibility of events exceeding  $M > 8$  (Dorel, 1981). Several publications also indicate a seismic gap in the center of the arc ( $\sim 15^\circ$ ) which is interpreted as a tear in the subducted American slab (e.g., Bouysse et al., 1990; Harris et al., 2018). This anomaly is also recognized in local tomography models as decreased relative P wave velocity perturbation compared to the surrounding arc structure (Harris et al., 2018) in the increased deep seismicity (Gonzalez et al., 2017) by S-phase splitting studies indicating mantle flow through the proposed gap in the subducting plate and in a study of the bulk-to-shear attenuation which found a high ratio anomaly near Dominica indicating melting and expelled fluids in the mantle wedge (Hicks et al., 2023). However, the structures on the subducting slab are still unknown or only limited resolved. Local 3D tomographic models (e.g., Bie et al., 2022) can give valuable insight into them but may not have sufficient resolution to identify small-scale structures. Recent studies examined the processes in the subducted slab top and relate the activity too much more complex tectonic structures than a slab tear as hinted by Bie et al. (2020) proposed by Braszus et al. (2021) and further discussed in the following part of this thesis using regional moment tensor (RMT) solutions. RMT inversion can help to identify the local stress regime and the geometry of small-scale structures.



**Figure 4.2:** Modern Lesser Antilles Arc. Islands marked in red are associated with the young inner Lesser Antilles Arc (iLAA), islands in blue to the older Limestone Caribbeans Arc (LCA). Active volcanos in the iLLA are indicated by yellow triangles (Lindsay et al., 2018). Atlantic Fracture Zones (red), Proto-Caribbean Fracture Zones (magenta), and Atlantic Aseismics (orange) are marked/observed as solid lines east to the trench and as projected as dotted lines west to the trench on the subducted slab.

## Chapter 5

# Bayesian regional moment tensor from ocean bottom seismograms recorded in the Lesser Antilles: Implications for regional stress field

This chapter features my work on the OBS dataset of the Lesser Antilles Arc subduction zone. The content of this chapter got published under Lindner et al. (2022) in the journal *Geophysical Journal International* with me as first author.

### 5.1 Abstract

Seismic activity in the Lesser Antilles (LA) is characterized by strong regional variability along the arc reflecting the complex subduction setting and history. Although routine seismicity monitoring can rely on an increasing number of island stations, the island-arc setting means that high-resolution monitoring and detailed studies of fault structures require a network of ocean bottom seismometers (OBS). As part of the 2016-2017 **V**olatile recycling at the **L**esser **A**ntilles arc (**V**oi**L**A) project, we deployed 34 OBS stations in the fore- and backarc. During the deployment time, 381 events were recorded within the subduction zone. In this paper, we perform full-waveform regional moment tensor (RMT) inversions, to gain insight into the stress distribution along the arc and at depth. We developed a novel inversion approach, Am $\Phi$ B - “Amphibious Bayesian”, taking into account uncertainties associated with OBS deployments. Particularly, the orientation of horizontal components (alignment uncertainty) and the high noise level on them due to ocean microseisms are accounted for using Am $\Phi$ B. The inversion is conducted using a direct, uniform importance sampling of the fault parameters within a multi-dimensional tree structure: the uniXtree-sampling algorithm. We show that the alignment of the horizontal OBS components, particularly in high noise level marine environments, influences the obtained source mechanism when using standard least-squares (L2) RMT inversion schemes, resulting in systematic errors in the recovered focal mechanisms including high artificial compensated linear vector dipole (CLVD) contributions. Our Bayesian formulation in Am $\Phi$ B reduces these CLVD components by nearly 60% and the aberration of the focal geometry as measured by the Kagan angle by around 40% relative to a standard L2 inversion. Subsequently, we use Am $\Phi$ B-RMT to obtain 45 ( $M_w > 3.8$ ) regional MT solutions, out of which 39 are new to any existing database. Combining our new results with existing solutions, we subsequently analyze a total of 151 solutions in a focal mechanism classification (FMC) diagram and map them to the regional tectonic setting. We also use our newly compiled RMT database to perform stress tensor inversions along the LA subduction zone. On the plate interface, we observe the typical compressional stress regime of a subduction zone and find evidence for upper-plate strike

slip and normal fault behaviour in the north that becomes a near arc-perpendicular extensional stress regime towards the south. A dominant slab perpendicular extensional stress regime is found in the slab at 100-200 km beneath the central part of the arc. We interpret this stress condition to be a result of slab pull varying along the arc due to partial slab detachment along previously hypothesized lateral slab tear near Grenada, at the southern end of the LA arc, leading to reactivation of pre-existing structures around the subducted Proto-Caribbean ridge.

## 5.2 Introduction

The Lesser Antilles (LA) island arc (Figure 5.1), located along the eastern margin of the Caribbean Sea, is part of a small yet highly-complex subduction zone system that is driven by south-westward motions of the conjoined North and South American plates (e.g., Bouysse et al., 1990; Harris et al., 2018; Allen et al., 2019). Regional seismicity strongly varies along the arc (e.g., Hayes et al., 2013; Schlaphorst et al., 2016; Bie et al., 2020). The incoming oceanic plate is marked by large bathymetric structures north of  $15^{\circ}\text{N}$  that significantly affect the activity within the shallow forearc. These prominent structures are the Barracuda Ridge entering the trench at around  $16.75^{\circ}\text{N}$  and the Tiburon Rise around  $15.25^{\circ}\text{N}$  (Laigle et al., 2013b). Earthquake activity follows the outline of the arc and reaches down to a maximum depth of  $\sim 190$  km around the island of Martinique. To the north of Martinique at  $\sim 14.5^{\circ}\text{N}$ , the seismicity rate is highest, especially for events with a magnitude greater than 5, whereas to the south, between St Lucia and Grenada, an area with a much lower seismicity rate can be found. Even further south, seismic activity increases again near Tobago.

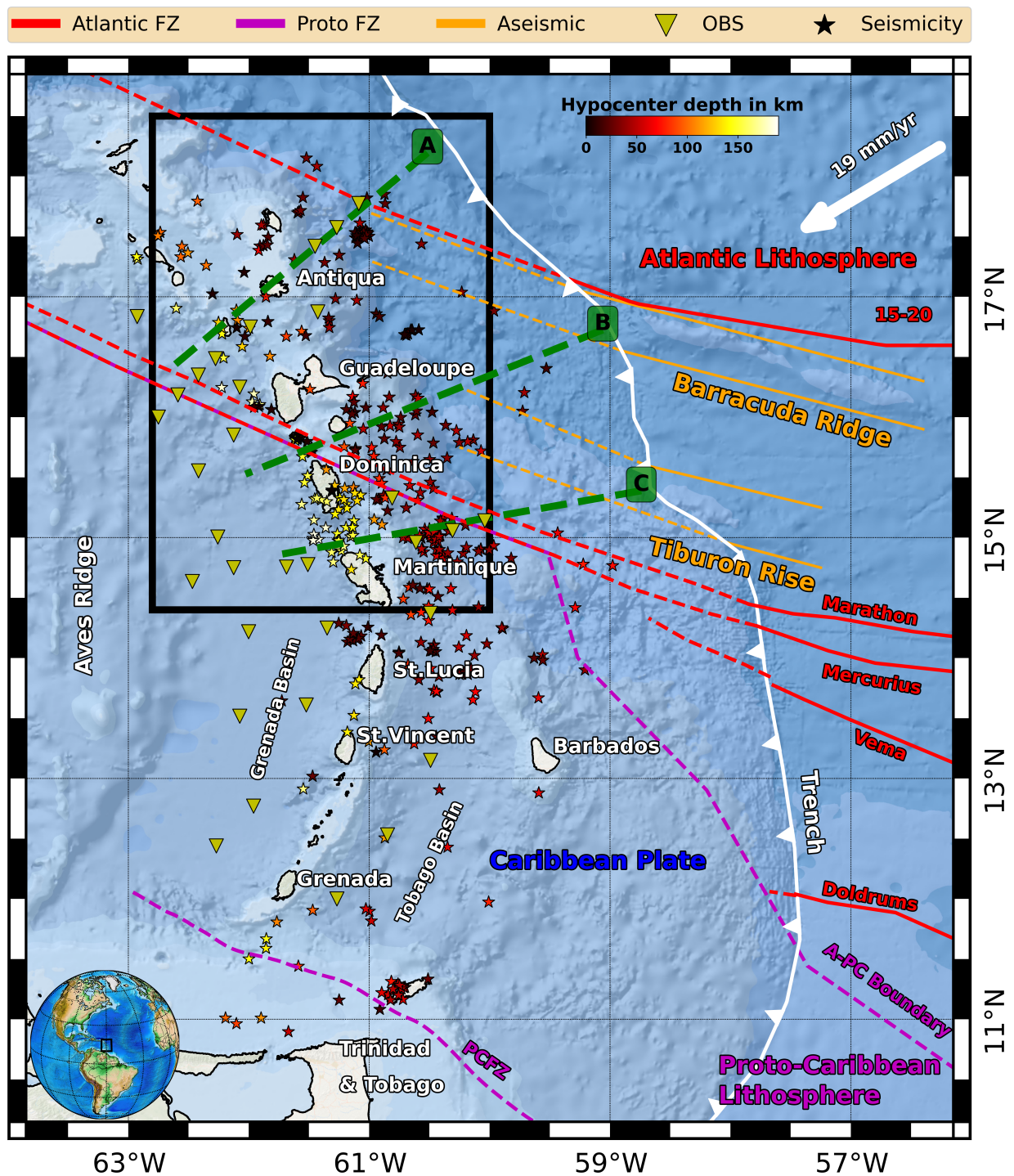
Recent studies (e.g., Ruiz et al., 2013; Laigle et al., 2013a; Laigle et al., 2013b; Gonzalez et al., 2017; Paulatto et al., 2017) focus mostly on the seismically-active northern part of the LA arc between  $14.5^{\circ}\text{N}$  and  $18.5^{\circ}\text{N}$ . The main structural features of the subducted slab in this part of the arc include three prominent fracture zones i.e., the 15-20, Marathon, and Mercurius (e.g., Harmon et al., 2019) and a domain boundary that separates plate material formed along the Proto-Caribbean and Equatorial Atlantic ridges (Cooper et al., 2020; Braszus et al., 2021). Although the exact orientations of these structures at depth are debated, the surface projections of the Marathon and Mercurius fracture zones and the domain boundary pass through the arc near Guadeloupe and Dominica, close to where the highest seismicity rate is also observed.

Since 1952, when regional instrumental earthquake recording started, the arc has been covered by internationally operated permanent stations overseen by the University of the West Indies (Seismic Research Center Trinidad): the current *TRN* Network consists of over 50 seismic stations covering the whole arc with further individual stations and local networks (e.g., CU, G, MQ, WI) from various agencies (e.g., IPGP, KNMI, USGS). The established extensive island instrumentation helped to significantly improve the regional earthquake data catalog over the years.

Earthquake focal mechanisms (FMs) provide valuable insights into seismic fault structures and regional stress fields. However, no routine operational catalog of focal mechanisms for the region exists. Available catalogs are based on retrospective, time-limited studies. Until 2021, to our knowledge, around 106 focal solutions of various quality were available for the northern part of the arc. Using local island stations, (Gonzalez et al., 2017) derived 29 solutions using available waveforms of land stations. Ruiz et al. (2013) derived 22 focal mechanisms using first motion polarities from a temporal amphibious OBS experiment in the forearc offshore Dominica. The remaining solutions are from various international agencies (e.g., GCMT, Geofone, and USGS), and are constrained by recordings at teleseismic distances.

Due to the shape of the LA island arc, regional land installations are restricted. This inherent coverage may bias the source mechanism solutions using land station data alone. An offshore extension of the local network is therefore essential to increase the database of regional FMs, particularly for small and intermediate-sized events. Compared to scarce large events with a

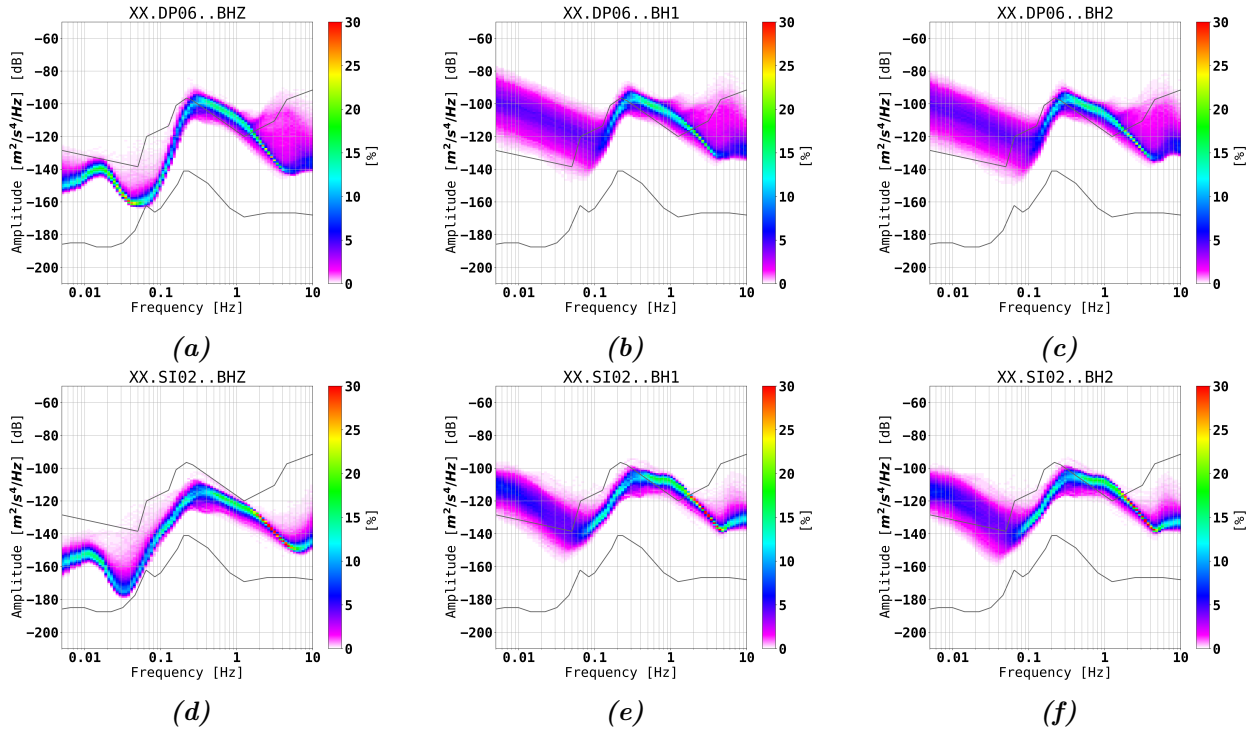




**Figure 5.1:** Bathymetric map of the Lesser Antilles subduction zone. The black box outlines the target area of this study. Triangles show the locations of the VoiLA OBS network, consisting of 32 broadband stations, within the fore- and backarc region. Prominent fracture zones on the Atlantic lithosphere are marked in red, aseismics in orange and inferred features of the Proto-Caribbean lithosphere are marked in magenta. The dashed lines show the projected positions of these features along the subducted slab. Three cross-sections (A-C) are marked as green dotted lines. Background seismicity (black stars) during the operational time is taken from (Bie et al., 2020).

magnitude greater than 7, more regularly occurring smaller events provide detailed insight into fault structures in the crust and the subducting Atlantic lithosphere. They also offer a chance to study the regional stress field and its variation along and across the arc.

Research projects investigating the physical properties of subduction zones now often incorporate OBS stations (e.g., Romanowicz et al., 1998; Ruiz et al., 2013; Cabieces et al., 2020; Leon-Rios et al., 2021). However, the recorded data often provide only a limited source of information for regional moment tensor (RMT) source modeling, for example polarity information in a joined RMT inversion (e.g., Ruiz et al., 2013; Cabieces et al., 2020) or in an inversion restricted to pure double-couple solutions. Two main sources of errors may affect the effective incorporation of OBS data in RMT full-waveform inversions. One are ocean microseisms of which the dominant frequencies around 1.0-0.05 Hz (Yang et al., 2012) have a strong influence on the horizontal components of OBS stations (Figure 5.2). The other source of error is the uncertainty in station locations and alignments of the sensors. Station locations have been assessed using direct arrival times and remaining uncertainties can be accepted if the recorded data are used for studies with wavelengths exceeding them. The influence of alignment, however, is frequency independent and directly affects waveform modeling analyses. Different methods have been developed to estimate the alignment angle of sensors relative to north, including ambient noise correlation (Zha et al., 2013), receiver functions (Janiszewski et al., 2015; Lim et al., 2017), P-wave polarity (Wang et al., 2016) and its combination with Rayleigh-wave polarization (Doran et al., 2017) using natural sources or even artificial ones like ship tracking (Trabattoni et al., 2020).



**Figure 5.2:** Probabilistic power spectral density (PPSD) at stations DP06 (a-c) and SI02 (d-f) computed for a total of 250 days of continuous data records in 2016.

Existing RMT inversion routines can handle uncertainties related to the specific requirements of OBS deployments which are (i) the increased noise level of the observations (e.g., Duputel et al., 2012; Vackář et al., 2017; Pugh et al., 2016; Vasyura-Bathke et al., 2020), (ii) uncertainties in the source localization (Duputel et al., 2012), and (iii) the timing uncertainties in respect to the 1D model e.g., Cut-and-Paste (Zhao et al., 1994). However, to our knowledge, none of these published approaches simultaneously consider the alignment uncertainty at an arbitrary station. Here we present a new inversion routine, AmΦB - Amphibious Bayesian, based on full waveform inversion

(Krizova et al., 2013) in a Bayesian framework (Duputel et al., 2012). We introduce two covariance matrices – one for data error  $\mathbf{C}_d$  associated with increased ambient noise and the second for the model error  $\mathbf{C}_T$  as a function of the sensor alignment uncertainty. The inverse problem (e.g., Yagi et al., 2008; Duputel et al., 2012) is then solved in a uniform tree-sampling search algorithm (Lomax et al., 2001), using the uniform Tape parameterization (Tape et al., 2015) for a deviatoric source mechanism. Other sources of theoretical error can be caused by an uncertain velocity model (Duputel et al., 2014), errors in the hypocenter location (Duputel et al., 2012) or the source time function (Staehler et al., 2014). While we will not examine their effects on our RMT results in particular, potential effects will be discussed.

In this study, we first demonstrate the effects of horizontal alignment uncertainties resulting from both error sources, using synthetic tests of two distinct focal solutions. Following these examinations, we apply our new RMT inversion routine to 45 events in the local earthquake catalog (Bie et al., 2020). We then compile an RMT database that includes newly-derived and pre-existing focal mechanism solutions for the northern part of the Lesser Antilles subduction zone and conduct an inversion for the regional stress orientations.

### 5.3 Method AmΦB - full waveform RMT inversion routine

An earthquake can be approximated mathematically as a point source by a symmetric second order moment tensor, which consists of six equivalent force couples (Aki et al., 2002). The displacement time-series  $d_j^{\text{obs}}(t)$  with  $j \in [Z, R, T]$  recorded at a surface station is not only governed by the source mechanism but also the structural and material properties between source (earthquake) and receivers (seismic stations, Jost et al., 1989). The structural model provides a set of Green's functions  $G_{ij}$  that subsequently construct the synthetic displacement time series in a linear weighted summation of the modeling elements  $m_i$  (e.g., moment tensor elements)

$$d_j^{\text{obs}}(t) = s(t) \cdot \sum_i^I G_{ij} \cdot m_i + e_j(t) \quad (5.1)$$

with source time function  $s(t)$  and residual  $e_j(t)$ . Design of  $\mathbf{G}$  and model vector  $\vec{m}$  is dependent on the number  $i \in I$  of fundamental mechanisms the source is decomposed into (e.g., Zhao et al., 1994; Krizova et al., 2013; Dahm et al., 2014). The radial symmetry of a 1D velocity model requires only three pure double-couple mechanisms to describe any arbitrary double-couple source. Hereby,  $\mathbf{G}$  is designed for displacement traces along pressure, tension and nodal axis, and assembled by incorporating the station azimuth as an additional parameter to the double-couple source mechanism defined by strike, dip and rake (Zhao et al., 1994). A full deviatoric model, on the other hand, is more sophisticated (Krizova et al., 2013) and uses five fundamental double-couple (DC) mechanisms at the given source-receiver geometry (e.g., Sokos et al., 2008; Sokos et al., 2013; Zhu et al., 2013). In the scope of this study we use a combination of both methods for a deviatoric source inversion. Equation 5.1 can be written in matrix form

$$\vec{d}^{\text{obs}} = \mathbf{G}\vec{m} + \vec{E} \quad (5.2)$$

where the source time function  $s(t)$  from Equation 5.1 is integrated into the Green's function matrix. The error  $\vec{E}$  is introduced to compensate differences between the synthetics and actual observation and has been used to comprise multiple uncertainties including source specific assumptions such as wrong centroid location (Duputel et al., 2012), variations in source time function (Staehler et al., 2014), fault structure complexities (Yagi et al., 2008), station alignments (this study) or general local background noise (this study). Considering these uncertainties in the moment tensor inversion problem, Equation 5.2 can be expressed in an ordinary least squares formulation (e.g., Yagi et al., 2008)

$$(\mathbf{G}\vec{m} - \vec{d}^{\text{obs}})^T \mathbf{C}_D^{-1} (\mathbf{G}\vec{m} - \vec{d}^{\text{obs}}) \rightarrow \min. \quad (5.3)$$



To statistically quantify the errors, we introduce a Gaussian distributed probability density. We construct the probability density function (PDF) as stochastic information of the model space

$$Q(\vec{m}) = ke^{-0.5[(\mathbf{G}\vec{m}-\vec{d}^{\text{obs}})^T\mathbf{C}_D^{-1}(\mathbf{G}\vec{m}-\vec{d}^{\text{obs}})]} \quad (5.4)$$

where  $k$  is a normalization factor satisfying  $\sum Q(\vec{m}) = 1$ . Here,  $\mathbf{C}_D$  represents the covariance matrix of error sum  $\vec{E}$ . Likewise, this matrix can be decomposed into the underlying error sources following the error propagation rule

$$\mathbf{C}_D = \mathbf{C}_d + \mathbf{C}_T. \quad (5.5)$$

We assume that error  $\vec{E}$  is attributed to the two largest contributions for an OBS deployment: Ambient noise of ocean microseism with data covariance  $\mathbf{C}_d$  and station dependent alignment of horizontal components defining model covariance matrix  $\mathbf{C}_T$ .

### 5.3.1 Ambient noise

While land stations might have to deal with strong noise due to human activities inducing frequencies greater than 1 Hz (e.g., Lecocq et al., 2020), OBS stations are comparably quiet in this range (Yang et al., 2012). Instead, OBS recordings show a much stronger ocean-induced microseism at frequencies between 1 - 0.05 Hz, which is most pronounced on the horizontal components. The noise at station  $n$  is assumed to follow Gaussian distributed white noise  $\nu_n(t)$  with mean  $\overline{\nu_n(t)} = 0$  and standard deviation  $d\nu_n(t)$  with

$$\sigma_n = \overline{\nu_n(t)} \pm d\nu_n(t). \quad (5.6)$$

For the construction of the data covariance matrix  $\mathbf{C}_d$  we follow the design by Duputel et al. (2012). A simple diagonal matrix design with  $\mathbf{C}_d = \sigma_n^2 \mathbf{I}$ ,  $\mathbf{I}$  being the identity matrix, may result in under-estimations of the uncertainties due to oversampling. This issue is tackled by additionally considering the sampling frequency of the bandpass filtered signal to compensate for this effect

$$(C_d^{ij})_n = \sigma_n^2 e^{-|\Delta t^{ij}|/t_0} \quad (5.7)$$

with  $t_0 = 1/f_{\min}$  and  $\Delta t^{ij}$  being the time difference between sample  $i$  and  $j$  (Duputel et al., 2012).

### 5.3.2 Station alignment

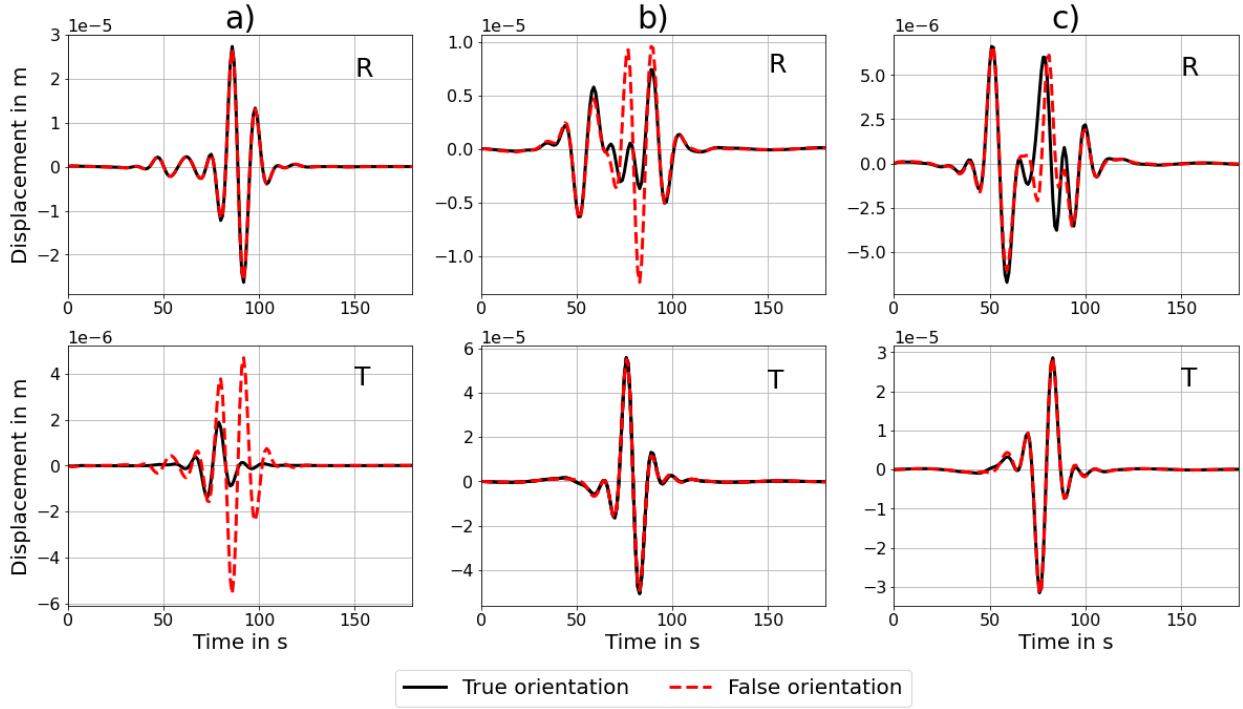
Aligning a seismometer to true north is an important step during installation to ensure data consistency within a seismic network. While the alignment appears straight forward, especially for land stations, large discrepancies to north have been observed throughout different networks (Ringler et al., 2013). The alignment of OBS stations, however, is completely arbitrary and has to be estimated after the deployment. Figure 5.3 displays the influence of a deviating alignment angle of  $d\Phi = 10^\circ$  from true north, which we deem a realistic uncertainty in actual networks, for different source mechanisms on the radial (R) and transverse (T) component on stations at different azimuths.

The three examples show that a false alignment strongly affects at least one of the components depending on station azimuth relative to the pressure, tension, and nodal axis of the mechanism. Correcting the alignment with angle  $\Phi_n$  at station  $n$  can be expressed by a rotation of the horizontal components around the vertical axis  $Z$ :

$$\vec{d}_n = \mathbf{R}(\Phi_n)\vec{d}'_n, \quad (5.8)$$

$\mathbf{R}$  being the rotational matrix around the vertical axis. Equation 5.8 can be interpreted as a linear energy redistribution between the horizontal components R and T scaled by angle  $\Phi_n$  at small deviating alignments. In practise, the true alignment angle  $\Phi_{n,\text{True}}$  cannot be derived exactly but has to be estimated within a reasonable uncertainty range

$$\Phi_{n,\text{true}} = \overline{\Phi}_n \pm d\Phi_n. \quad (5.9)$$



**Figure 5.3:** Influence of  $d\Phi = 10^\circ$  station alignments of horizontal recordings for different source mechanism and station azimuth  $\theta$  from a synthetic test.  $R$  = Radial;  $T$  = Transverse component. **a)** Dip-Slip  $(\psi, \theta, \lambda) = (0, 90, 90)$ ,  $\theta = 80^\circ$  near  $p$ -axis ( $90^\circ$ ), energy on  $T$  gets minimal **b)** Strike-Slip  $(\psi, \theta, \lambda) = (0, 90, 0)$ ,  $\theta = 20^\circ$  near  $n$ -axis ( $0^\circ$ ), energy on  $R$  gets minimal **c)** Normal Fault  $(\psi, \theta, \lambda) = (0, 45, -90)$ ,  $\theta = 30^\circ$  near  $p$ -axis ( $45^\circ$ ), energy on  $R$  gets minimal.

Uncertainty  $d\Phi_n$  can then be translated into a general expression for the covariance matrix for the moment tensor inversion (Duputel et al., 2012):

$$\mathbf{C}_T = \int [\vec{d}(\Phi_n) - \bar{\vec{d}}][\vec{d}(\Phi_n) - \bar{\vec{d}}]^\top \rho_a d\Phi \quad (5.10)$$

with  $\bar{\vec{d}}$  being the average data vector of a population of random deviating angles according to expression 5.9 and  $\rho_a$  the Gaussian probability density of the alignment. This equation can be solved by a Monte Carlo approach using a large population of Gaussian distributed uncertainties in the alignment at each station. However, instead of conducting a large-scale random simulation, we benefit from the data gradient following Equation 5.8, which allows us to consider the sensitivity of  $d\Phi$  to the horizontals for a given focal mechanism. Thus, we can give an expression for observations in the vicinity of the true alignment to the north with:

$$\vec{d}(\Phi_{n,true}) = \vec{d}(\Phi_n) + \nabla \vec{d}(\Phi_n)(d\Phi_n - \Phi_n). \quad (5.11)$$

Since  $d\Phi_n$  is assumed to be generally small, we are able to smooth near  $\Phi_n$  and write  $\bar{\vec{d}} = \vec{d}(\Phi_n)$  in Equation 5.10, leading to

$$\mathbf{C}_T = [\nabla \vec{d}(\Phi_n)] \mathbf{C}_{d\Phi_n} [\nabla \vec{d}(\Phi_n)]^\top \quad (5.12)$$

with  $\mathbf{C}_{d\Phi_n}$  being the variance of  $d\Phi$ . Alignment gradient  $\nabla \vec{d}(\Phi_n)$  is computed numerically as a second order approximation of Equation 5.8 to consider clockwise and anti-clockwise alignment uncertainty

$$\nabla \vec{d}(\Phi_n) = \frac{\vec{d}'_n(d\Phi_n) - \vec{d}'_n(-d\Phi_n)}{2d\Phi_n}. \quad (5.13)$$

### 5.3.3 uniXtree - uniform X-dimensional tree-importance sampling

Grid search analysis for seismic source inversion is a straightforward and robust technique to examine complex problems in arbitrary X-dimensional parameter space but at the cost of potentially large

computational times. It is therefore important to perform the inversion efficiently by avoiding non-uniformity but at the same time allowing for fast convergence to the global minimum.

Uniform sampling of the source parameters in an evenly spaced cartesian coordinate system, be it a direct sampling of 6-moment tensor elements or in a parameterization of five source parameters and seismic moment  $M_0$ , does not result in a uniform distribution of moment tensor solutions (Tape et al., 2016). Likely effects are under-or oversampling of relevant or irrelevant solutions that can cause an increase of the computation time, large sampling-based uncertainties, or even overestimations of local minima. A possible solution to this issue is the n-D hyperspace method (Tashiro, 1977) that enables uniform sampling of the moment tensor elements (Staehler et al., 2014) on an ellipsoid using 5 independent parameters and the seismic moment. This approach is straightforward as uncertainties become directly apparent on the elements. In further examinations, however, this leads to the general decomposition analysis for the full tensor to study isotropic changes and CLVD (Compensated Linear Vector Dipol) parts as well as the uncertainties in respect to the fault geometry. In this study, we employ the approach by Tape et al. (2015) where the source is represented in a geometric framework spanned by five independent angles that are directly connected to the source parameters. Strike, dip and rake are parameterized on a sphere whereas CLVD and isotropic parts are projected onto a lune. In this work, we only focus on deviatoric parameters, hence a general tectonic shear mechanism without volume changes. The remaining space has unique features with different behaviors at the boundaries:

- Strike with  $\psi \in [0, 2\pi]$
- Dip with  $\theta \in [0, \frac{\pi}{2}]$  and in the uniform Tape representation:  $h = \cos(\theta)$  and its inverse with  $\theta(h) = \arccos(h)$  with  $h \in [0, 1]$
- Rake with  $\lambda \in [-\pi, \pi]$
- CLVD  $\in [-100\%, 100\%]$  and in the uniform Tape representation:  $v = \frac{1}{3}\sin(3\gamma)$  with  $\gamma \in [-\frac{\pi}{6}, \frac{\pi}{6}]$  and its inverse with  $\gamma(v) = \frac{1}{3}\arcsin(3v)$  with  $v \in [-\frac{1}{3}, \frac{1}{3}]$ . Conversion between classical CLVD parameter to uniform parameterization  $\gamma$  is done by multiplying by 30/100 and back with 100/30 to convert gamma in degree and then to radian.

Using a direct sampling approach of the Tape parameters, we explore the tree-importance sampling algorithm that is extensively used for different computational problems in 3D visualizations (e.g., Meagher, 1982; Fujimura et al., 1984) or in more modern applications together with neural networks (Wang et al., 2017a). The application to geophysical problems was first applied by Lomax et al. (2001) for the octant sampling of the 3D hypocenter location. Compared to generally used techniques like the Monte Carlo or Metropolis-algorithm, it has been shown that an oct-tree algorithm is more global and complete while only depending on a few parameters. The general tree data sampling structure is recursively subdividing X-dimensional spaces into  $2^X$  sub-volumes. For 1-dimension the tree structure results in bisecting the search interval, whereas higher dimensions like in 3D lead to 8 subvolumes called octants (hence commonly referred to as an oct-tree). It drastically reduces the number of samples by an order of  $10^5$  with respective computational time while allowing for examinations of the whole model space in a robust manner. For the application to moment tensor inversion, we sample in a 4D space spanned by  $\psi$ ,  $h$ ,  $\lambda$ , and  $\gamma$ . Probability  $P_i$  of a source solution is then defined by Equation 5.4 with PDF  $Q(\vec{m})$  and weighted by the represented sub-volume  $V_i$  with:

$$P_i = V_i \cdot Q(\vec{m}) \quad (5.14)$$

The uniXtree approach deployed, enables an efficient way to increase resolution within the full model space around highly probable solutions while only sampling coarsely volumes of less importance.

## 5.4 Data




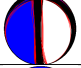

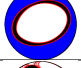

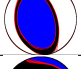

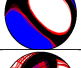


### 5.4.1 VoiLA OBS deployment

Between March 2016 to May 2017, a regional OBS network was installed as part of the NERC-funded international multidisciplinary consortium project - VoiLA, to study the **V**olatiles in the **L**esser **A**ntilles Island Arc (Goes et al., 2019). The network consists of 34 broad-band sensors deployed in the fore- and the backarc area (Collier, 2015) along the arc with a focus on the northern parts (Figure 5.1). During the operation time, 381 seismic events were located with high accuracy and assigned with local magnitudes (Bie et al., 2020). The stations were located at an average water depth of  $\sim 2800$  m with individual instruments as shallow as 812 m and as deep as 5054 m. Applying the empirical relation between water depth and the peak-frequency of related ocean induced microseismicity (Figure 5.2, Yang et al., 2012), we find dominant ocean microseism signals between 0.008 Hz to 0.01 Hz. Considering the resolution restriction of our local 1D velocity model (Bie et al., 2020), the usable frequency range is set between  $f_{min} = 0.03$  Hz and  $f_{max} = 0.1$  Hz. This frequency band is well below the expected dominant frequency of the source time functions for events with  $M_w < 6.0$ . Approximate horizontal sensor orientations were determined using the Rayleigh-wave polarisation analysis method of Doran et al. (2017); however, formal uncertainties in these azimuths,  $d\Phi_n$ , can reach up to  $12^\circ$ .

### 5.4.2 Data selection

In this study, we focus on the northern part of the LA arc. The target area spans between  $14.4^\circ\text{N}$  to  $18.5^\circ\text{N}$  and between  $60.0^\circ\text{W}$  in the forearc to  $62.75^\circ\text{W}$  in the backarc region (Figure 5.1; black box). For later interpretive approaches, the area is further split into upper plate crustal ( $z < 33$  km), slab interface ( $33 < z < 100$  km) and deep intraslab ( $z > 100$  km) layers as well as a northern ( $> \sim 16.5^\circ\text{N}$ ) and southern sector. Initial event selection is based on local magnitudes and reported source locations by Bie et al. (2020). For deep hypocenter locations, a minimum magnitude of  $M_L 4.1$  has shown to have a sufficiently high signal-to-noise ratio (SNR) while for crustal events (up to 33 km) we were able to examine events down to  $M_L 3.8$ . The minimum number of stations used in the inversions is set at 5, but the vast majority of the events have only a sufficiently good SNR on vertical components. 45 out of the 381 cataloged events (Bie et al., 2020) fulfill these conditions and display a sufficient enough SNR on at least the vertical components. The six largest events feature a focal solution in the USGS database (Table 5.1) and partially the GCMT catalog. For the modeling of these events, we use the reviewed source information by Bie et al. (2020) and for the construction of the Green Functions matrix  $\mathbf{G}$ , the therein published local 10 layered 1D velocity model. As hypocenter locations and velocity model derive from the same source, we assume the influence of location errors and uncertain velocity structures to be minor, especially at the low frequencies used in the inversion. In total 39 events are new moment tensor solutions not already published in any database. We define two sets of events - the first comprising six events with FMs reported by USGS and GCMT belong to a reference event set, and the rest assigned to a new event set.

**Table 5.1:** Table of reference events. The table features two different depth information (in order): the depth given by USGS and the depth (blue) derived by Bie et al. (2020). Lateral information are similar in both sources, displayed are the location by Bie et al. (2020) which we also use in the inversion process. Entries marked in blue are findings of this study. Our beachballs are displayed for 95% (black) and 97.5% (red) probability solution.

ID	Day Onset-Time	lat depth	lon depth	$M_w$ $M_w$	FM FM	CLVD CLVD	Lit. USGS	This Study
ev106	2016-05-09 13:36:27.76	16.179   23.9	-60.615 32.34	4.4 4.7	77,57,-115 78,57,-114	-22 —		
ev122	2016-10-14 17:25:24.00	16.723   25.3	-60.655 10.65	4.4 4.7	180,2,105 179,83,-79	-4 —		
ev123	2016-10-18 22:07:43.75	15.298   146.0	-61.352 159.62	5.6 5.6	248,44,-106 246,42,-93	2 8		
ev143	2017-02-03 19:53:52.86	15.065   44.0	-60.457 51.14	5.80 5.9	334,59,86 341,55,87	1 -2		
ev152	2017-04-17 06:24:41.40	17.513   18.7	-61.025 20.59	4.8 5.0	133,37,-87 140,68,-70	9 2		
ev155	2017-04-25 09:53:31.81	16.835   38.5	-60.915 15.71	4.4 4.5	336,79,82 9,61,80	11 —		

## 5.5 Synthetic tests

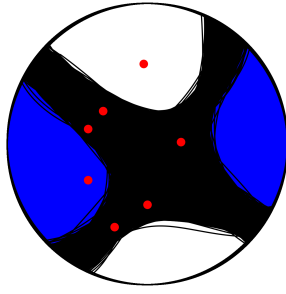
To evaluate the robustness and accuracy of our inversion algorithm, we conduct a series of synthetic tests. In the first part, we study a synthetic strike-slip mechanism recorded within the station arrangement of the VoiLA OBS network, to compare the standard linear source inversion with our new Bayesian approach that takes into account the station alignment and ambient noise individually. In the second part, we examine how our inversion routine performs with various source mechanisms and the number of OBS recordings.

### 5.5.1 Influence of station alignment

Let us assume a well-distributed sub-network within the given VoiLA geometry consisting of 7 receivers. The source is located at its center and set as a pure strike-slip with  $(\psi, \theta, \lambda) = (35, 75, -5)$  (Figure 5.4). We simulate 10,000 realizations with a normal distributed alignment error at  $\bar{\Phi}_n = 0^\circ$  and  $d\Phi_n = 15^\circ$  for each station and invert for the source mechanism in a linear L2 inversion. As expected, we observe variations between true and inverted mechanisms in strike, dip, and rake whereas the mean is at the true model. A noticeable change can be observed in the appearance of a non-neglectable CLVD component with a mean near zero and uncertainty of 15%. A CLVD acts as an amplitude compensation on the waveforms to adjust for missing or excessive mean energy content that cannot be fully described by a pure double-couple model. In the case of false station alignments, the amplitude discrepancies on the horizontals between synthetics and observables are governed by the energy redistribution following Equation 5.8. While the mean CLVD in a large population of solutions is still around zero, the increased (positive or negative) uncertainty may be mistakenly interpreted as an indicator of erroneous assumptions in the velocity model or a more complex source structure. Those assumptions might lead to a complex re-evaluation of the source and occur as a systematic error for projects using the network. A simple linear inversion algorithm is thus not able to handle such an error and will return large uncertainties.

### 5.5.2 The influence of ocean noise

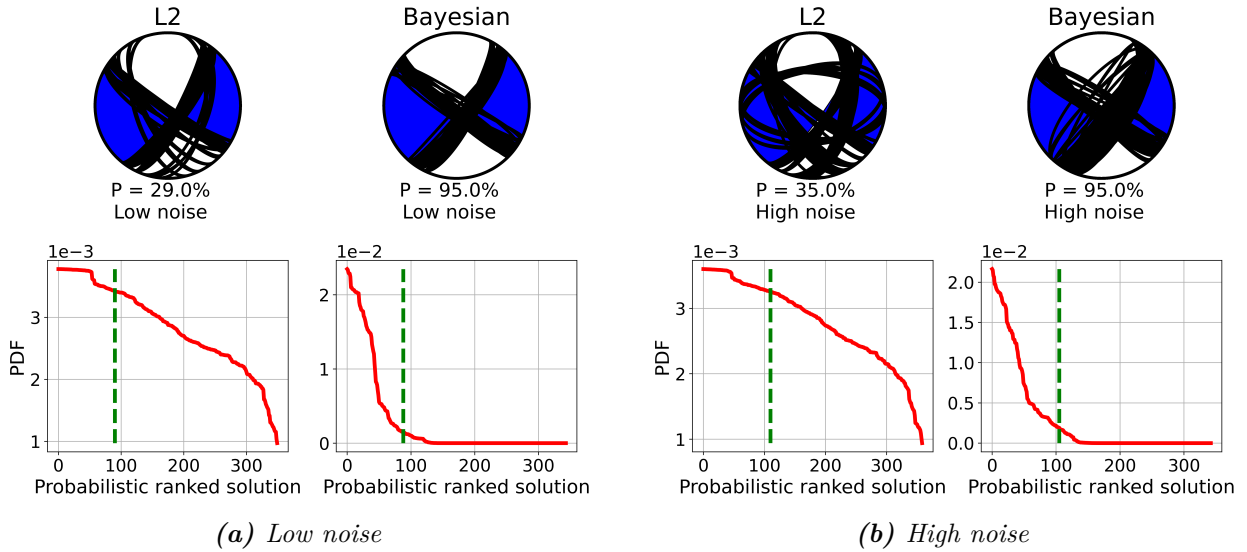
In extreme cases, noise can lead to unfavorable destructive or constructive alterations of the waveforms leading to misinterpretations of local minima with subsequent ambiguous solutions and



Error (NL2):  $0.191 \pm 0.056$   
 Probability:  $0.909 \pm 0.025$   
 True Solution:  $\psi = 35/126 \mid \delta = 75/85 \mid \lambda = -5/-164$   
 Inversion:  $\psi = 35.0 \pm 2.5 \mid \delta = 74.9 \pm 2.2 \mid \lambda = -4.8 \pm 5.1$   
 CLVD :  $0.384 \pm 15.745$   
 ISO :  $-0.000 \pm 0.000$

**Figure 5.4:** Influence of station alignments on a distinct strike-slip source solution. Effect of 10000 Gaussian distributed station alignments with mean  $\bar{\Phi}_n = 0$  and standard deviation  $d\Phi_n = 15^\circ$ . Red dots mark the piercing points of rays at the stations.

large uncertainties. We examine the difference between our Bayesian error formulation and an L2 (no covariance matrix) cost function (Equation 5.4). Figure 5.5 displays the results for a Bayesian (data covariance matrix  $\mathbf{C}_d$ ) formulation and a L2 cost function at two different signal-to-noise (SNR) levels. The top row shows the FMs for the true mechanism (blue) and the best inversion results (black). The number of the best solutions depends on the 95% confidence interval of the Bayesian run and is marked as a green dotted line in the PDF graphs. Importance sampling using a Bayesian formulation suppresses improbable solutions and highlights one with high probabilities as shown by the narrow PDF. This suppression is not applicable for an L2 formulation which results in a much wider PDF covering a larger volume in the parameter space representing potentially different solutions. For low (Figure 5.5a) and high (Figure 5.5b) noise the Bayesian formulation



**Figure 5.5:** Pure DC inversion results for a strike-slip mechanism using a L2 and a Bayesian error formulation. Simulations are performed for low noise a) and a high noise level b). True source solution is displayed in blue with top solutions marked by black lines. Below each beachball is the sorted probability density function, the green vertical dotted line marks the top 95% of the Bayesian solution and the corresponding number of samples in the L2 inversion at the same noise level.

yields the true source mechanism with a corresponding level of uncertainty. In the case of L2, however, we observe also a possible thrust fault solution parallel to the tension axis of the true strike-slip mechanism. Tensional and compressional areas of both mechanisms show similarities in the recorded waveforms and can lead to wrong identification for unfavorable network configurations. If we increase the noise level, the L2 approach returns two probable solutions in the form of a

normal and thrust fault parallel to the tension and pressure axis, respectively.

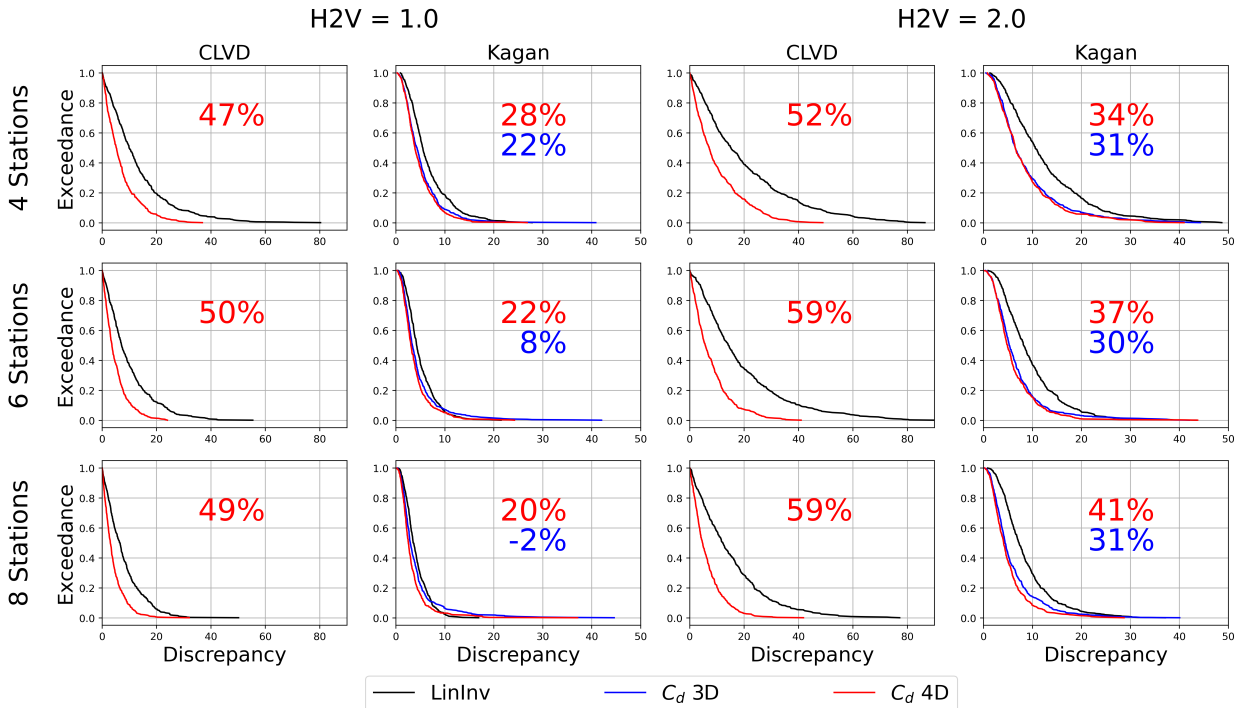
### 5.5.3 Influence of the VoiLA network geometry

Based on the network geometry of the VoiLA network, a subset consisting of a given number of stations within a source-receiver distance of 350 km are randomly chosen to perform source inversion for arbitrary double-couple mechanisms. We choose the location of ev123 - an earthquake located in the middle of the network - as fixed hypocenter location (Table 5.1). For each experimental setup at least 10.000 random realizations have been conducted. Discrepancies between true and resulting deviatoric source solution are measured using the Kagan angle (Kagan, 1991) and absolute percentile changes in the CLVD. All discrepancies are then ascending sorted and normalized on their number. Colored curves in the results plots represent the exceedance frequency for a given discrepancy of Kagan or CLVD. To compare the performance of different inversion approaches, we calculate a reduction percentage between the L2 and the Bayesian formulation:

$$\text{reduction} = 100 \cdot \left( 1 - \frac{\sum pdf_{Bayesian}}{\sum pdf_{L2}} \right). \quad (5.15)$$

#### Performance using data covariance $\mathbf{C}_d$

The Bayesian error formulation employs only the data covariance matrix  $\mathbf{C}_d$ . In the construction of the matrix, 50% of the simulated vertical peak noise amplitude of each trace is set as  $\sigma_n$  in Equation 5.7. The station-wise simulated noise on the horizontal components is then re-scaled with a constant factor between the horizontal to the vertical peak noise amplitude (H2V). Our tests were conducted for 4, 6, and 8 random distributed stations but with a fixed source location. To restrict the number of free parameters, we keep the magnitude fixed.



**Figure 5.6:** Synthetic noise test with base amplitude level at 50% of vertical peak signal. Marked as black curves are the results for a simple linear inversion while red is a Bayesian formulation using a data covariance matrix  $\mathbf{C}_d$  in a deviatoric tree-importance sampling. Corresponding percentage values are the relative reduction of the curve integral between the L2 to the Bayesian formulation.

Figure 5.6 summarizes the results of the random sample study at all setups. Displayed PDF curves

represent the ascending discrepancy normalized by the number of random realizations ( $> 10.000$ ). The average discrepancy in the Kagan angle and CLVD percentage increases proportionally to the H2V factor and with decreasing number of stations. Significant differences appear between the L2 and the Bayesian formulation, where the Kagan angle and CLVD percentage is predominantly smaller using the latter approach. Especially the error to the true CLVD could be reduced (relative reduction of the areas below the curves following Equation 5.15) by around 48% at a horizontal H2V factor of 1.0 and up to 59% at larger noise with H2V factor 2.0. Reduction of the Kagan discrepancy is again smaller for H2V factor 1.0 at 20% to 28% but much better at H2V factor 2.0 with a reduction of up to 41%. In all settings, however, we can observe significant outliers in the Bayesian approach of the Kagan angle at H2V factor 1.0. These outliers are due to the underestimation of errors, arising from the definition of the data covariance matrix  $\mathbf{C}_d$  (Equation 5.7), that are ignored in the L2 approach. Average noise amplitude  $\sigma_n$  is measured before the origin time at each station and assumed to be stationary and uncorrelated white noise. This assumption, however, depends on the absence of unknown transient signals (Vasyura-Bathke et al., 2021). Furthermore, the frequency band and sampling rate must be chosen with care to avoid pessimistic uncertainty estimations due to oversampling (Equation 5.7 Duputel et al., 2012).

### Performance using data and model covariance $\mathbf{C}_D$

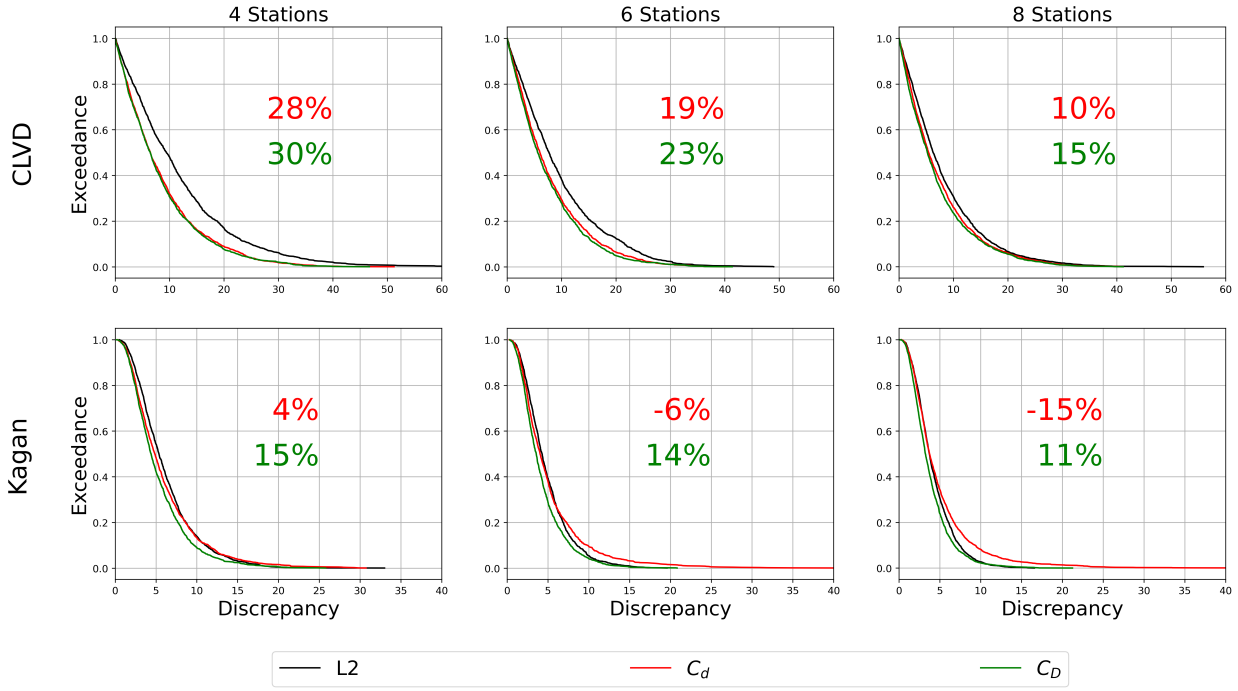
Station alignment on the observed data affects the full waveform information on the horizontal components, hence noise and transient signal. The model covariance matrix  $\mathbf{C}_T$  is constructed based on the synthetics, which display the pure transient signal without any noise. This allows us to directly examine the uncertainties on the earthquake signal itself, while noise is handled by the data covariance matrix  $\mathbf{C}_d$  (Equation 5.5). For the construction of  $\mathbf{C}_T$ , we assume an average alignment angle  $d\Phi_n$  (Equation 5.12) of  $10^\circ$  at all stations within a chosen network configuration. As this magnitude of  $d\Phi_n$  represents only a small variation, the inversion problem can be treated in a first-order approximation as a linear energy redistribution between the horizontal traces (Equation 5.11).

Alignment affects the recordings at the horizontal components with low energy content (Figure 5.3), so we need to consider a low noise level. This assumption stands valid, as small magnitude events within a comparatively high horizontal noise level, as is the case for OBS recordings, are mostly restricted to vertical recordings and hence are independent of this error source. In contrast to that, large events with a good signal-to-noise ratio are more affected by small alignment uncertainties as there are potential non-negligible inferences between the two error sources.

We design a synthetic study for a base noise of 30% of the vertical trace and no additional amplification H2V factor on the horizontal components (H2V factor 1.0). General settings are adopted from the previous noise examination for 4, 6, and 8 random distributed stations.

Figure 5.7 summarizes the results of the random study at all surveyed setups. Displayed curves follow the same notations as in Figure 5.6 but with a third one representing the discrepancy of a  $\mathbf{C}_D$  sampling. For the CLVD we observe a much smaller reduction between the L2 and Bayesian inversion. While the noise conditions are the same in the previous tests with horizontal H2V factor 1.0, it becomes apparent that changes are attributed to the additional station alignment. Differences, however, can be observed between a  $\mathbf{C}_d$  inversion and a  $\mathbf{C}_D$  inversion (Equation 5.5). While comparatively small, the  $\mathbf{C}_D$  setting is generally better compared to the  $\mathbf{C}_d$  inversion and increased with the number of stations. For the Kagan angle, we observe a strong worsening of the  $\mathbf{C}_d$  inversion in contrast to a  $\mathbf{C}_D$  inversion. Like in the previous test (Figure 5.6) low probable outliers become noticeable in a  $\mathbf{C}_d$  inversion but do not appear in the  $\mathbf{C}_D$  inversion.



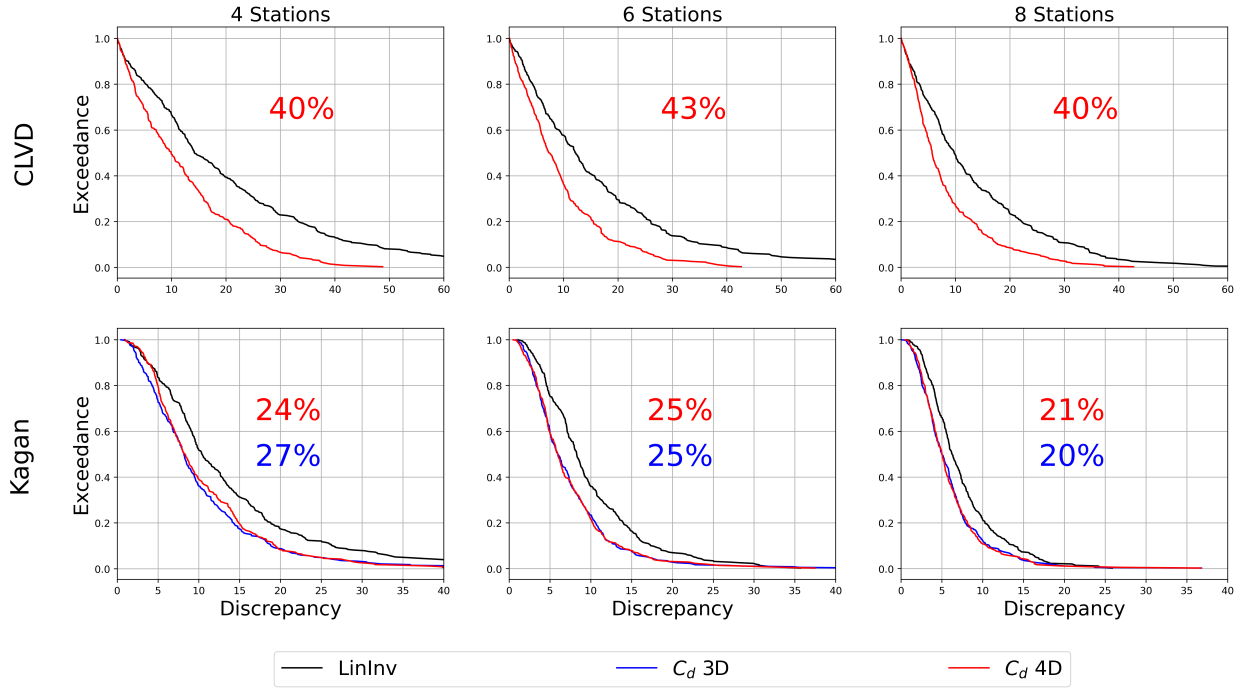


**Figure 5.7:** Synthetic alignment test at 30% vertical base amplitude with horizontal to the vertical peak noise amplitude ( $H2V$ ) factor of 1.0 and  $10^\circ$  mean Gaussian distributed station alignment angle. Displayed PDF curves follow the same notation as in Figure 5.6 but with a fourth curve (green) displaying the results of a Bayesian  $C_D$  formulation.

### Effects of restriction on vertical recordings

For most of the earthquakes in our OBS database, we expect a limitation to the vertical recordings, especially for events at the lower end of the resolvable magnitude range ( $M_w < 4.8$ ). In a final synthetic study, we examine the effects of a vertical component analysis in comparison to a three-component analysis. In practice, most inversions of small magnitude events are not only limited on the vertical recordings but also to a comparable small and potentially badly distributed network. A full deviatoric description of such sources might hereby be misleading as the CLVD affects the amplitudes of all three components on a different scale. We hereby follow our previous setup with a base noise level of 50% of the vertical peak amplitude.

As before we can observe a significant reduction of the CLVD discrepancy (Figure 5.8), but 10% to 20% smaller compared to an inversion employing three components (Figure 5.6). In an absolute comparison between a vertical and three-component inversion, we notice a drastic worsening compared to the case with an  $H2V$  factor of 1.0 and a similar level at  $H2V$  factor 2.0. Assuming that a restriction on only vertical data is attributed to an  $H2V$  factor exceeding 2.0, inversion results can be expected to be generally better compared to using all three components. A similar pattern can be observed for the Kagan angle. Interestingly the reduction of the discrepancy in the Kagan angle using a pure double-couple inversion becomes similar to that of a deviatoric inversion.



**Figure 5.8:** Comparison of a vertical trace (1C) data restricted inversion versus a three component (3C) inversion in a synthetic noise test at 50% vertical base amplitude. Displayed PDF curves follow the same notation as in Figure 5.6.

## 5.6 Results

### 5.6.1 Reference event set

During the VOILA deployment, various international agencies (e.g., USGS, GCMT, GEOPHONE) reported source mechanisms for 6 local earthquakes. These six events define our reference event set, which is used to test the performance of our inversion algorithm with real data. We find large discrepancies in the source depth between the USGS locations and the relocated hypocenters of Bie et al. (2020), that we fixed for all inversions. All derived MT solutions show a high degree of similarity with published solutions. In the following, we will highlight the inversion results and detailed comparison for the three largest events (Table 5.1). Event ev143, the largest earthquake in our observation period with a moment magnitude of  $M_w$ 5.9, occurred on February 03, 2017, at 19:54:22.86 UTC at a depth of around 50 km within the forearc region east of northern Martinique. We use a total of 19 OBS stations for the inversion but are restricted to using mainly vertical components as most horizontal components exhibit saturation due to strong ground motion in the near-field. The derived mechanism depicts a thrust fault with (strike, dip, rake) = (341, 55, 87) and a CLVD of -2%. Our result slightly differs in the dipping angle (by about  $11^\circ$ ) compared to the USGS solution (334, 66, 84) but shows much higher similarity to the GCMT solution (334, 59, 86). The derived half duration is, according to the USGS database, at 4.0 seconds, which is well above our defined frequency band. Event ev123 occurred on October 18, 2016, at 22:08:13.75 UTC offshore Martinique. With a depth of approximately 160 km and a moment magnitude of  $M_w$ 5.6, it is the strongest earthquake in this region since the 2007  $M_w$ 7.4 Martinique event. Its central location provides good azimuthal coverage and good SNR on all three components of at least 7 stations. We utilized a  $C_D$  Bayesian inversion, as we have a sufficient SNR on all three components. Our results (246, 42, -93) indicate a trench perpendicular normal fault that is in good agreement with the solutions obtained by USGS (251, 43, -100) and GCMT (248, 44, -106) but with an increased CLVD of  $\sim 8\%$  in our solution. The third event, ev152 with a magnitude of  $M_w$ 5.0, occurred on April 17, 2017, at 06:25:10.47 UTC at a depth of 21 km. It is part of the most active cluster in the northern shallow forearc offshore Antigua during our deployment. The derived mechanism displays

a trench parallel normal fault with a small positive CLVD part of 2% but shows discrepancies in the double-couple part between our (133,37,-87), the USGS (140, 68, -70), and the GCMT (106, 40, -125) solutions. The remaining three events are only listed in the USGS database but are generally consistent with our solutions (Table 5.1).

### 5.6.2 Combined MT catalog for northern LA subduction zone

We compile a catalog of 151 MTs that includes 29 local solutions by Gonzalez et al. (2017), 22 from Ruiz et al. (2013) who focused on a small area east of Dominica and Martinique, 55 teleseismic solutions from various agencies (GCMT, Geofone, and USGS), and 45 derived by Bayesian inversion of OBS waveforms in this study. We mapped this catalog into a focal mechanism classification (FMC) diagram (Álvarez-Gómez, 2019) and the crustal events are divided manually into 5 groups based on their FMC location and mechanisms (Figure 5.9). All events below 100 km depth form the sixth group that contains a variety of mechanisms but is dominated by NFs. We plot all events (color-coded for each group) in map view (Figure 5.10) together with key features such as projected fracture zones, slab depth-contours, and projected rupture areas of the 1839 and 1843 events. We show three cross-sections (A,B,C) that intersect important tectonic/geodynamic features. The unprecedented quantity of MTs enables a detailed analysis of the earthquake source mechanisms within our target area.

#### Plate interface seismicity

Seismic activity at the plate interface is marked by thrust events (dark blue mechanisms) at  $50 \pm 10$  km depth and shallow dipping thrust events (light blue mechanisms) close to the trench (Figure 5.10). The dip angles follow the subducting slab geometry. In the northern area ( $16.5^\circ\text{N}$  -  $18.5^\circ\text{N}$ ) particularly, the thrust events at various depths define a wide seismogenic interface between the subducting and overriding plates. This zone overlaps with the estimated rupture area of the 1843 M8.5 earthquake - the largest megathrust event in the LA recorded in history (Feuillet et al., 2011b). To its south ( $15.0^\circ\text{N}$  -  $16.5^\circ\text{N}$ ), a lack of thrusting and shallow dipping events is consistent with previous studies (e.g., Gonzalez et al., 2017). To the east of Martinique ( $15.0^\circ\text{N}$ ,  $-60.5^\circ\text{W}$ ), several thrust events are found within the estimated rupture area of the 1839 M7.5 megathrust event (Feuillet et al., 2011b, Figure 5.10, zoom box 2), and there are no shallow dipping thrust events near the trench as found in the north.

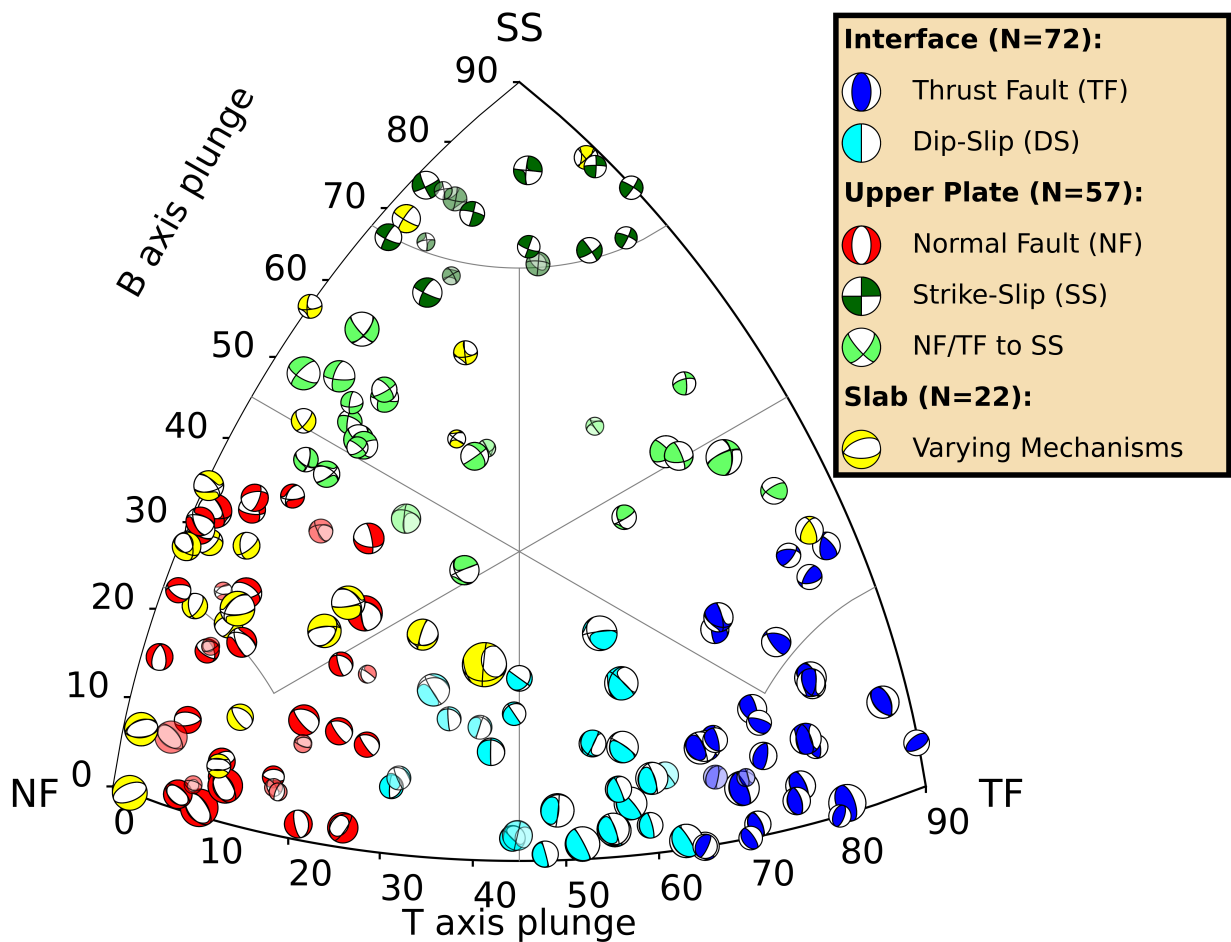
#### Upper-plate seismicity

Normal faulting (red mechanism) dominates the upper-plate seismicity, with sporadically scattered strike-slip (dark green mechanism) and oblique normal/thrust faulting to strike-slip (NF/TF to SS) events (light green mechanism). The northernmost sector of our target area shows an larger number of oblique events relative to the south. While the occurrence of oblique events decreases towards the south, normal faulting events become more frequent, especially near event ev152. The highly active cluster produces at least five  $M_L > 3.9$  events in a day (Bie et al., 2020) and features a mixture of normal and NF/TF to SS transitional events (Figure 5.10, zoom box 1). With an average depth of 20 km, this cluster is near the plate interface where we can also observe several shallow dipping thrust events just below and surrounding it. Normal faulting events in the crust increase in the southern sector particularly between Guadeloupe and Dominica ( $15.8^\circ\text{N}$ ,  $61.65^\circ\text{W}$ ). A prominent event of this cluster is the shallow 2004  $M_w 6.3$  Les Saintes earthquake which ruptured part of an arc-parallel en echelon fault system (Feuillet et al., 2011a). The mainshock triggered up to 30,000 aftershocks within the following two years and is one of the largest instrumentally recorded seismic events in the Lesser Antilles (Feuillet et al., 2011a). We observe additional normal faulting events close to the interpreted upper plate Moho (Figure 5.11, profile B), striking in the trench perpendicular direction. Further south, large-magnitude crustal events are rare.

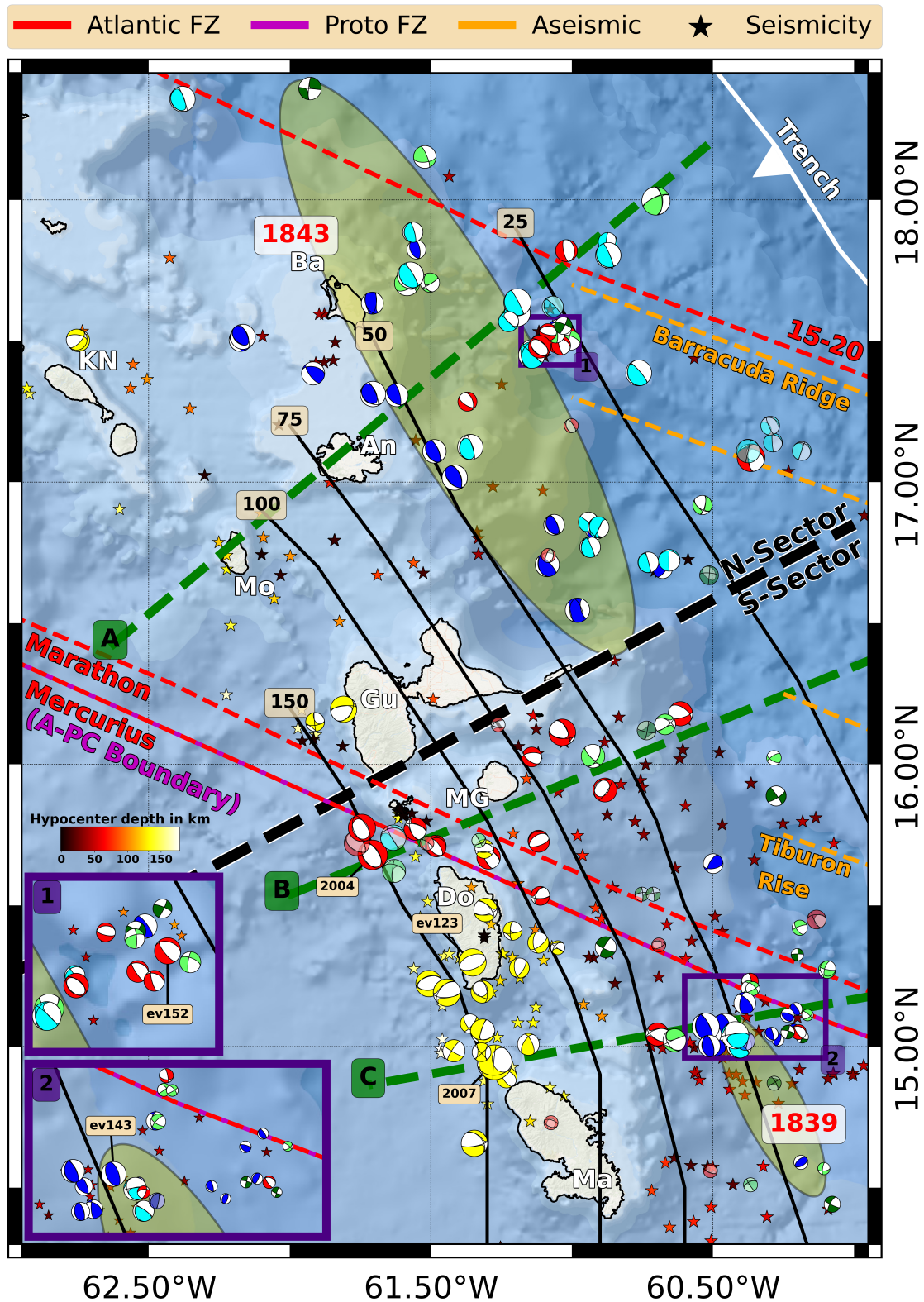
#### Slab seismicity

The deep group covers all seismic events with depths greater than 100 km and these locate within the subducted slab. In the northern sector, only three deep events were observed which may be attributed to comparably small magnitudes and unfavorable station coverage in these parts of the

arc. The most active zone is between Dominica and Martinique. At  $\sim 150$  km depth, this area hosts the majority of strong ( $M_w > 4.0$ ) deep earthquakes along the Lesser Antilles Arc within the instrumented period. MT solutions show highly complex faulting structures consisting mostly of normal faults but also a few strike-slip faults and one thrust fault. The normal faults display different fault orientations but are predominately aligned perpendicular to the trench. The largest earthquake within this group is the 2007  $M_w 7.4$  Martinique earthquake, the to-date strongest instrumentally recorded seismic event in the Lesser Antilles. The large  $\sim 95\%$  CLVD part of this event hints at a much more complex source mechanism than pure normal faulting.

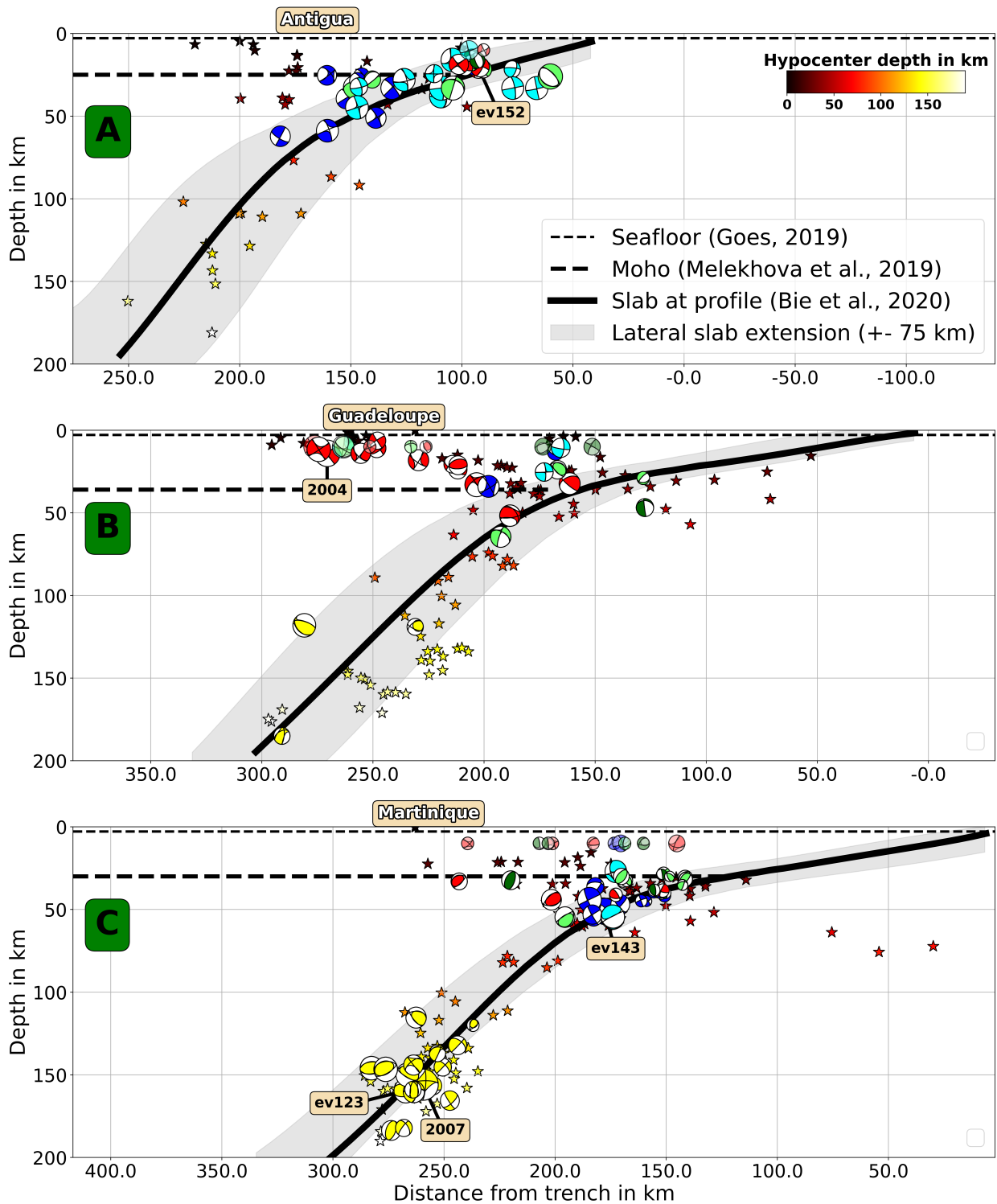


**Figure 5.9:** Focal mechanism classification (FMC) diagram. Displayed are all available focal solutions in the target area. The mechanisms are split into 6 groups manually, based on their locations in the FMC diagram: normal faults (NF; red), thrust faults (TF; blue) dip-slips (cyan), strike-slips (SS; dark green) transition events to strike-slips (NF/TF to SS; light green) and a special group containing all events below 70 km (yellow). Events without certain depth information (e.g., Gonzalez et al., 2017) are displayed in faded colors. The diagram was created using a modified python routine based on Álvarez-Gómez (2019).



**Figure 5.10:** Distribution of all existing focal mechanisms from USGS, GCMT, (Gonzalez et al., 2017) and this study corresponding to the color-coding displayed in the FMC-diagram (Figure 5.9). The map covers the islands of Antigua (An), Barbuda (Ba), Saint Kitts and Nevis (KN), Monserrat (Mo), Guadeloupe (GU), Marie-Gelante (MG), Dominica (Do) and Martinique (Ma). Depth profiles (green), subducted fracture zones (red: Atlantic; magenta: Proto-Caribbean), oceanic ridges (orange) and trench (white) are introduced in Figure 5.1. Displayed ellipsoidal patches represent the locations of the 1839 and 1843 events (Gonzalez et al., 2017). Black lines represent the depth profiles of the slab model and depth colored stars the re-located seismic events recorded during the VoiLA deployment (Bie et al., 2020).





**Figure 5.11:** Cross-section plots along depth profile A, B, and C. The featured seismicity and local slab model is derived by Bie et al. (2020). Gray shaded area surrounding the slab curve at the profiles indicates the lateral extension to north and south ( $\pm 75$  km). Thick dotted lines represent the average Moho depth at the profile intersection (Melekova et al., 2019) with the above thin dotted line being the average water depth of 2.8 km at which the OBS sensors are located (Goes et al., 2019). Color-coding of the displayed beachballs corresponds to the FMC-diagram (Figure 5.9). Faded beachballs do not have depth information and are set to a default depth of 10 km.

### 5.6.3 Stress inversion

The state of stress in the Lesser Antilles is governed to first order by the subduction of the Atlantic oceanic lithosphere beneath the Caribbean Plate. In most cases, especially for small and intermediate-sized events, rupture occurs on pre-existing weak faults that do not necessarily coincide with the current main stress axis (Plenefisch et al., 1997). The origin of small-scale stress perturbations includes anisotropy, fluid pressure variation, or mineral heterogeneity (Plenefisch, 1996). Large events in the subducted lithosphere are likely related to the reactivation of pre-existing faults that formed in past stress conditions (e.g., Delescluse et al., 2008; Garth et al., 2014). To gain insights into the local stress conditions, we perform stress inversions for the interface, crustal, and deep event groups based on our combined catalog. We use the STRESSINVERSE package (Vavryčuk, 2014) which is based on the approach by Michael (1984) but in an iterative joint inversion, reducing the ambiguity problem due to the identification of active and auxiliary planes. STRESSINVERSE takes as input the source geometry (strike/dip/rake) of a group of events and returns the principal stress directions with  $\sigma_1 > \sigma_2 > \sigma_3$  and the scalar quantity  $R$  ( $0 \leq R \leq 1$ ) describing the magnitude of  $\sigma_2$  relative to the others (Gephart et al., 1984):

$$R = \frac{\sigma_1 - \sigma_2}{\sigma_1 - \sigma_3}. \quad (5.16)$$

We assume for each inversion run a mean deviation of  $10^\circ$  from the given fault angles in a realization of 250 normally distributed variations.

Initial stress inversions were performed for the plate interface events and upper plate events separately. The former group includes 50 thrust MTs with the inversion showing a compressional stress regime with  $R = 0.52$ . The direction of  $\sigma_1$  is trending  $61^\circ$  and plunging  $25^\circ$  (Table 5.2) in good agreement with the local slab model (Bie et al., 2020) which depicts an average dip of  $30^\circ$  and a mean azimuth of about  $60^\circ$ . In the upper plate, inversion of 73 MT solutions depicts a trench parallel extension stress regime with  $\sigma_3$  azimuth at  $183^\circ$  and plunge  $3^\circ$  and  $R = 0.87$ . The southern sector contains a large number of trench perpendicular normal faults, suggesting a stress rotation compared to the northern sector. We further examine the local stresses of the northern and southern sectors separately.

**Table 5.2:** *Stress inversion.*

Layer	Region	N	$\sigma_1$ azimuth in $^\circ$ / plunge in $^\circ$	$\sigma_2$ azimuth in $^\circ$ / plunge in $^\circ$	$\sigma_3$ azimuth in $^\circ$ / plunge in $^\circ$	$R$
Interface	Arc	53	61/25	153/3	248/65	0.52
Interface	North	38	63/29	157/8	262/60	0.55
Interface	South	15	88/84	359/9	150/80	0.32
Upper plate	Arc	73	75/80	274/10	183/3	0.87
Upper plate	North	22	119/55	340/28	239/19	0.12
Upper plate	South	51	234/88	70/2	340/1	0.80
Slab	South	18	54/71	273/15	180/11	0.69

Interface activity in the northern sector shows widespread slab parallel thrusting and shallow dipping thrust events while we observe only a small active cluster in the south showing slightly different striking directions (Figure 5.10). The stress inversion for 38 events results in azimuth and plunge of  $\sigma_1$  consistent with the average slab geometry striking  $\sim 63^\circ$  and dipping  $\sim 29^\circ$  in these parts (Profile A Figure 5.11). Stress inversion for the 15 events further south, however, shows a nearly slab-dip parallel compressional regime with maximum stress  $\sigma_1$  at  $88^\circ$  and a near-horizontal thrust angle  $84^\circ$ . A reduced  $R$  (0.32) indicates a more complex stress field compared to the northern part.

Upper plate seismicity is mainly normal faulting with a subset of strike-slip and NF/TF to SS

transitional events. The stress inversion of 22 events in the northern crust reveals a transitional regime from strike-slip to normal faulting (Lund et al., 2007) with  $\sigma_1$  direction of  $119^\circ$ . The small scale quantity  $R = 0.12$  shows a large influence of  $\sigma_2$  and suggests a strike-slip component. Further south we observe a rotated, arc-perpendicular stress regime with  $\sigma_3$  trending  $340^\circ$  and  $\sigma_1$  plunging nearly vertically in a largely diffuse striking direction. The scale quantity indicates normal faulting dominates with  $R = 0.80$ , compared to the north.

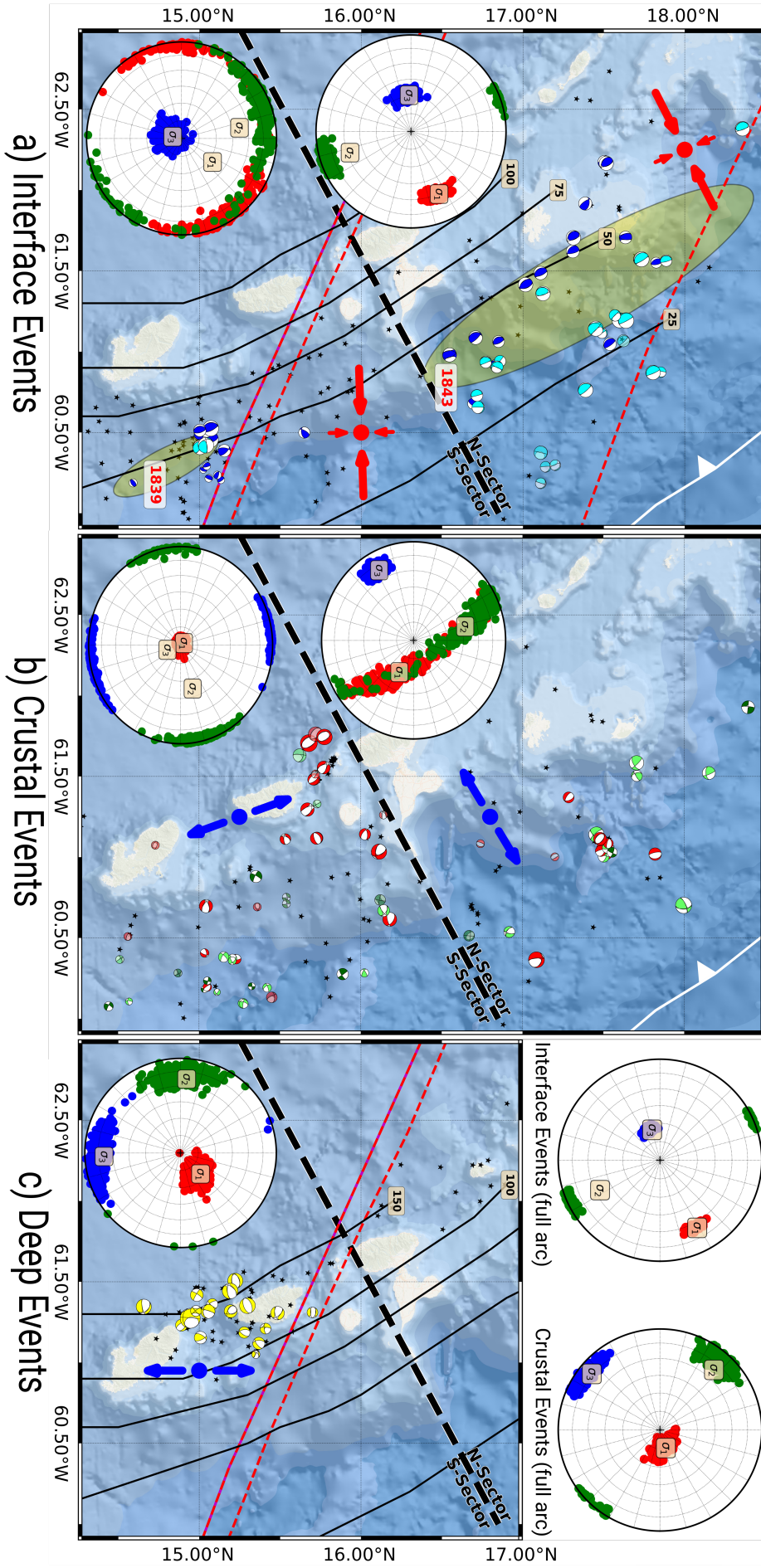
We perform a single stress inversion for the deep earthquake group in the southern sector. In this inversion, we include 20 deep events, spatially clustered between Dominica and Martinique at  $\sim 150$  km depth. Contrasting to the stress condition on the interface at shallow depth, the deep events depict a slab-dip perpendicular extensional stress regime with  $\sigma_1$  orientating parallel ( $54^\circ$ ) to the slab and plunging steeply at  $71^\circ$ . The scale quantity  $R$  equals 0.69.

## 5.7 Tectonic implications

**Interface activity** At depths shallower than 50 km, we find a dominance of thrust activity and further towards the trench, shallow dipping thrust events become more frequent. This agrees with previous studies in the region (e.g., Gonzalez et al., 2017) and implies seismic slip along the megathrust between the subducted slab and overriding plate. In the northern sector (Figure 5.12, a), the stereo plot of the stress regime depicts widespread activity with the pattern of a classical subduction zone. Most of the events are located within the estimated rupture area of the 1843 M8.5 earthquake (Feuillet et al., 2011b). The occurrence of these thrust events corroborates that the 1843 event was a megathrust earthquake that ruptured the seismogenic part of the plate interface, instead of being within the subducted lithosphere (van Rijsingen et al., 2021). The southern sector lacks such compressional events except for in a small but highly active cluster (Figure 5.10; Zoom Box 2) within the area of the 1839 M7.5 event to the east of Martinique which is also assumed to be a megathrust event (Feuillet et al., 2011b). The stereo plot for the southern sector indicates a much more diffuse pattern featuring a range of fault strikes, but still with an overall trench-perpendicular compressional stress that appears to rotate along with the curve of the island arc (Figure 5.12, a).

**Upper plate activity** Upper plate activity comprises a majority of normal faulting events but also includes a subset of SS and NF/TF to SS transitional mechanisms. Transitional events occur primarily in the northern sector, where our results (Figure 5.12, b) indicate a rotational stress regime (Lund et al., 2007). Such rotation may be related to the transition from a sinistral strike-slip system at the northern end of the LA subduction zone, towards an approximately arc perpendicular extensional faulting regime (Julien et al., 1989; Laurencin et al., 2017). In the midst of this area, we recognise a small cluster of events with a variety of mechanisms (Figure 5.10; Zoom Box 1) centered at a depth of around 20 km, still within the Caribbean crust but near to the interface zone. The cluster is located above the projected position of the Barracuda Ridge after subduction, inferring a possible link between them. Seaward of the trench, the Barracuda Ridge rises 1800 m above the surrounding seafloor and is topped by a very thin sedimentary drape (Patriat et al., 2011). Previous work did suggest this feature would have an effect on upper plate deformation (McCann et al., 1984; Laigle et al., 2013b), as seen in our study. The stress regime of the upper plate evolves from the transitional regime of the northern sector towards a dominance of arc-parallel extension in the south (Figure 5.12, b). However, even though the overall stress tensor in the southern sector indicates arc-parallel extension, events in the vicinity of the 2004 M6.3 Les Saintes earthquake reflect arc-perpendicular extension consistent with the arc-parallel en-echelon faults identified by Feuillet et al. (2011a). While interpretations for events to the east of Martinique are limited by the small event set and mostly missing depth information, we recognise on cross-section profile B (Figure 5.11; B) that the depths of upper plate normal faulting increase towards the east. The events with shallow depths west of and aligned with the arc correspond to arc parallel normal faulting of the Les Saintes earthquake swarm. Their shallow depths and overall smaller contribution to the total moment released in normal faulting in the southern segment, may be





**Figure 5.12:** Results of stress inversion of a) interface, b) crustal and c) deep events in the northern and southern sector. Top-right shows the inversion results of the interface and crust without regional sectoring.

due to the relatively high crustal temperatures at and near the arc. Eastwards, in the forearc, azimuthal directions of the normal faults become mostly arc perpendicular as their depths increase towards the interface zone. This change in style is consistent with change in orientation of the faulting structures identified by active seismic imaging (Feuillet et al., 2011a), and indicates that the forearc is characterised by stresses associated with along-arc bending and oblique subduction (Feuillet et al., 2002) while the arc and backarc are dominated by trench-perpendicular extension as expected due to pull of the underlying slab, possibly exploiting structures formed during previous phases of backarc opening (Allen et al., 2019).

**Slab activity** Seismic activity within the intermediate-depth range (70-300 km) concentrates between Dominica and Martinique. Here the comparably large size of our MT database ( $N=18$ ) and the high quality event locations (Bie et al., 2020) allow us to perform an examination of the activity that we attribute to intraslab seismicity. This cluster encloses several large magnitude events, including the 2007  $M_w 7.4$  Martinique event and the  $M_w 5.8$  ev123 event of the VoiLA catalog (Table 5.1). Both moment tensor solutions have a relatively large CLVD component suggesting a complex rupture history. In general, this cluster shows predominantly normal faulting activity with fault strikes in a trench perpendicular direction in the north (under Dominica) and trench parallel towards the south (between Dominica and Martinique). We also find a more variable set of mechanisms including some strike-slip and a single thrust mechanism in the vicinity of the 2007 Martinique event. The dominant stress condition is downdip compression (as  $\sigma_1$  axes are most strongly clustered) and slab parallel extension (Figure 5.12, c). Most subduction zones exhibit downdip extension at intermediate depths, but a few without deep seismicity (below 300 km depth) display downdip compression within the 100-200km depth range, including New Britain, Ryukyu and the central Aleutians, as well as a few other segments of trenches with deep seismicity (central Tonga, northern Kuriles, e.g., Chen et al., 2004; Alpert et al., 2010; Bailey et al., 2012). Some further exceptions of this can be found in more complex settings like South Sandwich that exhibits a local stress reversal in depth below 150 km (Giner-Robles et al., 2009), in Calabria with downdip compression between 200-300 km depth (Bailey et al., 2012) or the Hellenic arc with a slab perpendicular compressional stress regime at its center (Rontogianni et al., 2010).

Downdip compression at intermediate depths may be the result of a relative high resistance to sinking into the lower mantle (Goes et al., 2017), which would be consistent with the interpretation from Braszus et al. (2021), that subducted slab material from 70 Myr ago to present has accumulated in the upper mantle below the Antilles. In most of the slabs with downdip compression at intermediate depths however, the extension is oriented slab-perpendicular, while in the Antilles, the extension is dominantly slab-parallel (Figure 5.12, c). Geometric effects of a curved slab are not sufficient to explain the rotational behavior of the Antillean intermediate-depth normal faults. Along-strike bending would introduce along-strike compression on the inside of the bend as well as along-strike extension on the outside of the bend. One might expect that the compression closer to the colder slab top might be more prominent in seismicity, yet we see only extension. Trench-parallel extension was found in the northern Hikurangi subduction zone, New Zealand (Okuwaki et al., 2021); however, this stress pattern was attributed to a subducting oceanic plateau or seamounts in a centroid depth of only around 70 km, which is not a likely mechanism for the LA. Wadati-Benioff seismic activity below central LA has long been hypothesized to be influenced by a gap in the slab near  $15^\circ\text{N}$  (Bie et al., 2020). Seismic anisotropy from teleseismic SKS waves (Schlaphorst et al., 2017) was interpreted as due to mantle material flowing through a gap within the subducted lithosphere at around 170-200 km depth. A gap at this location was also supported by teleseismic tomography models (Benthem et al., 2013; Harris et al., 2018) of the central parts of the arc ( $\sim 15^\circ\text{N}$ ). A recent teleseismic tomography study, however, by (Braszus et al., 2021) showed that any gap is confined to the deep upper mantle and the slab looks continuous at the depths of the seismicity. Instead Braszus et al. (2021) observes a wavespeed anomaly that can be attributed to a signature of excess slab hydration within the subducted Proto-Caribbean plate, possibly near the subducted spreading center. The seismicity does reveal a change in slab dip (Figure 5.11), with the northern

part of the slab being steeper and deeper than the southern part, but the vertical offset is not sufficient to generate a gap in the slab (Bie et al., 2020). Furthermore, Bie et al. (2020) find no sharp changes in the slab dip angle that would be expected if there was a tear, but they do note a thickening of the Wadati–Benioff zone around  $\sim 150$  km. The lateral changes in deformation style revealed by our MT dataset do indicate that a structure within the subducted Proto-Caribbean plate may be present. The subducted domain boundary between plate material formed at the Proto-Caribbean (to the south) and Central Atlantic ridge (to the north) projects just north of the cluster (Figure 5.10; magenta-red line), and part of the extinct Proto-Caribbean spreading ridge is expected to lie below the central arc (Figure 5.13). A lateral variation in slab buoyancy (more buoyant in the south than north) might explain the along-strike variation in slab dip and introduce along-strike extensional stresses. However, the age, and hence negative buoyancy of the subducted plate increases southwards ( $\sim 30$  Myr older in the south, Braszus et al., 2021), although all of the plate is older than 70 Myr and hence age-related buoyancy gradients may be modest. On the other hand, a partial detachment of the southern end of the slab, along a lateral tear recognised at around 200 km depth below Grenada (Braszus et al., 2021), may be the cause of weaker slab pull in the south than in the north. Pre-existing Proto-Caribbean structures in the downgoing plate may govern both the localisation of Wadati–Benioff seismicity in response to the stress regime due to along-strike slab pull variations, and the orientation of the seismically activated structures (Figure 5.13).

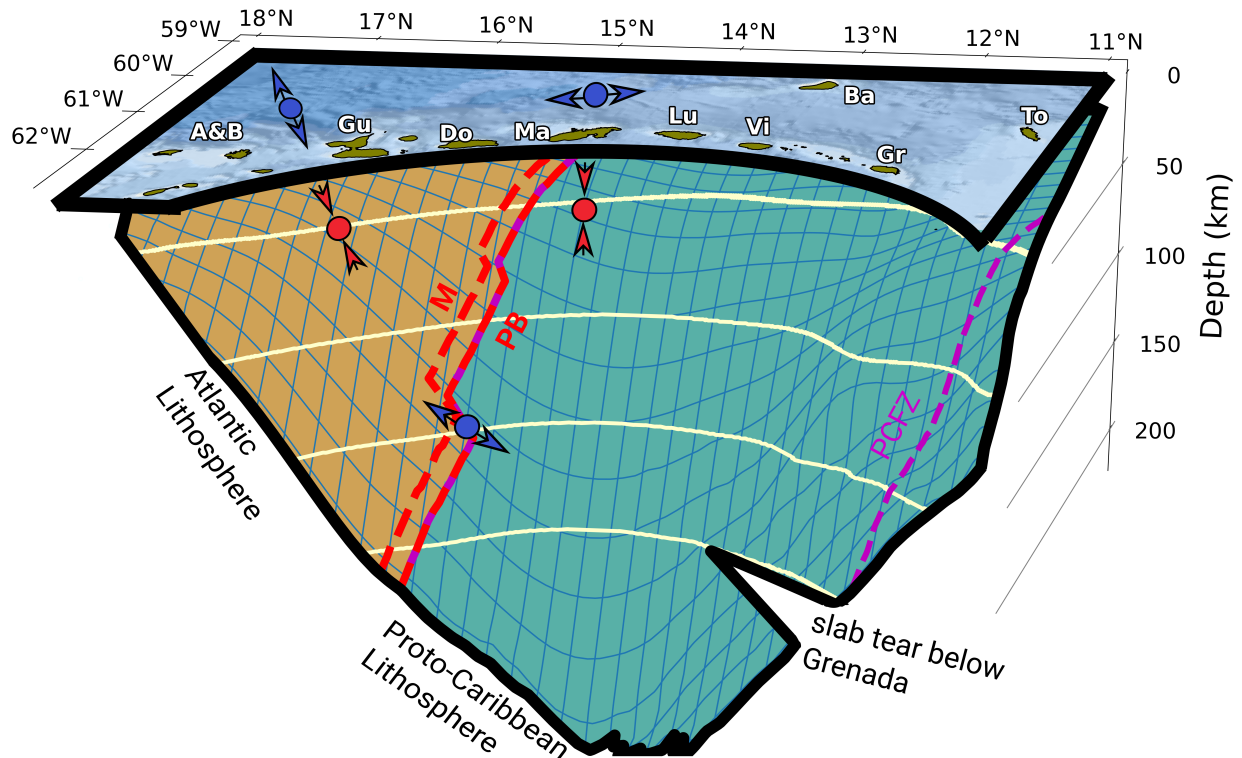
## 5.8 Conclusions

We have developed a novel Am $\Phi$ B-RMT approach which employs the uniXtree-sampling algorithm to mitigate the effects on RMT solutions from OBS data of uncertainties from horizontal station alignments and high levels of ocean microseisms. Our synthetic experiments show a reduction of the discrepancies between input and recovered CLVD percentage to be between 48% to 58% compared to a classical L2 approach, depending on the number of stations used and the noise levels. We also observe a reduction in error in the recovered Kagan angle at large noise amplitudes, with up to 40% improvement compared to a classical L2 approach. Inversions taking into account station alignment uncertainties at low noise are more robust if a model covariance matrix is included. Using only vertical traces it is possible and robust to solve in a double-couple inversion setup, as changes in CLVD are shown to mainly compensate for the effects of noise, but do not generally bias the retrieved planar fault geometry.

Application of our new method to the recorded OBS data of the VoiLA experiment in the Lesser Antilles subduction zone yields robust solutions as shown by the comparison with a teleseismically-derived reference event set. We compiled 151 MT solutions, including 39 new ones from this study for the north-central Lesser Antilles arc, and found 25% normal faulting (NF), 25% thrust faulting (TF), 10% strike-slip faulting (SS) with the remainder being a mixture of mainly NF to SS transitional mechanisms. TF is dominant along the slab-upper-plate interface, with a notable gap in seismic activity between  $\sim 15^\circ\text{N}$  and  $\sim 16.5^\circ\text{N}$ . The general stress regime follows the subduction geometry of the slab. We find that the areas of interface activity coincide with the inferred rupture areas of the 1839 M7.5 and 1843 M8.5 megathrust events. Upper plate activity shows a strong variability along the arc. The north is characterized by a SS to NF transitional regime while the stress condition further south is dominantly an arc parallel extensional regime probably due to along-arc stretching of the forearc to accommodate the tight arc curvature.

Stress inversion for an intermediate-depth central cluster offshore Martinique reflects down-dip compression and slab-parallel extension. Down-dip compression may reflect the dynamics of this relatively small subduction zone (van Benthem et al., 2010), which has led to the piling of slab material within the upper mantle below the LA (Braszus et al., 2021). The along-strike extensional stress regime is unusual and we propose it to be due to lateral buoyancy variations, where pull at the southern end of the LA slab may be reduced by partial slab detachment along a lateral slab tear

below Grenada (Braszus et al., 2021), causing slab deformation that localizes along pre-existing structures around the extinct Proto-Caribbean ridge subducted below Martinique (Figure 5.13).



**Figure 5.13:** 3D sketch of the Lesser Antilles subduction zone. Marked islands from north to south are Antigua and Barbuda (A&B), Guadeloupe (GU), Dominica (Do), Martinique (Ma), St. Lucia (Lu), St. Vincent (Vi), Barbados (Ba), Grenada (Gr) and Tobago (To). Outline of the slab is based on the local slab model by Bie et al. (2020) with spacial partition into Atlantic (brown) and Proto-Caribbean (green) lithosphere (Braszus et al., 2021). Relevant features are displayed in color coding following Figure 5.1 with M being the Marathon fracture zone, PB the plate boundary between the two lithospheres which also coincides with the Mercurius fracture zone and the unnamed Proto-Caribbean fracture zone PCFZ. Displayed arrows represent the dominant stress regime (red: compression, blue: extension), projected at the centroid location of the input data. The hypothesised lateral slab tear below Grenada is depicted at the depth outline of 200 km.



## Chapter 6

# Complex Martinique intermediate-depth quake reactivates early Atlantic break-up structures

This chapter features my work on the 2007  $M_w 7.4$  Martinique earthquake. The content of this chapter got submitted to the journal *Geophysical Research Letters* with me as first author.

### 6.1 Abstract

Earthquakes that rupture several faults occur frequently within the shallow lithosphere but have not been reported for intermediate-depth events. On November 29, 2007, the  $M_w 7.4$  Martinique earthquake struck the Lesser Antilles Island Arc near the deep end of the Wadati-Benioff-Zone. The sparse regional seismic network of 2007 previously hampered a detailed examination of the rupture process. Here, we combine seismic data from different studies with regional moment tensor inversion results and 3D full-waveform modeling. We show that the earthquake is a doublet consisting of dip-slip and strike-slip motion along two oblique structures, both activated under extensional stress along the strike of the slab. Comparison with tectonic reconstructions suggests that the earthquake ruptured along a re-activated ridge-transform segment of the subducted Proto-Caribbean spreading ridge. The unprecedented resolution sheds light on the complex source processes at the global intermediate-depth range and highlights the influence of pre-existing structures on localising slab deformation.

### 6.2 Introduction

Seismicity in the intermediate-depth range (70-300 km, Gutenberg et al., 1954) is prevalent in all large subduction zones (Astiz et al., 1988) and can be associated with intra-slab deformation of subducted lithosphere (Wadati, 1928). Yet the underlying physical mechanism is still debated (Prieto et al., 2012). Conventional mechanisms for shallow crustal earthquakes do not hold for the Wadati-Benioff seismicity (Green et al., 1995). The leading hypothesis is that intermediate-depth seismicity is caused/triggered by dehydration of hydrous minerals, leading either to dehydration embrittlement (Kirby et al., 1990), or to run-away plastic instabilities (Hobbs et al., 1988). Either way, these processes are governed by the breakdown of hydrous minerals in the slab (Green et al., 1995) that are likely more concentrated where fluids percolated into pre-existing faults created in the oceanic plate before its subduction (Hacker et al., 2003) or during bending at the trench (Ranero et al., 2005). Hence it has been proposed that intermediate-depth events re-activate such subducted fluid-rich structures (Green et al., 1995; Garth et al., 2014; Warren et al., 2015). The driving force for intermediate-depth events are stresses due to gravitational pull, distortions of

the slab in response to variations in slab buoyancy, and the increasing resistance to sinking and decreasing space with depth (Isacks et al., 1971; Astiz et al., 1988; Warren et al., 2015).

Complex deformation may be reflected in earthquake rupture complexity, e.g., leading to source doublets, seismic events that display different deformation styles on two temporally and spatially separated fault planes. Identifying source complexity for intermediate or deep earthquakes from aftershocks is challenging as the average aftershock-to-mainshock moment ratio is significantly lower than for similarly-sized shallow events (Persh et al., 2004). Indications of complexity can however be found in the moment tensor (MT) solution. A significant Compensated Linear-Vector Dipole (CLVD, Knopoff et al., 1970) component to the MT can be understood as an indicator for deviations from a single point shear source. (Frohlich, 1995).

The global distribution of intermediate-depth events (since 2000) can be evaluated for major subduction zones. We compile a catalog consisting of 4351 events from the USGS database, which is complete for magnitudes  $M_w \geq 5.2$ . The events follow a Gutenberg-Richter distribution with  $b = 0.9$ . We observe a decreasing trend of the absolute value of the CLVD contribution to the total moment with increasing magnitude (Figure 6.1). Seismic events between  $5.2 < M_w < 7.0$  with a  $|\text{CLVD}|$  exceeding 80% occur mainly at depths less than 125 km and exhibit a higher number of negative CLVD values (Figure 6.1, green cluster). Stronger events ( $M_w > 7.0$ ) with a  $|\text{CLVD}|$  larger than 40% show an increase of  $|\text{CLVD}|$  with the depth, while inverse in their magnitude (Figure 6.1, yellow cluster). Large earthquakes ( $M_w > 7.0$ ) with a  $|\text{CLVD}|$  smaller than 40% are most concentrated between 100 - 150 km and reduce in number with increasing depth (Figure 6.1, red cluster). The 2007  $M_w$ 7.4 Martinique earthquake ( $\sim 150$  km depth) stands out as an outlier in this global compilation, with an CLVD exceeding 90% (Figure 6.1, magenta star)

### 6.3 The 2007 $M_w$ 7.4 Martinique earthquake

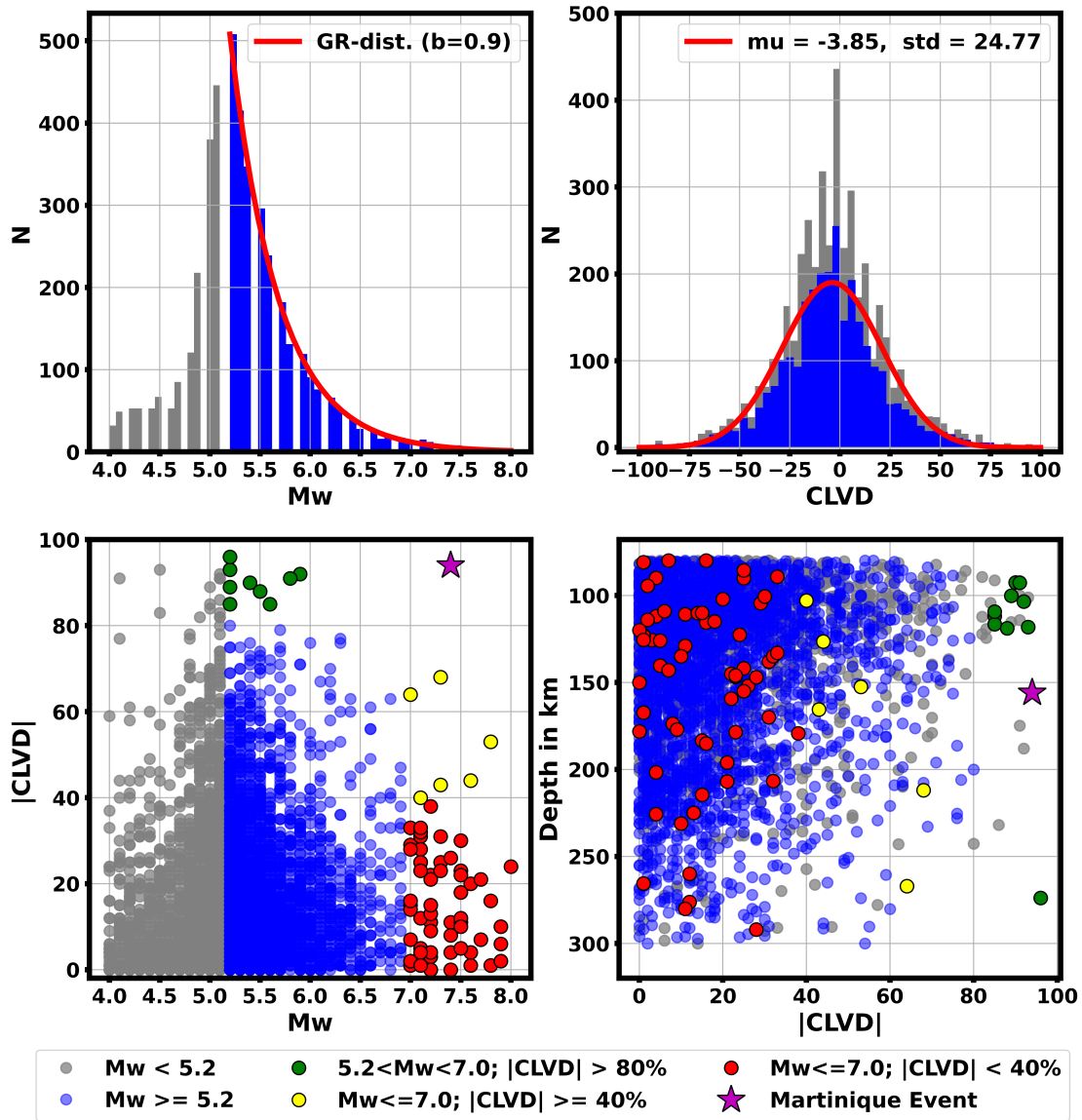
The Martinique earthquake is the largest instrumentally recorded seismic event in the Lesser Antilles Arc (LAA, e.g., Hayes et al., 2017; Schlaphorst et al., 2016). Pre-existing deviatoric teleseismic moment tensor solutions (Table C.2, ev014) of different agencies have a strong CLVD component ( $> 89\%$ ). The preferred USGS1 W-Phase solution reflects a dip-slip mechanism as underlying double-couple component, while the alternate USGS2 solution indicates a near strike-slip mechanism that strongly resembles the GCMT solution. Recent imaging of the subducted slab indicates a complex stress regime driven by substantial slab accumulation within the mantle transition zone and lateral variations in slab pull, which at the southern end of the LAA slab is reduced by partial detachment along a lateral slab tear below Grenada. The slab deformation in response to the variations in slab pull appears to concentrate close to a segment of the extinct Proto-Caribbean ridge subducted below Martinique (Lindner et al., 2023).

### 6.4 Data

We compiled a range of data to analyze the rupture process of this event in more detail. The automated IRIS back-projection solution (IRIS DMC, 2011) contains two energy peaks in the cumulative stack at 0.25 – 1 Hz between Dominica and Martinique. Its corresponding source-time function (STF) indicates two clearly separate sub-events with a peak-to-peak inter-event time of  $\sim 6$  seconds and a combined half-duration of  $\sim 12$  seconds (Figure 6.2). We assembled a database of MTs for 22 events (Table C.2), concentrated near 150 km depth around the Martinique event (Dziewonski et al., 1981; Ekström et al., 2012; Quinteros et al., 2021; U.S. Geological Survey, 2022; Gonzalez et al., 2017; Lindner et al., 2023). Mapped into the regional setting, we observe a north-to-south change in faulting mechanisms (Figure 6.2). The northernmost events are normal events (e.g., ev020) with fault planes approximately parallel to the inferred trace of the subducted Marathon and Mercurius fracture zones, which also form the domain boundary between lithosphere formed at the Atlantic and Proto-Caribbean spreading centres (Braszus et al., 2021; Lindner



et al., 2023). To the south, the fault planes of the normal faults are rotated (e.g., ev006), to near perpendicular to these fracture zones. And at around 15°N, near the latitude of the Martinique event (black beachball, ev014), the faulting style is predominantly strike-slip, (e.g., ev005), including a dip-slip (ev011) and oblique thrust event (ev007). Finally, the southernmost events are again normal faults similar to those in the northernmost part, i.e., with planes parallel to the fracture zone fabric. The strong changes in faulting styles and the twin energy peak of the back-projection solution strongly suggests a complex rupture of the Martinique event, involving at least two different faulting styles (Lindner et al., 2019).



**Figure 6.1:** Global statistics of intermediate-depth (70-300 km) earthquakes since 2000. The Gutenberg-Richter distribution of the complete catalog ( $M_w \geq 5.2$ ) follows a  $b$ -value of 0.9 indicating an increased activity of the larger events. Distribution of the CLVD part follows a normal distribution with  $\sigma = 24.77$  shifted by 3.85% into the negative range. Taking the absolute  $|CLVD|$  part in relation to the Magnitude, we select three groups of events (green, yellow, and red) and display them in depth v.s.  $|CLVD|$ . The 2007  $M_w 7.4$  Martinique event (magenta star) stands out as a significant outlier with a  $|CLVD|$  greater than 90%.



### 6.4.1 Source location update

Using the VoiLA earthquake database (Bie et al., 2020) we update the hypocenter locations for all ISC (Figure 6.5, heatmap) and aftershock events within the target area (Figure C.2). The initial locations were restricted by the azimuthal station coverage to north and south of the source locations leading to potentially large uncertainties in the longitude. We identified 44 common events in the VoiLA and ISC catalogs using the reported source times  $T_0$ , within an accuracy of 3 seconds. The average source time update ( $T_{0,\text{Bie}} - T_{0,\text{ISC}}$ ) is  $1.35 \pm 0.75$  seconds and average location shift is  $[d_{\text{lat}}, d_{\text{lon}}, d_{\text{depth}}] = [-0.1125^\circ, 0.1303^\circ, 23.71 \text{ km}]$ . Locations of events with MT solutions are treated as well-located under the assumption that these are derived from local studies with good location constraints or from good regional or global station coverage due to the large magnitudes.

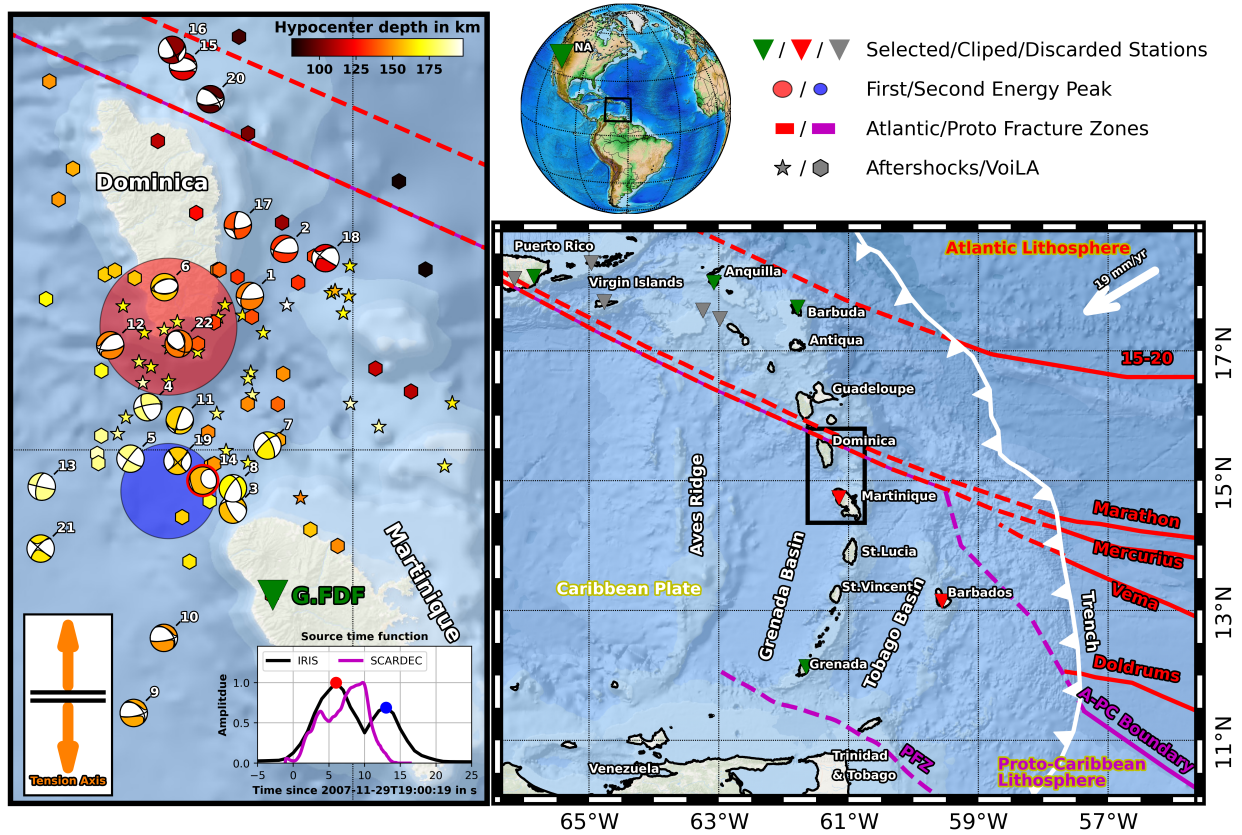
### 6.4.2 Aftershocks

One foreshock and 32 aftershocks are associated with the Martinique earthquake, spanning a period of around one and a half months (Table C.3). One day prior to the main shock, an  $M_w$ 3.7 event occurred roughly 15 km away from it (Figure 6.3, blue star). Then, within 24 hours, 13 events were observed in its vicinity, increasing up to 19 during the first week. The aftershock seismicity then faded, with a total number of 24 accumulating within a month, of which only two events exceeded a magnitude of  $M_w$ 5.0. Activity resurged after 37 days, with another sequence of 8 events (IRIS DMC, 2011). This is unusual for intermediate-depth seismic events: about 48% of all intermediate-depth earthquakes with  $M_w > 6.5$  have no and 37% only 1 to 5 aftershocks (Astiz et al., 1988).

We performed a cross-correlation analysis to group the aftershock events. Due to the sparse regional station coverage in 2007 and the limited availability of data in the FDSN service, we are restricted to the vertical component of station FDF in the French G network, which is installed in the northern part of Martinique.

Other stations running during that time period (e.g., CU network or NA network) are too far away and do not show clear signals for most of the smaller events. Grouping is done using P- and S-wave information in a rather narrow bandpass between 1 and 2 Hz to counter path effects and the effect of differences in magnitude. P and S onset are picked manually, using 5 seconds waveforms for P and 10 seconds for S. Cross-correlation coefficient matrices of P and S phases are calculated separately and rearranged per hand to identify groups that are common in both matrices or significant in only one of them (Figure 6.3). We selected several bridging events to join smaller subgroups together and could define two distinct groups. The bigger group G1, shows large similarities in the P phase, exceeding 0.8, and a common pattern for S, using bridging events, at 0.65. In contrast, group G2 is more distinct in S and shows nearly no correlation in P.

These groups are also spatially distinct. Group G1 events (red stars) are focused to the north of  $15^\circ\text{N}$ , at an average depth of 145 km, while events of group G2 (blue stars) are located south of  $15^\circ\text{N}$  and vary in depth. The remaining events (black stars), which include the mainshock (magenta star) and the foreshock (green star), occur primarily around  $15^\circ\text{N}$ , spatially separating groups G1 and G2. Associated with group G1 is the largest aftershock ev011 (Table C.2) with  $M_w$ 5.2. Its source mechanism has a similar double-couple component as the USGS1 solution of the mainshock and represents the faulting style of all events in its group. The GCMT double-couple component, being similar to the historical strike-slip events south of  $15^\circ\text{N}$ , might reflect the mechanisms of aftershock group G2. This suggests that the double-couple component of the USGS1 solution and the USGS2/GCMT solutions are close to the underlying mechanisms of the doublet.



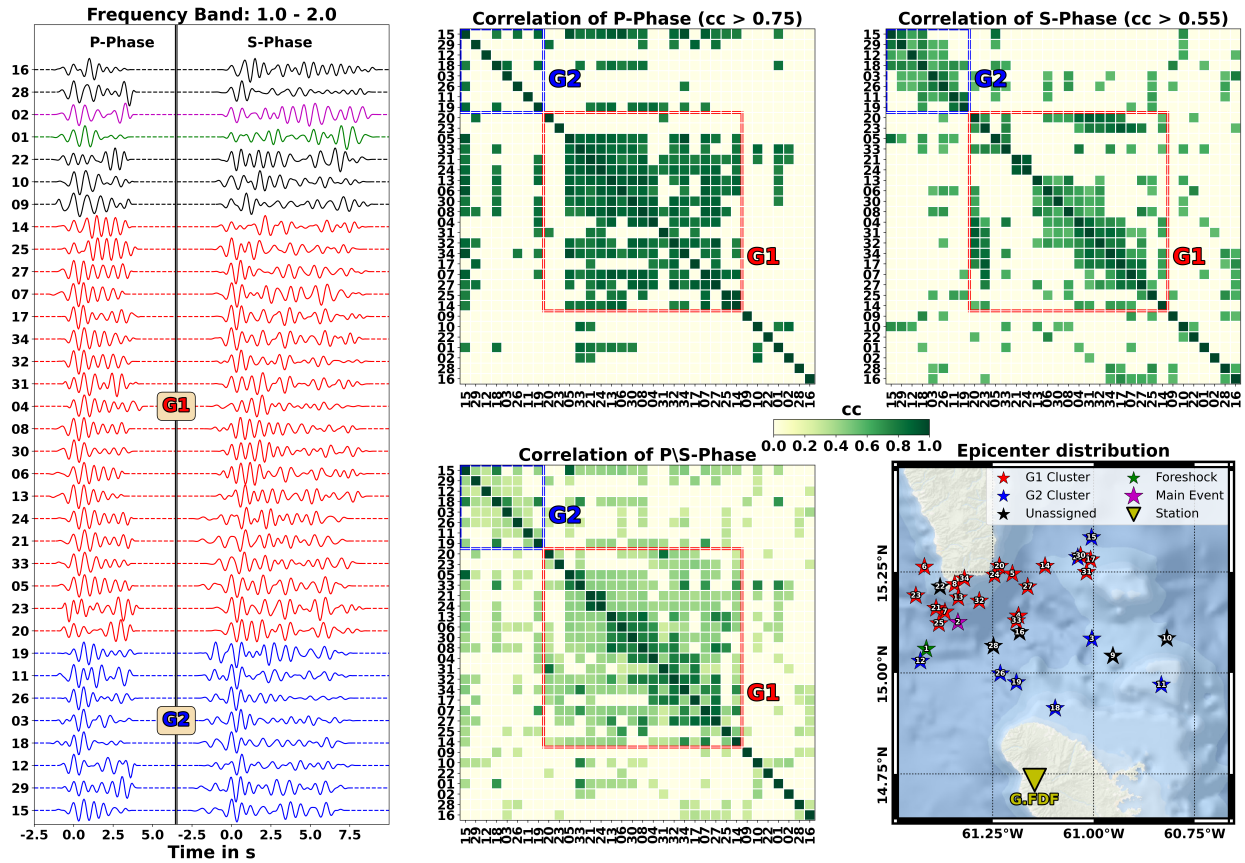
**Figure 6.2:** Bathymetric map of the Lesser Antilles subduction zone. Prominent fracture zones (solid before subduction, dashed projections after subduction) are marked in red on the Atlantic lithosphere, and inferred fracture zones of the Proto-Caribbean lithosphere are marked in magenta. The trench is shown in the white line, with plate motion relative to South America (Demets et al., 2010; Bie et al., 2020) along the white arrow. The domain boundary between the Atlantic and Proto-Caribbean lithosphere coincides with the Mercurius fracture zone at depth (red-magenta line). Triangles show the locations of the regional land network, where we only used stations marked in green. Stations marked by red triangles clipped during the main event while stations with gray triangles would either lead to over-represented azimuthal coverage or recorded complex waveforms that cannot be modeled. The black box, embracing Dominica and Martinique, outlines the target area of this study. The IRIS back-projection (IRIS DMC, 2011) results for the 2007 Martinique mainshock using data of the North-American seismic array (NA) show two distinct peaks in the source time function and on the map (red/blue circle). Well-located seismic activity during the 2016 to 2017 VoiLA deployment (Bie et al., 2020) is depicted as stars and the IRIS recognized (IRIS DMC, 2011) aftershocks are depicted as hexagons, all colored according to source depth. MTs for events around the 2007 Martinique earthquake from different publications are shown in the lower hemisphere projection. The Martinique event is highlighted with a red circle around the beachball. The overall inferred stress regime is depicted with the orange double arrow (Lindner et al., 2023).

## 6.5 Source modelling

To understand the contribution of the two sub-events, we perform regional moment tensor (RMT) modeling for the 2007  $M_w 7.4$  earthquake (Table C.1). Considering the limited network coverage at the time of the main event (Figure 6.2 or Table C.4), we expect discrepancies between the teleseismic solutions and our regional ones.

### 6.5.1 Data selection

For the time of the main event, we have only a few records with an unfavorable azimuthal coverage (Table C.4). Stations on Martinique, including the MQ-Network and the GEOSCOPE station FDF, are clipped and not usable for source inversion. Towards the southeast, the HH-sensor on Barbados also clipped while the strong motion HN-device recorded highly complex waveforms that cannot be explained by our velocity model. This left us with only one observation point south of the epicenter, on Granada. Coverage in the north is slightly better, but concentrates in northwestern direction; only three stations (Barbuda, Antigua, and Puerto Rico) are selected, to provide reasonable azimuthal coverage while avoiding an over-representation of data in the north compared to the south.



**Figure 6.3:** Cross-correlation clustering of the fore- and aftershock seismicity associated to the 2007  $M_w 7.4$  Martinique earthquake. We used the bandpass filtered (1-2 Hz) P and S-phase waveform data of the vertical trace at station G.FDF (Table C.4). Correlation is done for P and S separately and arranged by hand in the correlation matrix using a correlation coefficient (cc) of  $> 0.75$  for P and  $> 0.55$  for S. P and S correlations are then evenly weighted with  $[cc(P) + cc(S)]/2$  and plotted together. The identified groups G1 and G2 display a spatial clustering along the NS-axis. Events not belonging to either group arrange predominantly around  $15^\circ$  N.

### 6.5.2 Full waveform modeling for Green's function based on 3D velocity model

To improve the accuracy of the MTs, which are usually biased due to the inaccuracy of the regional velocity structure, we used the Spectral Element Method Salvus (Afanasiev et al., 2019) to simulate the Greens' Functions, based on a regional 3D velocity model derived from teleseismic tomography (Braszus et al., 2021). We add the imaged isotropic  $V_P$  perturbations to the AK135 background model and assume the same perturbations (in %) to the  $V_S$ . Long-wavelength surface topography from the EGM2008 Geoid (Pavlis et al., 2012) and Earth2014 global topography model (Hirt et al., 2015) with Earth ellipticity according to WGS84 are implemented by deforming the mesh grid vertically. Surface and Moho topography retrieved from crust1.0 (Laske et al., 2013) have been filtered with maximum angular order  $l_{max} = 512$ , equivalent to a spatial resolution of 40 km. The spectral-element mesh is for an up to 3 seconds dominant period (12 km element size in the crust and 15-20 km in the upper mantle), to guarantee the accuracy of the numerical simulations. We adopted a Heaviside source time function for the simulations.

### 6.5.3 Inversion strategy

Moment tensor modeling is done using AmΦB - Amphibious Bayesian (Lindner et al., 2023) -, which is based on full waveform inversion (Krizova et al., 2013) in a Bayesian framework (Duputel et al., 2012). The inverse problem is solved in a uniform tree-sampling search algorithm (Lomax et al., 2001), using the uniform Tape parameterization (Tape et al., 2015) for a deviatoric source mechanism – uniXtree. We modeled six different source settings (Figure 6.4 and Table C.1, A-F), for a single (A-C) and doublet fault (D-F) assumption, using forward simulations (A, B, D) to check existing solutions, and inversions (C, E, F) to get the best solutions with our database.

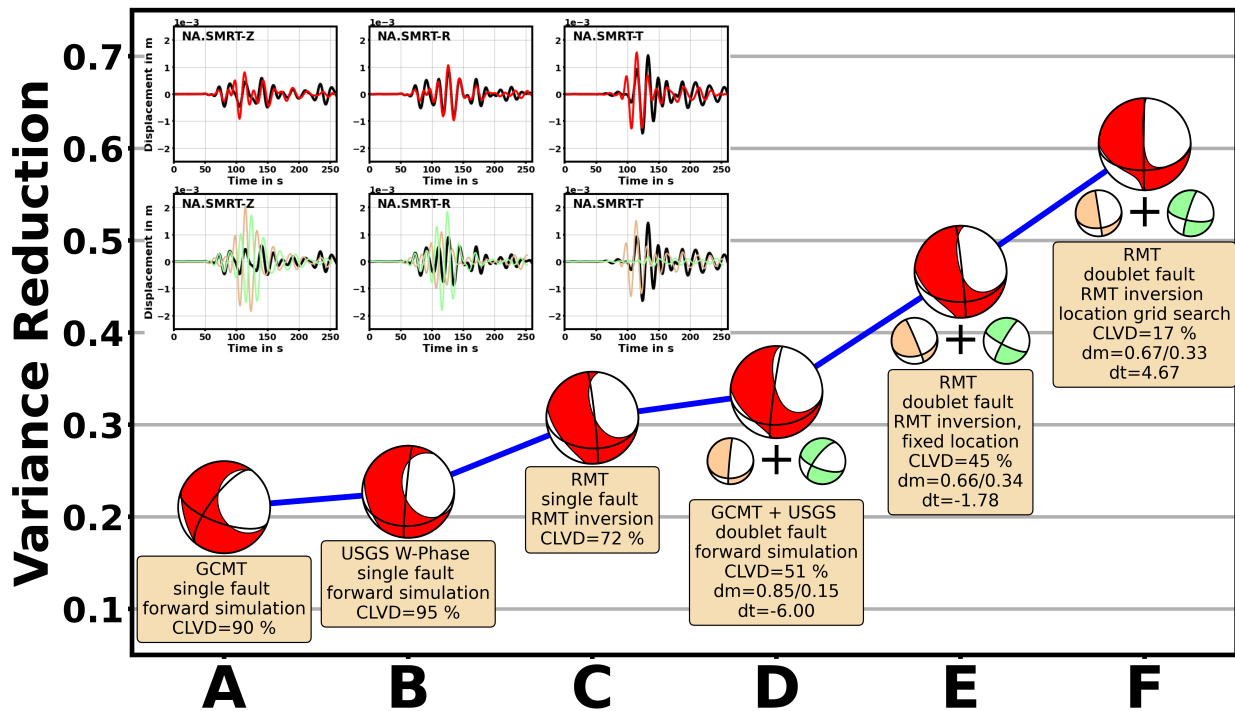
#### Single fault

We conducted three single-source experiments: two forward simulations and one inversion. Issues with mismatches in timing are handled using a restricted cross-correlation time-shift update. We distinguish between uncertainties in the origin time and station delays by introducing a common 4 second time shift at all locations, and 6 seconds for the three-component waveforms at each station. This generous time update is conditioned by the limitations of the used P-wave travel-time velocity model (Braszus et al., 2021) which does not provide a sufficient resolution within our depth range and above and neglects the complex structure above the Martinique hypocenter (e.g., Schlaphorst et al., 2018; Hicks et al., 2023).

Our initial forward simulations, of the GCMT (Figure 6.4, A) and USGS (Figure 6.4, B) solutions at a fixed hypocenter location using the regional network, suggest a rather poor match between observations and synthetics, with a small variance reduction (VR) of 0.21 and 0.23, respectively. A subsequent deviatoric single fault inversion (Figure 6.4, C) returns a slightly improved VR of 0.31, for a double-couple mechanism similar to the USGS1 solution. The inversion is done unbounded, where we allow an uniXtree importance sampling in full 4-dimensional parameter space: strike  $\psi \in [0, 2\pi)$ , dip  $\delta \in [0, \frac{\pi}{2}]$  in the uniform Tape representation  $h = \arccos(\delta)$  with  $h \in [0, 1]$ , rake  $\lambda \in [-\pi, \pi)$  and CLVD  $\in [-100\%, 100\%]$  in the uniform Tape representation  $\gamma(v) = \frac{1}{3} \arcsin(3v)$  with  $v \in [-\frac{1}{3}, \frac{1}{3}]$ ,  $\gamma \in [-\frac{\pi}{6}, \frac{\pi}{6}]$  and CLVD  $= \gamma \cdot \frac{600}{\pi}$ . The main discrepancy of model C to model B is the strike direction, which we suggest to be a result of the network arrangement.

#### Doublet fault

Doublet modeling follows the same procedure as for single fault cases but includes more parameters. We assume that the CLVD of a deviatoric single fault solution can be explained by two appropriately temporally and spatially-separated double-couple sub-events: a major and minor couple, each described by a set of strike, dip, and rake (Frohlich, 1995). The synthetic waveforms of both sub-events are simulated separately in a forward simulation and combined in a weighted summation of the time series. Sub-event succession in time is described by time  $dt \in [-15, 15]$ , of F2 relative to F1. Negative times place F2 before, and positive times after F1. Magnitude differences are modeled using the moment ratio  $dm \in [0.0, 1.0]$ , relating to the total moment of the two sub-events.



**Figure 6.4:** Regional 3D full waveform inversion. Displayed are our source models using a single fault (A-C) and doublet (D-F) assumption. Combined doublet beachballs (red) represent the weighted summation of the two double-couple mechanisms F1 (orange) and F2 (green). We performed forward simulations (A, B, D) and inversions (C, E, F) at fixed hypocenter locations (A-E) and in a location grid search (F). Inter-event-time  $dt$  is given relative to F1 (dip-slip, orange) and moment  $dm$  are fractions of the total released moment of  $M_w 7.4$ . Displayed waveform fits at station NA.SMRT are the results of experiment F. Color-coding of the combined synthetics and individual contributions is as for the focal mechanisms.

The amplitude of F2 is defined by  $dm$ , while the contribution of F1 is determined by  $(1 - dm)$ . Including the two hypocenter locations, the doublet problem comprises 14 parameters: relative time  $dt$ , relative moment  $dm$ , two sets of three hypocenter location parameters and two sets of three fault-orientation parameters. This introduces large ambiguities in the solution if solved in the full parameter space. Therefore, we do a restricted inversion around a starting solution and/or fixed source locations.

Given that the GCMT and USGS solutions indicate two different mechanisms, which agree with nearby historical mechanisms, we assume them to resemble the actual doublet. Our initial doublet test is composed of a combined forward simulation, with sampling of  $dt$  and  $dm$ , using the USGS1 double-couple as fault mechanism  $F1^D$  and the GCMT double-couple as fault mechanism  $F2^D$ , at the USGS1 hypocenter location. The resulting doublet mechanism (Figure 6.4, D) is strongly influenced by the  $F1^D$  mechanism,  $(1 - dm) = 0.85$ , and is preceded by around 6 seconds by  $F2^D$ . However, the waveform fit increased only marginally compared to the single fault inversion to  $VR = 0.34$ . In the next step, we relax the constraints on fault mechanisms. Both couples are set as starting solutions in the restricted uniXtree-inversion (Lindner et al., 2023), allowing for a maximum deviation in strike, dip, and rake of  $25^\circ$ , together with the same range for  $dt$  and  $dm$  as before. The resulting doublet (Figure 6.4, E) has a smaller CLVD component, and a  $VR = 0.47$  and  $dm = 0.34$ . The offset time is 1.78 seconds, with  $F2^E$  prior to  $F1^E$ . Finally, we solve for the spatial arrangement of the doublets  $F1^F$  and  $F2^F$  in a restricted uniXtree-inversion using a grid search. The location grid is constructed around the aftershocks (Figure C.5a or Figure C.5b) and informed by the re-located hypocenters (Bie et al., 2020).  $F1^F$  is searched in the northern grid and  $F2^F$  in the southern one (Figure C.6). The inversion shows that the mechanisms of  $F1^F$  and  $F2^F$  do not change significantly; the spatial separation increases the waveform fit to  $VR = 0.54$ .

## 6.6 Discussion

Our detailed MT inversion demonstrates that the Martinique earthquake was most likely a source doublet. It consisted of two sequential sub-events in time and space: a  $M_w7.1$  strike-slip event followed, with a  $\sim 4.23$  seconds delay, by a  $M_w7.25$  dip-slip event. Using a scaling relationship for intra-slab earthquakes (Blaser et al., 2010), we can estimate the rupture length of the two sub-events, yielding  $\sim 55$  km for each. The temporal and spatial succession is reversed relative to the IRIS back-projection results but aligns well with the SCARDEC-STF (Figure 6.2). Both mechanisms are consistent with the faulting pattern in the region and reconcile the discrepancy between the two published double-couple solutions. This leaves us with the question of which large(r) structure(s) at depth may have ruptured during this complex earthquake.

Seismicity at this depth represents intra-slab deformation (Bie et al., 2020; Lindner et al., 2023). Figure 6.5 displays our compiled results relative to the slab surface. Seismicity (heatmap) concentrates north of the Martinique event on the Proto-Caribbean lithosphere near the domain boundary to the Atlantic lithosphere. We made a qualitative assumption of the active nodal planes (preferred strike direction) of the events in our RMT catalogue (white lines). The displayed pattern does not coincide with the Marathon-Mercurius fracture zones/domain boundary, but proceeds in a southward trend at first perpendicular, then approximately parallel to the fracture zone trend and finally perpendicular to it again.

Two recent studies (Braszus et al., 2021; Chen et al., 2023) predicted from the plate reconstruction by (Müller et al., 2019) and comparison with tomography that the northernmost end of the ancient Proto-Caribbean spreading ridge subducted near the location of this deep earthquake cluster. This part of the Proto-Caribbean Ridge separated around 90 Ma ago from the Atlantic triple junction (North-Atlantic, Central-Atlantic and Proto-Caribbean), migrating westwards along the southern side of the Mercurius fracture zone. The overall structure indicated by the nodal planes strongly resembles a ridge-transform fault system on oceanic lithosphere, with a spatial succession of strike-slip motion parallel to the fracture zones and dip-slip faulting on the perpendicular ridges.



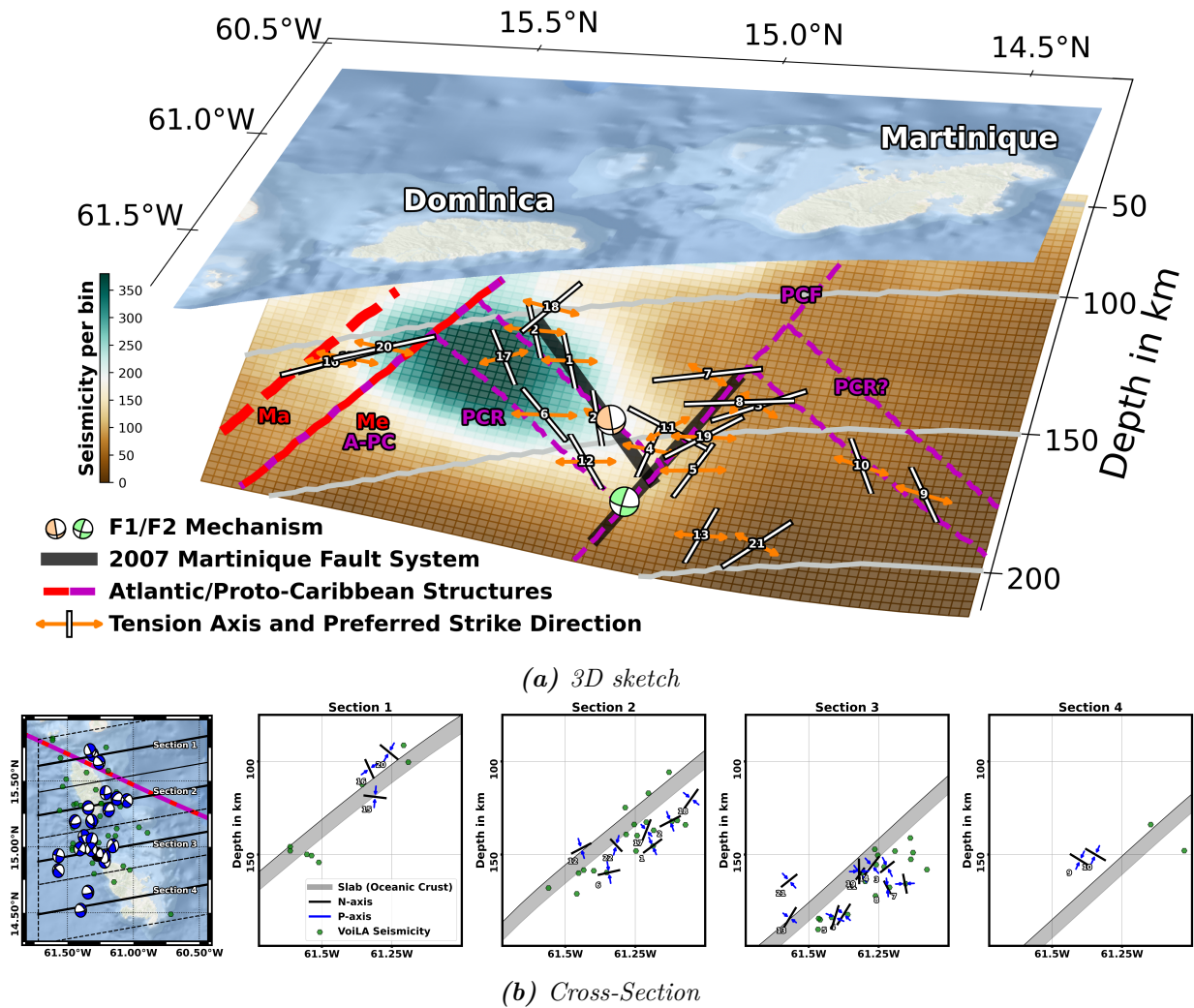
The 2007 main doublet event occurs near where we observe a transition between these faulting styles, which is likely the location of a ridge-transform intersection. Shallow-source doublet events, with large CLVD contributions when inverting for a single fault mechanism, have also been found to be most common near such fault intersections (Frohlich, 1995).

In a view along vertical cross-sections (Figure 6.5), we find along Section 1 and 4 that N-axes (null-axes) are near perpendicular and P-axes (pressure-axes) parallel to the down-dip direction of the slab. Events in these cross sections with MTs as well as other events located using the regional stations and seismic structure (Bie et al., 2020) fall in an approximately 10 km wide band near the estimated position of the slab surface. The style of deformation and width of the Wadati-Benioff zone (WBZ) in these two sections is similar to that found in other subduction zones, and reflects compression due to mantle resistance to slab sinking. The relatively shallow occurrence of down-dip compression is consistent with the large amount of accumulated slab material within the upper mantle below the LAA as inferred from the tomographic images (Braszus et al., 2021). Section 2 hosts mostly normal faults with extension parallel to the trench, with N-axes parallel and P-axes perpendicular to the down-dip direction of the slab. Stress orientations are similar along Section 3, but with an increased number of strike-slip events and a mixture of N-axes parallel and perpendicular to the slab. The state of stress along Sections 2/3 is consistent with along-strike slab bending to accommodate the change in dip (Bie et al., 2020) between the steeper slab north and more shallow dipping slab south of Martinique.

As suggested by Lindner et al. (2022), such a change in dip could be due to partial slab detachment below Grenada. The change in event style around the Martinique event thus does not reflect a change in stress, but solely a change in orientation of the ridge-transform inherited weakening structures present in the slab that are activated in response to this stress. The seismicity in Sections 2/3, including the aftershocks, extends over a significantly larger depth range (20-30 km) below the inferred slab top location. Thickening of the WBZ near the Marathon fracture zone was previously reported (Bie et al., 2020). It could either reflect that the Martinique event and its aftershocks ruptured deep into the slab, possibly due to deep hydration along the fracture zones/ridge structure (Braszus et al., 2021), or the WBZ may appear wide because of the superposition of events in two sections of the slab that are somewhat vertically offset due to along-strike folding or vertical motion along a tear to accommodate the dip change.

## 6.7 Conclusion

Our new findings indicate that the Martinique doublet is connected to a re-activation of pre-existing weak structures in the subducted plate associated with the fossil Proto-Caribbean spreading ridge. The re-activation is governed by a predominant trench-parallel extensional stress regime (Lindner et al., 2023) and slab bending influenced by along-strike changes in slab pull due to partial slab detachment (Braszus et al., 2021; Lindner et al., 2023), which lead to local distortion of the slab. Our results show that large intermediate-depth earthquakes can occur on pre-existing distributed fault systems inherited from the creation of oceanic lithosphere. Apparently such systems facilitate the localization of seismic deformation even under high-pressure conditions in WBZ, e.g., due to a concentration of hydration and/or weaker rheology because of inherited grain size or fabric. The potential of such earthquake doublets makes estimating maximum rupture sizes for intermediate-depth earthquakes challenging.



**Figure 6.5:** 3D sketch and depth cross-sections of the slab segment between Dominica and Martinique. *Top:* Illustration of the re-activation of the old ridge-transform system on the Proto-Caribbean plate, south of the Atlantic-Proto-Caribbean domain boundary (A-PC), under the influence of local trench parallel extension which probably accommodates the steepening of the slab from south to north (Lindner et al., 2023). Associated with the domain boundary are two Atlantic fracture zones: Mercurius (Me) which cannot be distinguished from the boundary at depth and Marathon (Ma). Proto-Caribbean structures (magenta) consist of an unnamed fracture zone (PCF) and two offset ridge segments to the north (PCR) and south (PCR?). The outline of these structures is motivated by the source solutions and seismicity. Tension axes of known source mechanisms in the region are predominantly trench parallel and the nodal planes fit well to the suggested Proto-Caribbean structures. The Martinique doublet (F1/F2 mechanism) is located at the ridge-transform intersection, suggesting a rupture along these perpendicular structures. *Bottom:* Trench perpendicular cross-sections showing the seismicity within the dotted boxes surrounding the profiles (map view). Sections 1 and 4 contain MTs with similar stress directions and seismicity overlaps with the estimated position and thickness of the subducted oceanic crust at depth. The middle sections host the highest seismic activity over a depth range significantly exceeding the expected thickness of the subducted oceanic crust. In both sections, mechanisms reflect along-strike extension and slab-perpendicular compression, but along Section 2 this stress is released mainly by normal fault events perpendicular to the A-PC while in Section 3 there is increased strike-slip activity.





## Part III

# Moment tensor inversion outside the Lesser Antilles



## Chapter 7

# Induced seismicity due to hydraulic fracturing near Blackpool, UK: Source modeling and event detection

This chapter features my collaborative work on hydraulic fracturing-induced seismic activity near Blackpool, UK. The content of this chapter got published under Karamzadeh et al. (2021) in the *Journal of Seismology* with me as second author. My contributions include the moment tensor inversion, interpretations of results, writing MT-relevant sections of the paper, creating several of the displayed figures and tables, and conducting internal reviews. Throughout this process, I had regular discussions with Dr. Nasim Karam Zadeh Toularoud, the first author of the paper.

### 7.1 Abstract

Monitoring small magnitude induced seismicity requires a dense network of seismic stations and high quality recordings in order to precisely determine events' hypocentral parameters and mechanisms. However, microseismicity (e.g., swarm activity) can also occur in an area where a dense network is unavailable and recordings are limited to a few seismic stations at the surface. In this paper, we aim to study shallow microseismic events related to hydrofracking using recordings of a seismic network which was not designed to detect and locate such small events. A sequence of microseismicity caused by a hydraulic fracturing of the PNR-2 well near Blackpool, UK in 2019 is studied, mainly using data recorded at a single station at the surface, about 1.3 km from the events' epicenters. The sequence comprises of 133 events from August 15 to September 14, 2019, as catalogued by the British Geological Survey (BGS). Our aim is to detect smaller events that might be missing from the BGS catalog and to study the temporal and spatial pattern of the seismicity as well as focal mechanism of the larger events. We used a template matching technique to extract smaller events and clustered the new detections based on their waveform similarity. The 6 largest events in the BGS catalog, with magnitude greater than  $M_L 1$ , were used as template events. During the stimulation period, temporal changes in event detection rate were in agreement with injection times. Focal mechanisms of the events with high quality recordings at multiple stations indicate a strike-slip mechanism, while a cross-section of 34 relocated events matches the dip angle of the active fault. More than 2200 events are detected in a 7-week long analysis time period. Of these we verify 20 % as small earthquakes with clear waveforms. In addition 50 % of detections coincide with an event reported in the operator catalog.

## 7.2 Introduction

Hydraulic stimulation for oil and gas exploitation causes induced seismicity, often detectable at the surface, and changes the pattern of background seismicity by increasing the number and magnitude of microseismic events. Induced seismic activity is often too small to be felt by humans, let alone cause structural damage at the surface. However, the occurrence of felt earthquakes is possible, which can then cause public alarm and concern and may impact the operator through temporary or long term suspension of production, especially in regions that are not seismically active. For instance, prior to the seismicity studied herein, magnitude 1.5 and 2.3 earthquakes occurred near Blackpool, UK, during a previous shale gas reservoir development in 2011 (British Geological Survey, 2017). These were the largest events in a sequence of induced tremors and led to a temporary UK-wide shutdown of hydraulic fracturing activities until 2018. While the majority of induced seismicity is minor, in rare cases events can be sufficiently large to pose a risk to structures at the surface. For example, a  $M_w$ 4.6 earthquake was caused by fluid injection during hydraulic fracturing in northeast British Columbia in 2015 (Clay, 2015).

Monitoring induced seismicity is, therefore, clearly very important and crucial to the safe and economical operation of any site where induced events are expected, whether shale gas, geothermal or carbon capture storage. The distribution of event locations, and their mechanisms can lead to the identification of hidden faults intersecting or close to the injection well-bores. In addition, the source characteristics of the events provides a criterion on which to discriminate fault related and fracture related events (Kratz et al., 2012). The occurrence of larger microseismic events is an indication of fault reactivation (Davies et al., 2013) due to the interaction between injected fluid and the fault, either by permeation of the fluid into the fault plane, or perturbation of the stress state of the fault. Furthermore, microseismic monitoring allows us to infer the fracture propagation length and the extent of stress changes (Wilson et al., 2018).

Generally, recording and locating weak seismic events requires high quality seismic data acquisition with a very dense network of seismic sensors at surface and/or depth, which is very often not available or restricted to the operator. Besides data availability, the hydrofracking related activity (such as traffic) increases seismic background noise level and environmental vibrations. This makes seismic monitoring from the surface more challenging, as small magnitude earthquakes might be buried in the background noise and not be detectable using techniques based on time-domain amplitude inspection. Template matching (TM) techniques offer a solution to detect such weak seismic events (Gibbons et al., 2006; Meng et al., 2018) and have been shown to increase detection capabilities in other applications (Yoon et al., 2015; Beaucé et al., 2019; Skoumal et al., 2016).

As a consequence of hydraulic fracturing activities in the subsurface near Blackpool, several sequences of earthquakes occurred and were reported by the BGS. In 2011, on April 1 and May 27, two earthquakes with magnitudes  $M_L$ 2.3 and  $M_L$ 1.5, respectively, were detected and felt in the Blackpool area. These events were part of a sequence that occurred between March 31 and May 27 comprising a total of 52 tremors, with magnitudes ranging between  $M_L$ -2 and  $M_L$ 2.3 (Clarke et al., 2014). On October 18, 2018, fracking restarted at the nearby Preston New Road site, after a 7-year UK-wide moratorium, and consequently earthquakes with magnitude of  $M_L$ 1.1 and  $M_L$ 1.5 occurred on October 29 and December 11, 2018. These two events were the largest, and felt, earthquakes in a series of 57 events with magnitude between  $M_L$ -0.9 and  $M_L$ 1.5 (Galloway, 2019). After restarting operations in 2019, at a second well at the same site, the occurrence of two earthquakes with  $M_L$ 1.6 and 2.1, in a sequence of 137 events, led hydraulic fracturing at the site to be suspended on August 24. The largest event,  $M_L$ 2.9, occurred two days later on August 26. The largest event was associated with reports of minor damage to local belongings and was assigned EMS-98 intensity VI by the BGS. Edwards et al. (2021) found that this was likely an overestimate, with intensity V being more representative of the reported and modelled effects. As a result of a regulator-led scientific review of induced seismicity near Blackpool, the UK government again imposed an indefinite UK-wide suspension to onshore hydraulic fracturing in late 2019.

Analysis of the sequence of seismic tremors in 2011, using 4 local stations at 1 to about 2 km distance from the epicenters, revealed the location of a hidden fault that was activated during hydraulic fracturing (Clarke et al., 2014). Source modelling of the biggest event in the sequence indicated a strike-slip mechanism with left-lateral motion (Clarke et al., 2014). Induced seismicity related to the 2018 sequence was recorded by a dense surface network of 26 surface broadband sensors and 24 downhole geophones (15 Hz) at the depth at which injection took place. Seismicity was strongly clustered in space and time, and associated with known periods of injection. In addition, the observed seismicity migrated from west to east, in agreement with the spatial locations of different stages of hydraulic fracturing (Baptie, 2018). Analysis of induced seismicity related to the 2019 hydrofracking stimulation by Kettlety et al. (2020) concluded that the aftershocks of the  $M_L 2.9$  event were distributed along a near vertical plane with a strike and dip of  $130^\circ$  and  $80^\circ$ , respectively. In addition, the focal mechanism of the mainshock determined from surface array data using first motion polarities of both P- and S-waves and P-to-S-wave amplitude ratios, indicated a strike of  $127^\circ$ , dip of  $84^\circ$  and rake of  $-160^\circ$ , i.e, the orientation of the northwest-southeast nodal plane consistent with the plane fitted to the aftershocks. According to Kettlety et al. (2020), the spatial distribution of events in 2018 and 2019 indicates that the seismicity occurred on two different faults, as the stimulated well in 2019 was 100 m above the previous one. The fault reactivated in 2018 had a northeast strike, whereas the fault reactivated in 2019 had a southeast strike (Kettlety et al., 2020).

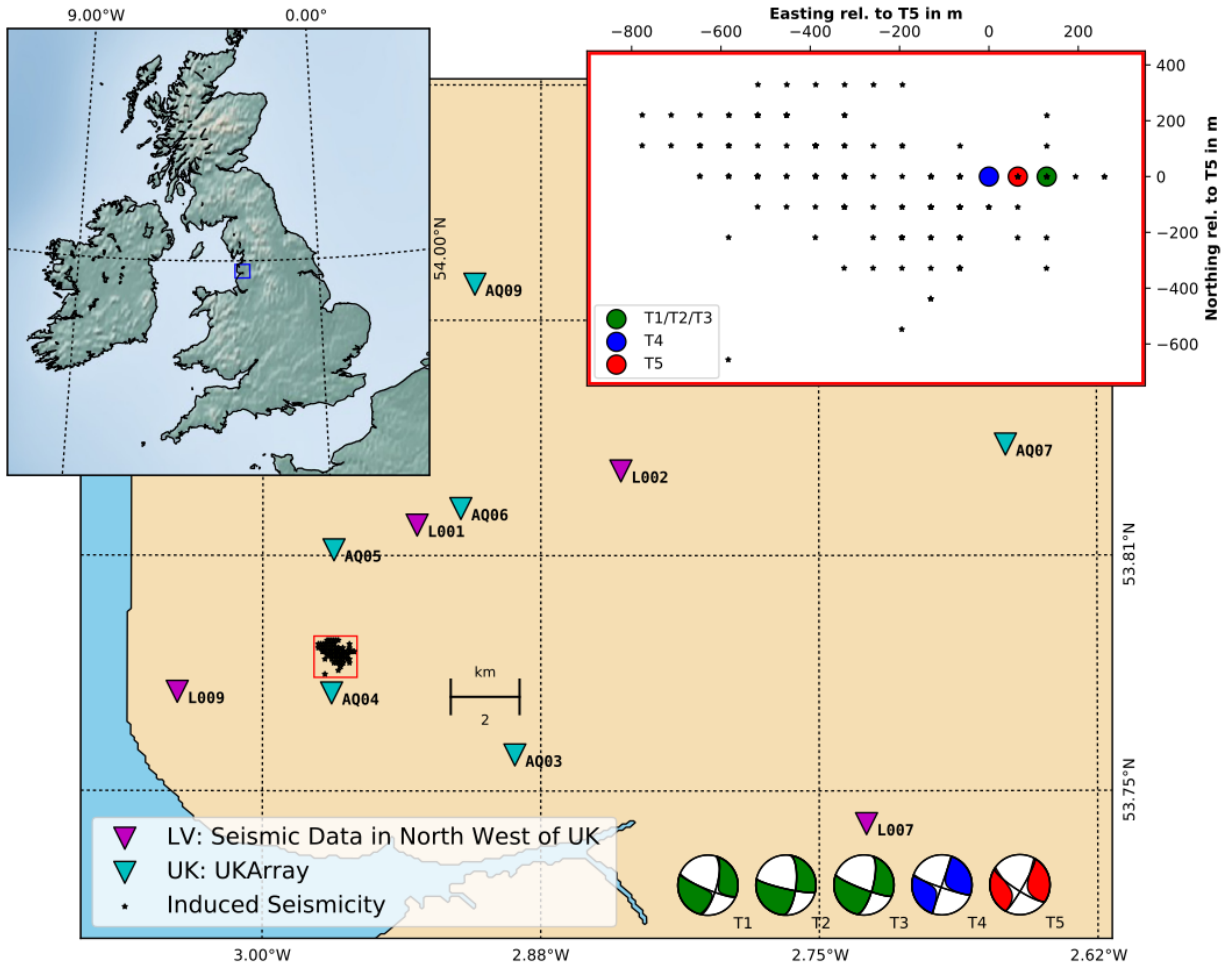
In this study, we aim to show the capabilities of surface stations alone to detect and characterize the induced seismicity in Blackpool during hydraulic fracturing of the second well PNR-2, using modern waveform based analysis tools. By utilizing a sparse network of surface stations a number of seismic events are detected using template matching technique. The temporal behavior of the detections are studied and compared with the stages of hydraulic fracking operations taking place at about 2 km depth. In addition, we applied a full-waveform moment tensor inversion to study the focal mechanisms of large events ( $M_L > 1$ ) and used the double-difference location technique for events with high quality and similar waveforms to obtain accurate relative locations.

### 7.3 Data and data quality

The data includes continuous seismograms recorded at stations of two local broadband seismic networks, ‘UK Array’, with network code UR (Bristol University, B.G.S., 2015), operated by the British Geological Survey (BGS) and ‘Seismic Data in Northwest UK’, operated by the university of Liverpool, network code LV (Liverpool University, 2014). Figure 7.1 shows the location of the nine selected stations used for event detection and focal mechanism modelling. The sampling rate of most stations in the UR network is 200 sps, however, stations AQ07 and AQ09 are exceptions with 100 sps. The sampling rate of all LV stations is 100 sps. The data, spanning about 7-weeks duration (from July 30, 2019 to Sep 20, 2019), is processed, starting from 3 weeks before the first ‘large’ event in the sequence ( $M_L 1.6$  on August 21) until 3 weeks after the biggest event,  $M_L 2.9$  (August 26). While data of all stations are explored to detect events, we mainly focus on the nearest station to the observed seismicity, site AQ04.

In the processing time period, BGS reported 133 events with magnitude above zero within 1 km radius around the location of the  $M_L 2.9$  event. Locations of the earthquakes are shown by black stars in Figure 7.1. The red inlay in this figure includes the epicenter of the events relative to the largest event (T5) which is shown with a red circle. The number of phases which contributed to the BGS location procedure is between 4 to 28 phases from recordings of UR and the operator networks. Time, magnitude and location of the 6 largest events in the time period investigated in this study are listed in Table 7.1.

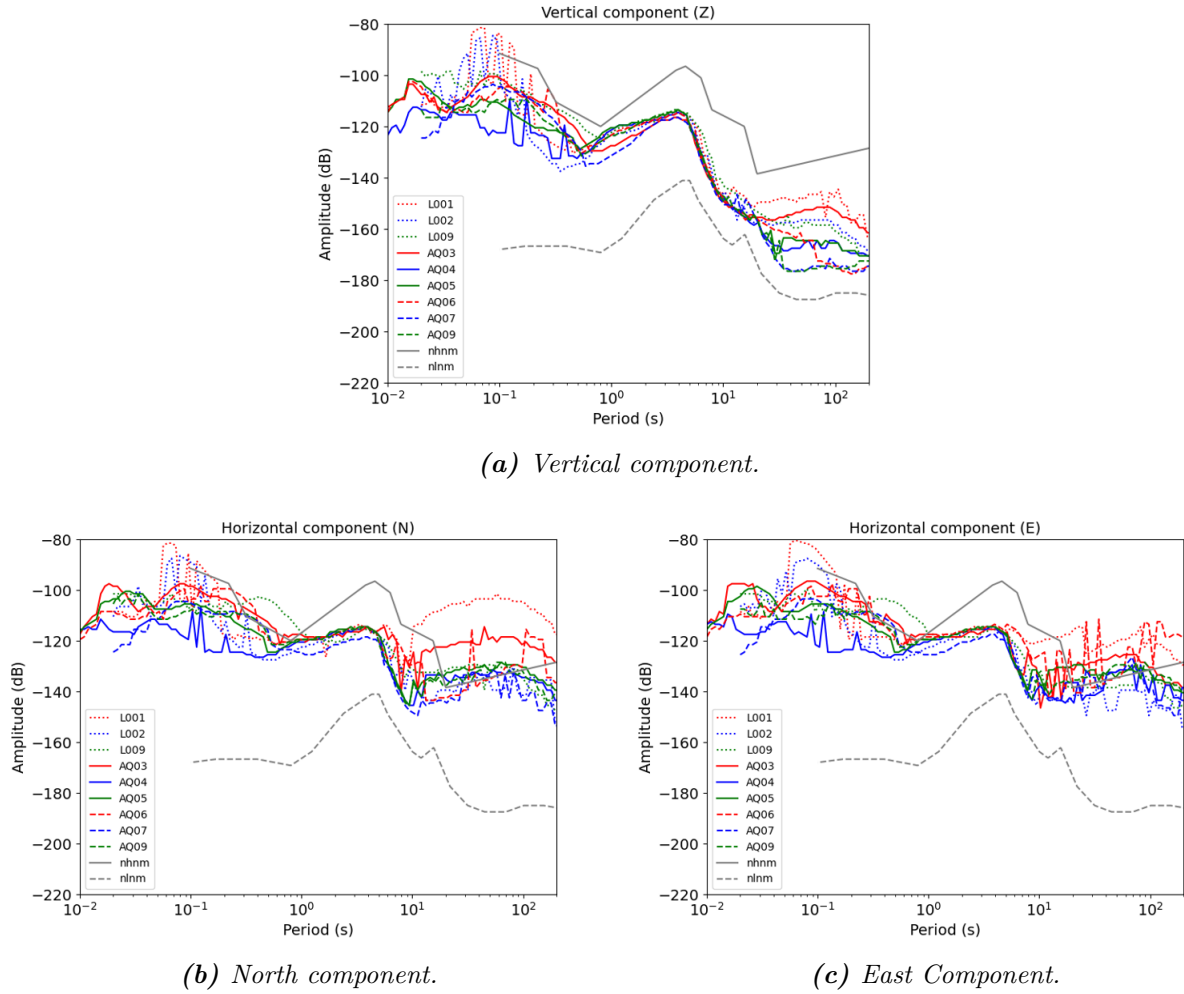
The probabilistic power spectral densities (PPSD, McNamara et al., 2004) of seismic recordings indicate the quality of signals. For all stations, modal values of PPSD are shown in Figure 7.2. We note that the stations of LV network were unusable between August 8 to August 17 due to



**Figure 7.1:** Overview map. The blue triangles show the stations of the BGS (UKArray) and the purple triangles show the stations of university of Liverpool, LV. The black stars inside the red square represent the location of the seismic events that happened in August 2019, according to the BGS catalog and the red inlay shows the epicenter of events relative to the largest event (T5). The focal mechanisms shown are calculated for each of template events except T6 which lacks of enough high quality recordings (see Table 7.1).

**Table 7.1:** Information of the 6 largest events, template events, according to the BGS catalog,  $M_w$  is calculated using source modelling in this study and  $M_L(op)$  indicate the magnitude reported in operator catalog.

ID	Date	$M_L$	$M_w$	$M_L(op)$	Depth in km	Lat	Lon
T1	2019-08-21 19:46:33.300	1.6	1.5	1.145	2.8	53.787	-2.961
T2	2019-08-22 15:23:33.900	1.0	0.9	1.12	2.3	53.787	-2.961
T3	2019-08-23 22:22:08.600	1.1	1.0	1.05	2.8	53.787	-2.964
T4	2019-08-24 22:01:35.100	2.1	1.9	1.034	2.5	53.787	-2.962
T5	2019-08-26 07:30:47.000	2.9	2.6	-	2.5	53.787	-2.964
T6	2019-08-26 21:18:29.200	1.0	—	0.7	2.7	53.787	-2.96



**Figure 7.2:** Background noise recorded at different stations during the analysis. The mode of the PPSD is plotted for each station and each component.

segmented data and several gaps. In general, the PPSD mode curves are rather close to the high noise level for the processed time duration of all stations. The difference in noise level between stations can reach up to 30 dB, while AQ04 experiences the lowest noise level at high frequency (above 5 Hz). Stations of the LV network show more fluctuations and exhibit the highest level of noise in high frequency band. The high and variable noise levels are due to the predominantly urban or residential and near-coastal localities of the seismic networks, which for cases where induced seismicity poses a risk, will be unavoidable.

## 7.4 Processing method

Hydrofracking sites are often noisy and the induced events are of relatively low magnitude. Most of the events are, therefore, not detectable at the surface using a detection technique based on single-station time-domain amplitude inspection. However, template matching techniques offer a possible solution to overcome this high noise situation, increasing the detection capability of weak events at the surface (Gibbons et al., 2006; Meng et al., 2018). Template matching methods make use of the waveforms of already extracted events as templates, e.g., a few large events with a sufficient quantity of high quality phase picks. These templates are used to scan through the continuous waveform data, prior or posterior to the template timestamp, and to find new similar events. The comparison is made by means of correlation measurement, and detection is declared once the value of the correlation between a template waveform and the piece of signal under analysis



exceeds a predefined threshold. This technique is particularly useful when the noise level is high compared to the size of the events of interest, and the seismicity happens in a relatively small seismogenic zone, which is the case for induced seismicity related to fluid injection (Gibbons et al., 2006; Shelly et al., 2007).

By applying TM approach to our data set, we anticipate that weak events which might be buried in seismic background noise are detectable and we can extract as many events as possible to compile an event catalog with lower detection threshold. The aim is to see if we can detect and process the smaller events identified by few stations at surface and link observations at surface with the actual process that is happening at seismogenic depth. We assume that the events are generated in a region smaller compared to the source-receiver distances so the time difference between S- and P-phase arrivals are consistent for all events at one station. We used EQcorrscan (Chamberlain et al., 2017) which is an open-source software package written in Python, for detection and analysis of seismicity. The TM algorithm is applied to recordings of the nearest station, AQ04, and waveforms of all detected events are extracted and further analysed using a waveform based clustering approach. In this way, a number of trusted clustered events are extracted from all detected events. The detectability of the small events from distant stations is then studied by comparing the results of the TM as a function of the reference station. In addition, for each detected event, the P-phase onset time is re-picked. Events with multi-station picks are extracted for further analysis. While event detection is performed by measuring the stack of cross-correlation of the three-component traces, P-phase re-picking is performed simply by calculating the correlation of each component of a detected event with the same component of the template event, and measuring the time shift. As a result, for a detected event there might be no P-phase picking in one component if the value of the correlation on that component is not above the threshold value of 0.4 (out of 1). If all 3 components of a detected event correlate well (greater than 0.4) with the related template waveforms then 3 identical P-phase picking times are measured.

We study the activated fault mechanism by waveform modelling for events whose signal quality at an appropriate number of stations is high. Source modelling for pure deviatoric moment tensors is performed using full waveform information. The inversion is based on an oc-tree grid search approach (Lomax et al., 2001) solving a tensor combination method (Krizova et al., 2013). Sampling is done in a 4-D parameter space for strike, dip, rake and compensated linear vector dipole (CLVD) following the uniform parameterization by Tape et al. (2015). The 1-D velocity model for the UK (Booth et al., 2001) is used and a synthetic green's function database is computed by the Fomosto extension of the Pyrocko framework (Heimann et al., 2017). Our approach allows for non-linear inversion taking into account uncertainties on the underlying source parameters. Finally, to support and verify the source modelling results, the event locations are also investigated using a relative location technique. Therefore, P- and S-phase differential travel times are calculated for each event-template pairs and the hypoDD program is used (Waldhauser, 2001) to calculate double-difference hypocenter relative locations.

## 7.5 Application and results

### 7.5.1 Event detection

**Templates:** The six large events, with magnitude greater than  $M_L 1$ , are used as three-component templates at each station. The time window of a template signal starts 0.1 seconds before P-phase onset time and includes both P- and S-phases signals, e.g., the window length for the station AQ04 is 2.0 seconds. Waveforms of template events at station AQ04 are plotted in Figure 7.3, applying a bandpass filter of 20-80 Hz. Waveforms are aligned in time, based on the arrival time of P-phases and are scaled to the maximum value of each trace. According to Figure 7.3, scattered coda phases coming after the P-phase of T5 (the  $M_L 2.9$  event) show higher amplitude than the P-phase on the vertical component, and this is obviously different from the other templates. Similarly the S-phase coda shows higher amplitude than the first arrival S-phase on the horizontal components.

**Table 7.2:** Values of the cross channel correlation between all template pairs.

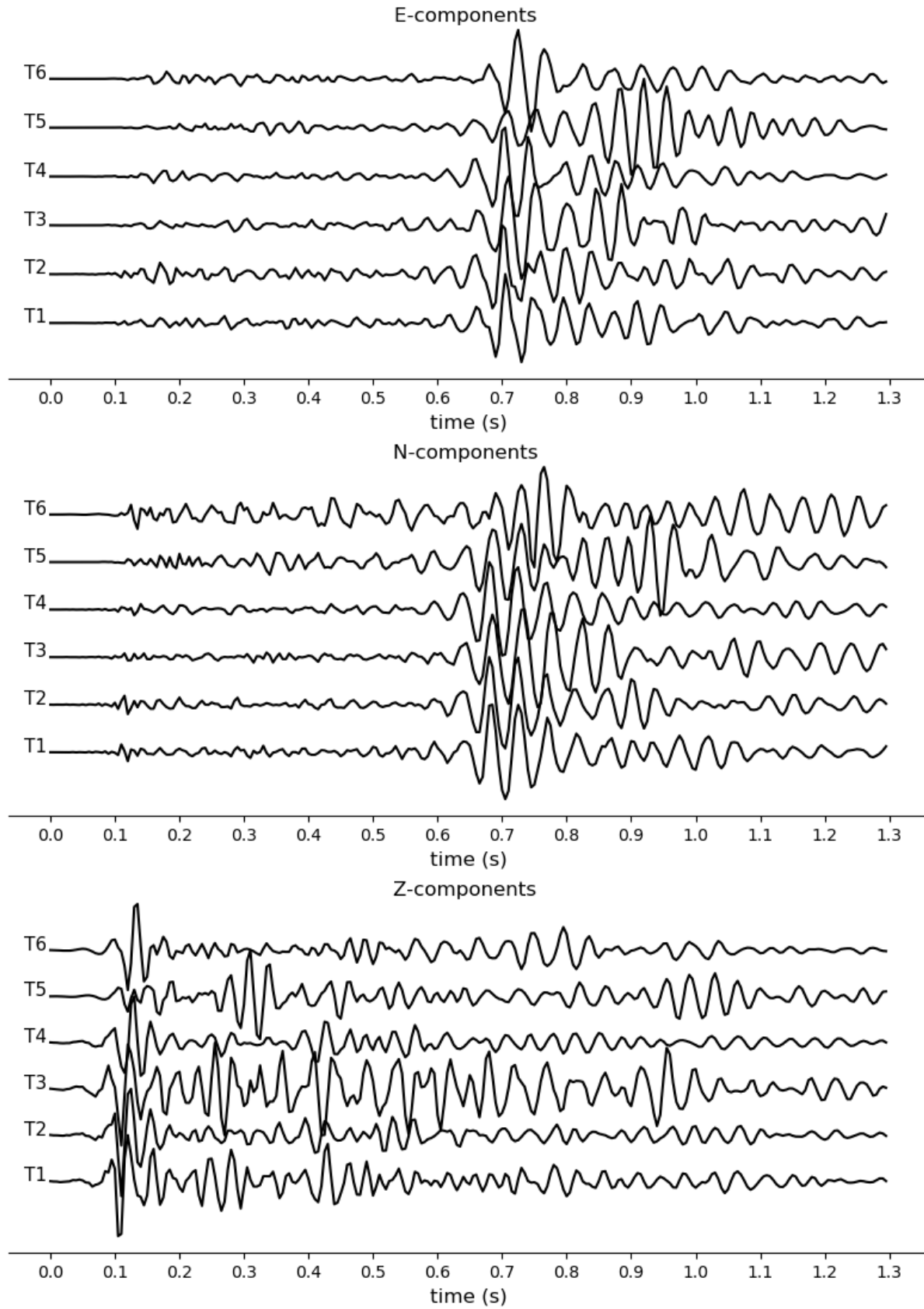
Low frequency (1-20 Hz)							High frequency (20-80 Hz)						
	T1	T2	T3	T4	T5	T6		T1	T2	T3	T4	T5	T6
T1	1.0	0.95	0.87	0.93	0.27	0.56	T1	1.0	0.71	0.44	0.7	0.37	0.02
T2		1.0	0.91	0.96	0.2	0.45	T2		1.0	0.42	0.77	0.31	-0.01
T3			1.0	0.87	0.28	0.3	T3			1.0	0.29	0.32	0.17
T4				1.0	0.28	0.57	T4				1.0	0.34	0.09
T5					1.0	0.25	T5					1.0	0.00

In addition, strong P-phase coda waves are visible on vertical component traces of T1 and T3, whereas such phases are relatively weak on T2, T4 and T6.

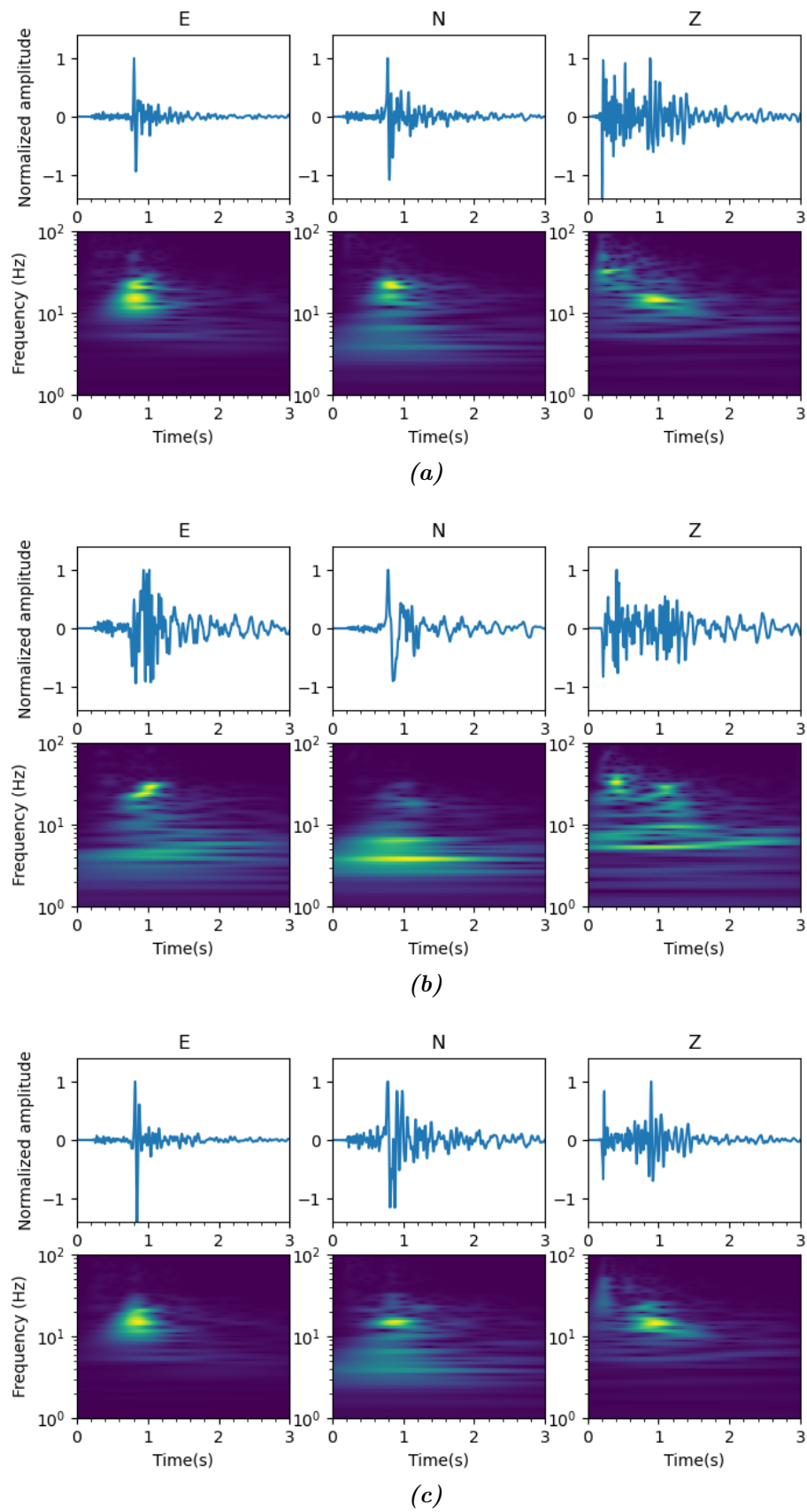
Spectral properties of the templates are studied over a frequency range of 1 to 100 Hz using spectrograms calculated by Continuous Wavelet Transform (CWT, Stark, 2005). This analysis further refines the appropriate frequency bands to investigate using TM technique. Figure 7.4 shows the three-component traces of templates T1, T5 and T6 and corresponding CWT coefficients. The traces are normalized so that the maximum value of each trace is 1, however CWTs are calculated on raw traces (bandpass filtered between 1-100 Hz). Comparing spectral behaviour of the east-west (E) components, we see that T5 shows higher but narrower frequency content of S-phases (in about 1 second) compared to the other two events. The second distinctive feature is observed on the north-south horizontal component (N) when compared to the other templates: template T5 shows much lower frequency energy in almost the entire event time span, with a maximum value at about the onset of S-phase. The predominant frequency of the S-phase (i.e., frequency components with higher wavelet coefficients) is slightly smaller for T6 compared to T1. In vertical components (Z), the highest signal energy of T1 and T3 are related to the S-phases, whereas for T5 the P-phase carries the most energy.

Waveform similarity between all template pairs are investigated by measuring the cross-channel correlation between two frequency bands. We then interpret the outcomes of different frequency bands. The values of cross-channel correlations are listed in Table 7.2. In the low frequency band (2-20 Hz), templates T1, T2, T3, T4 are highly correlated to each other, i.e., cross-channel correlation values are greater than 0.8, while in the high frequency band (20-80 Hz) template T3 shows less similarity to the others. Templates T5 and T6 are not correlated to the other templates or to each other, in both frequency bands. Template T5 shows slightly higher correlation to the T1-T4 and T6 in the high frequency band (correlations coefficient 0.31-0.37) than the low frequency band (0.2-0.28). On the other hand, template T6 shows higher correlation to T1-T5 in the lower frequency band (0.25-0.56) compared to the higher frequency band ( $< 0.17$ ).

**Template matching (AQ04):** Median absolute deviation (MAD) of daily stacked three-component cross-correlation traces is used as a threshold parameter in the TM detection procedure. The TM method is applied employing different threshold values and band pass filters, some of the outcomes are listed in Table 7.3, where the total number of detections, detection thresholds, frequency bands and the number of common detections with BGS catalog are provided. This table highlights that the frequency band of a template event influences the number of detections, as the value of cross-correlation between events is frequency dependent. The frequency band of 20-80 Hz is an appropriate frequency band for event detection and the threshold value is selected to be 9 MAD in the detection procedure, since using these values we get a smaller number of missing events compared to BGS catalog. By using 20-80 Hz filter band, 2217 events are detected (see Table 7.3). Including lower frequency content to the event detection procedure leads to a decrease in number of detections. For instance using band pass filter of 2-20 Hz and 10-80 Hz, the total number of detections is 372 and 578 events respectively. In addition, in the low frequency band of 2-20 Hz T5 does not make any detection. In Figure 7.5, the cumulative number of detections at station AQ04



**Figure 7.3:** Three-components of template waveforms recorded at station AQ04 bandpass filtered between 20-80 Hz. The trace amplitudes are normalized. For information about each template event see Table 7.1.



**Figure 7.4:** Spectral components of template  $T1$ ,  $T5$  and  $T6$  using continuous wavelet transform.

**Table 7.3:** Results of TM at different stations as a function of bandpass filter and threshold (Thr).

Station	Bandpass in Hz	Thr	Detections (#)	Common with BGS # (%)
AQ04	20-80; 20-50	9	2217; 2126	130 (98%); 127 (95%)
AQ04	2-20; 10-80; 5-80	9	419; 578; 1624	101 (76%); 101 (76%); 112 (84%)
AQ04	20-80	10; 9.5	736; 1238	121 (90%); 127 (95%)
AQ03	2-20; 20-50; 20-80	9; 8; 9	1419; 27825; 2863	43 (32%); 57 (42%); 47 (35%)
AQ05	20-50; 2-20; 20-80	9	239; 107; 324	52 (40%); 61 (46%); 58 (43%)
AQ06	2-20; 20-50; 20-80	9	17; 110; 1347	17 (13%); 30 (22%); 32 (24%)
AQ07	20-50	9	2523	8 (0.06%)
L001	2-20; 20-50	9	385; 2467	26 (20%); 21 (16%)
L009	2-20; 20-50	9	7; 858	7 (0.05%); 12 (0.09%)
L002	2-20; 20-50	9	2956; 1501	20 (15%); 9 (0.06%)

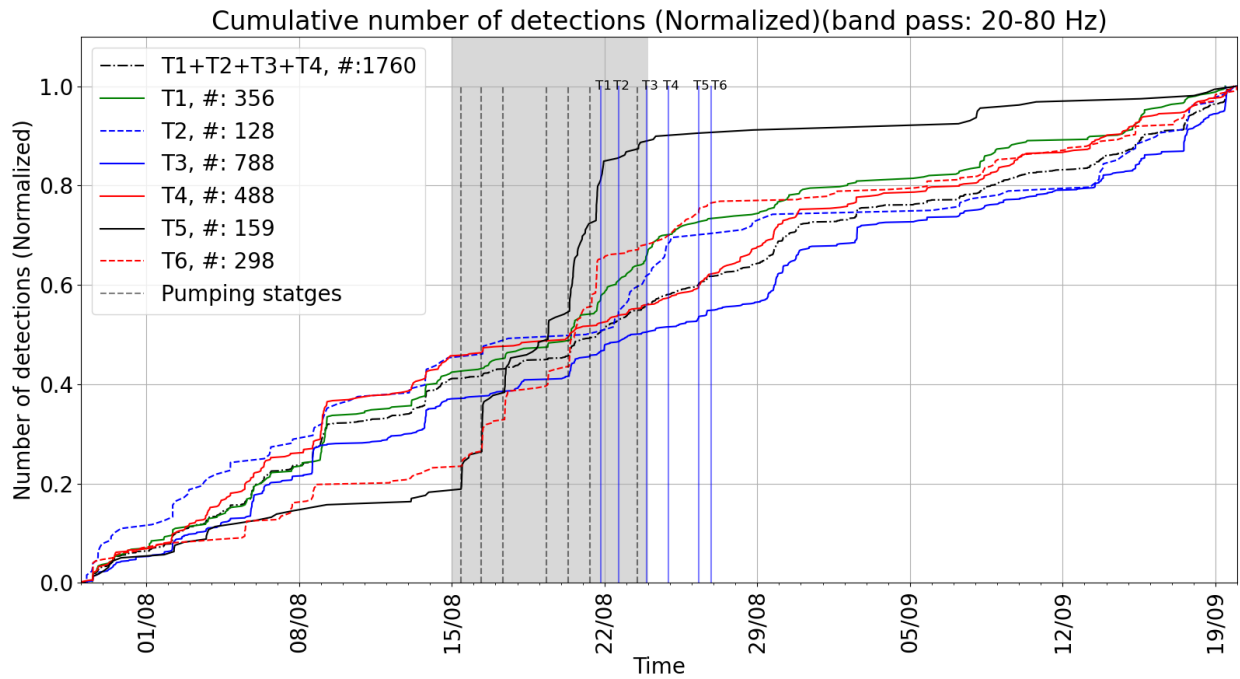
for each template event is shown for a frequency band of 20-80 Hz. The gray area in Figure 7.5 shows the time period when the fluid injection was activated, between August 15 and August 23. The sum of detections made by templates T1, T2, T3 and T4 are also plotted in Figure 7.5 as according to Table 7.2 those templates have waveform similarities.

In Figure 7.5, temporal jump-like changes to the number of detections are observed using all templates. The lowest and highest number of detections are related to T2 and T3, respectively. During hydraulic fracturing (inside the gray area), the growth rate of detections with individual templates as well as overall cumulative curve exhibit fast changes in some periods, which are in agreement with the timing of pumping stages (dashed vertical lines). It is interesting that the general pattern of detection rate for T5 and T6 is more similar to one another than to the other templates. Templates, T1, T2, T3 and T5 show similar patterns of detection rate before the occurrence of T1. The number of detections with T5 and T6 increases during the hydraulic fracturing until the occurrence of T1, after which, for both cases, the cumulative number of detections is almost flat. In addition, slight changes are observable on all curves at the occurrence time of template events. For example, after the occurrence of T1, the number of detections with T1 (green curve) increases.

Results of event detections at station AQ04 are summarized in Figure 7.6. September 6th was excluded from the analysis because of a data gap. The highest number of detections in a single day (128 detections) happened on August 20, one day before the magnitude 1.6 event (T1), and at which point the sequence of events with magnitude above  $M_L 1$  starts. A temporal jump in cumulative detection also occurs at that day for each template event and overall detections (see Figure 7.5). In Figure 7.6b shows the value of three-component cross-correlation, i.e., stacked trace, at a detection time against the time of each detection. The total number of detections in the analysed time period is 2217 events, 729 of which happened during the night hours (30 percent). Figure 7.6b also indicates 130 events that are reported in the BGS catalog.

**Clustering of detected events:** Waveforms of all 2217 detections are further explored to extract similar events. Detected events are clustered by setting the average cross correlation threshold to 0.6. The total number of re-clustered events are 485 extracted from all detections. By checking waveforms of all extracted clustered events manually, a cluster of 43 detections was recognised to be identical noise segments, and 10 other clustered detections were not verified as earthquakes. In total, 432 clustered events were therefore confirmed as earthquake events by visual inspection, 159 events of which (about 36 percent) occurred during night hours. In Figure 7.6b, the red circles represent the 432 confirmed events that are distributed from the July 31 to September 18, spanning almost the entire processing time. The six template events are distinguishable among the other detections by their time and the detection values, which are 3 for all of them. We also see that the largest event in the sequence, T5, is not among the re-clustered events.

In the time period for which the BGS reports earthquakes associated with the PNR site, between

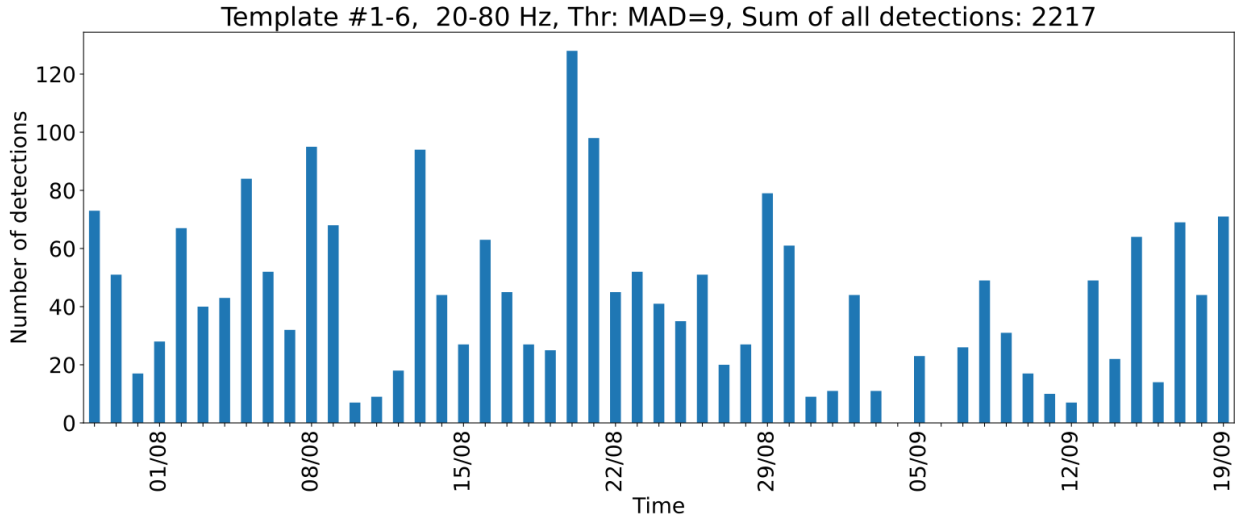


**Figure 7.5:** Cumulative number of detections for each template in 20-80 Hz frequency band. Each curve is normalized to one by considering its individual total number. Gray color in both plots shows the time period when the hydrofracturing was undergoing. The gray dashed vertical lines show the stages of the pumping. The blue vertical lines indicate the time of occurrence of the template events. The total number of detection for each plot is indicated in the related legend.

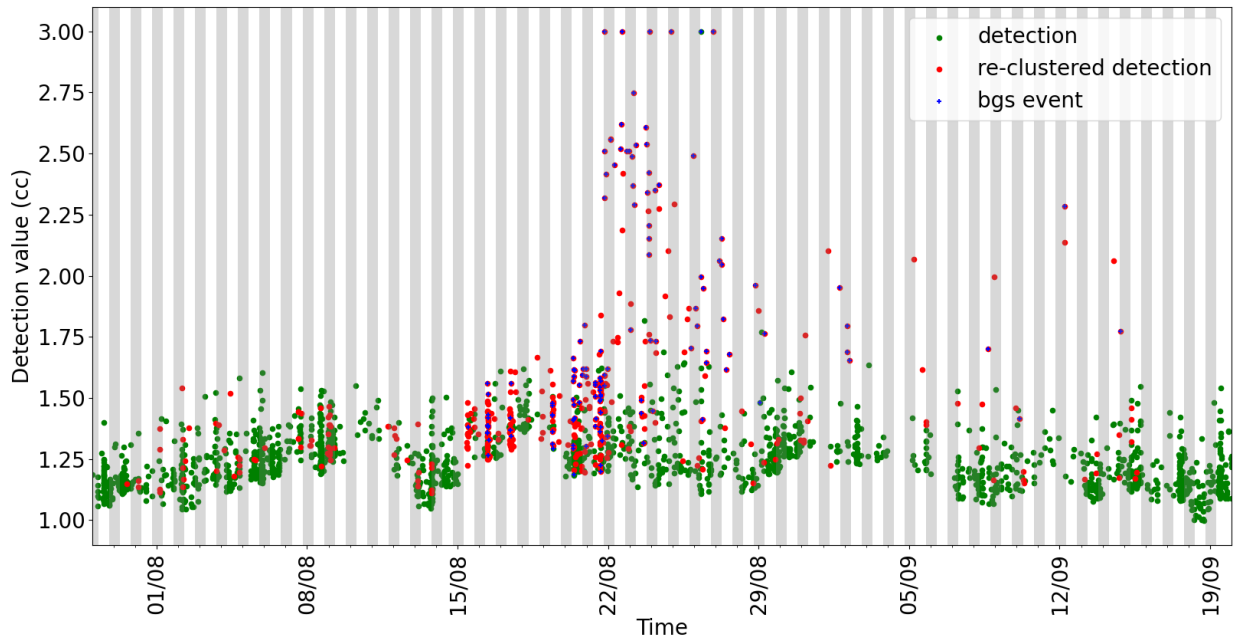
August 15 and September 14, the total number of detections is 1133. 271 are confirmed by visual check of the outcomes of the re-clustering method (almost 24 percent). Some of the events missing in the BGS catalog are detected by the TM approach with detection values above 2 (maximum value of cc is 3). In addition, there are many confirmed events with low detection values. It should be noted that total number of true events are not limited to the 432 confirmed events, and among the non-clustered events there are also small events, however we could not check all of them case by case. Considering the magnitude of template events as references, the relative magnitude (Schaff et al., 2014) of the confirmed events are estimated to be above  $M_L - 0.5$  with uncertainty of  $\pm M_L 0.5$ . For each event, all templates are used to estimate the relative magnitudes and the uncertainty is estimated by considering standard deviation of all estimated values.

Figure 7.7 summarizes the results of the waveform based re-clustering of all detections. Events in clusters with more than 10 detections are shown. Cluster C3, with 115 events, is the most populated cluster. Events in this cluster happened between August 15 and September 14. Among them 38 events (33 percent) are reported events by BGS. In addition, template T6 belongs to this cluster and the majority of the events in this cluster happened before T6. Cluster C5 with 69 events is the second largest cluster and 47 of those events are also reported by BGS. Template T1, T2, T3 and T4 are in this cluster. Events of this cluster occurred between the August 21 and September 14. The events in cluster C6 are verified as small seismic events, with one reported in the BGS catalog.

**Detections at other stations:** Waveforms of other more distant stations, such as AQ03, AQ05, AQ06, AQ07, L001, L002 and L009 have been scanned using the single station template matching algorithm. The number of detections and common detections with BGS catalog decreases dramatically for the furthest stations, such as L009 and AQ07. Detections with at least one picked P-phase are selected from all stations and are merged if their arrival time difference matches with the theoretical values. For 98 events, more than two P-phase pickings (different stations) are found.

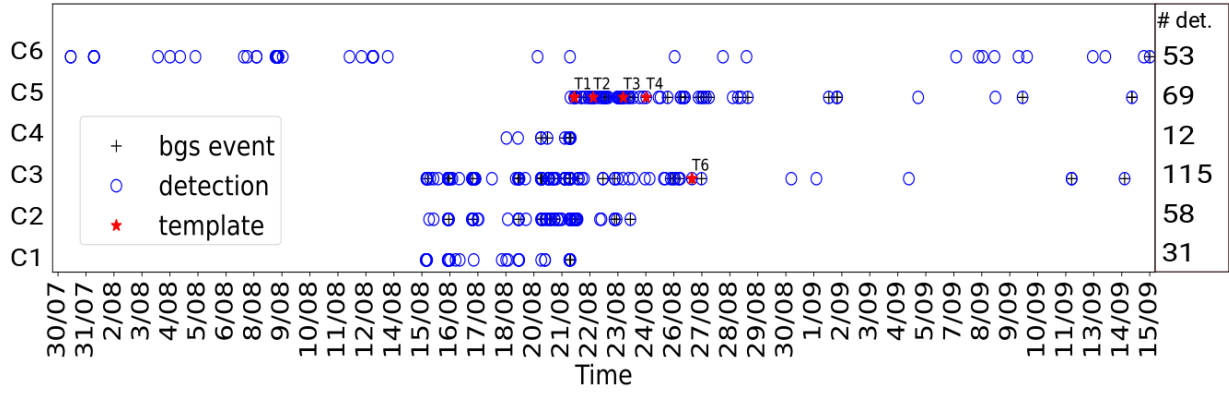


(a) Histogram of all detections.

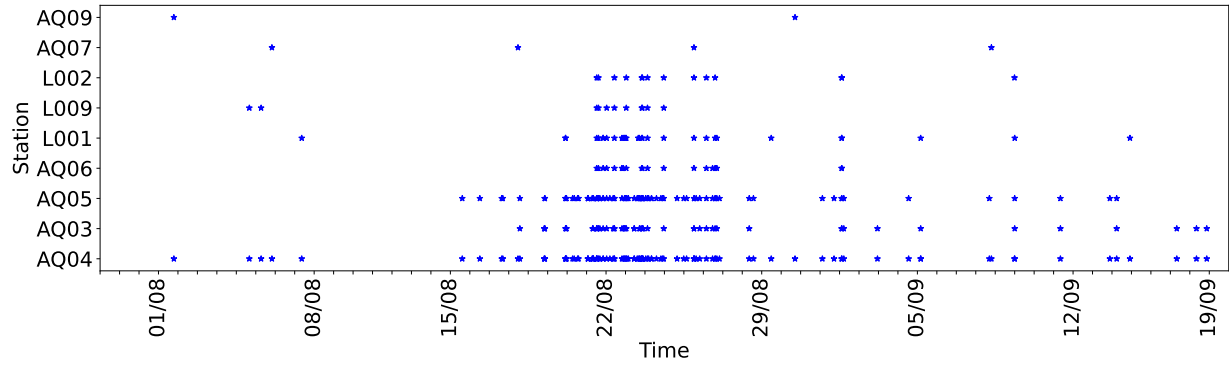


(b) Detection values (value of the stacked cross-correlation trace) for each detection.

**Figure 7.6:** Results of applying template matching event detection technique on seismic recordings at stations AQ04. In (b) each circle shows a detected event and the gray and white stripes distinguish between night (19:00 to 7:00 UTC) and day (7:00 to 19:00 UTC) hours



**Figure 7.7:** Clustering the detected events in AQ04. Vertical axis show the cluster index, numbers in right show the number of events in each cluster. Template events are indicated by red circles on cluster C5 and C3. Events which are reported in BGS catalog are marked by cross sign.



**Figure 7.8:** Multi stations event association. Stars indicate the detected events with  $p$ -phase picked at more than one station.

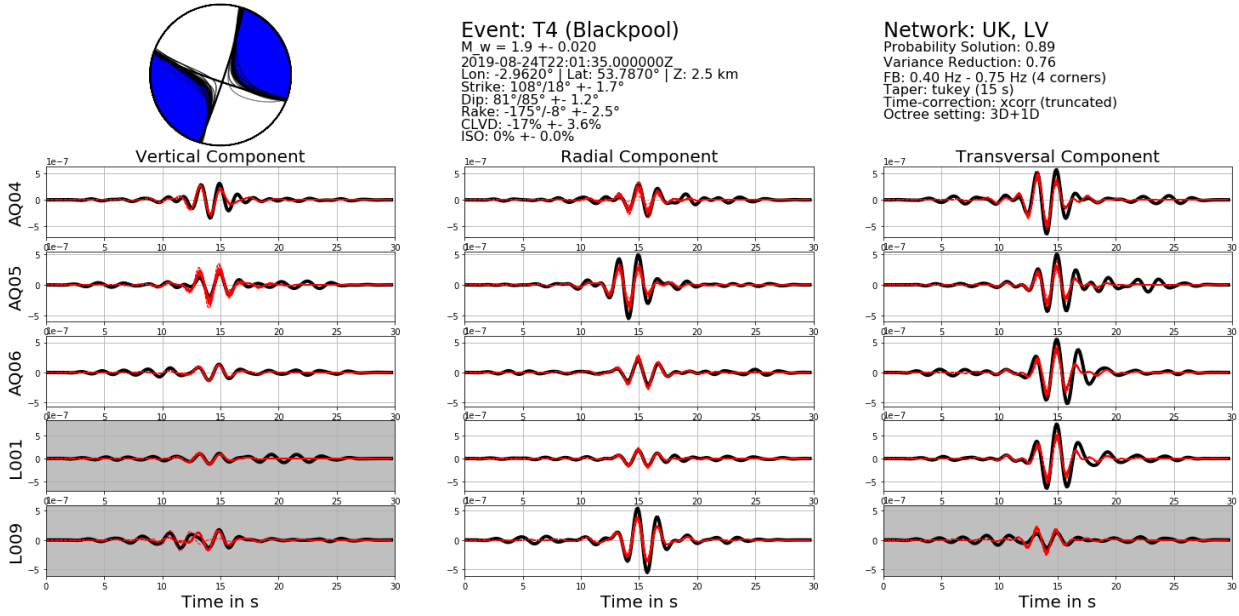
Results are shown in Figure 7.8, with stations sorted based on their distance to the epicenters.

### 7.5.2 Source modelling

Moment tensor solutions for the largest events were derived in two steps: 1) solving for the predominant pure double-couple (DC) mechanism in the full parameter space and 2) including a CLVD while allowing for small changes of the DC part (3D+1D). During the inversion, we tolerate small restricted station-wise time-shifts to account for path effects and erroneous locations. Output results contain uncertainties of the four selected source parameters within 10% of the highest probable solution and the moment magnitude (compare Figs. 7.9 and 7.10).

Event selection is based on the initial local magnitude taken from the BGS catalogue ( $M_L \geq 1.0$ ), the signal quality in the analyzed frequency band and number of usable traces. Selection of the traces was performed manually considering signal to noise ratio and quality among each component in comparison to nearby stations. We only inverted for events that show clear signals at a minimum of four stations and at least 6 traces. The BGS event locations are considered in modelling process. With an exception of T6, we were able to invert the source mechanism for all template events. Furthermore, only results with a variance reduction (VR) exceeding 50% in a 4 seconds (T1-T3) and 30 seconds (T4 and T5) signal time interval are used for interpretation. Event T4 and T5 were further examined in different frequency bands and source depths and the first motion polarities were included. T4 contains no source signal below 0.3 Hz and returns unstable solutions for frequencies larger than 0.85 Hz. T5 excites signals up to 0.15 Hz while becoming unstable for frequencies larger than 0.75 Hz. Inversion results in the stable frequency range are insensitive to changes in depth





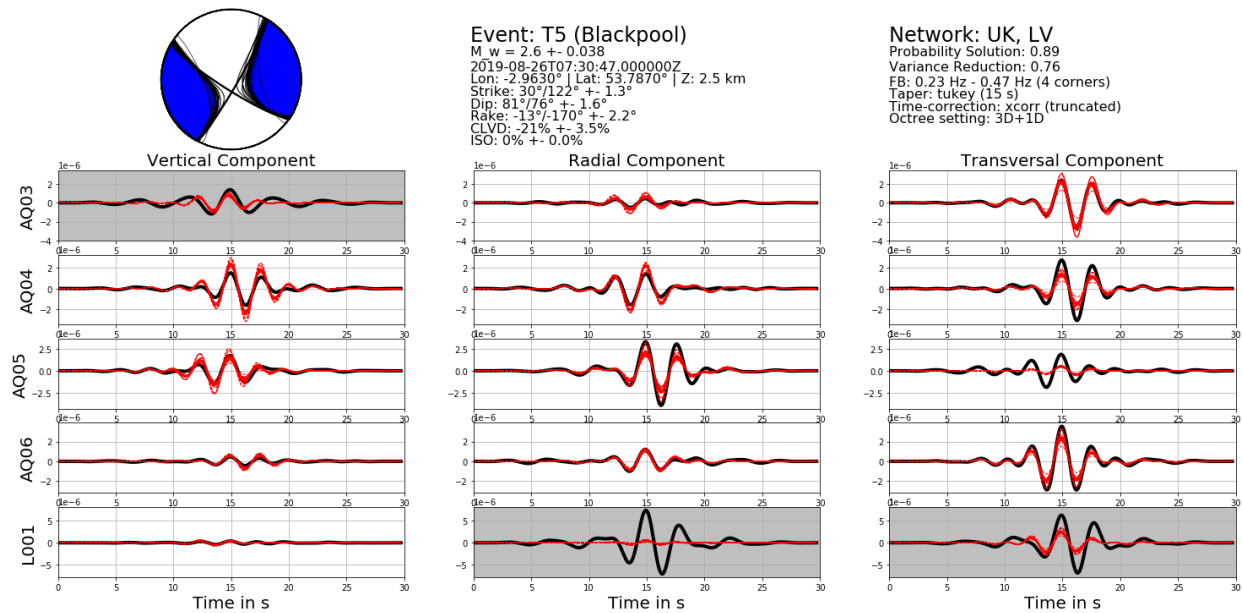
**Figure 7.9:** Inversion results including uncertainty information and waveform fit of selected stations for event T4. Black lines represent the observed displacement seismograms and red ones the synthetics solutions of the inverted source mechanism within 10% of the highest probability. Traces highlighted in gray were not used during the inversion.

**Table 7.4:** Moment tensor inversion of 5 good-quality template events: input and results.

ID	Bandpass in Hz	Traces (#)	s, d, r (NP1/NP2)	CLVD	VR
T1	1.0-3.0	6	112/16, 77/64, -153/-14	-6	65
T2	1.0-3.0	8	103/7, 79/60, -149/-12	0	53
T3	1.0-3.0	8	112/17, 78/64, -153/-13	0	65
T4	0.4-0.75	11	108/18, 82/85, -174/-8	-17	76
T5	0.23-0.47	15	122/30, 77/81, -170/-13	-21	76

within 1 km to the recorded BGS locations. Remaining events (T1-T3) contain no clear source signal below 1 Hz and are limited at 3 Hz due to model restrictions.

We investigated, within the 4-dimensional parameter space, the best solution and, if existing, multiple minima that would indicate alternative mechanisms. Our tests show that the inversions result in stable and unique solutions of all examined events. The resulting 1-D moment tensor solutions (Table 7.4 and Figs. 7.9 and 7.10) display predominantly strike-slip solutions (see Figure 7.1). Observed strike directions are  $15^\circ \pm 4.5^\circ$  (T1-T4), with an exception of the largest event (T5) at around  $30^\circ$ . With a dip angle of  $81^\circ$  and  $85^\circ$ , event T4 and T5 are steeper than T1 to T3 that show dip angles between  $60^\circ$  and  $64^\circ$ . The rake angles for all five events are between  $-14^\circ$  and  $-7^\circ$ . Overall, events T1 to T3 exhibit large similarities in their derived source mechanism with a Kagan angle of  $3.9 \pm 0.8$  at a variance reduction (VR) between 0.53 and 0.65. T4 and T5 reach a VR of 0.76 for a full deviatoric tensor. For the inversions of the three largest events (T1, T4 and T5) we allow for additional CLVD contributions as we deemed a sufficient enough signal quality on all three components. Smaller events (T2 and T3) show limited, or mostly low, signal quality on the vertical traces, which forced us to solely rely on horizontal recordings. As a result, we did not invert for the CLVD components of smaller events.

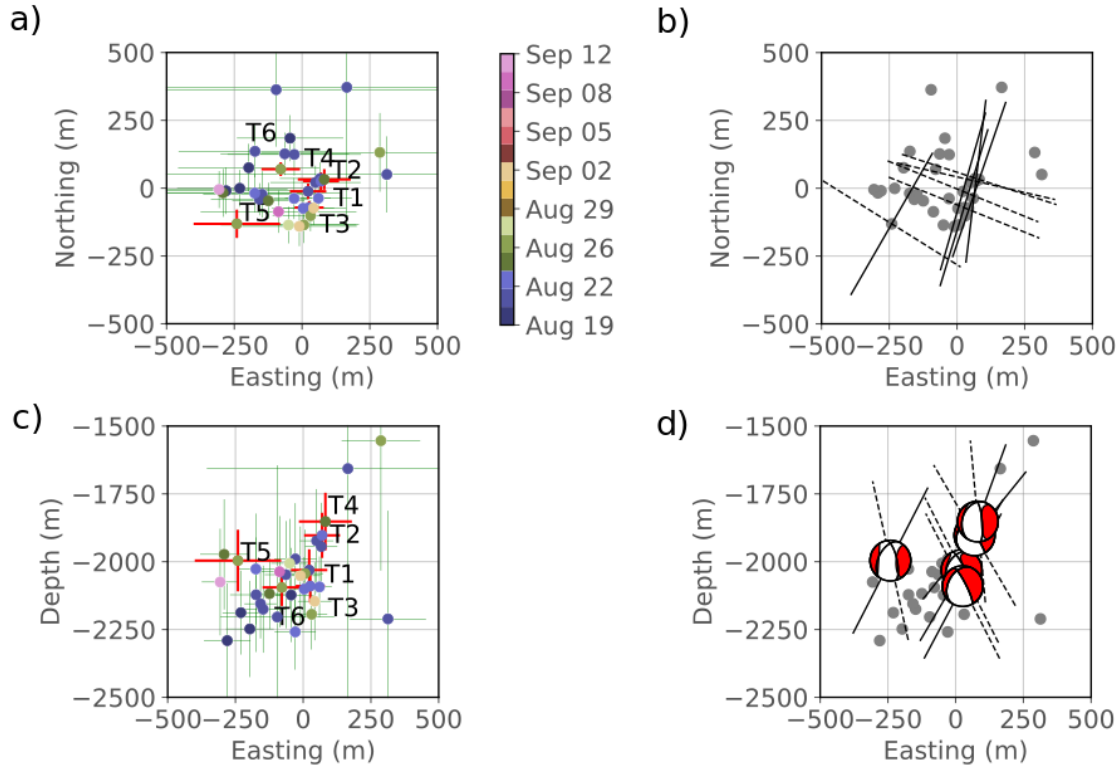


**Figure 7.10:** Inversion results including uncertainty information and waveform fit of selected stations for event T5. Black lines represent the observed displacement seismograms and red ones the synthetics solutions of the inverted source mechanism within 10% of the highest probability. Traces highlighted in gray were not used during the inversion.

### 7.5.3 Event relocation

The aim of event location undertaken herein is to support the recognition of the active and auxiliary fault plane based on the spatial distribution of events, and to distinguish between right and left lateral mechanisms. High quality phases from the analysed data are used along with the hypoDD algorithm to carry out double-difference relocation. The double-difference equations are solved using singular value decomposition. For all pairs of events recorded at each station, where each pair includes a verified event and a template event, differential travel times of P- and S-phase are calculated using cross-correlation. The hypoDD method requires a weighting factor for individual differential travel time data in order to take into account the confidence in each measurement. The cross-correlation coefficient between the template's waveform and each event is used as weighting coefficient for each differential travel time. A minimum threshold value of 0.8 (out of 1) is taken for filtering out the less accurate data. In addition, dynamic weighting is necessary to exclude outlier and large (beyond 0.7 km) inter-event separations. The initial locations of all events are assumed to be at the location of the biggest event, T5 and the Preese Hall Vp model is used (Eisner et al., 2011). Waveforms of 6 stations close to the event's epicenter, i.e., stations AQ03, AQ04, AQ05, AQ06, L001 and L009 are used initially to calculate differential travel times. Stations L001 and L009 only include waveforms of the template events. Only events with at least 6 picks are included in the relative location process. P- and S-phases data are considered with equal weights.

Out of 235 events with double difference picks, we could calculate relative locations for 26 events using the selection and weighting criteria detailed above. The locations relative to the cluster centroid are plotted in Figure 7.11. The date of occurrence of the earliest event is August 16, and for the latest is September 12. Epicentral errors in easting direction are larger than northing direction for most of the events due to the array geometry. In Figure 7.11b the strike orientation of two fault plane solutions are shown, while in Figure 7.11c, the depth cross-section of events is shown. Figure 7.11d uses beach-ball plots to represent the depth cross-section of the focal mechanisms of the 5 template events. The dip angles of the fault planes in the depth-east cross-section are shown according to each focal mechanism solution. The depth-easting pattern of the event locations can be seen to match with the calculated dipping angle of the focal mechanism solutions, clearly



**Figure 7.11:** Relative location of 34 verified events obtained using HypoDD program, a) in easting and northing plane relative to cluster centroid, c) in depth (absolute) and easting (relative) plane. T1-T6 are template events. Vertical and horizontal green lines show the location error bars. Colorbar shows the time. In (b) the dashed and solid lines show the strike orientations of the focal mechanism solutions. Focal mechanisms shown in (d) are related to the 5 template events and the dashed and solid lines show dipping angles of the nodal planes. The dashed lines are related to the NW to SE strike direction and the solid lines are related to the NE-SW direction.

differentiating the active fault plane.

#### 7.5.4 Interpretation and discussion

If we set the BGS catalog as a benchmark, it is clear that the number of common events between TM detections and the BGS events is very good for site AQ04, where 98% of events can be detected using only the single station. On the other hand, the detection rate is rather small for the stations at greater epicentral distances. For instance, applying a bandpass filter of 20-50 Hz, and using MAD 9 as the threshold value, just 12 cataloged events at station L009 are common (Table 7.2). This is due to decreasing amplitude of small magnitude events with increasing epicentral distance along with high and variable noise levels. The noise PPSD (McNamara et al., 2004) calculated for the 3 components of all recording stations (Figure 7.2) shows that station AQ04 experiences the lowest noise level in the high frequency bands, which, along with the close proximity to the event epicentres, explains the highest number of common detections at that station. Stations AQ03 and AQ05 show noise level differences in the high frequency band, with AQ03 (nearer the coast) slightly noisier than AQ05. However, the number of detections at AQ03 is larger than at AQ05, suggesting proximity to the events is more important than the observed variability in noise level. The temporary stations of LV network show higher noise level than the other stations (which are semi-permanent). This can explain lower number of valid event detections at LV sites (see Table 7.3).

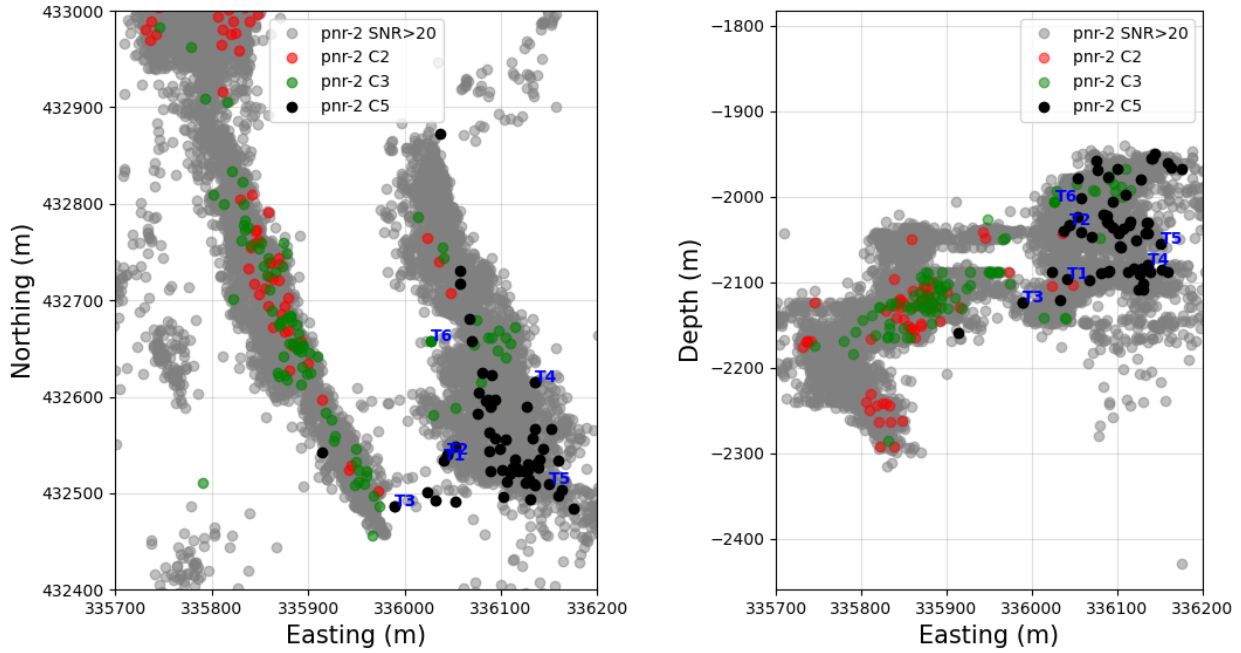
The characteristics of templates in the time and frequency domain, in particular templates T5

( $M_L 2.9$ ) and T6 ( $M_L 1$ ), explain their different temporal detection rates. T5 does not correlate with any event in the low frequency band (2-20 Hz) as its strong low frequency content (see Figure 7.4) is unique and is even different from the other template events. On the contrary, in the higher frequency range, above 20 Hz, T5 does contribute to new event detections. Although T5 and T6 show no waveform correlation to one another in 20-80 Hz band, the cumulative detection curves obtained from those templates, during the time period when the fluid injection was activated, show similar trends (Figure 7.5).

Hydraulic fracturing of the horizontal well at a depth of 2.1 km, with horizontal extension of 750 m, at this site began on August 15, 2019, and was suspended on August 23, 2019 (OGA, 2019; Cuadrilla, 2019). The template matching technique could detect events that happened prior to this fluid injection. All cumulative plots show jumps on August 8, probably related to well/flow testing, followed by almost constant cumulative numbers until August 15. We could verify some of these pre-injection detections as seismic events by re-clustering and visual inspection of their waveforms (red circles in Figure 7.6b). Confirmed events are distributed from the July 31 to September 18, over the entire processing time, suggesting the existence of background seismicity prior to, and throughout injection. However, lower detection values (assuming  $cc=1.6$  as a threshold where the maximum value is 3.) for events happening before 17 August points out that the related waveforms are not well-correlated with template events, suggesting they might be contaminated with noise and are therefore more likely to be smaller magnitude events. During fluid injection, jumps in the cumulative detection curves obtained with each template are in agreement with the injection times (see vertical gray lines in Figure 7.5). This indicates that the change in detection rate at a surface station can be of physical meaning and be linked to the process that is happening in the sub-surface, down to about 2 km in this case. After occurrence of T1, the first ‘large’ event in the sequence ( $M_L 1.6$ ), the detection rate with T6 and T5 decreases while the number of detections with the other templates increases. This behaviour indicates a significant change in characteristics of the events being detected after the initiation of larger events. The change in character and size of events may, therefore, be indicative of a change in the source of seismicity.

About 90 events occurring between August 15 and September 14 are detected at multiple stations using template matching technique (see Figure 7.8). At least two distinctive sequences of clustered events are observed (Cluster C5 and C3, see Figure 7.7), with high waveform similarity. Each of these clusters include at least one template event. Template T6 is included in the largest cluster, C3, with 115 events occurring between August 15 and September 14. Templates T1, T2, T3, and T4 fall in another sequence, C5, which includes 69 events and starts from the August 20 and lasts until the September 14. The different characteristics of T6 from the other templates might indicate that this event is related to fluid migration (as injection has ceased) and is not related to the preceding fault reactivation. The difference could also be linked to the location difference, with T1-T4 belonging to a fault different to T6 (see Figure 7.11). The T6 fault would be first reactivated followed by that related to T1-4. Comparing the locations of events in clusters C2, C3 and C4 based on the operator’s micro-seismic event catalog, we clearly see that the waveform clustering also indicates spatial clustering. Events of cluster C5 are separated from two other clusters both in map and depth view (Figure 7.12). This suggests that T6 may be activated by fracture propagation, while other templates are generated by the reactivation of an existing fault, or fracture propagation in a different direction.

From analysis of six of the largest events of 2018 stimulation, Clarke et al. (2019) obtained focal mechanisms implying either left-lateral strike-slip on a near-vertical fault striking northeast–southwest, or right-lateral strike slip on a near-vertical fault striking northwest–southeast. Based on stress analysis, they concluded that the maximum and minimum horizontal stresses are oriented in north–south and east–west directions, respectively, thus the main plane causing the events is optimally-oriented for left-lateral strike-slip motion. Based on spatial distribution of aftershocks and stress orientation analysis, Kettlety et al. (2020) concluded a right-lateral strike-slip mechanism for the  $M_L 2.9$  event from the 2019 stimulation. The fault plane solutions that we calculated for 5

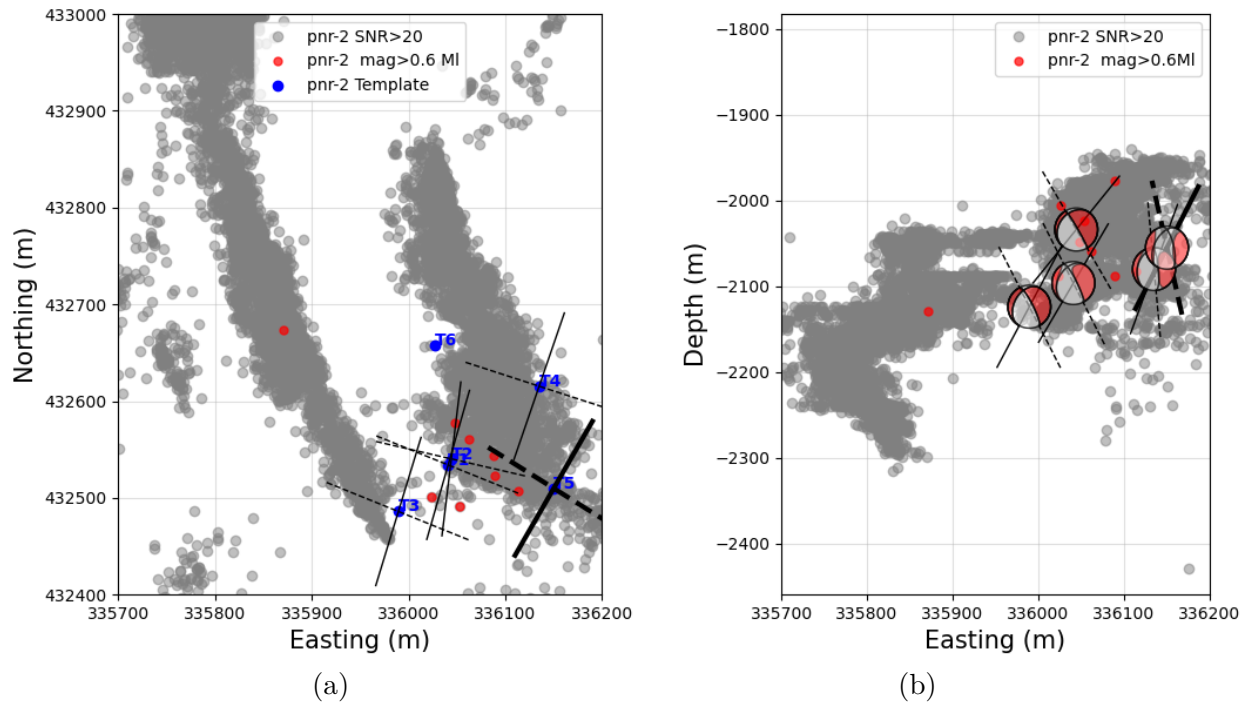


**Figure 7.12:** Location of the events in cluster C2, C3 and C5, in map view (a) and depth view (b) based on the operator catalog. For more explanation please see Figure 7.13.

template events are in agreement with both studies, implying a strike-slip mechanism. In our study, the distribution of located events including templates T1-T4 indicate a clear spatial distribution in north-east south-west direction, which is almost perpendicular to the horizontal wellbore profile (Cuadrilla, 2019). This pattern is in agreement with our fault plane solutions and might indicate the strike direction of the fault and the left-lateral movement of the activated fault. Although the locations of microseismicity using downhole stations show similar spatial pattern (see Figure 7.13), the aftershocks of the  $M_L 2.9$  event occurred on a plane whose strike direction is northwest-southeast (Kettlety et al., 2020). Templates T5 and T6 locate to the west with respect to the other templates (Figure 7.11a) and at a greater depth (Figure 7.11c). The clear pattern of decreasing event depth toward the east (see Figure 7.11c) can support the northeast-southwest strike direction, but the number of events is not sufficient to make a certain conclusion. The depth view of the obtained focal mechanisms is also plotted in Figure 7.11 (excluding T6 for which the data quality did not facilitate modelling). The dip angle (dashed line) related to the northeast-southwest strike direction shows better agreement to the pattern of located events.

Kettlety et al. (2020) reported in total 55555 microseismic events (mostly above  $M_w > -2$ ) using a dense down-hole array at about 2 km depth and an automatic event detection technique, about 400 of those events are larger than 0.0  $M_w$  and might be observed at the surface. The catalog that they published, does not include the location of large events such as T1 and T5 ( $M_L 1.6$  and  $M_L 2.9$ ). At the occurrence time of T5 (3 days after the pumping was terminated) the downhole array were not operating. From 1590 detections with TM (since August 13), 815 events could be confirmed by comparing with operator catalog (about 50 %). Surprisingly, their magnitude ranges between  $M_L -2.3$  to  $M_L 1.145$ . The magnitude estimated for T6 is lower ( $M_L 0.7$ ) in the operator catalog compared to the BGS catalog. Figure 7.13 shows the location of some of the events according to the operator catalog. In both Figure 7.13a (map view) and Figure 7.13b (cross-section), the location of events with high SNR (above 20) are shown, highlighting those with magnitude above  $M_L 0.6$  along with the template events. For template T5, the location is according to Kettlety et al. (2020) which is estimated from the surface arrays and verified based on the spatial distribution of its aftershock.

The nodal lines, calculated for each template event are shown in Figure 7.13. In this figure while



**Figure 7.13:** Location of some of the selected events from the operator catalog (pnr-2) (a) map view and (b) cross-section view in easting direction. The northing and easting units are Ordnance Survey United Kingdom grid system. The gray circles show the location of events with high SNR (above 20), and the red circles show the events with magnitude above  $M_L 0.5$ . The location of the templates T2, T3 and T4 are marked with blue circles. Focal mechanisms shown in (b) are related to the 4 template events and the dashed and solid lines show the strikes (in a) and the dipping angles of the nodal planes (in b), while the thicker lines are related to the T5.



the operator catalog events indicate a general northwest-southeast direction, the alignment of T2, T4 and T3 in a northeast-southwest direction can be verified in agreement with relative location we obtained with hypoDD (Figure 7.11). However, the location of T5 is shifted to the east compared to that shown in Figure 7.11. In the cross-section view (Figure 7.13b) the pattern of larger events is more in favour of west-dipping nodal planes, indicating the left-lateral mechanism. The predominantly negative CLVD of up to -21% for the largest event T5 and -17% for the second largest event T4, might suggest a closing or collapsing mechanism due to changes in fluid pressure or an additional non-strike-slip event, presumably a normal faulting minor couple, with similar strike and dip angle.

### 7.5.5 Conclusion

In this study our aim was to examine the induced microseismicity related to the August 2019 hydrofracking that took place near Blackpool, UK. We used data recorded at a sparse network of surface stations; the closest station to the fracking zone, AQ04, was located at a distance of only 1.3 km away. Scanning the continuous waveform data recorded at station AQ04 using the template matching technique with 6 template events (magnitude above  $M_L 1.0$ ), more than 2200 detections were made within a 7-week time period. This included and preceded the time that fluid injection was actively performed. By using waveform based clustering technique and visual inspection, at least 20% of all detections are confirmed as earthquake events. It does not mean that the remaining detections are not valid earthquake records. Although the number of verified events is 3 times larger than the number of events reported by BGS for the same time span, it is much lower than the total number of events detected and located by the operator's microseismic down-hole network. Numerous small events prior to the main stimulation are detected by the TM technique, which indicates the background seismicity related to the existing faults and the pre-stimulation well/flow testing.

According to the waveform similarity of T1, T2, T3 and T4, their aligned location and the similarity of their focal mechanism we can conclude these events are related to the same fault with northeast-southwest striking direction between  $7^\circ$  to  $18^\circ$  and dipping angle between  $60^\circ$  to  $85^\circ$ . T5 and T6 locate further away from the other template events according to the relative location we obtained using hypoDD and the operator's microseismic catalog. While the relative location of T6 to the other aligned templates T1-T4 are in agreement in both cases, T5 locates towards the west based on relative locations and to the east side based on Kettlety et al. (2020).

Using relative magnitude estimation technique (Schaff et al., 2014), we concluded that the average magnitude of the clustered events is  $M_L - 0.5$  to  $M_L 0.5$ . This indicates that the rest of the detected events which are not clustered based on the applied waveform similarity threshold, might be smaller magnitude events whose high amplitude background noise influenced their waveform similarity and visibility. Weeks after the fracking was terminated, microseismic events continued to occur, and waveforms of later events show similarity to both clusters of templates (cluster C5 and C3).

Our newly derived moment tensor solutions for the largest events in the 2019 sequence are in good agreement with mechanisms derived during previous sequences in 2011 and 2018 (Clarke et al., 2019). They are also consistent with the analysis of the 2019 sequence using the dense surface and downhole stations (Kettlety et al., 2020). In our study, with the occurrence of several events exceeding a local magnitude of 1.0, we were able to perform a robust full waveform moment tensor inversion considering source uncertainties and including additional non-double-couple components. All derived mechanisms show similarities in their major double-couple part, which is also supported by the grouping of the TM results. The predominantly negative CLVD of up to 21% for the largest events leads us to suggest a collapsing or even a potential minor normal faulting mechanism additional to the major strike-slip movement, which might be related to the pressure release that took place after the termination of the experiment and before the occurrence of events T4 and T5.

A northeast-southwest pattern that appears on double-difference relative location of 34 events is in

agreement with the strike of the north-east trending focal plane and might imply the left-lateral orientation of the strike-slip fault system. The displayed pattern in the cross-section plot shows a westward increase in depth of the re-localized events. This trend is in good agreement with the dipping angles (black dotted lines) of the derived focal mechanism for the template events. Template T5 (the largest event), which shows limited correlation to the remaining events and does not fit in any TM clustering group, is located noticeably outside the main seismic cluster, and potentially activates a much larger source than previous events.

Comparing the moment magnitude calculated for 5 template events with local magnitude estimated by BGS shows that local magnitude is greater than the moment magnitude for all processed events (see Table 7.1). For smaller events ( $M_L < 2.1$ ) the deviation is 0.1 and for the largest  $M_L 2.1$  and  $M_L 2.9$  events the values of deviation are 0.2 and 0.3, respectively. The moment magnitude for the largest event is consistent with the  $M_w$  used in the risk analysis by Edwards et al. (2021). Excluding T2, for all other cases the magnitudes reported in operator catalog (5th column in Table 7.1) is lower than the BGS magnitudes. The value of deviation between local magnitude in BGS and operator catalog for T4 ( $M_L 2.1$ ) and T1 ( $M_L 1.6$ ) indicates that the employed method by the operator underestimate the magnitude for larger events.

We conclude that the repeating nature and waveform similarity of fracking related induced seismicity is perfectly suited for the application of match filter technique to detect multiple events by just using a single surface station. In addition, changes in detection rate at the single station at the surface can give insights about the ongoing process at the subsurface giving rise to microseismicity. Thus, in the case of occurrence of natural swarms or increasing microseismicity with unknown reasons, such techniques can be of great value in absence of a well-distributed array of stations.





## Chapter 8

# Unfolding a horse tail structure: Analysis of the 2020 $M_w$ 6.5 Monte Christo Range, Nevada earthquake sequence

This chapter features my collaborative work on the 2020  $M_w$ 6.5 Monte Christo Range, Nevada earthquake sequence. Its content was planned for rapid publication but was never finalized due personal situations of my co-authors. I was set as second author with Dr. Lidong Bie leading the project. The following text summarizes my work on moment tensor inversion and includes some geodetic findings by Dr. Lidong Bie to support them.

### 8.1 Abstract

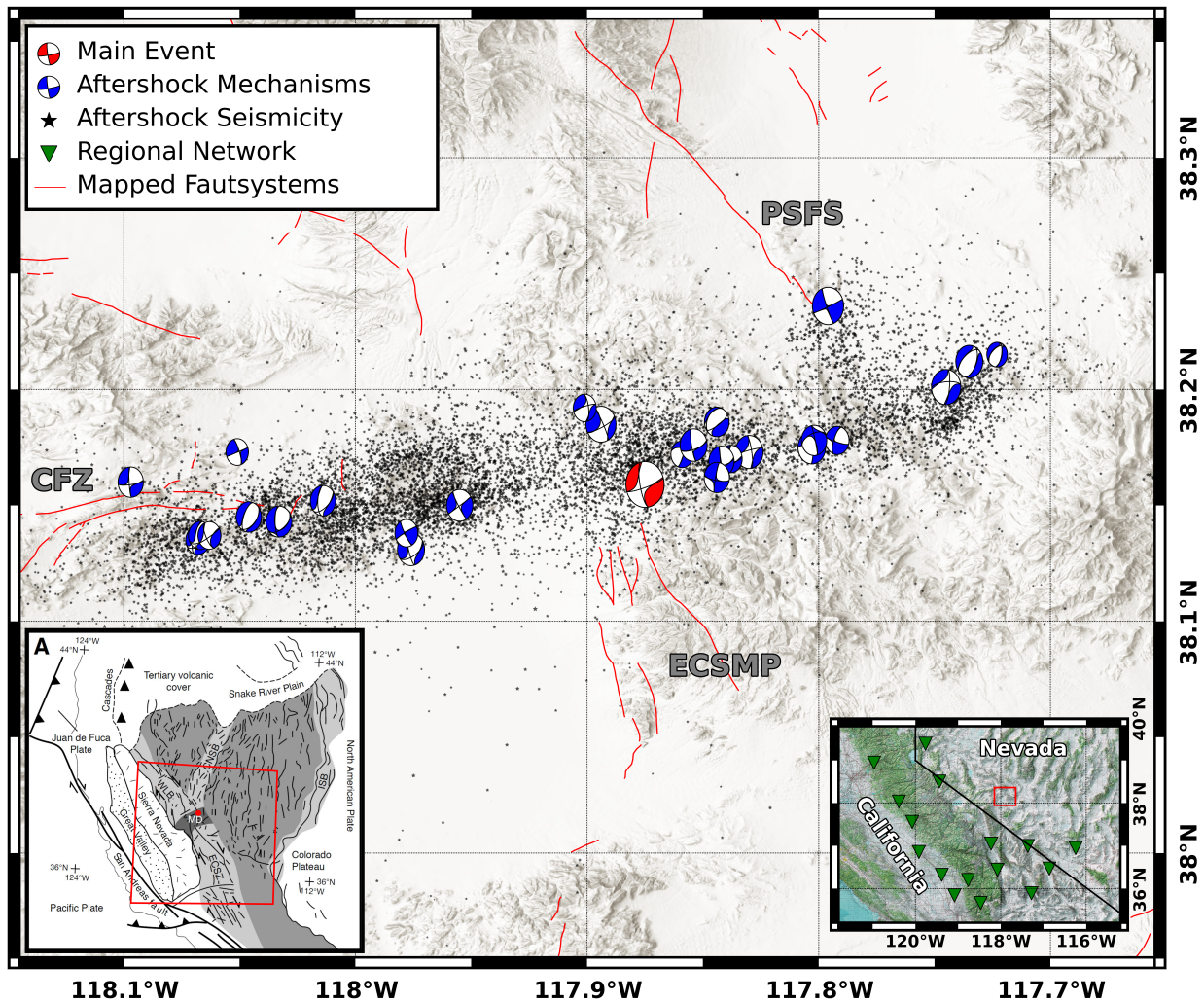
On 15 May 2020, the  $M_w$ 6.5 Monte Christo Range earthquake struck southwest Nevada, an area hosting complex faulting styles that accommodate partly the motion between the North American plate and the Pacific Plate. Here, we present a regional seismic and geodetic analysis of the kinematic rupture sequence. InSAR observations indicate the rupture of at least two faults – with normal faulting in the West and strike-slip faulting in the East. A joint inversion of InSAR ground displacements and seismic data suggest  $\sim 5$  seconds between the centroid moment release of the two ruptures with the normal fault rupturing first. The energy release of the normal fault rupture is smaller compared to the strike-slip faulting. Independent probabilistic moment tensor inversions using regional waveforms show consistent source parameters and the centroid gap between the two subevents at different frequency ranges show a higher frequency content for the normal fault compared to the lower frequency content of the strike-slip fault. This may hint at a fast rupture or the breaking of multiple small asperities for the normal fault rupture. At the eastern end of the deformation area, the aftershock distribution suggests abundant orthogonal faulting that is perpendicular to the main coseismic rupture. In summary, the  $M_w$ 6.5 Nevada earthquake shows a complex rupture of a horsetail structure.

### 8.2 Introduction

On 15 May 2020, a  $M_w$ 6.5 earthquake struck near the Nevada-California border in the US. The earthquake moment tensor reported by USGS shows strike-slip faulting with a 68% double-couple component. Following this event, abundant aftershocks are reported, aligning roughly in the ENE-WSW direction for  $\sim 35$  km. Focal mechanisms reported by USGS for aftershocks show a

mixture of normal faulting and strike-slip faulting rupture. The available seismological observations suggest a complex rupture that may involve multiple asperity failures during the mainshock.

The 2020 Nevada earthquake sequence is located in the eastern part of the Mina deflection (Figure 8.1), a stepover within the eastern California shear zone (ECSZ) - Walk Lane Belt (WLB). The ENE-WLB is a seismically-active tectonic unit to the east of the San Andreas fault system and accommodates a quarter of the motion between the North American Plate and Pacific Plate (e.g., Dixon et al., 1995; Dixon et al., 2000; Bennett et al., 2003) mainly along NNW-to-NW striking dextral faults. The faulting style in the Mina deflection stepover, as summarised by DeLano et al. (2019), may be explained by kinematic models of (1) sinistral faulting and clockwise rotation proposed by Wesnousky (2005), (2) normal faulting dominated releasing stepover (Oldow et al., 1994) and (3) both sinistral and normal faults within the transtensional stepover (Oldow, 2003).



**Figure 8.1:** Seismic data and geological setting. Displayed beachballs and aftershock seismicity are taken from the USGS database. The mapped fault systems are downloaded from <https://www.usgs.gov/programs/earthquake-hazards/faults>. Stations of the regional seismic network are listed in Table 8.2. The geological subfigure is a modified version of Nagorsen-Rinke et al. (2013).

The available information regarding this event offers interesting aspects worth further investigation. For example, as shown by the ENE-striking aftershock alignment, the slip direction of the 2020 event differs from the dextral shear motion in this area. The non-double-couple component of the USGS moment tensor further raises questions about the fault structure and rupture process during this event, such as whether the sub-events share similar rupturing style or they are on separate fault structures, but ruptured near simultaneously. The occurrence of the 2020 sequence may also

help further distinguish the kinematic models responsible for the deformation within the Mina deflection.

In this study, we present geodetic and regional observations for the 2020 Nevada sequences and conduct independent experiments of multiple moment tensor inversion, and joint geodetic and seismic inversion for understanding the kinematic rupture process. Our results indicate that the 2020 earthquake involves sinistral- and normal faulting on at least two main faults. The two main sub-events started first with normal faulting in the west on a short, south-dipping normal fault, and later sinistral fault rupture in the east on a long, steeply-dipping fault.

## 8.3 Data

### 8.3.1 Geodetic data

We collect six C-band radar images from European Space Agency’s Sentinel-1a and 1b satellites to form three interferograms – two in descending track and one in ascending track (Table 8.1 and Figure D.1). We use three arc-second Shuttle Radar Topography Mission (SRTM) digital elevation models for topographic phase removal and geocoding. The short spatial- and temporal baseline allows good coherence over the epicentral region.

**Table 8.1:** SAR images for construction of coseismic interferograms.

Flight direction	Track ID	Reference SAR image	Second SAR image	Perpendicular baseline in m
Ascending	64	2020-05-11	2020-05-17	20
Descending	144	2020-05-04	2020-05-16	-60
Descending	71	2020-05-11	2020-05-17	19

### 8.3.2 Seismic data

We collected data from regional seismographs up to 300 km from the 2020 Nevada earthquake. Within the circular range, nine seismic networks are available (BK, CI, IM, US, NN, CE, NC, NP, WR), including strong motion and broadband stations. We manually select traces based on the signal quality and filter the waveforms with frequency bandpass as needed at various steps of inversion as described in the methodology section. We exclude waveforms that are clipped due to proximity to the earthquake, and that are from short-period stations. This leads to a database of seismic waveforms from 12 strong motion and four broadband stations for probabilistic moment tensor inversion (see Table 8.2).

**Table 8.2:** Regional seismic network.

Station	Network	Latitude	Longitude
CMB	BK	38.0350	-120.3870
CWC	CI	36.4390	-118.0800
FUR	CI	36.4670	-116.8630
GRA	CI	36.9960	-117.3660
ISA	CI	35.6630	-118.4740
SLA	CI	35.8910	-117.2830
TIN	CI	37.0540	-118.2300
VES	CI	35.8410	-119.0850
VOG	CI	36.3210	-119.3820
TPNV	US	36.9490	-116.2490
REDF	NN	39.3900	-119.7650
WAK	NN	38.5040	-119.4380
SPG2	CI	36.2010	-118.7660
AFD	NC	38.9460	-120.9690
MBUB	NC	37.5590	-120.0760
MGS	NC	36.8580	-119.9200

## 8.4 Source inversion

### 8.4.1 Geodetic inversion

We use the simultaneous multiple fault source inversion method by Frietsch et al. (2019) to simulate a two-fault model. Being only preliminary results, I will not further discuss or excessively interpret them. Initial results of the two-fault model are displayed in Figure D.2 and Table D.1. The inferred fault top model is displayed in Figure 8.2 to highlight our results.

### 8.4.2 Probabilistic moment tensor

In this study, we perform the nonlinear moment tensor inversion in five steps. First, we invert the full deviatoric moment tensor for this event, and compare it with that reported by various earthquake monitoring agencies. Second, we test how the pure double-double (DC) mechanism depends on the frequency bands. In this step, we fix the event location as reported by Nevada Seismological Lab (NSL), and search for strike, dip, and rake in each inversion with different frequency bands. The first two steps allow us to confirm the complexity of this event based on the inversion of the selected regional seismic waveforms. Next in the third step, we search for the moment ratio relative to  $M_w6.5$  and the time difference between sub-events relative to the origin time using 2D grid searching. In the fourth step, we allow changes in the centroid position by fixing other source parameters. The search range for the centroid positions is informed by the InSAR observations and inversion results. Finally, we derive the source time function in the frequency range 0.02-0.1 Hz. We iteratively run the last three steps until optimal solutions are retrieved.

Our first inversion for a single source solution shows consistency in the negative CLVD component with that reported by the U.S. Geological Survey (USGS), SCADEC, and NSL. It suggests either the complex velocity model or earthquake rupture that might involve multiple fault segments. Indeed, at low-frequency bands ( $fb = 0.02\text{-}0.04/0.05$  Hz), the DC solutions (probability > 0.8) show left-lateral strike-slip faulting (average rake of  $10^\circ$ ) on an EW-striking (average strike of  $80^\circ$ ), steeply dipping fault (an average dip of  $74^\circ$ ). Increasing the lower bandpass corner frequency to 0.03 Hz and setting the high corner up to 0.07 Hz, we find normal faulting solutions at a significant probability in addition to the most probable strike-slip mechanism. For the normal faulting component, the average strike, dip, and rake are  $50^\circ$ ,  $30^\circ$ , and  $-65^\circ$ , respectively. Our

initial investigations indicate that the 2020 event involves rupture on multiple fault segments with various focal mechanisms, and consists of a low-frequency strike-slip faulting component and a relatively higher frequency normal faulting component.

To obtain the ratio of moment release of two sub-events, we run grid searching with a sampling rate of 0.025 in the range from zero to one, where zero represents 100% normal faulting, and one for 100% strike-slip faulting. Similarly, for the inter-event time (tshift), we set a sampling rate of 0.5 seconds within the range of -10 seconds to 10 seconds. Here, a negative tshift indicates that the normal fault ruptures before the strike-slip fault. We find that the normal fault ruptured first, and  $\sim 5$  seconds later a larger moment release occurred on the strike-slip fault. By further searching the centroid position in the range suggested by InSAR and aftershock distribution, we obtain optimal centroid positions for the two sub-events that are consistent with distributed slip models (Figure D.2). In our inversion, the centroid position for the main- and later-strike-slip rupture is at  $\sim 6$  km depth, and for the normal fault rupture, it is  $\sim 5$  km depth with a standard deviation of 1.5 km. Overall, the solution of the strike-slip major couple is highly robust to variation in the parameters of the minor couple and its own. For the normal fault sub-event, uncertainties related to the moment tensor parameters are relatively higher than that of the major strike-slip sub-event, especially for the source depth and half-duration of the source time function. This is likely because the major energy release for this earthquake was on the strike-slip fault, which obscures the signal related solely to the early normal fault rupture.

### 8.4.3 Stress inversion

We perform stress inversions with the STRESSINVERSE package (Vavryčuk, 2014) using the known aftershock source mechanisms. STRESSINVERSE takes as input the source geometry (strike/dip/rake) of a group of events and returns the principal stress directions with  $\sigma_1 > \sigma_2 > \sigma_3$  and the scalar quantity  $R$  ( $0 \leq R \leq 1$ ) describing the magnitude of  $\sigma_2$  relative to the others (Gephart et al., 1984):

$$R = \frac{\sigma_1 - \sigma_2}{\sigma_1 - \sigma_3}. \quad (8.1)$$

We assume for each inversion run a mean deviation of  $10^\circ$  from the given fault angles in a realization of 250 normally distributed variations.

We found a prominent shear stress regime with the minimal stress  $\sigma_3(\text{az}, \text{pl}) = (125, 1)$  trending parallel and the maximum stress  $\sigma_1(\text{az}, \text{pl}) = (35, 1)$  perpendicular to the ECSZ/WLB. The intermediate stress is  $\sigma_2(\text{az}, \text{pl}) = (246, 89)$  with a scalar quantity of  $R = 0.21$ .

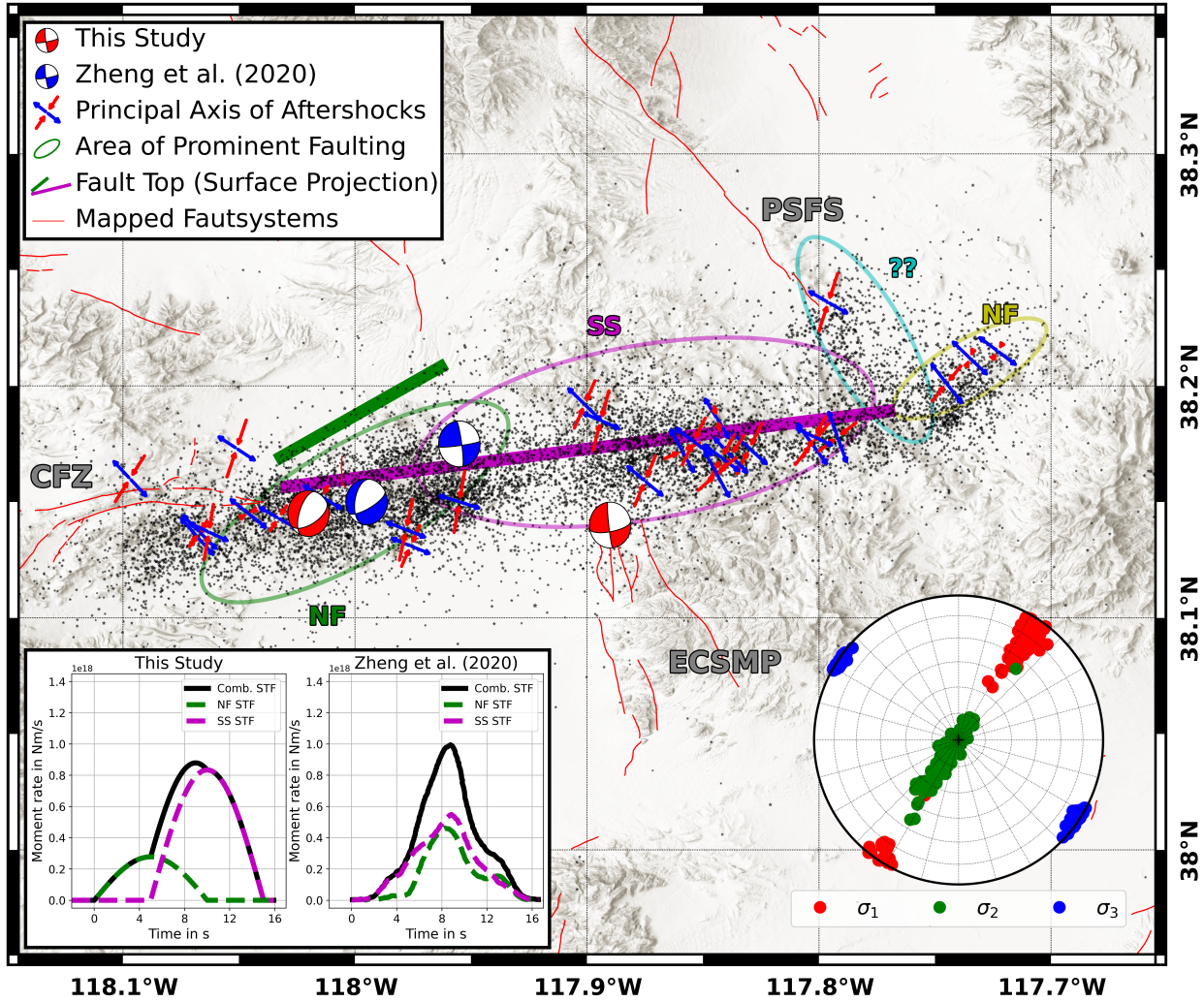
## 8.5 Comparison with other studies

The earliest publication about the earthquake sequence was by Zheng et al. (2020) who also recognized the occurrence of at least two distinct active fault segments. Similar to our study, they employed the regional permanent network, but only focused on the south, and further included teleseismic recordings in NNE, NNW, and SSE. The teleseismic data largely increased the azimuthal coverage compared to our RMT setting, however, introduced a difference in their single fault CLVD part with only 5% compared to the 68% by USGS. The authors relate these differences to the noise amplitude in the w-phase inversion of the teleseismic data. With our restriction to only regional stations, we were able to recreate the USGS single-fault solution, however, missed out on the azimuthal coverage offered by the teleseismic stations. Their findings also indicated a sinistral strike-slip motion on the eastern segment and an oblique normal fault in the western part, separated by the hypocenter. Likewise, they used the same InSAR data (see Table 8.1) as we did to and performed a joint inversion together with the seismic data. Their results agree (see Table 8.3, <sup>1</sup>)

<sup>1</sup>Zheng et al. (2020) specified 0.5 Hz as the upper-frequency corner. This value is suspicious, and I assume it might be a simple typo with 0.05 Hz as the true value.



with ours and show only a difference in the dipping angles of both sub-events, which are slightly steeper than ours.



**Figure 8.2:** Map view of the mainshock rupture history. The two-fault models (strike-slip and normal fault) are color-coded according to their publications. Areas of prominent faulting are chosen by hand from the known aftershock mechanisms. The fault tops are taken from our initial InSAR modeling. The source-time function of Zheng et al. (2020) was re-drawn in Python by hand from the online publication. Inversion for the overall stress regime is done with *STRESSINVERSE* package (Vavryčuk, 2014).

Like our study, Zheng et al. (2020) used only data from the permanent stations of the unfavorable network arrangement at the time of the main sequence. Valuable data for subsequent publication got acquired by a rapid deployment of eight temporary local seismic stations in the aftermath of the mainshock by Bormann et al. (2021), to monitor the aftershock decay. The acquired data enabled several independent studies (e.g., Lomax, 2020; Dee et al., 2021; Ruhl et al., 2021; Chorsi et al., 2022; Sethanant et al., 2023) to recognize the full complexity in the fault geometry of the earthquake sequence.

These studies focused on the aftershock localization and thereupon achieved identification of active fault planes. The rapid deployment ensured the qualitative recording of up to 16,714 locatable earthquakes within 3.5 months with a magnitude of completeness of  $M1.5$ . Ruhl et al. (2021) noted that the fault length of the mainshock inferred by the aftershocks is up to 2 times longer than expected for an  $M_w6.5$  earthquake. Using the high-quality locations, Ruhl et al. (2021) identified two prominent intersecting structures in the east and west relative to the latitude ( $\sim 117.9^\circ\text{W}$ )

**Table 8.3:** Comparison with Zheng et al. (2020), Cui et al. (2021) and Sethanant et al. (2023).  $T_0$  relates to the origin time and  $dt$  to the inter-event time. FB is the frequency band used for the doublet modeling. Values marked with  $^\dagger$  are not mentioned in the respective paper or supplementary material. I identified these by hand from the displayed figures. Zheng et al. (2020) further used two different frequency bands for the regional and the teleseismic data. Sethanant et al. (2023) and Cui et al. (2021) used only geodetic methods.

	This Study		Zheng et al. (2020)	
Param.	East	West	East	West
Strike	$80 \pm 0$	$60 \pm 0$	83	62
Dip	$64 \pm 8$	$47 \pm 8$	83	63
Rake	$-7 \pm 10$	$-60 \pm 10$	$10^\dagger$	$-60^\dagger$
$t_{\text{half}}$	$5.0 \pm 0.5$	$5.5 \pm 1.0$	$7^\dagger$	$5^\dagger$
$M_0$	$5.3 \pm 0.13 \cdot 10^{18}$	$1.3 \pm 0.004 \cdot 10^{18}$	$3.57 \cdot 10^{18\dagger}$	$2.74 \cdot 10^{18\dagger}$
Lat	$38.139 \pm 0.02$	$38.137 \pm 0.03$	$38.175^\dagger$	$38.150^\dagger$
Lon	$-117.885 \pm 0.04$	$-118.045 \pm 0.06$	$-117.955^\dagger$	$-117.995^\dagger$
Z in m	$6000 \pm 500$	$5000 \pm 1500$	$6000^\dagger$	4000
$M_w$	6.5		6.5	
$dt$ in s	$5 \pm 0.5$ (SS after NF)		1 (NF after SS)	
$T_0$ in UTC	2020-05-15T11:03:32.457 $\pm$ 0.91		—	
FB in Hz	0.02-0.1 Hz		0.01-0.1/0.5 Hz	

of the hypocenter location. They showed that the seismicity lineaments indicate a mixture of left-lateral, right-lateral, and normal faulting structures on at least four known fault zones.

The western part displayed a near-vertical (dip  $\sim 70^\circ$ ) fault structure at depth striking at  $70^\circ$  and a shallow negative-flower-structure-like network of en echelon dipping normal and obliquely-slipping faults with an average dip of  $\sim 60^\circ$  and strike of  $\sim 60^\circ$ . The lack of aftershock seismicity above 3 km depth further hints at an area of high slip.

The eastern part displays a much more complex fault setting of multiple steeply dipping oblique structures at depths between 3 and 10 km with an overall left-lateral shear movement. The NW-trend of the seismicity at the eastern end of the aftershock zone is peculiar. Ruhl et al. (2021) suggested a fault-fracture mesh rather than a well-defined, through-going northwest-trending right-lateral fault. While we also recognized this fault structure, we did not conclude the modeling.

Furthermore, Ruhl et al. (2021) found, that the sequence started with a smaller initial earthquake and was followed by a larger earthquake with a 2-3 seconds delay. This fits well with our results but also highlights the uncertainty in the rupture timing.

## 8.6 Conclusion

The 2020  $M_w$ 6.5 Monte Christo Range earthquake sequence was a complex intermediate-sized seismic event in the western USA. Well-mapped fault systems, quick response in setting up a temporal seismic network, and the generally easy access to the source region offer a large qualitative database of different products. These are further extended by seismo-geodetic measurements. The large public interest initiated several detailed studies of its source process. Our quick response study, initiated shortly after the occurrence of the sequence, gave us valuable insights into its complex rupture history. Our results hereby do not fully represent the complexities of the rupture sequence. Early aftershock locations were imprecise and the joint seismo-geodetic inversion was still in its first iteration before the termination of this project. Nevertheless, my moment tensor modeling compares well with an early publication by Zheng et al. (2020) and is supported by later more detailed studies. Variations in the frequency band used in the RMT inversion revealed the different faulting styles and gave a first hint on the size and complexity of the activated structures.



We were able to identify and localize the prominent rupture mechanisms – left-lateral strike-slip in the east and oblique normal faulting in the west. The state of stress inferred by the known aftershock mechanisms in the Mina deflection is in agreement with the NNW to SSE trending ECSZ and WLB (e.g., Nagorsen-Rinke et al., 2013).

Our study highlights that the occurrence of an increased CLVD part in the single-source solution may suggest a much more complex rupture history. To fully understand the complete source process we need a dense local network and highly precise hypocenter locations, especially of the aftershocks. Furthermore, geodetic measurements and on-site observations contribute valuable information to identify the major faulting styles and the fault orientations. These information supports RMT modeling by offering constraints on selected parameters (e.g., strike, dip, or the volume of the hypocenter) during the inversion.

## Part IV

# Conclusion and outlook



## Chapter 9

# Conclusion and outlook

In my thesis, I developed a new robust regional moment tensor inversion in complex settings. This has been achieved by a Bayesian formulation of prominent error sources. I created the “AmΦB - uniXtree” Python package, which uses a uniform X-dimensional tree-sampling algorithm to solve the Bayesian error formulation. The versatility and adaptability of my inversion code allowed me to explore diverse sources of errors and test different approaches to mitigate their effects on the source solution.

The application of my new method is focused on the Lesser Antilles Arc subduction zone, where I used ocean bottom seismometer (OBS) recordings that were acquired between 2016 and 2017 as part of the multidisciplinary VoiLA project. Uncertainties associated with OBS data are imprecise sensor alignments and strong noise on the horizontal seismometer components (high horizontal noise). Furthermore, the insufficiently known velocity structure of the arc, especially the seafloor and oceanic lithosphere, introduces large travel time residua between observed and modeled data. These sources of errors are described in a prior co-variance matrix for data (noise) and model (alignments) errors, and using cross-correlation time updates. AmΦB yields robust solutions that are in agreement with a teleseismically-derived reference event set. I compiled 151 MT solutions, including 39 new ones from this study for the Lesser Antilles arc, and found 25% normal faulting (NF), 25% thrust faulting (TF), 10% strike-slip faulting (SS) with the remainder being a mixture of mainly NF to SS transitional mechanisms. This unprecedented database allowed me to examine small-scale structures in detail and perform stress inversion for different parts of the subduction zone. Most notable is a trench parallel extensional stress regime in the deep slab, which is unusual for similar subduction zones.

My new findings motivated a case study at the end of the Wadati-Benioff Zone, in which the  $M_w 7.4$  Martinique earthquake struck the central islands in 2007. A global comparison of events in similar depths revealed its uniqueness of the reported source mechanism. I showed, that this earthquake is a doublet on the ancient Proto-Caribbean spreading ridge, which got re-activated under the current stress regime.

Further applications outside the Lesser Antilles include a case study for hydraulic fracturing-induced earthquakes at Blackpool in England and a rapid analysis of the 2020  $M_w 6.4$  Monte Christo Range earthquake sequence in Nevada.

The quality of the seismic recordings at Blackpool exceeded the ones in the Lesser Antilles and the local seismic network was carefully deployed by trained personnel. However, the small magnitudes, the coarse velocity model for the UK, and the initial low-quality hypocenter locations complicated the inversion process. This allowed me to test the performance of my code in a high-frequency band (1 to 3 Hz) with limited information about the Earth’s shallow structure. I modeled five events between  $M_w 0.9$  and  $M_w 2.6$ . The mechanisms shed light on a fluid-induced activation of a pre-existing fault structure.

While land stations are usually affected by strong noise at frequencies larger than 1 Hz, strong earthquakes like the Nevada events excited frequencies well below it. The seismic noise conditions in this range are low, the seismometers are orientated with high precision to the north direction, and the local velocity structure is relatively well known. Source modeling was hence stable without a Bayesian formulation and I could focus on examining the complexities of the source mechanism. My results depict a sequence of normal faulting and a strike-slip mechanism which are further supported by the InSAR finding and the qualitative USGS moment tensor database of the aftershock events.

## 9.1 Conclusion

Using my new moment tensor inversion routine `AmΦB – uniXtree`, I worked on different earthquake source to explored the key questions formulated in Chapter 1. My findings are as followed:

### 1. Can three-component OBS data be successfully used for full-waveform moment tensor inversion?

Studies at coastal regions (e.g., subduction zones, island arcs) offer only a limited space for installments of seismometers on land. OBS stations are a valuable extension of the seismic network and crucial for coastal or full off-shore studies. I identified three prominent error sources: (1) high horizontal noise, (2) sensor alignment uncertainties, and (3) imprecise travel times. Using a restricted cross-correlation time update, I was able to mitigate issue (3). For my applications in the Lesser Antilles, I could depend on well-localized hypocenters and a local 1D velocity model tuned for the network which already strongly mitigated potential timing issues.

Noise and alignments mainly affect the horizontal components. For most cases ( $M_w < 4.8$  of the VoiLA database), the noise amplitude vastly exceed the signal amplitude which resulted in the removal of the affected traces after a quality check. I conducted a synthetic test (Section 5.5.3) to examine the influence of using three components with noisy horizontals versus using only the vertical components. My Bayesian error formulation significantly decreased the noise-induced uncertainties in the source solution (i.e., CLVD and Kagan angle) compared to the true solutions. However, I could not identify significant differences in the Kagan angle using three components or only the vertical component. This experiment showed that, with large horizontal noise, a pure double-couple inversion is to be preferred as non-double-couple contributions are not resolvable.

Inversion using data from all three components depends on the magnitude and source-receiver geometry. A  $M_w 5.9$  event, the strongest local earthquake recorded on the OBS, caused a clipping of nearly all horizontal traces due to its shallow location and restricted me to using only vertical recordings. Only event `ev123` (Table 5.1), with  $M_w 5.6$  in the central parts at a depth of  $\sim 146$  km, displayed a very good signal-to-noise ratio on all three components. I was able to reduce the uncertainties in the CLVD and Kagan angle using the Bayesian formulation compared to a simple L2 error. My results listed in Table 5.1 are in good agreement with reference events of external studies.

In conclusion, it is possible to use three-component OBS data in regional full waveform moment tensor inversion if we can qualitatively describe the prominent error sources in, e.g., an prior co-variance matrix.

### 2. What can we learn about the seismotectonic setting of the Lesser Antilles?

I used 34 OBS stations to invert for 45 local earthquakes (Chapter 5) and employed the regional land station network to model a source doublet in the intermediate-depth range (Chapter 6). I separated the tectonic setting (compare Figure 5.12) into the slab-upper-plate interface ( $z \sim 30 - 70$  km), the crust ( $z < 30$  km), and the slab ( $z > 70$  km) and distinguished between a northern and southern region within the northern half of the arc ( $14.3^\circ\text{N}$  to  $18.5^\circ\text{N}$ ).

The interface region is dominated by thrust faulting, with a notable gap in seismic activity between  $\sim 15^\circ\text{N}$  and  $\sim 16.5^\circ\text{N}$ . North of this gap is a large seismogenic zone that inhibits the inferred rupture area of the 1843  $M8.5$  megathrust event, which can be assumed to be close to the upper potential of this section if not even the whole arc. Stress inversion of all events within this zone shows the typical down-dip compression in the subduction direction. The southern region is marked by a local activity of thrust faulting within the inferred rupture area of the 1839  $M7.5$  megathrust event. Just north of it proceeds the inferred profile of the Mercurius Fracture zone, indicating a possible structural connection to it. The  $M_w5.8$  VoiLA event ev143 is part of this cluster and highlights the seismic potential for large thrust events in this region. Most curious is the gap of large thrust events, which might relate to the retreating slab in the central arc.

This is also supported by my findings in the forearc region of the Caribbean crust. Seismic source activity shows a strong variability along the arc. The north is characterized by a strike-slip to normal faulting transitional regime while the stress condition further south is dominantly an arc parallel extensional regime probably due to along-arc stretching of the forearc to accommodate the tight arc curvature. Analysis of the  $M_w4.8$  VoiLA event ev152 in the north (Table 5.1) inferred a local interaction of the aseismic Barracuda Ridge on the oceanic plate with the Caribbean crust. Noticeable is also a chain of eastwards dipping arc-parallel normal faults between Guadeloupe and the slab top, which could depict a pathway to the 2004  $M_w6.4$  Guadeloupe event for volatiles.

Activity on the slab is concentrated at the center of the arc within the intermediate-depth zone offshore the island of Martinique. Stress inversion for this cluster reflects down-dip compression and slab-parallel extension. Down-dip compression may reflect the dynamics of this relatively small subduction zone, which has led to the piling of slab material within the upper mantle below the Lesser Antilles. The along-strike extensional stress regime is unusual and may be due to lateral buoyancy variations, where pull at the southern end of the slab may be reduced by partial slab detachment along a lateral slab tear below Grenada, causing slab deformation that localizes along pre-existing structures around the extinct Proto-Caribbean ridge subducted below Martinique.

I used the 2007  $M_w7.4$  Martinique event, the strongest ever to be instrumentally recorded earthquake in the region, to shed light onto the local tectonic structure at depth. My findings indicate that the Martinique event is likely a doublet and connected to a re-activation of pre-existing weakening structures associated with the ancient Proto-Caribbean spreading ridge.

### 3. Can CLVD information be connected to a physical cause?

A CLVD is at first only a mathematical construct that compensates for differences between observed and synthetic time series by adding or subtracting energy along the principal axes of a double-couple. A physical interpretation of its occurrence is usually not straightforward and demands a thoughtful analysis of the given setting, data, and model.

We first need to rule out inversion artifacts that may arise from, e.g., wrong parameter settings that result in erroneous synthetics, leading to an CLVD contribution. Here, a robust and for the user-friendly inversion code is crucial.

Next are issues with the observed data and model assumptions. Large noise amplitudes interfere with the signal by adding or removing energy from it. In section 5.5.2, I examined the effects of high horizontal noise on the source solution, and in section 5.5.1 the effects of alignment uncertainties for small and potentially unfavorably arranged networks. Both tests showed that these uncertainties influence the CLVD part of the MT solution and can result in significant deviations of the true solutions and hence seismological interpretations of the source process. My Bayesian formulation of these uncertainties helped to reduce these effects and mitigates the resulting CLVD contributions by up to 60%. Furthermore, I developed a rule of thumb to decide if I allow for CLVD contribution during the inversion or not: If at least four stations and at least six horizontal components are deemed usable, and the source-network geometry displays a good azimuthal coverage, then full

deviatoric inversions can be conducted<sup>1</sup>.

Travel times depend on the geological structures in the Earth's interior along the source-receiver path, e.g., local high/low-velocity zones or complex geometries like a subducting slab. In practical applications, this information is stored in the Green's tensor (see Chapter 2). The quality of these models varies strongly between research regions and may range from simple layered 1D to high-resolution 3D structures.

To mitigate the effects of low-resolution velocity models on the MT solutions I decided on implementing a restricted cross-correlation time shift update for the synthetic waveforms to increase their fit with the observables. This was achieved in two steps within set time windows, i.e., we perform a time shift within  $\pm T$  seconds relative to the known origin or phase arrival time. A first shift over the full network (all stations and components) can be used to return an update of the origin time but indirectly introduces uncertainties to the source depth. Next, each station can be updated with an average time shift of all available components. This is useful if station delay times are unknown or epicenter locations are inaccurate. The magnitude of the allowed time shift has to be chosen relative to the highest frequency content of the bandpass-filtered waveforms to avoid cycle shifts. Cycle shifts can result in good fits, but in false source mechanisms (e.g., polarity reversal).

The scope of this thesis is set on the physical description of the source process. If other causes for an increased CLVD are taken care of, it is possible to relate its occurrence to the source process itself.

For the largest Blackpool events, I observed a predominantly negative CLVD of up to 21%, which led us to suggest a collapsing or even a potential minor normal faulting mechanism in addition to the major strike-slip movement. We assumed that it is related to the pressure release which took place after the termination of the experiment and before the occurrence of these events. However, without further information, this interpretation cannot be fully confirmed.

My study on the Monte Christo event got initiated by InSAR results depicting two active faults and an unstable solution in a pure double-couple inversion. Motivated by the changes in the source mechanism with increasing frequency, I decided on implementing a doublet inversion scheme to include a second event with its own set of source parameters (strike, dip, rake, CLVD percentage, and isotropic percentage) which is given in strength and onset time relative to the first event – introducing the parameters  $dm$  and  $dt$ . The fundamental synthetics can be computed for different locations, which allows me to include an outer grid loop for the doublet locations. Furthermore, both sub-events should have their own frequency content. This was straightforward in the respected synthetics, however, the observable needs to contain both bands. I decided on using a single bandpass filter between the lowest and the highest corner frequency. Both sub-event bands should inter-lap at the center frequency. This way I avoid gaps in the combined frequency band of both sets of synthetics but need to assume similar magnitudes of the sub-events if I use two narrow bands. The implementation into my code works well with the uniXtree sampling algorithm and the cross-correlation time update.

This new feature allowed me to examine the 2007  $M_w 7.4$  Martinique earthquake. The earthquake stood out in a global and regional comparison due to its very high CLVD part. Variations in this component from different, independent source solutions using different data sets (e.g., regional and teleseismic) are neglectable and range from 89% to 95%, leading to a strong assumption of a complex source mechanism rather than other issues. Due to its location and the time of its occurrence, seismic data within a regional distance are not sufficient. Differences in the double-couple part of different independent solutions and a back-projection hinted towards at least two distinct faults. To describe the rupture process and hence resolve the CLVD part, I included nearby historical moment tensor solutions, aftershock locations/cross-correlations, and performed regional moment

---

<sup>1</sup>Influences of the source-network geometry are not studied in detail in this thesis.

tensor inversion for a source doublet. The interpretation of the structure stemmed from a tectonic reconstruction that roughly assumed the Proto-Caribbean spreading ridge to be in this area.

My study showed that it is important to rule out non-source effects on the CLVD. This is possible using a robust and adequate inversion code for a given problem, a high-resolution velocity model, good hypocenter locations, and a high-quality data selection. Using RMT inversion, it is possible to describe the temporal evolution of complex source mechanisms but at the cost of an increasing number of free parameters. It is therefore important to constrain the parameterization, which can be achieved by introducing additional information into the inversion. Geodetic methods (e.g., InSAR) have a good and robust spatial resolution but are limited to large or near-surface events. In-Situ observations or tectonic models are valuable to classify the larger structures. Well-located aftershocks can highlight the full complexity of the activated faults but are considerably rarer for deep events. Non-double-couple contributions of induced events can be understood if the man-made process, i.e., pumping rates, is known.

## 9.2 Outlook

My study in the Lesser Antilles shed light on different tectonic structures, most notably the intermediate-depth cluster offshore Martinique. However, several new questions emerged that should be further studied in detail.

The “Global Significant Earthquake Database” by NOAA lists 11 earthquakes in the arc exceeding a magnitude of 7.0 since 1690 with two notable events for my study.

In 1906 an  $M7.9$  event occurred west of Martinique at a depth of about 100 km (NOAA) or in 50 km east to it (Dorel, 1981). If I set the NOAA location as the approximate hypocenter location, I can assume a pseudo-period of 100 years for the Martinique event. However, this shows that a magnitude of  $M_w7.4$  might not represent the upper potential of this cluster.

Peculiar is also the deep activity just west of Guadeloupe where the most recent January 20, 2023  $M_w6.1$  event occurred in a depth of  $\sim 170$  km and showed a CLVD part of up to 42%. Previous events in my database show different faulting styles and may be connected to the Marathon fracture zone which proceeds parallel to the Proto-Caribbean domain boundary.

The potential for megathrust events exceeding a magnitude of  $M8$  has been shown on two occasions in 1843 and 1690. Dorel (1981) proposed a  $\sim 150$  year long pseudo-period, which led him to suggest a re-occurrence at the end of the last century. The 1690 event is, with considerable uncertainties, assumed to have occurred near Barbuda, which is in line with the projected Barracuda Ridge. Here, we may ask the question of how this ridge relates to a potentially imminent megathrust event.

Still unanswered is the tectonic significance represented by the chain of trench perpendicular normal faults between Guadeloupe and Dominica (see Figure 5.10 or Figure 5.11, profile B) and if there is a connection to the 2004  $M_w6.3$  Les Saintes earthquake.

Next up are possible extensions of my inversion code. Here I have yet to employ the full potential of the Cut-and-Paste approach which further leads to a phase-dependent consideration of arrival time uncertainties.

In my thesis, I focussed on tectonic events that are represented in deviatoric mechanisms and hence neglected volumetric changes by, e.g., induced fluids in Blackpool or magma production in the Lesser Antilles. Initial tests showed that the introduction of an isotropic component can influence the robustness of an inversion and may interact with the CLVD part.

Lastly, I would like to examine different formulations of the co-variance matrix (e.g., Vasyura-Bathke et al., 2021) and explore different sources of uncertainties.





# Acknowledgments

I would like to express my appreciation and gratitude to my colleagues, friends, and my family without whom this work would not have been possible.

First of all, I would like to thank **Prof. Dr. Andreas Rietbrock** for supervising this thesis and giving me the opportunity to work with exciting OBS data. I appreciate the freedom he gave me to pursue different approaches to moment tensor inversion and create my original inversion code. I also thank him for the opportunity to participate in numerous national and international conferences and exciting research projects.

Next, I would like to thank **apl. Prof. Dr. Frank Krüger** for being the second supervisor of this thesis.

I thank the **Karlsruhe House of Young Scientists (KHYS)** for providing the framework of a Ph.D. program and offering different helpfull workshops.

It was a pleasure to be part of the Horizon 2020 project "Delivering Agile Research Excellence on European e-Infrastructures" (DARE), which got financed by the European Union. Here I like to give a special thank to my WP6 colleagues, **Dr. Federica Magnoni** and **Dr. Emanuele Casarotti** of the INGV in Rome, Italy.

My second project contribution was in the context of KIT's "Research Infrastructures in Research-Oriented Teaching" (RIRO) a project in cooperation with the Black Forest Observatory (BFO) and the Geodetic Institute (GIK). Here I like to give a special thanks to **Dr. Thomas Forbriger**, **Dr. Malte Westerhaus** and **Dr. Michael Mayer** as well as the whole team at the BFO and PEBA.

I would like to thank the co-authors of my publications for the valuable discussions and references. For my work in the Lesser Antilles, I like to give a special thanks to **Prof. Dr. Saskia Goes**, **Prof. Dr. Jenny Collier** and **Dr. Lidong Bie**. For my work on the Blackpool data, I would like to thank **Dr. Nassim Karamzadeh Toularoud** for the great cooperation and helpful discussions.

I am immensely grateful to all members of the Geophysical Institute (GPI) at the KIT for providing the environment to make this thesis possible. I thank **Dr. Michael Fritsch**, **Dr. Thomas Hertweck** and our secretary **Ms. Dick** for solving technical and organizational issues during my time at the GPI. A special thank goes also to **Dr. Ellen Gottschämmer**, **Dr. Sofia-Katerina Kufner**, **Dr. Michael Grund** and **Dr. Toni Zieger** for countless helpfull scientific and organizational discussions. Also many thanks to **Dr. Ya-Jian Gao**, **Dr. Michael Fritsch**, **Dr. Laura Gaßner**, **Dr. Lidong Bie** and **Dr. Thomas Hertweck** for proofreading this thesis, providing constructive feedback, and helping me with the L<sup>A</sup>T<sub>E</sub>X formatting. I am grateful for numerous scientific but also non-scientific discussions with the colleagues with whom I shared my office; **Adam**, **Sergio**, and most recently **Yvonne**. Lastly, I would like to express my gratitude to the colleagues and students not explicitly mentioned here for various enjoyable encounters over the last few years.

Finally but equally important, I am grateful to thank my parents, my younger brother, and the whole family and all my friends for their support and understanding during the last few years.



# Bibliography

- Afanasiev, M., Boehm, C., Van Driel, M., Krischer, L., Rietmann, M., May, D. A., Knepley, M. G., and Fichtner, A. (2019). “Modular and flexible spectral-element waveform modelling in two and three dimensions”. *Geophysical Journal International* 216.3, pp. 1675–1692. DOI: 10.1093/gji/ggy469.
- Agnew, D. C. (2002). “1 - History of Seismology”. In: *International Handbook of Earthquake and Engineering Seismology, Part A*. Ed. by W. H. Lee, H. Kanamori, P. C. Jennings, and C. Kisslinger. Vol. 81. International Geophysics. Academic Press, pp. 3–11. DOI: 10.1016/S0074-6142(02)80203-0.
- Aki, K. (1966). “Generation and Propagation of G Waves from the Niigata Earthquake of June 16, 1964: Part 2. Estimation of earthquake moment, released energy, and stress-strain drop from the G wave spectrum.” *Bulletin of the earthquake research institute*. 44.1, pp. 73–88.
- Aki, K. and Richards, P. G. (2002). *Quantitative seismology*. Sausalito, Calif.: University Science Books.
- Allen, R. W., Collier, J. S., Henstock, T. J., and The VoiLA Consortium (2022). “The Role of Crustal Accretion Variations in Determining Slab Hydration at an Atlantic Subduction Zone”. *Journal of Geophysical Research: Solid Earth* 127.8. DOI: 10.1029/2022JB024349.
- Allen, R., Collier, J., Stewart, A., Henstock, T., Goes, S., Rietbrock, A., and the VoiLA Team (2019). “The role of arc migration in the development of the Lesser Antilles: A new tectonic model for the Cenozoic evolution of the eastern Caribbean”. *Geology* 47.9, pp. 891–895. DOI: 10.1130/G46708.1.
- Alpert, L. A., Becker, T. W., and Bailey, I. W. (2010). “Global slab deformation and centroid moment tensor constraints on viscosity”. *Geochemistry, Geophysics, Geosystems* 11.12. DOI: 10.1029/2010GC003301.
- Álvarez-Gómez, J. A. (2019). “FMC–Earthquake focal mechanisms data management, cluster and classification”. *SoftwareX* 9, pp. 299–307. DOI: 10.1016/j.softx.2019.03.008.
- Ammon, C., Velasco, A., Lay, T., and Wallace, T. (2020). *Foundations of Modern Global Seismology*. Elsevier Science.
- Astiz, L., Lay, T., and Kanamori, H. (1988). “Large intermediate-depth earthquakes and the subduction process”. *Physics of the Earth and Planetary Interiors* 53.1, pp. 80–166. DOI: 10.1016/0031-9201(88)90138-0.
- Backus, G. and Mulcahy, M. (1976a). “Moment Tensors and other Phenomenological Descriptions of Seismic Sources—I. Continuous Displacements”. *Geophysical Journal International* 46.2, pp. 341–361. DOI: 10.1111/j.1365-246X.1976.tb04162.x.
- Backus, G. and Mulcahy, M. (1976b). “Moment tensors and other phenomenological descriptions of seismic sources—II. Discontinuous displacements”. *Geophysical Journal International* 47.2, pp. 301–329. DOI: 10.1111/j.1365-246X.1976.tb01275.x.

- Backus, G. E. (1977a). “Interpreting the seismic glut moments of total degree two or less”. *Geophysical Journal of the Royal Astronomical Society* 51.1, pp. 1–25. DOI: 10.1111/j.1365-246x.1977.tb04187.x.
- Backus, G. E. (1977b). “Seismic sources with observable glut moments of spatial degree two”. *Geophysical Journal of the Royal Astronomical Society* 51.1, pp. 27–45. DOI: 10.1111/j.1365-246x.1977.tb04188.x.
- Bailey, I. W., Alpert, L. A., Becker, T. W., and Miller, M. S. (2012). “Co-seismic deformation of deep slabs based on summed CMT data”. *Journal of Geophysical Research: Solid Earth* 117.B4. DOI: 10.1029/2011JB008943.
- Baptie, B. (2018). *Earthquake seismology 2017/2018*. British Geological Survey.
- Barth, A. (2007). “Frequency sensitive moment tensor inversion for light to moderate magnitude earthquakes in eastern Africa and derivation of the regional stress field.” PhD thesis. Universität Karlsruhe (TH). DOI: 10.5445/IR/1000005857.
- Bassin, C., Laske, G., and Masters, G. (2000). “The current limits of resolution for surface wave tomography in North America.” *EOS Trans AGU* 81:F897 81, F897.
- Beaucé, E., Frank, W. B., Paul, A., Campillo, M., and van der Hilst, R. D. (2019). “Systematic detection of clustered seismicity beneath the Southwestern Alps”. *Journal of Geophysical Research: Solid Earth* 124, pp. 11531–11548. DOI: 10.1029/2019JB018110.
- Ben-Menahem, A. and Singh, S. J. (1981). *Seismic waves and sources*. New York, Heidelberg, Berlin: Springer.
- Bennett, R. A., Wernicke, B. P., Niemi, N. A., Friedrich, A. M., and Davis, J. L. (2003). “Contemporary strain rates in the northern Basin and Range province from GPS data”. *Tectonics* 22.2. DOI: 10.1029/2001TC001355.
- Benthem, S., Govers, R., Spakman, W., and Wortel, R. (2013). “Tectonic evolution and mantle structure of the Caribbean”. *Journal of Geophysical Research: Solid Earth* 118.6, pp. 3019–3036. DOI: 10.1002/jgrb.50235.
- Beyreuther, M., Barsch, R., Krischer, L., Megies, T., Behr, Y., and Wassermann, J. (2010). “ObsPy: A Python Toolbox for Seismology”. *Seismological Research Letters* 81.3, pp. 530–533. DOI: 10.1785/gssrl.81.3.530.
- Bie, L., Hicks, S., Rietbrock, A., Goes, S., Collier, J., Rychert, C., Harmon, N., and Maunder, B. (2022). “Imaging slab-transported fluids and their deep dehydration from seismic velocity tomography in the Lesser Antilles subduction zone”. *Earth and Planetary Science Letters* 586. DOI: 10.1016/j.epsl.2022.117535.
- Bie, L., Rietbrock, A., Hicks, S., Allen, R., et al. (2020). “Along-Arc Heterogeneity in Local Seismicity across the Lesser Antilles Subduction Zone from a Dense Ocean-Bottom Seismometer Network”. *Seismological Research Letters* 91. DOI: 10.1785/0220190147.
- Blaser, L., Krueger, F., Ohrnberger, M., and Scherbaum, F. (2010). “Scaling Relations of Earthquake Source Parameter Estimates with Special Focus on Subduction Environment”. *Bulletin of the Seismological Society of America* 100.6, pp. 2914–2926. DOI: 10.1785/0120100111.
- Blom, N., Gokhberg, A., and Fichtner, A. (2020). “Seismic waveform tomography of the central and eastern Mediterranean upper mantle”. *Solid Earth* 11.2, pp. 669–690. DOI: 10.5194/se-11-669-2020.
- Bonjer, K.-P. (1997). “Seismicity pattern and style of seismic faulting at the eastern borderfault of the southern Rhine Graben”. *Tectonophysics* 275.1, pp. 41–69. DOI: 10.1016/S0040-1951(97)00015-2.

- Booth, D., Bott, J., and O'Mongain, A. (2001). "The UK seismic velocity model for earthquake location—a baseline review". *British Geological Survey Internal Report, IR/01/188*, p. 20.
- Bormann, J. M., Morton, E. A., Smith, K. D., Kent, G. M., Honjas, W. S., Plank, G. L., and Williams, M. C. (2021). "Nevada Seismological Laboratory Rapid Seismic Monitoring Deployment and Data Availability for the 2020 Mww 6.5 Monte Cristo Range, Nevada, Earthquake Sequence". *Seismological Research Letters* 92.2A, pp. 810–822. DOI: 10.1785/0220200344.
- Bormann, P. and Wielandt, E. (2013). "Chapter 4: Seismic Signals and Noise". *Bormann, P. (Ed.), New Manual of Seismological Observatory Practice 2 (NMSOP-2)*. DOI: 10.2312/GFZ.NMSOP-2\_ch4.
- Boschman, L. M., van Hinsbergen, D. J., Torsvik, T. H., Spakman, W., and Pindell, J. L. (2014). "Kinematic reconstruction of the Caribbean region since the Early Jurassic". *Earth-Science Reviews* 138, pp. 102–136. DOI: 10.1016/j.earscirev.2014.08.007.
- Bouysse, P., Westercamp, D., and Andreieff, P. (1990). "The Lesser Antilles Island Arc". *Proceedings of the Ocean Drilling Program, Scientific Results* 110, pp. 29–44. DOI: 10.2973/odp.proc.sr.110.166.1990.
- Braszus, B., Goes, S., Allen, R., Rietbrock, A., et al. (2021). "Subduction history of the Caribbean from upper-mantle seismic imaging and plate reconstruction". *Nature Communications* 12.1, p. 4211. DOI: 10.1038/s41467-021-24413-0.
- Bristol University, B.G.S. (2015). *UK Array. International Federation of Digital Seismograph Networks*. <https://doi.org/10.7914/SN/UR>.
- British Geological Survey (2017). *Earthquakes induced by hydraulic fracturing operations near Blackpool, UK*. Last accessed 2020-02-20. URL: <http://www.earthquakes.bgs.ac.uk/research/BlackpoolEarthquakes.html>.
- Buchs, D., Hoernle, K., Hauß, F., and Baumgartner, P. (2016). "Evidence from accreted seamounts for a depleted component in the early Galapagos plume". *Geology* 44, G37618.1. DOI: 10.1130/G37618.1.
- Burridge, R. and Knopoff, L. (1964). "Body force equivalents for seismic dislocations". *Bulletin of the Seismological Society of America* 54.6A, pp. 1875–1888. DOI: 10.1785/BSSA05406A1875.
- Cabieces, R., Bufo, E., Cesca, S., and Pazos, A. (2020). "Focal Parameters of Earthquakes Offshore Cape St. Vincent Using an Amphibious Network". *Pure and Applied Geophysics* 177. DOI: 10.1007/s00024-020-02475-3.
- Caputa, A., Rudziński, Ł., and Cesca, S. (2021). "How to Assess the Moment Tensor Inversion Resolution for Mining Induced Seismicity: A Case Study for the Rudna Mine, Poland". *Frontiers in Earth Science*. DOI: 10.3389/feart.2021.671207.
- Cassinis, R. (2013). *Digital Seismology and Fine Modeling of the Lithosphere*. Ettore Majorana International Science Series. Springer US. ISBN: 9781489967619. DOI: 10.1007/978-1-4899-6759-6.
- Cesca, S., Bufo, E., and Dahm, T. (2006). "Amplitude spectra moment tensor inversion of shallow earthquakes in Spain". *Geophysical Journal International* 166.2, pp. 839–854. DOI: 10.1111/j.1365-246X.2006.03073.x.
- Cesca, S. and Dahm, T. (2008). "A frequency domain inversion code to retrieve time-dependent parameters of very long-period volcanic sources". *Computers and Geosciences* 34, pp. 235–246. DOI: 10.1016/j.cageo.2007.03.018.
- Cesca, S., Heimann, S., Stammer, K., and Dahm, T. (2010). "Automated procedure for point and kinematic source inversion at regional distances". *Journal of Geophysical Research: Solid Earth* 115.B6. DOI: 10.1029/2009JB006450.

- Chamberlain, C. J., Hopp, C. J., Boese, C. M., Warren-Smith, E., Chambers, D., Chu, S. X., Michailos, K., and Townend, J. (2017). “EQcorrscan: Repeating and Near-Repeating Earthquake Detection and Analysis in Python”. *Seismological Research Letters* 89.1, pp. 173–181. DOI: 10.1785/0220170151.
- Chen, P.-F., Bina, C. R., and Okal, E. A. (2004). “A global survey of stress orientations in subducting slabs as revealed by intermediate-depth earthquakes”. *Geophysical Journal International* 159.2, pp. 721–733. DOI: 10.1111/j.1365-246X.2004.02450.x.
- Chen, W., Ni, S., Kanamori, H., Wei, S., Jia, Z., and Zhu, L. (2015). “CAPjoint, A Computer Software Package for Joint Inversion of Moderate Earthquake Source Parameters with Local and Teleseismic Waveforms”. *Seismological Research Letters* 86.2A, pp. 432–441. DOI: 10.1785/0220140167.
- Chen, Y.-W., Wu, J., and Goes, S. (2023). “Lesser Antilles slab reconstruction reveals lateral slab dragging under the Caribbean since 50 Ma”. *Submitted to Earth and Planetary Science Letters*.
- Chorsi, T. S., Braunmiller, J., Deng, F., Mueller, N., Kerstetter, S., Stern, R. J., and Dixon, T. H. (2022). “The May 15, 2020 M 6.5 Monte Cristo Range, Nevada, earthquake: eyes in the sky, boots on the ground, and a chance for students to learn”. *International Geology Review* 64.19, pp. 2683–2702. DOI: 10.1080/00206814.2021.2000507.
- Christeson, G. L., Mann, P., Escalona, A., and Aitken, T. J. (2008). “Crustal structure of the Caribbean-northeastern South America arc-continent collision zone”. *Journal of Geophysical Research: Solid Earth* 113.B8. DOI: 10.1029/2007JB005373.
- Clarke, H., Eisner, L., Styles, P., and Turner, P. (2014). “Felt seismicity associated with shale gas hydraulic fracturing: The first documented example in Europe”. *Geophysical Research Letters* 41.23, pp. 8308–8314. DOI: 10.1002/2014GL062047.
- Clarke, H., Verdon, J. P., Kettlety, T., Baird, A. F., and Kendall, J. (2019). “Real-Time Imaging, Forecasting, and Management of Human-Induced Seismicity at Preston New Road, Lancashire, England”. *Seismological Research Letters* 90.5, pp. 1902–1915. DOI: 10.1785/0220190110.
- Clay, A. (2015). *August Seismic Event Determination*. Last accessed 2020-02-20. URL: <https://www.bcogc.ca/node/12951/download>.
- Clévéde, E., Bouin, M.-P., Bukchin, B., Mostinskiy, A., and Patau, G. (2004). “New constraints on the rupture process of the 1999 August 17 Izmit earthquake deduced from estimates of stress glut rate moments”. *Geophysical Journal International* 159.3, pp. 931–942. DOI: 10.1111/j.1365-246X.2004.02304.x.
- Collier, J. S. (2015). “VoiLA - Volatile recycling in the Lesser Antilles arc: RRS James Cook cruise report JC133.” *Imperial College London* 89. URL: [https://www.bodc.ac.uk/resources/inventories/cruise\\_inventory/reports/jc133.pdf](https://www.bodc.ac.uk/resources/inventories/cruise_inventory/reports/jc133.pdf).
- Cooper, G., Macpherson, C., Blundy, J., Maunder, B., et al. (2020). “Variable water input controls evolution of the Lesser Antilles volcanic arc”. *Nature* 582, pp. 525–529. DOI: 10.1038/s41586-020-2407-5.
- Cuadrilla (2019). *Hydraulic Fracture Plan PNR 2*. Last accessed 2020-08-6. URL: [https://consult.environment-agency.gov.uk/onshore-oil-and-gas/information-on-cuadrillas-preston-new-road-site/user\\_uploads/hydraulic-fracture-plan-preston-new-road-2--v2.0.pdf](https://consult.environment-agency.gov.uk/onshore-oil-and-gas/information-on-cuadrillas-preston-new-road-site/user_uploads/hydraulic-fracture-plan-preston-new-road-2--v2.0.pdf).
- Cui, Y., Ma, Z., Aoki, Y., Liu, J., Yue, D., Hu, J., Zhou, C., and Li, Z. (2021). “Refining slip distribution in moderate earthquakes using Sentinel-1 burst overlap interferometry: a case study over 2020 May 15 Mw 6.5 Monte Cristo Range Earthquake”. *Geophysical Journal International* 229.1, pp. 472–486. DOI: 10.1093/gji/ggab492.

- Dahlen, F. A. and Tromp, J. (1998). *Theoretical Global Seismology*. Princeton University Press. (Visited on 01/11/2023).
- Dahm, T. and Krüger, F. (1999). “Higher-degree moment tensor inversion using far-field broadband recordings: theory and evaluation of the method with application to the 1994 Bolivia deep earthquake”. *Geophysical Journal International* 137.1, pp. 35–50. DOI: 10.1046/j.1365-246x.1999.00761.x.
- Dahm, T. and Krüger, F. (2014). “Moment tensor inversion and moment tensor interpretation.” *New Manual of Seismological Observatory Practice 2 (NMSOP-2)*. Ed. by P. Bormann, pp. 1–37. DOI: 10.2312/GFZ.NMSOP-2\\_IS\\_3.9.
- Dahm, T. (1993). “Relativmethoden zur Bestimmung der Abstrahlcharakteristik von seismischen Quellen”. PhD thesis. Universität Karlsruhe (TH).
- Dal Zilio, L. and Ampuero, J.-P. (2023). “Earthquake doublet in Turkey and Syria”. *Communications Earth & Environment* 4.1, p. 71. DOI: 10.1038/s43247-023-00747-z.
- D’Amico, S. (2018). *Moment Tensor Solutions: A Useful Tool for Seismotectonics*. Springer Natural Hazards. Springer International Publishing.
- Davies, R., Foulger, G., Bindley, A., and Styles, P. (2013). “Induced seismicity and hydraulic fracturing for the recovery of hydrocarbons”. *Marine and petroleum geology* 45, pp. 171–185.
- Debayle, E., Dubuffet, F., and Durand, S. (2016). “An automatically updated S-wave model of the upper mantle and the depth extent of azimuthal anisotropy”. *Geophysical Research Letters* 43.2, pp. 674–682. DOI: 10.1002/2015GL067329.
- Dee, S., Koehler, R., Elliott, A., Hatem, A., et al. (2021). “Surface rupture map of the 2020 M 6.5 Monte Cristo Range earthquake, Esmeralda and Mineral counties”. *Nevada: Nevada Bureau of Mines and Geology Map 190*. URL: <https://pubs.nbmng.unr.edu/Monte-Cristo-Range-EQ-p/m190.htm>.
- DeLano, K., Lee, J., Roper, R., and Calvert, A. (2019). “Dextral, normal, and sinistral faulting across the eastern California shear zone–Mina deflection transition, California-Nevada, USA”. *Geosphere* 15.4, pp. 1206–1239. DOI: 10.1130/GES01636.1.
- Delescluse, M., Montési, L. G. J., and Chamot-Rooke, N. (2008). “Fault reactivation and selective abandonment in the oceanic lithosphere”. *Geophysical Research Letters* 35.16. DOI: 10.1029/2008GL035066.
- Demets, C., Gordon, R., and Argus, D. (2010). “Geological current plate motions”. *Geophysical Journal International* 181, pp. 1–80. DOI: 10.1111/j.1365-246X.2009.04491.x.
- Dettmer, J., Dosso, S., and Holland, C. (2007). “Uncertainty estimation in seismo-acoustic reflection travel time inversion”. *The Journal of the Acoustical Society of America* 122, pp. 161–76. DOI: 10.1121/1.2736514.
- Dixon, T., Farina, F., Demets, C., Suarez-Vidal, F., Fletcher, J., Azúa, B., Miller, M., Sanchez Zamora, O., and Umhoefer, P. (2000). “New kinematic models for Pacific-North America Motion from 3 Ma to Present, II: Evidence for a “Baja California Shear Zone””. *Geophysical Research Letters* 27, pp. 3961–3964. DOI: 10.1029/2000GL008529.
- Dixon, T. H., Robaudo, S., Lee, J., and Reheis, M. C. (1995). “Constraints on present-day Basin and Range deformation from space geodesy”. *Tectonics* 14.4, pp. 755–772. DOI: 10.1029/95TC00931.
- Donner, S. (2021). “Chapter Three - Rotational ground motion measurements for regional seismic moment tensors: A review”. In: *Inversion of Geophysical Data*. Ed. by C. Schmelzbach. Vol. 62. Advances in Geophysics. Elsevier, pp. 141–186. DOI: 10.1016/bs.agph.2021.06.002.



- Doornbos, D. (1982). “Seismic source spectra and moment tensors”. *Physics of the Earth and Planetary Interiors* 30.2. Special Issue Earthquake Algorithms, pp. 214–227. DOI: 10.1016/0031-9201(82)90109-1.
- Doran, A. K. and Laske, G. (2017). “Ocean-Bottom Seismometer Instrument Orientations via Automated Rayleigh-Wave Arrival-Angle Measurements”. *Bulletin of the Seismological Society of America* 107.2, pp. 691–708. DOI: 10.1785/0120160165.
- Dorel, J. (1981). “Seismicity and seismic gap in the Lesser Antilles arc and earthquake hazard in Guadeloupe”. *Geophysical Journal of the Royal Astronomical Society* 67.3, pp. 679–695. DOI: 10.1111/j.1365-246X.1981.tb06947.x.
- Dreger, D. S. (2003). “85.11 – TDMT\_INV: Time Domain Seismic Moment Tensor INVersion”. *International Geophysics* 81, p. 1627. DOI: 10.1016/S0074-6142(03)80290-5.
- Dreger, D. S. and Helmberger, D. V. (1993). “Determination of source parameters at regional distances with three-component sparse network data”. *Journal of Geophysical Research: Solid Earth* 98.B5, pp. 8107–8125. DOI: 10.1029/93JB00023.
- Duputel, Z., Agram, P. S., Simons, M., Minson, S. E., and Beck, J. L. (2014). “Accounting for prediction uncertainty when inferring subsurface fault slip”. *Geophysical Journal International* 197.1, pp. 464–482. DOI: 10.1093/gji/ggt517.
- Duputel, Z., Rivera, L., Fukahata, Y., and Kanamori, H. (2012). “Uncertainty estimations for seismic source inversions”. *Geophysical Journal International* 190.2, pp. 1243–1256. DOI: 10.1111/j.1365-246X.2012.05554.x.
- Dziewonski, A. M. and Anderson, D. L. (1981). “Preliminary reference Earth model”. *Physics of the Earth and Planetary Interiors* 25.4, pp. 297–356. DOI: 10.1016/0031-9201(81)90046-7.
- Edwards, B., Crowley, H., Pinho, R., and Bommer, J. J. (2021). “Seismic Hazard and Risk Due to Induced Earthquakes at a Shale Gas Site”. *Bulletin of the Seismological Society of America* 111.2, pp. 875–897. DOI: 10.1785/0120200234.
- Eisner, L., Hallo, M., Matousek, P., Oprsal, I., and Janska, E. (2011). “Seismic analysis of the events in the vicinity of the Preese Hall well”.
- Ekström, G., Nettles, M., and Dziewoński, A. (2012). “The global CMT project 2004–2010: Centroid moment tensors for 13,017 earthquakes”. *Physics of the Earth and Planetary Interiors* 200–201, pp. 1–9. DOI: 10.1016/j.pepi.2012.04.002.
- Ekström, G. (1994). “Anomalous earthquakes on volcano ring-fault structures”. *Earth and Planetary Science Letters* 128.3, pp. 707–712. DOI: 10.1016/0012-821X(94)90184-8.
- Feuillet, N., Beauducel, F., Jacques, E., Tapponnier, P., Delouis, B., Bazin, S., Vallée, M., and King, G. C. P. (2011a). “The Mw = 6.3, November 21, 2004, Les Saintes earthquake (Guadeloupe): Tectonic setting, slip model and static stress changes”. *Journal of Geophysical Research: Solid Earth* 116.B10. DOI: 10.1029/2011JB008310.
- Feuillet, N., Manighetti, I., Tapponnier, P., and Jacques, E. (2002). “Arc parallel extension and localization of volcanic complexes in Guadeloupe, Lesser Antilles”. *Journal of Geophysical Research: Solid Earth* 107.B12. DOI: 10.1029/2001JB000308.
- Feuillet, N., Beauducel, F., and Tapponnier, P. (2011b). “Tectonic context of moderate to large historical earthquakes in the Lesser Antilles and mechanical coupling with volcanoes”. *Journal of Geophysical Research* 116. DOI: 10.1029/2011JB008443.
- Forbriger, T. (2012). *Recommendations for seismometer deployment and shielding*. Ed. by P. Bormann. Potsdam. DOI: 10.2312/GFZ.NMSOP-2\_IS\_5.4.

- Foulger, G. R. and Julian, B. R. (2014). “Non-Double-Couple Earthquakes”. In: *Encyclopedia of Earthquake Engineering*. Ed. by M. Beer, I. A. Kougiumtzoglou, E. Patelli, and I. S.-K. Au. Springer Berlin Heidelberg, pp. 1–31. DOI: 10.1007/978-3-642-36197-5\_290-1.
- Frietsch, M., Ferreira, A. M. G., Funning, G. J., and Weston, J. (2019). “Multiple fault modelling combining seismic and geodetic data: the importance of simultaneous subevent inversions”. *Geophysical Journal International* 218.2, pp. 958–976. DOI: 10.1093/gji/ggz205.
- Frohlich, C. (1987). “Kiyoo Wadati and early research on deep focus earthquakes: Introduction to Special Section on Deep and Intermediate Focus Earthquakes”. *Journal of Geophysical Research: Solid Earth* 92.B13, pp. 13777–13788. DOI: 10.1029/JB092iB13p13777.
- Frohlich, C. (1992). “Triangle diagrams: ternary graphs to display similarity and diversity of earthquake focal mechanisms”. *Physics of the Earth and Planetary Interiors* 75.1, pp. 193–198. DOI: 10.1016/0031-9201(92)90130-N.
- Frohlich, C. (1995). “Characteristics of well-determined non-double-couple earthquakes in the Harvard CMT catalog”. *Physics of the Earth and Planetary Interiors* 91.4, pp. 213–228. DOI: 10.1016/0031-9201(95)03031-Q.
- Fujimura, K., Kunii, T., Yamaguchi, K., and Toriya, H. (1984). “Octree-Related Data Structures and Algorithms”. *IEEE Computer Graphics and Applications* 4.01, pp. 53–59. DOI: 10.1109/MCG.1984.275901.
- Fukuyama, E., Ishida, M., Dreger, D. S., and Kawai, H. (1998). “Automated Seismic Moment Tensor Determination by Using On-line Broadband Seismic Waveforms”. *Journal of the Seismological Society of Japan* 51, pp. 149–156. DOI: 10.4294/zisin1948.51.1\_149.
- Gaebler, P., Ceranna, L., Nooshiri, N., Barth, A., et al. (2019). “A multi-technology analysis of the 2017 North Korean nuclear test”. *Solid Earth* 10.1, pp. 59–78. DOI: 10.5194/se-10-59-2019.
- Galloway, D. (2019). “Bulletin of British earthquakes 2018”. *British Geological Survey Internal Report, OR/19/002*. URL: <http://nora.nerc.ac.uk/id/opteprint/519078/1/OR16011.pdf>.
- Gao, Y., Tilmann, F., Yuan, X., Schurr, B., et al. (2022). “Seismic structure in the crust and upper mantle beneath the Hindu Kush and Pamir from Full Waveform Inversion”. In: DOI: 10.5194/egusphere-egu22-11377.
- Garth, T. and Rietbrock, A. (2014). “Order of magnitude increase in subducted H<sub>2</sub>O due to hydrated normal faults within the Wadati-Benioff zone”. *Geology* 42.3, pp. 207–210. DOI: 10.1130/G34730.1.
- Gephart, J. and Forsyth, D. (1984). “An improved Method for Determining the Regional Stress Tensor Using Earthquake Focal Mechanism Data: Application to the San Fernando Earthquake Sequence”. *Journal of Geophysical Research* 89, pp. 2177–2180. DOI: 10.1029/JB089iB11p09305.
- Gibbons, S. J. and Ringdal, F. (2006). “The detection of low magnitude seismic events using array-based waveform correlation”. *Geophysical Journal International* 165.1, pp. 149–166. DOI: 10.1111/j.1365-246X.2006.02865.x.
- Gilbert, F. and Dziewonski, A. M. (1975). “An Application of Normal Mode Theory to the Retrieval of Structural Parameters and Source Mechanisms from Seismic Spectra”. *Philosophical Transactions of the Royal Society of London Series A* 278, pp. 187–269. DOI: 10.1098/rsta.1975.0025.
- Giner-Robles, J., Perez-Lopez, R., Rodriguez-Pascua, M., Martinez-Diaz, J., and Gonzalez-Casado, J. (2009). “Present-day strain field on the South American slab underneath the Sandwich Plate (Southern Atlantic Ocean): A kinematic model”. *Geological Society London Special Publications* 328, pp. 155–167. DOI: 10.1144/SP328.6.

- Goes, S., Agrusta, R., van Hunen, J., and Garel, F. (2017). “Subduction-transition zone interaction: A review”. *Geosphere* 13.3, pp. 644–664. DOI: 10.1130/GES01476.1.
- Goes, S., Collier, J., Blundy, J., Davidson, J., et al. (2019). “Project VoiLA: Volatile Recycling in the Lesser Antilles”. *Eos Transactions American Geophysical Union* 100. DOI: 10.1029/2019EO117309.
- Gonzalez, O., Clouard, V., and Zahradník, J. (2017). “Moment tensor solutions along the central Lesser Antilles using regional broadband stations”. *Tectonophysics* 717, pp. 214–225. DOI: 10.1016/j.tecto.2017.06.024.
- Govorčin, M., Wdowinski, S., Matoš, B., and Funning, G. J. (2020). “Geodetic Source Modeling of the 2019 Mw 6.3 Durrës, Albania, Earthquake: Partial Rupture of a Blind Reverse Fault”. *Geophysical Research Letters* 47.22. DOI: 10.1029/2020GL088990.
- Green, H. W. and Houston, H. (1995). “The Mechanics of Deep Earthquakes”. *Annual Review of Earth and Planetary Sciences* 23.1, pp. 169–213. DOI: 10.1146/annurev.ea.23.050195.001125.
- Gu, C., Marzouk, Y. M., and Toksöz, M. N. (2017). “Waveform-based Bayesian full moment tensor inversion and uncertainty determination for the induced seismicity in an oil/gas field”. *Geophysical Journal International* 212.3, pp. 1963–1985. DOI: 10.1093/gji/ggx517.
- Gutenberg, B. and Richter, C. (1954). *Seismicity of the Earth and Associated Phenomena*. Princeton University Press. URL: <https://books.google.de/books?id=YOCkAQAAIAAJ>.
- Gutenberg, B. and Richter, C. (1944). “Frequency of Earthquakes in California.” *Report of the State Investigation Commission* 34, pp. 185–188. DOI: 10.1038/156371a0.
- Hacker, B. R., Peacock, S. M., Abers, G. A., and Holloway, S. D. (2003). “Subduction factory 2. Are intermediate-depth earthquakes in subducting slabs linked to metamorphic dehydration reactions?” *Journal of Geophysical Research: Solid Earth* 108.B1. DOI: 10.1029/2001JB001129.
- Hanks, T. C. and Kanamori, H. (1979). “A moment magnitude scale”. *Journal of Geophysical Research: Solid Earth* 84.B5, pp. 2348–2350. DOI: 10.1029/JB084iB05p02348.
- Hardebeck, J. and Shearer, P. (2002). “A New Method for Determining First-Motion Focal Mechanisms”. *Bulletin of the Seismological Society of America* 92, pp. 2264–2276. DOI: 10.1785/0120010200.
- Hardebeck, J. L. (2015). “Stress orientations in subduction zones and the strength of subduction megathrust faults”. *Science* 349, pp. 1213–1216. DOI: 10.1126/science.aac5625.
- Harmon, N., Rychert, C., Collier, J., Henstock, T., van Hunen, J., and Wilkinson, J. J. (2019). “Mapping geologic features onto subducted slabs”. *Geophysical Journal International* 219.2, pp. 725–733. DOI: 10.1093/gji/ggz290.
- Harris, C. W., Miller, M. S., and Porritt, R. W. (2018). “Tomographic Imaging of Slab Segmentation and Deformation in the Greater Antilles”. *Geochemistry, Geophysics, Geosystems* 19.8, pp. 2292–2307. DOI: 10.1029/2018GC007603.
- Hawkins, R. and Sambridge, M. (2015). “Geophysical imaging using trans-dimensional trees”. *Geophysical Journal International* 203.2, pp. 972–1000. DOI: 10.1093/gji/ggv326.
- Hayes, G. P., McNamara, D. E., Seidman, L., and Roger, J. (2013). “Quantifying potential earthquake and tsunami hazard in the Lesser Antilles subduction zone of the Caribbean region”. *Geophysical Journal International* 196.1, pp. 510–521. DOI: 10.1093/gji/ggt385.
- Hayes, G. P., Meyers, E. K., Dewey, J. W., Briggs, R. W., et al. (2017). “Tectonic summaries of magnitude 7 and greater earthquakes from 2000 to 2015”. *U.S. Geological Survey Open-File Report*, pp. 2016–1192. DOI: 10.3133/ofr20161192.

- Heimann, S., Kriegerowski, M., Isken, M. P., Cesca, S., et al. (2017). “Pyrocko - An open-source seismology toolbox and library”. *GFZ Data Services*. DOI: 10.5880/GFZ.2.1.2017.001.
- Hicks, S., Bie, L., Rychert, C. A., Harmon, N., et al. (2023). “Slab to back-arc to arc: Fluid and melt pathways through the mantle wedge beneath the Lesser Antilles”. *Science Advances* 9.5. DOI: 10.1126/sciadv.add2143.
- Hicks, S. and Rietbrock, A. (2015). “Seismic slip on an upper-plate normal fault during a large subduction megathrust rupture”. *Nature Geoscience* 8, pp. 955–960. DOI: 10.1038/ngeo2585.
- Hill, E., Yue, H., Barbot, S., Lay, T., et al. (2015). “The 2012 Mw 8.6 Wharton Basin sequence: A cascade of great earthquakes generated by near-orthogonal, young, oceanic mantle faults”. *Journal of Geophysical Research: Solid Earth* 120, pp. 3723–3747. DOI: 10.1002/2014JB011703.
- Hirt, C. and Rexer, M. (2015). “Earth2014: 1 arc-min shape, topography, bedrock and ice-sheet models – Available as gridded data and degree-10,800 spherical harmonics”. *International Journal of Applied Earth Observation and Geoinformation* 39, pp. 103–112. DOI: 10.1016/j.jag.2015.03.001.
- Hobbs, B. E. and Ord, A. (1988). “Plastic instabilities: Implications for the origin of intermediate and deep focus earthquakes”. *Journal of Geophysical Research: Solid Earth* 93.B9, pp. 10521–10540. DOI: 10.1029/JB093iB09p10521.
- Hudson, J. A., Pearce, R. G., and Rogers, R. M. (1989). “Source type plot for inversion of the moment tensor”. *Journal of Geophysical Research: Solid Earth* 94.B1, pp. 765–774. DOI: 10.1029/JB094iB01p00765.
- IRIS DMC (2011). *Data Services Products: BackProjection P-wave back-projection rupture imaging*. DOI: 10.17611/DP/112180. URL: <https://ds.iris.edu/ds/products/backprojection/> (visited on 05/04/2022).
- IRIS-SAGE (2023). *Data Services Products: EMC-EarthModels*. URL: <https://ds.iris.edu/ds/products/emc-earthmodels/> (visited on 04/28/2023).
- Isacks, B. and Molnar, P. (1971). “Distribution of stresses in the descending lithosphere from a global survey of focal-mechanism solutions of mantle earthquakes”. *Reviews of Geophysics* 9.1, pp. 103–174. DOI: 10.1029/RG009i001p00103.
- Janiszewski, H. A. and Abers, G. A. (2015). “Imaging the Plate Interface in the Cascadia Seismogenic Zone: New Constraints from Offshore Receiver Functions”. *Seismological Research Letters* 86.5, pp. 1261–1269. DOI: 10.1785/0220150104.
- Jia, Z., Zhan, Z., and Helmberger, D. (2022). “Bayesian differential moment tensor inversion: theory and application to the North Korea nuclear tests”. *Geophysical Journal International* 229.3, pp. 2034–2046. DOI: 10.1093/gji/ggac053.
- Jost, M. L. and Herrmann, R. B. (1989). “A Student’s Guide to and Review of Moment Tensors”. *Seismological Research Letters* 60.2, pp. 37–57. DOI: 10.1785/gssrl.60.2.37.
- Julien, P. and Bonneton, J.-R. (1989). “Regional stress field in the Lesser Antilles between Guadeloupe and Barbuda Islands”. *Geophysical Research Letters* 16.11, pp. 1313–1316. DOI: 10.1029/GL016i011p01313.
- Kagan, Y. Y. (1991). “3-D rotation of double-couple earthquake sources”. *Geophysical Journal International* 106.3, pp. 709–716. DOI: 10.1111/j.1365-246X.1991.tb06343.x.
- Kajitani, Y., Chang, S. E., and Tatano, H. (2013). “Economic Impacts of the 2011 Tohoku-Oki Earthquake and Tsunami”. *Earthquake Spectra* 29, pp. 457–478. DOI: 10.1193/1.4000108.

- Karamzadeh, N., Lindner, M., Edwards, B., Gaucher, E., and Rietbrock, A. (2021). “Induced seismicity due to hydraulic fracturing near Blackpool, UK: source modeling and event detection”. *Journal of Seismology* 25, pp. 1385–1406. DOI: 10.1007/s10950-021-10054-9.
- Kennett, B. L. N. (2001). *The Seismic Wavefield*. Vol. 1. Cambridge University Press. DOI: 10.1017/9781108780315.
- Kennett, B. L. N. and Engdahl, E. R. (1991). “Traveltimes for global earthquake location and phase identification”. *Geophysical Journal International* 105.2, pp. 429–465. DOI: 10.1111/j.1365-246X.1991.tb06724.x.
- Kennett, B. (2009). *Seismic Wave Propagation In Stratified Media*. Vol. 86. ANU Press. ISBN: 9781921536731. DOI: 10.26530/OAPEN\_459524.
- Kennett, B., Engdahl, E., and Buland, R. (1995). “Constraints on seismic velocities in the Earth from travel-times”. *Geophysical Journal International* 122, pp. 108–124. DOI: 10.1111/j.1365-246X.1995.tb03540.x.
- Kettlety, T., Verdon, J. P., Butcher, A., Hampson, M., and Craddock, L. (2020). “High-Resolution Imaging of the ML 2.9 August 2019 Earthquake in Lancashire, United Kingdom, Induced by Hydraulic Fracturing during Preston New Road PNR-2 Operations”. *Seismological Research Letters* 92.1, pp. 151–169. DOI: 10.1785/0220200187.
- Kikuchi, M. and Kanamori, H. (1991). “Inversion of complex body waves—III”. *Bulletin of the Seismological Society of America* 81.6, pp. 2335–2350. DOI: 10.1785/BSSA0810062335.
- Kirby, S., Hemingway, B. S., and Lee, R. (1990). “Anomalous Fracture and Thermal Behavior of Hydrous Minerals”. In: *The Brittle-Ductile Transition in Rocks*. American Geophysical Union, pp. 119–126. DOI: 10.1029/GM056p0119.
- Knopoff, L. and Randall, M. J. (1970). “The compensated linear-vector dipole: A possible mechanism for deep earthquakes”. *Journal of Geophysical Research* 75.26, pp. 4957–4963. DOI: <https://doi.org/10.1029/JB075i026p04957>.
- Komatitsch, D., Vilotte, J.-P., Tromp, J., Ampuero, J.-P., et al. (1999). “SPECFEM3D Cartesian [software]”. URL: <https://geodynamics.org/cig/software/specfem3d/>.
- Kratz, M., Aulia, A., and Hill, A. (2012). “Identifying fault activation in shale reservoirs using microseismic monitoring during hydraulic stimulation: Source Mechanisms, b Values, and energy release rates”. *CSEG Recorder* 20.06. URL: <https://csegrecorder.com/articles/view/identifying-fault-activation-in-shale-reservoirs-using-microseismic-monitor>.
- Krizova, D., Zahradnik, J., and Kiratzi, A. (2013). “Resolvability of Isotropic Component in Regional Seismic Moment Tensor Inversion”. *Bulletin of the Seismological Society of America* 103, pp. 2460–2473. DOI: 10.1785/0120120097.
- Kubo, A., Fukuyama, E., Kawai, H., and Nonomura, K. (2002). “NIED seismic moment tensor catalogue for regional earthquakes around Japan: quality test and application”. *Tectonophysics* 356.1. Seismic Source Mechanism through Moment Tensors, pp. 23–48. DOI: 10.1016/S0040-1951(02)00375-X.
- Kufner, S.-K., Bie, L., Gao, Y., Lindner, M., Waizy, H., Kakar, N., and Rietbrock, A. (2023). “The Devastating 2022 M6.2 Afghanistan Earthquake: Challenges, Processes, and Implications”. *Geophysical Research Letters* 50.11. DOI: 10.1029/2022GL102176.
- Kwong, K. B., DeShon, H. R., Kim, J. W., and Lu, Z. (2019). “Resolving Teleseismic Earthquake Catalog and InSAR Data Discrepancies in Absolute Space to Explore Rupture Complexity Along the Ecuadorian Megathrust Fault”. *Journal of Geophysical Research: Solid Earth* 124.7, pp. 6703–6719. DOI: 10.1029/2018JB016271.

- Laigle, M., Hirn, A., Sapin, M., Bécel, A., et al. (2013a). “Seismic structure and activity of the north-central Lesser Antilles subduction zone from an integrated approach: Similarities with the Tohoku forearc”. *Tectonophysics* 603, pp. 1–20. DOI: 10.1016/j.tecto.2013.05.043.
- Laigle, M., Becel, A., de Voogd, B., Sachpazi, M., Bayrakci, G., Jean-Frédéric, L., and Evain, M. (2013b). “Along-arc segmentation and interaction of subducting ridges with the Lesser Antilles Subduction forearc crust revealed by MCS imaging”. *Tectonophysics* 603, pp. 32–54. DOI: 10.1016/j.tecto.2013.05.028.
- Laske, G., Masters, G., Ma, Z., and Pasyanos, M. (2013). “Update on CRUST1.0 – A 1-degree Global Model of Earth’s Crust”. In: EGU General Assembly Conference Abstracts, EGU2013-2658, EGU2013–2658.
- Laurencin, M., Marcaillou, B., Graindorge, D., Klingelhoefer, F., Lallemand, S., Laigle, M., and Jean-Frédéric, L. (2017). “The polyphased tectonic evolution of the Anegada Passage in the northern Lesser Antilles subduction zone”. *Tectonics* 36, pp. 945–961. DOI: 10.1002/2017TC004511.
- Lecocq, T., Hicks, S. P., Noten, K. V., van Wijk, K., et al. (2020). “Global quieting of high-frequency seismic noise due to COVID-19 pandemic lockdown measures”. *Science* 369, pp. 1338–1343. DOI: 10.1126/science.abd2438.
- Lei, W. (2017). *pycmt3d [software]*. Version 1.0. Last accessed 2023-05-26. URL: <https://github.com/wjlei1990/pycmt3d>.
- Leon-Rios, S., Agurto-Detzel, H., Rietbrock, A., Alvarado, A., et al. (2019). “1D-velocity structure and seismotectonics of the Ecuadorian margin inferred from the 2016 Mw7.8 Pedernales aftershock sequence”. *Tectonophysics* 767, p. 228165. DOI: 10.1016/j.tecto.2019.228165.
- Leon-Rios, S., Bie, L., Agurto-Detzel, H., Rietbrock, A., et al. (2021). “3D Local Earthquake Tomography of the Ecuadorian Margin in the Source Area of the 2016 Mw7.8 Pedernales Earthquake”. *Journal of Geophysical Research: Solid Earth* 126.3. DOI: 10.1029/2020JB020701.
- Lim, H., Kim, Y., Song, T.-R. A., and Shen, X. (2017). “Measurement of seismometer orientation using the tangential P-wave receiver function based on harmonic decomposition”. *Geophysical Journal International* 212.3, pp. 1747–1765. DOI: 10.1093/gji/ggx515.
- Lindner, M., Rietbrock, A., Bie, L., Clouard, V., et al. (2019). “Re-evaluation of the 2007 Mw7.4 intermediate-depth Martinique earthquake: evidence for rupture on orthogonal faults”. In: *AGU Fall Meeting Abstracts*. Vol. 2019, T31D-0277, T31D–0277.
- Lindner, M., Rietbrock, A., Bie, L., Goes, S., Collier, J., Rychert, C., Harmon, N., Hicks, S. P., Henstock, T., and the VOILA working group (2022). “Bayesian regional moment tensor from ocean bottom seismograms recorded in the Lesser Antilles: implications for regional stress field”. *Geophysical Journal International* 233.2, pp. 1036–1054. DOI: 10.1093/gji/ggac494.
- Lindner, M., Rietbrock, A., Bie, L., Goes, S., and Gao, Y.-J. (2023). “Complex Martinique intermediate-depth earthquake reactivates early Atlantic break-up structures”. *Geophysical Research Letters*. Submitted.
- Lindsay, J. M. and Robertson, R. E. A. (2018). “Integrating Volcanic Hazard Data in a Systematic Approach to Develop Volcanic Hazard Maps in the Lesser Antilles”. *Frontiers in Earth Science* 6:42. DOI: 10.3389/feart.2018.00042.
- Liu, Q., Polet, J., Komatitsch, D., and Tromp, J. (2004). “Spectral-Element Moment Tensor Inversions for Earthquakes in Southern California”. *Bulletin of the Seismological Society of America* 94.5, pp. 1748–1761. DOI: 10.1785/012004038.
- Liverpool University (2014). *Seismic Data in North West of UK*. Last accessed 2023-05-26. DOI: 10.7914/SN/LV. URL: <https://www.fdsn.org/networks/detail/LV/>.

- Lizurek, G. (2017). “Full Moment Tensor Inversion as a Practical Tool in Case of Discrimination of Tectonic and Anthropogenic Seismicity in Poland”. *Pure and Applied Geophysics* 174, pp. 1–16. DOI: 10.1007/s00024-016-1378-9.
- Lloyd, A. J., Wiens, D. A., Zhu, H., Tromp, J., et al. (2020). “Seismic Structure of the Antarctic Upper Mantle Imaged with Adjoint Tomography”. *Journal of Geophysical Research: Solid Earth* 125.3. DOI: 10.1029/2019JB017823.
- Lomax, A. (2020). “The 2020 Mw 6.5 Monte Cristo Range, Nevada earthquake: relocated seismicity shows rupture of a complete shear-crack system”. *PREPRINT (not submitted)*. DOI: 10.31223/X5X015.
- Lomax, A. and Curtis, A. (2001). “Fast probabilistic earthquake location in 3D models using Oct-Tree importance sampling”. *Geophysical Research Abstract* 3.
- Lund, B. and Townend, J. (2007). “Calculating horizontal stress orientations with full or partial knowledge of the tectonic stress tensor”. *Geophysical Journal International* 170.3, pp. 1328–1335. DOI: 10.1111/j.1365-246X.2007.03468.x.
- Madariaga, R. and Olsen, K. (2002). “2 Earthquake Dynamics”. *International Geophysics* Vol. 81A. DOI: 10.1016/S0074-6142(02)80215-7.
- McCann, W. R. and Sykes, L. R. (1984). “Subduction of aseismic ridges beneath the Caribbean Plate: Implications for the tectonics and seismic potential of the northeastern Caribbean”. *Journal of Geophysical Research: Solid Earth* 89.B6, pp. 4493–4519. DOI: 10.1029/JB089iB06p04493.
- McGuire, J. J., Zhao, L., and Jordan, T. H. (2001). “Teleseismic inversion for the second degree moments of earthquake space–time distributions”. *Geophysical Journal International* 145.3, pp. 661–678. DOI: 10.1046/j.1365-246x.2001.01414.x.
- McKenzie, D. P. (1969). “The relation between fault plane solutions for earthquakes and the directions of the principal stresses”. *Bulletin of the Seismological Society of America* 59.2, pp. 591–601. DOI: 10.1785/BSSA0590020591.
- McNamara, D. E. and Buland, R. P. (2004). “Ambient Noise Levels in the Continental United States”. *Bulletin of the Seismological Society of America* 94.4, pp. 1517–1527. DOI: 10.1785/012003001.
- Meagher, D. (1982). “The Octree Encoding Method for Efficient Solid Modeling”. Technical report.
- Melekhova, E., Schlaphorst, D., Blundy, J., Kendall, J.-M., Connolly, C., McCarthy, A., and Arculus, R. (2019). “Lateral variation in crustal structure along the Lesser Antilles arc from petrology of crustal xenoliths and seismic receiver functions”. *Earth and Planetary Science Letters* 516, pp. 12–24. DOI: 10.1016/j.epsl.2019.03.030.
- Meng, X., Chen, H., Niu, F., Tang, Y., Yin, C., and Wu, F. (2018). “Microseismic Monitoring of Stimulating Shale Gas Reservoir in SW China: 1. An Improved Matching and Locating Technique for Downhole Monitoring”. *Journal of Geophysical Research: Solid Earth* 123.2, pp. 1643–1658. DOI: 10.1002/2017JB014488.
- Michael, A. J. (1984). “Determination of stress from slip data: Faults and folds”. *Journal of Geophysical Research: Solid Earth* 89.B13, pp. 11517–11526. DOI: 10.1029/JB089iB13p11517.
- Müller, R. D., Zahirovic, S., Williams, S. E., Cannon, J., et al. (2019). “A Global Plate Model Including Lithospheric Deformation Along Major Rifts and Orogens Since the Triassic”. *Tectonics* 38.6, pp. 1884–1907. DOI: 10.1029/2018TC005462.
- Nabelek, J. L. (1984). “Determination of earthquake source parameters from inversion of body waves”. PhD thesis. Massachusetts Institute of Technology: Department of Earth, Atmospheric, and Planetary Sciences.

- Nagorsen-Rinke, S., Lee, J., and Calvert, A. (2013). “Pliocene sinistral slip across the Adobe Hills, eastern California–western Nevada: Kinematics of fault slip transfer across the Mina deflection”. *Geosphere* 9.1, pp. 37–53. DOI: 10.1130/GES00825.1.
- Nakano, H. (1923). “Notes on the nature of forces which give rise to the earthquake motions”. *Seismol Bull Centr Meteorol Obs, Tokyo* 1, pp. 92–120.
- Nakano, M., Kumagai, H., and Inoue, H. (2008). “Waveform inversion in the frequency domain for the simultaneous determination of earthquake source mechanism and moment function”. *Geophysical Journal International* 173.3, pp. 1000–1011. DOI: 10.1111/j.1365-246X.2008.03783.x.
- Nishimura, T. (2011). *Volcanic Earthquakes and Tremor in Japan*. Kyoto University Press. URL: <https://books.google.de/books?id=hxSiuAAACAAJ>.
- OGA (2019). *The Oil and Gas Authority, Interim report of the scientific analysis of data gathered from Cuadrilla’s operations at Preston New Road. 2019*. Last accessed 2020-08-6. URL: <https://www.ogauthority.co.uk/media/6149/summary-of-pnr1z-interim-reports.pdf>.
- Okuwaki, R., Hicks, S. P., Craig, T. J., Fan, W., Goes, S., Wright, T. J., and Yagi, Y. (2021). “Illuminating a Contorted Slab With a Complex Intraslab Rupture Evolution During the 2021 Mw 7.3 East Cape, New Zealand Earthquake”. *Geophysical Research Letters* 48.24. DOI: 10.1029/2021GL095117.
- Oldow, J. S. (2003). “Active transtensional boundary zone between the western Great Basin and Sierra Nevada block, western U.S. Cordillera”. *Geology* 31.12, pp. 1033–1036. DOI: 10.1130/G19838.1.
- Oldow, J. S., Kohler, G., and Donelick, R. A. (1994). “Late Cenozoic extensional transfer in the Walker Lane strike-slip belt, Nevada”. *Geology* 22.7, pp. 637–640. DOI: 10.1130/0091-7613(1994)022<0637:LCETIT>2.3.CO;2.
- Patriat, M., Pichot, T., Westbrook, G., Umler, M., Deville, E., Bénard, F., Roest, W., Loubrieu, B., and the ANTIPLAC Cruise Party (2011). “Evidence for Quaternary convergence across the North America–South America plate boundary zone, east of the Lesser Antilles”. *Geology* 39.10, pp. 979–982. DOI: 10.1130/G32474.1.
- Paulatto, M., Laigle, M., Galve, A., Charvis, P., Sapin, M., Bayrakci, G., Evain, M., and Kopp, H. (2017). “Dehydration of subducting slow-spread oceanic lithosphere in the Lesser Antilles”. *Nature Communications* 8. DOI: 10.1038/ncomms15980.
- Pavlis, N. K., Holmes, S. A., Kenyon, S. C., and Factor, J. K. (2012). “The development and evaluation of the Earth Gravitational Model 2008 (EGM2008)”. *Journal of Geophysical Research: Solid Earth* 117.B4. DOI: 10.1029/2011JB008916.
- Persh, S. E. and Houston, H. (2004). “Strongly Depth-Dependent Aftershock Production in Deep Earthquakes”. *Bulletin of the Seismological Society of America* 94.5, pp. 1808–1816. DOI: 10.1785/012003191.
- Petersen, G. M., Cesca, S., Heimann, S., Niemz, P., Dahm, T., Kühn, D., Kummerow, J., Plenefisch, T., and the AlpArray and AlpArray-Swath-Dworking groups (2021). “Regional centroid moment tensor inversion of small to moderate earthquakes in the Alps using the dense AlpArray seismic network: challenges and seismotectonic insights”. *Solid Earth* 12.6, pp. 1233–1257. DOI: 10.5194/se-12-1233-2021.
- Peterson, J. (1993). “Observations and modeling of seismic background noise”. *U.S. Geological Survey Open-File Report*, pp. 93–322.
- Pindell, J., Kennan, L., Maresch, W., Stanek, K., Draper, G., and Higgs, R. (2005). “Plate-kinematics and crustal dynamics of circum-Caribbean arc-continent interactions: Tectonic controls on basin



- development in Proto-Caribbean margins”. *Special Paper of the Geological Society of America* 394, pp. 7–52. DOI: 10.1130/2005.2394(01).
- Pindell, J. L. (1994). “Evolution of the Gulf of Mexico and the Caribbean”. In: *Caribbean Geology: An Introduction*. Ed. by S. Donovan, T. Jackson, and the University of the West Indies Publishers’ Association. University of the West Indies Publishers’ Association. Chap. 10, pp. 13–39.
- Plenefisch, T. and Bonjer, K.-P. (1997). “The stress field in the Rhine Graben area inferred from earthquake focal mechanisms and estimation of frictional parameters”. *Tectonophysics* 275.1, pp. 71–97. DOI: 10.1016/S0040-1951(97)00016-4.
- Plenefisch, T. (1996). “Untersuchungen des Spannungsfeldes im Bereich des Rheingrabens mittels der Inversion von Herdflächenlösungen und Abschätzung der bruchspezifischen Reibungsparameter”. PhD thesis. University of Karlsruhe.
- Pondrelli, S. (2002). *European-Mediterranean Regional Centroid-Moment Tensors Catalog (RCMT) [Data set]*. <https://doi.org/10.13127/rcmt/euromed>. DOI: 10.13127/rcmt/euromed.
- Pondrelli, S., Salimbeni, S., Morelli, A., Ekström, G., Postpischl, L., Vannucci, G., and Boschi, E. (2011). “European–Mediterranean Regional Centroid Moment Tensor catalog: Solutions for 2005–2008”. *Physics of the Earth and Planetary Interiors* 185.3, pp. 74–81. DOI: 10.1016/j.pepi.2011.01.007.
- Prieto, G., Beroza, G., Barrett, S., López, G., and Florez, M. (2012). “Earthquake nests as natural laboratories for the study of intermediate-depth earthquake mechanics”. *Tectonophysics* 570–571, pp. 42–56. DOI: 10.1016/j.tecto.2012.07.019.
- Pugh, D. J., White, R. S., and Christie, P. A. F. (2016). “A Bayesian method for microseismic source inversion”. *Geophysical Journal International* 206.2, pp. 1009–1038. DOI: 10.1093/gji/ggw186.
- Pugh, D. J. (2015). “Bayesian Source Inversion of Microseismic Events.” PhD thesis. University of Cambridge.
- Quinteros, J., Strollo, A., Evans, P. L., Hanka, W., et al. (2021). “The GEOFON Program in 2020”. *Seismological Research Letters* 92.3, pp. 1610–1622. DOI: 10.1785/0220200415.
- Ramos, M. D., Thakur, P., Huang, Y., Harris, R. A., and Ryan, K. J. (2022). “Working with Dynamic Earthquake Rupture Models: A Practical Guide”. *Seismological Research Letters* 93.4, pp. 2096–2110. DOI: 10.1785/0220220022.
- Ranero, C. R., Villaseñor, A., Phipps Morgan, J., and Weinrebe, W. (2005). “Relationship between bend-faulting at trenches and intermediate-depth seismicity”. *Geochemistry, Geophysics, Geosystems* 6.12. DOI: 10.1029/2005GC000997.
- Reid, H. (1910). “The Mechanics of the Earthquake, The California Earthquake of April 18, 1906”. *Report of the State Investigation Commission* 2.
- Riedesel, M. A. and Jordan, T. H. (1989). “Display and assessment of seismic moment tensors”. *Bulletin of the Seismological Society of America* 79.1, pp. 85–100. DOI: 10.1785/BSSA0790010085.
- Ringler, A. T., Hutt, C. R., Persefield, K., and Gee, L. S. (2013). “Seismic Station Installation Orientation Errors at ANSS and IRIS/USGS Stations”. *Seismological Research Letters* 84.6, pp. 926–931. DOI: 10.1785/0220130072.
- Rogers, J. and Santosh, M. (2004). *Continents and Supercontinents*. Oxford University Press.
- Romanowicz, B., Stakes, D., Montagner, J.-P., Tarits, P., Uhrhammer, R., Begnaud, M., Pasyanos, M., Karczewski, J., Etchemendy, S., and Neuhauser, D. (1998). “MOISE: A pilot experiment towards long term sea-floor geophysical observatories”. *Earth Planets Space* 50, pp. 927–937. DOI: 10.1186/BF03352188.

- Rontogianni, S., Konstantinou, K., Melis, N., and Evangelidis, C. (2010). “Slab stress field in the Hellenic subduction zone as inferred from intermediate depth earthquakes”. *AGU Fall Meeting Abstracts* 63. DOI: 10.5047/eps.2010.11.011.
- Rösler, B. and Stein, S. (2022). “Consistency of Non-Double-Couple Components of Seismic Moment Tensors with Earthquake Magnitude and Mechanism”. *Seismological Research Letters* 93.3, pp. 1510–1523. DOI: 10.1785/0220210188.
- Rösler, B., Stein, S., and Spencer, B. (2023). “When are Non-Double-Couple Components of Seismic Moment Tensors Reliable?” *Seismica* 2. DOI: 10.26443/seismica.v2i1.241.
- Ruhl, C., Morton, E., Bormann, J., Hatch-Ibarra, R., Ichinose, G., and Smith, K. (2021). “Complex Fault Geometry of the 2020 M<sub>w</sub> 6.5 Monte Cristo Range, Nevada, Earthquake Sequence”. *Seismological Research Letters* 92, pp. 1876–1890. DOI: 10.1785/0220200345.
- Ruiz, M., Galve, A., Monfret, T., Sapin, M., et al. (2013). “Seismic activity offshore Martinique and Dominica islands (Central Lesser Antilles subduction zone) from temporary onshore and offshore seismic networks”. *Tectonophysics* 603, pp. 68–78. DOI: 10.1016/j.tecto.2011.08.006.
- Russo, R. M., Okal, E. A., and Rowley, K. C. (1992). “Historical seismicity of the southeastern Caribbean and tectonic implications”. *Pure and Applied Geophysics* 139.1, pp. 87–120. DOI: 10.1007/BF00876827.
- Satake, K. (2014). “Advances in earthquake and tsunami sciences and disaster risk reduction since the 2004 Indian Ocean tsunami”. *Geoscience Letters* 1. DOI: 10.1186/s40562-014-0015-7.
- Saul, J., Becker, J., and Hanka, W. (2011). “Global moment tensor computation at GFZ Potsdam”. *AGU 2011 Fall Meeting (San Francisco 2011)*. URL: [https://gfzpublic.gfz-potsdam.de/pubman/item/item\\_244630](https://gfzpublic.gfz-potsdam.de/pubman/item/item_244630).
- Scarinci, A., Waheed, U. b., Gu, C., Ren, X., Dia, B. M., Kaka, S., Fehler, M., and Marzouk, Y. (2023). “Robust Bayesian moment tensor inversion with optimal transport misfits: layered medium approximations to the 3-D SEG-EAGE overthrust velocity model”. *Geophysical Journal International* 234.2, pp. 1169–1190. DOI: 10.1093/gji/ggad116.
- Schaff, D. P. and Richards, P. G. (2014). “Improvements in magnitude precision, using the statistics of relative amplitudes measured by cross correlation”. *Geophysical Journal International* 197.1, pp. 335–350. DOI: 10.1093/gji/ggt433.
- Scherbaum, F. (2013). *Of Poles and Zeros: Fundamentals of Digital Seismology*. Modern Approaches in Geophysics. Springer Dordrecht. DOI: 10.1007/978-1-4020-6861-4.
- Schlaphorst, D., Kendall, J.-M., Baptie, B., Latchman, J. L., and Tait, S. (2017). “Gaps, tears and seismic anisotropy around the subducting slabs of the Antilles”. *Tectonophysics* 698, pp. 65–78. DOI: 10.1016/j.tecto.2017.01.002.
- Schlaphorst, D., Kendall, J.-M., Collier, J. S., Verdon, J. P., Blundy, J., Baptie, B., Latchman, J. L., Massin, F., and Bouin, M.-P. (2016). “Water, oceanic fracture zones and the lubrication of subducting plate boundaries—insights from seismicity”. *Geophysical Journal International* 204.3, pp. 1405–1420. DOI: 10.1093/gji/ggv509.
- Schlaphorst, D., Melekhova, E., Kendall, J.-M., Blundy, J., and Latchman, J. (2018). “Probing layered arc crust in the Lesser Antilles using receiver functions”. *Royal Society Open Science* 5.11. DOI: 10.1098/rsos.180764.
- Schmidt-Aursch, M. C., Almendros, J., Geissler, W., and Wilcock, W. (2022). “Noise characteristics of ocean-bottom seismometer data in the Bransfield Strait, Antarctica”. In: *48. Sitzung der AG Seismologie*.

- Scognamiglio, L., Tinti, E., Casarotti, E., Pucci, S., Villani, F., Cocco, M., Magnoni, F., Michelini, A., and Dreger, D. (2018). “Complex Fault Geometry and Rupture Dynamics of the MW 6.5, 30 October 2016, Central Italy Earthquake”. *Journal of Geophysical Research: Solid Earth* 123.4, pp. 2943–2964. DOI: 10.1002/2018JB015603.
- Sen, A. T., Cesca, S., Bischoff, M., Meier, T., and Dahm, T. (2013). “Automated full moment tensor inversion of coal mining-induced seismicity”. *Geophysical Journal International* 195.2, pp. 1267–1281. DOI: 10.1093/gji/ggt300.
- Serpetsidaki, A., Sokos, E., and Tselentis, G.-A. (2016). “A ten year Moment Tensor database for Western Greece”. *Physics and Chemistry of the Earth, Parts A/B/C* 95. Studying Seismic Sources: Theory, Methods and Applications, pp. 2–9. DOI: 10.1016/j.pce.2016.04.007.
- Serrano, L., Ferrari, L., Martínez, M. L., Petrone, C. M., and Jaramillo, C. (2011). “An integrative geologic, geochronologic and geochemical study of Gorgona Island, Colombia: Implications for the formation of the Caribbean Large Igneous Province”. *Earth and Planetary Science Letters* 309.3, pp. 324–336. DOI: 10.1016/j.epsl.2011.07.011.
- Sethanant, I., Nissen, E., Pousse-Beltran, L., Bergman, E., and Pierce, I. (2023). “The 2020 Mw 6.5 Monte Cristo Range, Nevada, Earthquake: Anatomy of a Crossing-Fault Rupture through a Region of Highly Distributed Deformation”. *Bulletin of the Seismological Society of America* 113.3, pp. 948–975. DOI: 10.1785/0120220166.
- Shearer, P. M. (2009). *Introduction to Seismology*. 2nd ed. Cambridge University Press. DOI: 10.1017/CBO9780511841552.
- Shelly, D. R., Beroza, G. C., and Ide, S. (2007). “Non-volcanic tremor and low-frequency earthquake swarms”. *Nature* 446.7133, pp. 305–307. DOI: 10.1038/nature05666.
- Simmons, N. A., Myers, S. C., Johannesson, G., and Matzel, E. (2012). “LLNL-G3Dv3: Global P wave tomography model for improved regional and teleseismic travel time prediction”. *Journal of Geophysical Research: Solid Earth* 117.B10. DOI: 10.1029/2012JB009525.
- Simmons, N. A., Myers, S. C., Morency, C., Chiang, A., and Knapp, D. R. (2021). “SPiRaL: a multiresolution global tomography model of seismic wave speeds and radial anisotropy variations in the crust and mantle”. *Geophysical Journal International* 227.2, pp. 1366–1391. DOI: 10.1093/gji/ggab277.
- Skoumal, R. J., Brudzinski, M. R., and Currie, B. S. (2016). “An efficient repeating signal detector to investigate earthquake swarms”. *Journal of Geophysical Research: Solid Earth* 121.8, pp. 5880–5897. DOI: 10.1002/2016JB012981.
- Snoke, J. A. (2003). “85.12 FOCMEC: FOCal MECHANism determinations”. *International Geophysics* 81, pp. 1629–1630. DOI: 10.1016/S0074-6142(03)80291-7.
- Sokos, E. and Zahradnik, J. (2013). “Evaluating Centroid-Moment-Tensor Uncertainty in the New Version of ISOLA Software”. *Seismological Research Letters* 84, pp. 656–665. DOI: 10.1785/0220130002.
- Sokos, E. N. and Zahradnik, J. (2008). “ISOLA a Fortran code and a Matlab GUI to perform multiple-point source inversion of seismic data”. *Computers and Geosciences* 34.8, pp. 967–977. DOI: 10.1016/j.cageo.2007.07.005.
- Staehler, S. and Sigloch, K. (2014). “Fully probabilistic seismic source inversion – Part 1: Efficient parameterisation”. *Solid Earth* 5, pp. 1055–1069. DOI: 10.5194/se-5-1055-2014.
- Stark, H.-G. (2005). *Wavelets and Signal Processing: An Application-Based Introduction*. Springer Berlin, Heidelberg. DOI: 10.1007/3-540-27481-2.

- Stein, S. and Wysession, M. (2009). *An Introduction to Seismology, Earthquakes, and Earth Structure*. 9. Malden, Mass.: Blackwell.
- Stump, B. W. and Johnson, L. R. (1977). "The determination of source properties by the linear inversion of seismograms". *Bulletin of the Seismological Society of America* 67.6, pp. 1489–1502. DOI: 10.1785/BSSA0670061489.
- Stump, B. W. and Johnson, L. R. (1982). "Higher-degree moment tensors – the importance of source finiteness and rupture propagation on seismograms". *Geophysical Journal International* 69.3, pp. 721–743. DOI: 10.1111/j.1365-246X.1982.tb02772.x.
- Tape, W. and Tape, C. (2012). "A geometric setting for moment tensors". *Geophysical Journal International* 190, pp. 476–498. DOI: 10.1111/j.1365-246X.2012.05491.x.
- Tape, W. and Tape, C. (2013). "The classical model for moment tensors". *Geophysical Journal International* 195.3, pp. 1701–1720. DOI: 10.1093/gji/ggt302.
- Tape, W. and Tape, C. (2015). "A uniform parametrization of moment tensors". *Geophysical Journal International* 202.3, pp. 2074–2081. DOI: 10.1093/gji/ggv262.
- Tape, W. and Tape, C. (2016). "A confidence parameter for seismic moment tensors". *Geophysical Journal International* 205.2, pp. 938–953. DOI: 10.1093/gji/ggw057.
- Tape, W. and Tape, C. (2018). "The eigenvalue lune as a window on moment tensors". *Geophysical Journal International* 216.1, pp. 19–33. DOI: 10.1093/gji/ggy373.
- Tarantola, A. (2004). *Inverse Problem Theory and Methods for Model Parameter Estimation*. USA: Society for Industrial and Applied Mathematics. ISBN: 0898715725.
- Tarantola, A. and Valette, B. (1982). "Inverse problems = Quest for information". *Journal of Geophysics* 50, pp. 159–170.
- Tashiro, Y. (1977). "On methods for generating uniform random points on the surface of a sphere." *Annals of the Institute of Statistical Mathematics* 29, pp. 295–300. DOI: 10.1007/BF02532791.
- Thurin, J., Tape, C., and Modrak, R. (2022). "Multi-Event Explosive Seismic Source for the 2022 Mw 6.3 Hunga Tonga Submarine Volcanic Eruption". *The Seismic Record* 2.4, pp. 217–226. DOI: 10.1785/0320220027.
- Trabattoni, A., Barruol, G., Dreo, R., Boudraa, A.-O., and Fontaine, F. (2020). "Orienting and locating ocean-bottom seismometers from ship noise analysis". *Geophysical Journal International* 220, pp. 1774–1790. DOI: 10.1093/gji/ggz519.
- Tsang, L. L., Vergnolle, M., Twardzik, C., Sladen, A., Nocquet, J.-M., Rolandone, F., Agurto-Detzel, H., Cavalié, O., Jarrin, P., and Mothes, P. (2019). "Imaging rapid early afterslip of the 2016 Pedernales earthquake, Ecuador". *Earth and Planetary Science Letters* 524. DOI: 10.1016/j.epsl.2019.115724.
- Uchide, T. (2020). "Focal mechanisms of small earthquakes beneath the Japanese islands based on first-motion polarities picked using deep learning". *Geophysical Journal International* 223.3, pp. 1658–1671. DOI: 10.1093/gji/ggaa401.
- U.S. Geological Survey (2022). *Earthquake Hazards Program, 2017, Advanced National Seismic System (ANSS) Comprehensive Catalog of Earthquake Events and Products: Various*. DOI: 10.5066/F7MS3QZH. (Visited on 10/07/2022).
- Vackář, J., Burjánek, J., Gallovič, F., Zahradník, J., and Clinton, J. (2017). "Bayesian ISOLA: new tool for automated centroid moment tensor inversion". *Geophysical Journal International* 210.2, pp. 693–705. DOI: 10.1093/gji/ggx158.

- Van Benthem, S. and Govers, R. (2010). “The Caribbean plate: Pulled, pushed, or dragged?” *Journal of Geophysical Research: Solid Earth* 115.B10. DOI: 10.1029/2009JB006950.
- Van Rijnsingen, E. M., Calais, E., Jolivet, R., de Chabali er, J.-B., Jara, J., Symithe, S., Robertson, R., and Ryan, G. A. (2021). “Inferring Interseismic Coupling Along the Lesser Antilles Arc: A Bayesian Approach”. *Journal of Geophysical Research: Solid Earth* 126.2, e2020JB020677. DOI: 10.1029/2020JB020677.
- Vasyura-Bathke, H., Dettmer, J., Dutta, R., Mai, P. M., and J  nsson, S. (2021). “Accounting for theory errors with empirical Bayesian noise models in nonlinear centroid moment tensor estimation”. *Geophysical Journal International* 225.2, pp. 1412–1431. DOI: 10.1093/gji/ggab034.
- Vasyura-Bathke, H., Dettmer, J., Steinberg, A., Heimann, S., Isken, M. P., Zielke, O., Mai, P. M., Sudhaus, H., and J  nsson, S. (2020). “The Bayesian Earthquake Analysis Tool”. *Seismological Research Letters* 91.2A, pp. 1003–1018. DOI: 10.1785/0220190075.
- Vavry  uk, V. (2014). “Iterative joint inversion for stress and fault orientations from focal mechanisms”. *Geophysical Journal International* 199, pp. 69–77. DOI: 10.1093/gji/ggu224.
- Vavry  uk, V., Adamov  , P., Doubravov  , J., and Hor  lek, J. (2022). “Moment tensor catalogue of earthquakes in West Bohemia from 2008 to 2018”. *Earth System Science Data* 14.5, pp. 2179–2194. DOI: 10.5194/essd-14-2179-2022.
- Vavry  uk, V. (2011). “Tensile earthquakes: Theory, modeling, and inversion”. *Journal of Geophysical Research: Solid Earth* 116.B12. DOI: 10.1029/2011JB008770.
- Vavry  uk, V. (2015). “Moment tensor decompositions revisited”. *Journal of Seismology* 19, 231–252. DOI: 10.1007/s10950-014-9463-y.
- Vavry  uk, V. and K  hn, D. (2012). “Moment tensor inversion of waveforms: a two-step time-frequency approach”. *Geophysical Journal International* 190.3, pp. 1761–1776. DOI: 10.1111/j.1365-246X.2012.05592.x.
- Voigt, W. (1928). *Lehrbuch der Kristallphysik (mit Ausschluss der Kristalloptik)*. Teubner Verlag, Leipzig, Germany. URL: <https://books.google.de/books?id=lHm5nQEACAAJ>.
- Wadati, K. (1928). “Shallow and deep earthquakes.” *Geophysical Magazine* 1, pp. 162–202.
- Wadge, G. (1984). “Comparison of volcanic production rates and subduction rates in the Lesser Antilles and Central America”. *Geology* 12.9, pp. 555–558. DOI: 10.1130/0091-7613(1984)12<555:COVPRA>2.0.CO;2.
- Wadge, G. and Shepherd, J. (1984). “Segmentation of the Lesser Antilles subduction zone”. *Earth and Planetary Science Letters* 71.2, pp. 297–304. DOI: 10.1016/0012-821X(84)90094-3.
- Waldhauser, F. (2001). “hypoDD – A Program to Compute Double-Difference Hypocenter Locations”. In: DOI: 10.3133/ofr01113.
- Wang, P.-S., Liu, Y., Guo, Y.-X., Sun, C.-Y., and Tong, X. (2017a). “O-CNN: Octree-Based Convolutional Neural Networks for 3D Shape Analysis”. *ACM Transactions on Graphics* 36.4. DOI: 10.1145/3072959.3073608.
- Wang, R. (1999). “A simple orthonormalization method for stable and efficient computation of Green’s functions”. *Bulletin of the Seismological Society of America* 89.3, pp. 733–741. DOI: 10.1785/BSSA0890030733.
- Wang, R., Heimann, S., Zhang, Y., Wang, H., and Dahm, T. (2017b). “Complete synthetic seismograms based on a spherical self-gravitating Earth model with an atmosphere-ocean-mantle-core structure”. *Geophysical Journal International* 210.3, pp. 1739–1764. DOI: 10.1093/gji/ggx259.

- Wang, X., Chen, Q.-f., Li, J., and Wei, S. (2016). “Seismic Sensor Misorientation Measurement Using P-Wave Particle Motion: An Application to the NECsaids Array”. *Seismological Research Letters* 87, pp. 901–911. DOI: 10.1785/0220160005.
- Wang, X. and Zhan, Z. (2020). “Seismotectonics and Fault Geometries of the 2019 Ridgecrest Sequence: Insight From Aftershock Moment Tensor Catalog Using 3-D Green’s Functions”. *Journal of Geophysical Research: Solid Earth* 125.5. DOI: 10.1029/2020JB019577.
- Warren, L. M., Baluyut, E. C., Osburg, T., Lisac, K., and Kokkinen, S. (2015). “Fault plane orientations of intermediate-depth and deep-focus earthquakes in the Japan-Kuril-Kamchatka subduction zone”. *Journal of Geophysical Research: Solid Earth* 120.12, pp. 8366–8382. DOI: 10.1002/2015JB012463.
- Wesnousky, S. G. (2005). “Active faulting in the Walker Lane”. *Tectonics* 24.3. DOI: 10.1029/2004TC001645.
- Westbrook, G. K., Mascle, A., and Biju-Duval, B. (1984). “Geophysics and the Structure of the Lesser Antilles Forearc”. *Proceedings of the Ocean Drilling Program, Scientific Results* 78a. DOI: 10.2973/DSDP.PROC.78A.102.1984.
- Wilson, M. P., Worrall, F., Davies, R. J., and Almond, S. (2018). “Fracking: How far from faults?” *Geomechanics and Geophysics for Geo-Energy and Geo-Resources* 4.2, pp. 193–199. DOI: 10.1007/s40948-018-0081-y.
- Yagi, Y. and Fukahata, Y. (2008). “Importance of covariance components in inversion analyses of densely sampled observed data: an application to waveform data inversion for seismic source processes”. *Geophysical Journal International* 175.1, pp. 215–221. DOI: 10.1111/j.1365-246X.2008.03884.x.
- Yagi, Y. and Fukahata, Y. (2011). “Introduction of uncertainty of Green’s function into waveform inversion for seismic source processes”. *Geophysical Journal International* 186.2, pp. 711–720. DOI: 10.1111/j.1365-246X.2011.05043.x.
- Yang, X., Stump, B. W., and Macphail, M. D. (2018). “The Frequency-Domain Moment-Tensor Inversion: Retrieving the Complete Source Moment-Tensor Spectra and Time Histories”. In: *Moment Tensor Solutions: A Useful Tool for Seismotectonics*. Ed. by S. D’Amico. Cham: Springer International Publishing, pp. 55–74. DOI: 10.1007/978-3-319-77359-9\_3.
- Yang, Z., Sheehan, A. F., Collins, J. A., and Laske, G. (2012). “The character of seafloor ambient noise recorded offshore New Zealand: Results from the MOANA ocean bottom seismic experiment”. *Geochemistry, Geophysics, Geosystems* 13.10. DOI: 10.1029/2012GC004201.
- Yannick, C., Deville, E., Desaubliaux, G., Griboulard, R., Huyghe, P., Mascle, A., Mascle, G., Noble, M., Padron, C., and Schmitz, J. (2010). “The Orinoco turbidite system: Tectonic controls on sea-floor morphology and sedimentation”. *AAPG Bulletin* 94, pp. 869–887. DOI: 10.1306/11020909021.
- Yoon, C. E., O’Reilly, O., Bergen, K. J., and Beroza, G. C. (2015). “Earthquake detection through computationally efficient similarity search”. *Science advances* 1.11. DOI: 10.1126/sciadv.1501057.
- Zha, Y., Webb, S. C., and Menke, W. (2013). “Determining the orientations of ocean bottom seismometers using ambient noise correlation”. *Geophysical Research Letters* 40.14, pp. 3585–3590. DOI: 10.1002/grl.50698.
- Zhao, L.-S. and Helmberger, D. V. (1994). “Source estimation from broadband regional seismograms”. *Bulletin of the Seismological Society of America* 84.1, pp. 91–104. DOI: 10.1785/BSSA0840010091.
- Zheng, A., Chen, X., and Xu, W. (2020). “Present-Day Deformation Mechanism of the Northeastern Mina Deflection Revealed by the 2020 Mw 6.5 Monte Cristo Range Earthquake”. *Geophysical Research Letters* 47.22. DOI: 10.1029/2020GL090142.

- Zhu, L. and Ben-Zion, Y. (2013). "Parametrization of general seismic potency and moment tensors for source inversion of seismic waveform data". *Geophysical Journal International* 194.2, pp. 839–843. DOI: 10.1093/gji/ggt137.
- Zhu, L. and Zhou, X. (2016). "Seismic moment tensor inversion using 3D velocity model and its application to the 2013 Lushan earthquake sequence". *Physics and Chemistry of the Earth, Parts A/B/C* 95, pp. 10–18. DOI: 10.1016/j.pce.2016.01.002.

## Part V

# Appendix



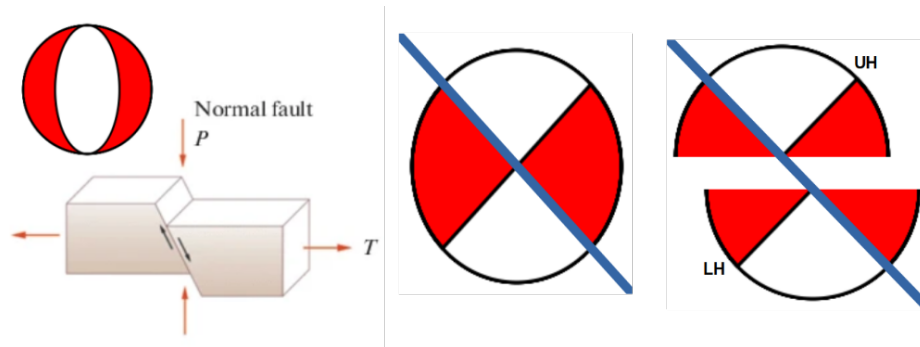


# Appendix A

## Chapter 3

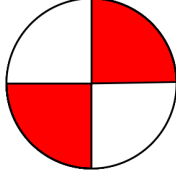
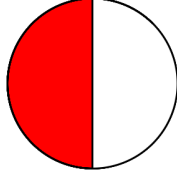
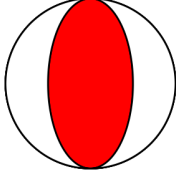
### Upper/Lower hemisphere projection

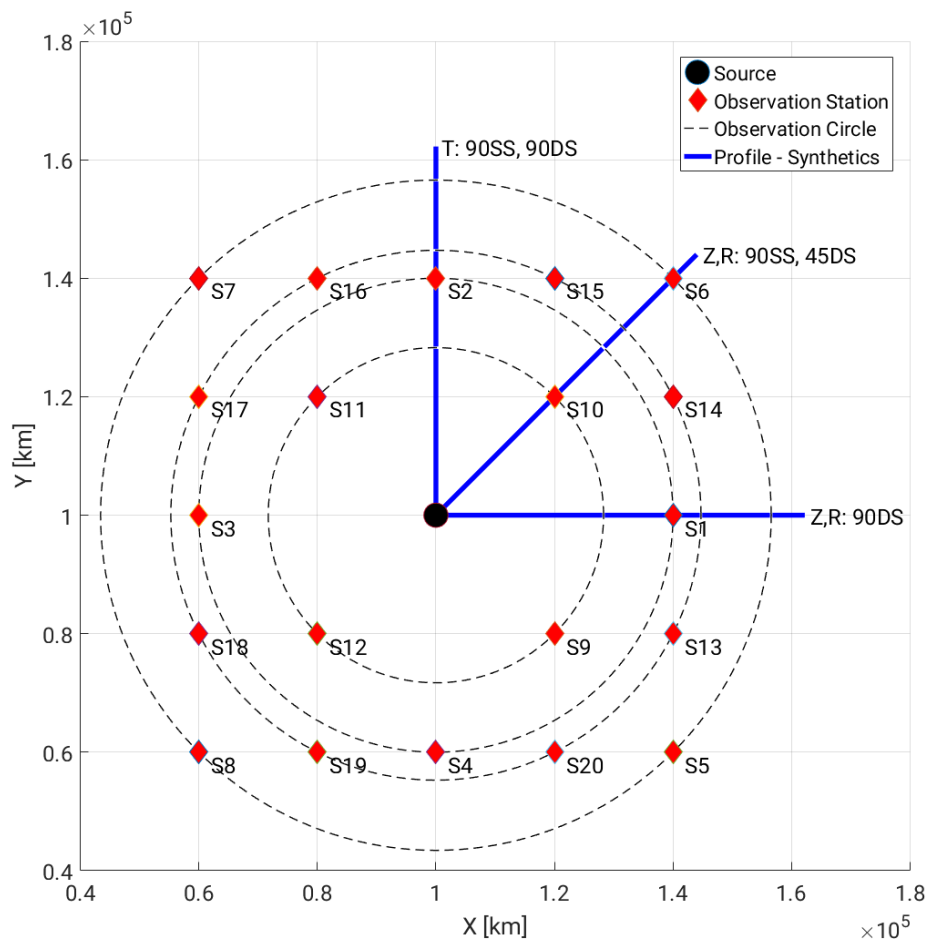
The beachball representation is projected onto the earth's surface, hence it depicts the fault from either top down or bottom up. Tension axis T, which represents the direction of extension, is associated to the red area. Pressure axis P, which represents the direction of compression, is associated to the white area. This is depicted in the schematic plot, which gives you a cross-section view on the fault system. In some publications, you will stumble upon such cross-section plots which can give you additional information like how the active plane (blue) relates to other mapped geological features e.g., slab, fault. However, depending on which direction you are looking along the vertical axis (down- or upwards), the orientation of the active plane changes. Here we have to distinguish between the “Upper Hemisphere” (UH) and the “Lower Hemisphere” (LH) projection. These projections are historically motivated as we are looking at the direction of the radiated rays. In a teleseismic application, we usually observe first the down going rays which relate to the lower part of the sphere, hence the name. Usually, publications use the LH projection if not noted otherwise.



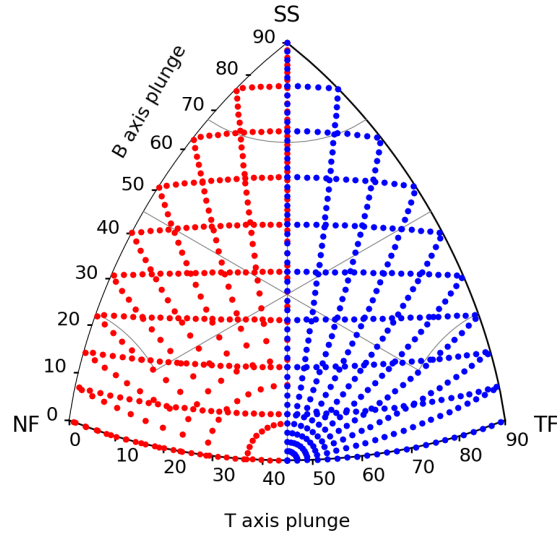
**Figure A.1:** Upper/Lower hemisphere projection of a normal fault

**Table A.1:** Fundamental mechanism for CAP.

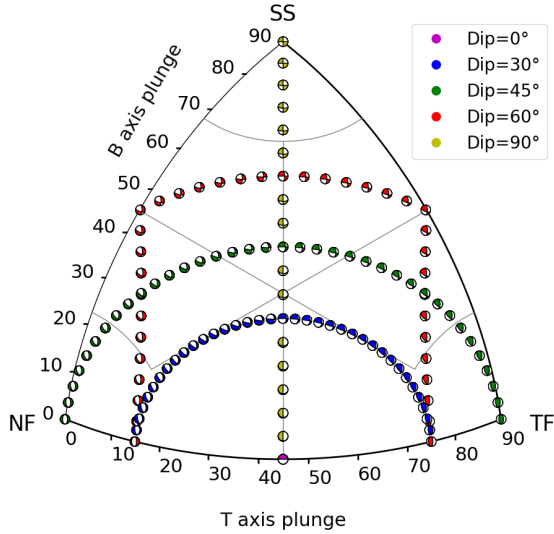
Green's functions Fundamental faults			
Beachball	Strike-Slip (90SS) 	Dip-Slip (90DS) 	Thrust fault (45DS) 
Fault angle	Strike: $\psi_s = 0^\circ$ Dip: $\delta = 90^\circ$ Rake: $\lambda = 0^\circ$	Strike: $\psi_s = 0^\circ$ Dip: $\delta = 90^\circ$ Rake: $\lambda = 90^\circ$	Strike: $\psi_s = 0^\circ$ Dip: $\delta = 45^\circ$ Rake: $\lambda = 90^\circ$
Moment tensor	$\mathbf{M} = \frac{1}{\sqrt{2}} \begin{pmatrix} 0 & 0 & 0 \\ 0 & 0 & -1 \\ 0 & -1 & 0 \end{pmatrix}$	$\mathbf{M} = \frac{1}{\sqrt{2}} \begin{pmatrix} 0 & 0 & 1 \\ 0 & 0 & 0 \\ 1 & 0 & 0 \end{pmatrix}$	$\mathbf{M} = \frac{1}{\sqrt{2}} \begin{pmatrix} 0 & 0 & 0 \\ 0 & 1 & 0 \\ 0 & 0 & -1 \end{pmatrix}$
Profil	Z \ R - Comp.: 45° to north along the T-axis T - Comp.: 0° to north along the N-axis (nodal line)	Z \ R - Comp.: 90° to north along P-axis T - Comp.: 0° to north along the N-axis (nodal line)	Z \ R - Comp.: 45° to north along the T-axis T - Comp.: not needed, CAP only used informa- tion from Z and R
Weight	$A_1 = 0.5(M_{xx} - M_{yy})\cos(2\theta) + M_{xy}\sin(2\theta)$ $A_2 = M_{xz}\cos(\theta) + M_{yz}\sin(\theta)$ $A_3 = -0.5(M_{xx} + M_{yy})$ $A_4 = 0.5(M_{xx} - M_{yy})\sin(2\theta) - M_{xy}\cos(2\theta)$ $A_5 = -M_{yz}\cos(\theta) + M_{xz}\sin(\theta)$ which is same if above equations are solved by substituting in the expressions for the element wise MT rotation $A_1 = \sin(2(\theta - \phi_s))\cos(\lambda)\sin(\delta) + 0.5\cos(2(\theta - \phi_s))\sin(\lambda)\sin(2\delta)$ $A_2 = \cos(\theta - \phi_s)\cos(\lambda)\cos(\delta) - \sin(\theta - \phi_s)\sin(\lambda)\cos(2\delta)$ $A_3 = 0.5\sin(\lambda)\sin(2\delta)$ $A_4 = \cos(2(\theta - \phi_s))\cos(\lambda)\sin(\delta) - 0.5\sin(2(\theta - \phi_s))\sin(\lambda)\sin(2\delta)$ $A_5 = -\sin(\theta - \phi_s)\cos(\lambda)\cos(\delta) - \cos(\theta - \phi_s)\sin(\lambda)\cos(2\delta)$ If the MT elements are calculated in the USE-system above equation change in the azimuthal rotational sense $\theta + \phi_s$ hence, the azimuth gets rotated counterclockwise		



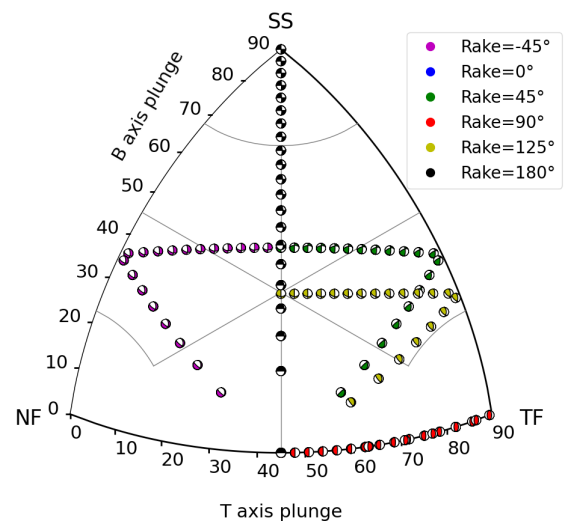
*Figure A.2: Profils used in CAP.*



(a) Comparison between direct sampling of dip in  $^{\circ}$  (blue) and parameterized sampling (dip as  $h$ ).



(b) Sampling of rake at fixed dip angles.






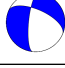
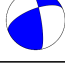
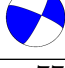
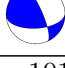
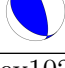



(c) Sampling of dip at fixed rake angles.






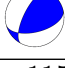
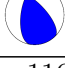
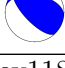







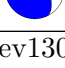
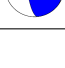
**Figure A.3:** Uniform and non-uniform sampling in a FMC - focal mechanism diagram.

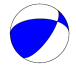
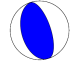

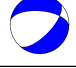
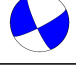
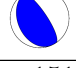
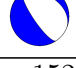










## Appendix B

### Chapter 5


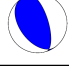
**Table B.1:** Inversion results. Depth ( $Z$ ) information is given for the located depth by (Bie et al., 2020) and the synthetic depth used for the Green's functions. The mechanisms are given in  $(s, d, r, C) = (\text{strike}, \text{dip}, \text{rake}, \text{CLVD})$ . Waveform fit is described by the variance reduction  $VR = 1 - Nl2$  (data normalized  $L2$  error). Frequency band (FB) might change for different events.

ID	$T_0$	Lat,Lon,Z	Mw	s	d	r	C	VR	FB in Hz
ev46 	2017-04-15	17.531	3.63	256	30	-116	0	0.62	0.04
	18:48:26.36	-61.085	$\pm 0.03$	106	63	-75	$\pm 0$	$\pm 0.0$	0.07
		20.77/20		$\pm 9$	$\pm 1$	$\pm 10$			
ev48 	2017-04-17	17.489	3.58	239	19	-177	0	0.58	0.04
	08:28:51.30	-61.115	$\pm 0.01$	147	89	-70	$\pm 0$	$\pm 0.0$	0.07
		14.38/15		$\pm 1$	$\pm 4$	$\pm 1$			
ev49 	2017-04-17	17.532	4.17	36	76	14	0	0.47	0.04
	16:08:01.04	-61.056	$\pm 0.1$	303	76	166	$\pm 0$	$\pm 0.0$	0.07
		14.55/15		$\pm 19$	$\pm 2$	$\pm 12$			
ev50 	2017-04-19	17.502	4.12	294	51	-152	0	0.59	0.04
	20:31:33.41	-61.003	$\pm 0.01$	185	68	-42	$\pm 0$	$\pm 0.01$	0.07
		21.67/20		$\pm 4$	$\pm 3$	$\pm 3$			
ev54 	2017-04-22	17.525	3.74	248	55	159	0	0.64	0.04
	03:48:17.91	-61.057	$\pm 0.02$	350	73	36	$\pm 0$	$\pm 0.0$	0.07
		17.76/17.5		$\pm 5$	$\pm 3$	$\pm 4$			
ev55 	2017-04-22	17.554	3.75	293	77	166	0	0.37	0.04
	09:13:53.49	-61.03	$\pm 0.03$	26	76	12	$\pm 0$	$\pm 0.01$	0.07
		16.29/15		$\pm 3$	$\pm 5$	$\pm 1$			
ev77 	2016-05-01	18.152	5.17	87	47	29	0	0.55	0.04
	10:35:05.55	-61.521	$\pm 0.09$	336	68	133	$\pm 0$	$\pm 0.01$	0.07
		30.48/30		$\pm 11$	$\pm 6$	$\pm 12$			
ev101 	2016-03-22	17.308	4.45	343	62	105	0	0.54	0.04
	14:09:06.17	-61.621	$\pm 0.02$	133	31	63	$\pm 0$	$\pm 0.0$	0.07
		39.38/40		$\pm 3$	$\pm 2$	$\pm 4$			
ev102 	2016-03-29	17.851	3.94	185	74	-101	0	0.44	0.04
	06:48:21.42	-60.873	$\pm 0.06$	43	19	-53	$\pm 0$	$\pm 0.0$	0.07
		21.6/20		$\pm 13$	$\pm 4$	$\pm 11$			
ev104 	2016-04-12	15.711	4.24	199	44	-69	0	0.37	0.04
	12:36:33.62	-61.483	$\pm 0.2$	351	48	-109	$\pm 0$	$\pm 0.01$	0.07
		10.91/10		$\pm 4$	$\pm 0$	$\pm 5$			
ev105 	2016-05-08	17.705	5.02	57	49	23	0	0.69	0.03
	13:47:34.53	-61.584	$\pm 0.08$	311	71	137	$\pm 0$	$\pm 0.0$	0.07

		32.53/32.5		$\pm 4$	$\pm 2$	$\pm 3$			
ev106 	2016-05-09	16.179	4.74	77	57	-115	0	0.41	0.035
	13:36:27.76	-60.615	$\pm 0.09$	299	40	-55	$\pm 0$	$\pm 0.0$	0.07
		32.34/32.5		$\pm 3$	$\pm 2$	$\pm 5$			
ev110 	2016-06-12	16.858	4.07	31	23	-6	0	0.64	0.04
	08:56:55.92	-60.941	$\pm 0.07$	127	87	-113	$\pm 0$	$\pm 0.01$	0.07
		13.19/12.5		$\pm 4$	$\pm 3$	$\pm 4$			
ev111 	2016-06-13	15.278	4.19	35	52	-55	0	0.43	0.035
	18:31:31.84	-61.186	$\pm 0.01$	166	49	-126	$\pm 0$	$\pm 0.01$	0.07
		145.38/150		$\pm 2$	$\pm 1$	$\pm 7$			
ev112 	2016-06-29	15.368	4.24	54	59	-52	0	0.55	0.035
	15:54:22.87	-61.119	$\pm 0.01$	178	46	-136	$\pm 0$	$\pm 0.01$	0.07
		132.18/130		$\pm 3$	$\pm 1$	$\pm 3$			
ev113 	2016-07-11	15.779	4.08	228	39	-104	0	0.66	0.035
	06:58:09.61	-61.118	$\pm 0.12$	67	52	-78	$\pm 0$	$\pm 0.01$	0.07
		23.81/20		$\pm 43$	$\pm 1$	$\pm 26$			
ev114 	2016-07-19	15.648	3.83	207	57	58	0	0.49	0.035
	18:57:40.51	-60.499	$\pm 0.02$	76	44	129	$\pm 0$	$\pm 0.01$	0.07
		36.06/35		$\pm 6$	$\pm 3$	$\pm 4$			
ev115 	2016-08-02	15.154	4.04	316	56	54	0	0.28	0.03
	07:58:32.85	-60.387	$\pm 0.01$	189	47	131	$\pm 0$	$\pm 0.02$	0.07
		46.81/45		$\pm 8$	$\pm 5$	$\pm 9$			
ev116 	2016-08-08	17.385	4.18	136	59	112	0	0.53	0.03
	10:15:56.26	-61.917	$\pm 0.03$	277	37	57	$\pm 0$	$\pm 0.01$	0.07
		62.15/60		$\pm 6$	$\pm 1$	$\pm 5$			
ev118 	2016-08-23	14.89	4.41	306	31	-106	0	0.61	0.035
	01:09:49.90	-61.231	$\pm 0.02$	146	59	-79	$\pm 0$	$\pm 0.02$	0.07
		156.59/150		$\pm 11$	$\pm 5$	$\pm 6$			
ev119 	2016-09-08	15.081	4.11	150	55	-153	0	0.29	0.05
	21:39:51.28	-61.361	$\pm 0.01$	44	68	-37	$\pm 0$	$\pm 0.0$	0.07
		182.18/180		$\pm 4$	$\pm 2$	$\pm 3$			
ev120 	2016-09-19	14.985	4.46	120	75	-19	0	0.54	0.035
	14:33:31.06	-61.418	$\pm 0.07$	216	71	-164	$\pm 0$	$\pm 0.01$	0.07
		183.69/180		$\pm 3$	$\pm 2$	$\pm 7$			
ev122 	2016-10-14	16.723	4.66	298	12	-150	0	0.42	0.03
	17:25:24.00	-60.655	$\pm 0.09$	179	83	-79	$\pm 0$	$\pm 0.0$	0.07
		10.65/10		$\pm 15$	$\pm 0$	$\pm 16$			
ev123 	2016-10-18	15.298	6.0	246	42	-93	8	0.58	0.04
	22:07:43.75	-61.352	$\pm 0.04$	71	47	-86	$\pm 0$	$\pm 8.01$	0.07
		159.62/160.0		$\pm 4$	$\pm 1$	$\pm 2$			
ev126 	2016-10-26	17.82	4.7	162	64	-95	0	0.62	0.035
	17:50:38.94	-61.019	$\pm 0.06$	354	26	-78	$\pm 0$	$\pm 0.0$	0.07
		20.27/20		$\pm 3$	$\pm 1$	$\pm 3$			
ev127 	2016-11-17	15.008	4.25	333	56	53	0	0.34	0.035
	09:53:58.83	-61.154	$\pm 0.0$	207	47	132	$\pm 0$	$\pm 0.01$	0.07
		165.62/165		$\pm 3$	$\pm 1$	$\pm 3$			
ev129 	2016-11-22	12.88	4.11	336	50	-40	0	0.22	0.035
	04:12:25.36	-59.592	$\pm 0.01$	94	60	-132	$\pm 0$	$\pm 0.0$	0.07
		61.18/60		$\pm 3$	$\pm 1$	$\pm 2$			
ev130 	2016-12-02	15.006	4.08	174	67	114	0	0.36	0.03
	22:11:59.64	-60.491	$\pm 0.01$	303	32	44	$\pm 0$	$\pm 0.0$	0.12
		52.72/50		$\pm 4$	$\pm 1$	$\pm 4$			

ev131 	2016-12-05	16.692	3.99	269	45	133	0	0.69	0.035
	23:55:59.38	-60.678	$\pm 0.02$	35	58	54	$\pm 0$	$\pm 0.0$	0.07
		13.0/12.5		$\pm 6$	$\pm 4$	$\pm 6$			
ev143 	2017-02-03	15.065	5.86	165	34	93	-2	0.76	0.04
	19:53:52.86	-60.457	$\pm 0.07$	341	55	87	$\pm 5$	$\pm 0.0$	0.07
		51.14/50.0		$\pm 16$	$\pm 1$	$\pm 12$			
ev144 	2017-03-10	17.502	4.54	31	56	-118	0	0.66	0.04
	06:00:47.60	-62.749	$\pm 0.08$	256	42	-54	$\pm 0$	$\pm 0.0$	0.07
		102.63/100.0		$\pm 4$	$\pm 1$	$\pm 6$			
ev146 	2017-03-14	17.505	4.15	275	49	-51	0	0.5	0.035
	00:18:35.57	-62.755	$\pm 0.02$	45	53	-125	$\pm 0$	$\pm 0.0$	0.07
		105.29/105		$\pm 4$	$\pm 1$	$\pm 4$			
ev149 	2017-04-07	12.429	4.36	156	76	-166	0	0.45	0.04
	21:45:04.57	-60.35	$\pm 0.01$	63	76	-13	$\pm 0$	$\pm 0.01$	0.07
		60.04/60		$\pm 2$	$\pm 1$	$\pm 3$			
ev150 	2017-04-15	17.537	4.51	326	68	86	0	0.8	0.04
	18:15:47.98	-61.047	$\pm 0.06$	156	21	99	$\pm 0$	$\pm 0.0$	0.07
		19.09/20		$\pm 4$	$\pm 1$	$\pm 4$			
ev151 	2017-04-17	17.493	4.31	297	22	-117	0	0.8	0.04
	04:12:41.10	-61.054	$\pm 0.08$	147	70	-79	$\pm 0$	$\pm 0.0$	0.07
		14.74/15		$\pm 12$	$\pm 4$	$\pm 12$			
ev152 	2017-04-17	17.513	4.97	276	28	-130	0	0.65	0.04
	06:24:41.40	-61.025	$\pm 0.06$	140	68	-70	$\pm 0$	$\pm 0.0$	0.07
		20.59/20.0		$\pm 9$	$\pm 2$	$\pm 9$			
ev153 	2017-04-17	17.484	3.96	163	65	-71	0	0.59	0.04
	15:11:30.58	-61.038	$\pm 0.1$	304	30	-124	$\pm 0$	$\pm 0.0$	0.07
		18.25/20		$\pm 3$	$\pm 4$	$\pm 3$			
ev154 	2017-04-21	15.044	4.2	342	56	109	0	0.58	0.035
	10:16:01.46	-60.507	$\pm 0.01$	129	38	63	$\pm 0$	$\pm 0.01$	0.07
		54.42/55		$\pm 3$	$\pm 1$	$\pm 2$			
ev155 	2017-04-25	16.835	4.55	9	61	80	0	0.79	0.035
	09:53:31.81	-60.915	$\pm 0.09$	209	29	107	$\pm 0$	$\pm 0.0$	0.07
		15.71/15		$\pm 3$	$\pm 1$	$\pm 3$			
ev171 	2016-09-05	17.285	3.73	342	46	-48	0	0.61	0.04
	12:12:19.98	-61.37	$\pm 0.02$	110	57	-124	$\pm 0$	$\pm 0.0$	0.07
		29.76/30		$\pm 9$	$\pm 5$	$\pm 12$			
ev187 	2016-10-03	15.352	3.89	212	73	-162	0	0.63	0.035
	15:18:58.80	-60.88	$\pm 0.03$	117	73	-16	$\pm 0$	$\pm 0.01$	0.07
		32.29/32.5		$\pm 4$	$\pm 3$	$\pm 3$			
ev281 	2016-07-11	15.726	4.07	61	58	-73	0	0.63	0.035
	06:58:09.58	-61.117	$\pm 0.11$	211	35	-115	$\pm 0$	$\pm 0.01$	0.07
		21.22/20		$\pm 10$	$\pm 2$	$\pm 14$			
ev331 	2016-04-12	15.706	3.86	326	55	-80	0	0.55	0.04
	15:24:27.59	-61.48	$\pm 0.01$	130	35	-102	$\pm 0$	$\pm 0.01$	0.07
		6.33/5		$\pm 4$	$\pm 2$	$\pm 4$			
ev332 	2016-08-19	16.026	3.67	251	52	-118	0	0.5	0.035
	07:21:38.12	-61.142	$\pm 0.01$	113	45	-57	$\pm 0$	$\pm 0.01$	0.07
		20.6/20		$\pm 10$	$\pm 1$	$\pm 2$			
ev340 	2016-11-26	17.716	3.9	152	26	62	0	0.77	0.04
	08:07:50.43	-61.569	$\pm 0.01$	2	66	102	$\pm 0$	$\pm 0.0$	0.07
		28.59/30		$\pm 6$	$\pm 1$	$\pm 6$			



	ev341	2016-11-26	15.888	4.18	61	70	8	0	0.19	0.035
		19:50:13.31	-60.276	$\pm 0.28$	328	82	160	$\pm 0$	$\pm 0.01$	0.07
			46.84/45		$\pm 2$	$\pm 4$	$\pm 3$			
	ev345	2017-02-11	17.824	4.19	343	57	101	0	0.53	0.04
		03:46:46.20	-61.551	$\pm 0.12$	143	34	72	$\pm 0$	$\pm 0.01$	0.07
			26.01/25		$\pm 50$	$\pm 3$	$\pm 5$			

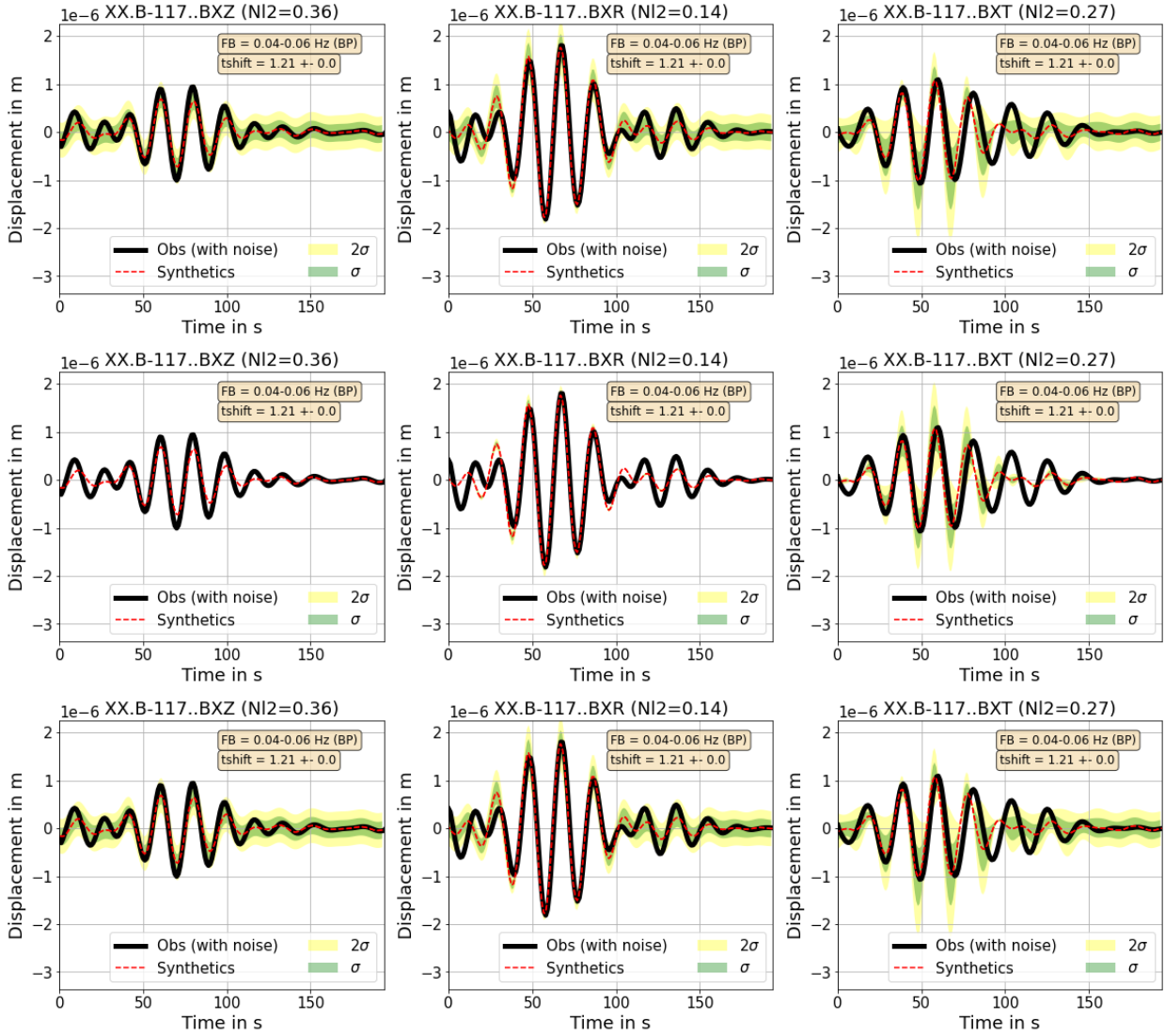
**Table B.2:** Overview of 151 local moment tensor solutions. The mechanisms are given in  $(s, d, r, C) = (\text{strike}, \text{dip}, \text{rake}, \text{CLVD})$ . The source of the MT solutions are as followed: SrcA are from international agencies (e.g., USGS, GEOPHONE, GCMT), SrcB from Ruiz et al. (2013), SrcC from Gonzalez et al. (2017) and SrcD are original to this study.

Time	Lat	Lon	Z	Mw	s	d	r	C	Src
1996-09-24T11:42:18.00	15.191	-61.443	146.7	5.8	86	58	-61	-4	SrcA
1998-06-25T21:03:44.00	17.733	-61.572	44.7	5.6	145	18	86	2	SrcA
1999-06-08T12:04:00.00	15.04	-60.421	54.6	5.8	262	81	63	-7	SrcA
1999-08-28T04:27:47.00	17.124	-61.36	28.0	5.4	341	75	81	-5	SrcA
1999-12-20T10:43:00.00	17.312	-61.705	58.8	5.4	125	23	60	-6	SrcA
2000-02-16T07:10:00.00	17.804	-60.871	33.0	5.4	139	10	73	0	SrcA
2000-02-23T19:26:00.00	17.387	-60.763	33.0	5.5	319	77	83	0	SrcA
2000-10-27T19:52:00.00	17.598	-61.194	37.9	5.6	5	85	84	-9	SrcA
2000-10-30T03:10:00.00	17.637	-61.193	33.0	5.8	137	7	75	0	SrcA
2001-01-05T08:46:00.00	16.113	-61.034	33.0	5.7	334	55	-49	4	SrcA
2001-04-05T13:26:00.00	15.909	-60.883	51.7	5.1	221	19	-83	19	SrcA
2001-09-25T23:54:00.00	17.016	-61.415	33.0	5.4	138	43	74	0	SrcA
2001-12-07T15:48:00.00	16.707	-61.087	33.0	5.1	315	69	77	2	SrcA
2002-12-21T18:54:00.00	18.357	-62.38	52.9	5.4	141	10	72	-4	SrcA
2003-06-30T00:27:00.00	17.457	-61.14	33.0	5.7	39	62	-19	0	SrcA
2004-03-01T06:07:00.00	15.043	-60.697	44.1	4.9	124	53	-51	-3	SrcA
2004-03-30T16:36:00.00	17.504	-62.174	70.4	4.9	113	34	41	10	SrcA
2004-11-21T11:07:00.00	15.679	-61.706	14.0	6.3	327	54	-88	2	SrcA
2004-11-21T13:58:00.00	15.74	-61.633	10.0	5.4	149	80	-70	-13	SrcA
2004-11-21T18:02:00.00	15.721	-61.762	10.0	5.4	320	51	-80	3	SrcA
2004-11-27T23:23:00.00	15.622	-61.63	10.0	4.9	183	77	-50	15	SrcA
2004-12-02T14:54:00.00	15.67	-61.295	18.2	5.0	156	58	-66	-13	SrcA
2005-02-08T02:23:00.00	15.484	-61.306	115.4	5.0	317	54	-46	-5	SrcA
2005-02-14T18:59:00.00	15.775	-61.744	11.6	5.8	157	32	-82	9	SrcA
2005-06-06T01:04:00.00	15.771	-61.555	14.0	4.8	159	51	-49	-3	SrcA
2005-08-30T14:44:00.00	15.022	-60.636	54.6	4.9	147	33	-11	-6	SrcA
2007-01-19T13:13:04.41	15.272	-60.0952	30.91	3.67	95	70	-34	0	SrcB
2007-01-19T16:16:29.82	15.2767	-60.0923	31.78	3.29	100	75	-37	0	SrcB
2007-02-02T01:31:46.97	15.4208	-60.1921	28.43	3.24	145	50	-23	0	SrcB
2007-02-27T09:40:00.00	17.109	-61.487	51.0	5.0	146	31	81	4	SrcA
2007-03-08T06:54:40.54	15.3255	-60.2009	28.85	2.62	270	80	172	0	SrcB
2007-03-16T19:40:29.67	16.0226	-60.2837	28.96	3.12	120	50	141	0	SrcB
2007-05-18T05:21:10.47	14.5896	-60.1879	41.62	3.01	60	45	97	0	SrcB
2007-05-23T03:13:05.83	15.0343	-60.1833	40.01	2.64	20	89	160	0	SrcB
2007-05-28T03:15:07.37	14.4414	-60.0771	29.14	3.44	115	80	-25	0	SrcB
2007-06-03T02:57:54.22	15.0345	-60.4067	41.13	3.19	20	60	-132	0	SrcB
2007-06-04T09:45:46.94	15.0236	-60.2692	44.92	2.61	20	55	90	0	SrcB

2007-06-09T22:04:08.40	15.23	-60.3687	32.89	3.59	100	40	-153	0	SrcB
2007-06-16T18:27:24.65	15.1327	-60.2063	39.64	2.76	145	25	90	0	SrcB
2007-06-21T05:34:24.44	15.0573	-60.2163	39.39	2.85	25	70	90	0	SrcB
2007-06-23T08:17:57.97	15.1106	-60.236	39.32	2.92	135	30	116	0	SrcB
2007-06-23T13:28:08.05	15.1115	-60.1647	29.97	2.48	55	50	-156	0	SrcB
2007-06-26T10:51:52.72	15.0512	-60.196	38.53	3.18	145	70	-76	0	SrcB
2007-07-04T07:04:38.61	15.0443	-60.2927	44.76	2.89	135	25	61	0	SrcB
2007-07-29T12:57:44.41	14.5676	-60.1068	35.16	2.6	85	55	-23	0	SrcB
2007-08-10T17:56:08.68	15.0513	-60.2348	38.3	2.9	15	85	-164	0	SrcB
2007-08-12T20:55:13.98	15.2063	-60.3728	32.44	3.26	55	85	-136	0	SrcB
2007-08-12T21:10:42.10	15.2053	-60.3586	32.41	2.95	60	75	-144	0	SrcB
2007-08-16T08:28:24.02	15.1527	-60.3824	30.0	3.87	120	60	-28	0	SrcB
2007-11-29T19:20:00.00	14.944	-61.274	156.0	7.4	85	22	-10	28	SrcA
2007-12-05T12:23:00.00	15.054	-61.316	160.3	5.2	86	27	-23	1	SrcA
2008-02-06T18:57:00.00	15.003	-60.407	27.0	5.3	304	78	77	-2	SrcA
2010-01-24T22:23:00.00	16.029	-60.925	64.5	5.0	30	50	-23	1	SrcA
2010-05-07T23:10:00.00	16.546	-60.98	34.0	5.2	338	58	78	27	SrcA
2011-08-09T05:49:00.00	15.534	-61.112	33.0	4.0	88	64	-47	-5	SrcA
2013-04-30T06:48:00.00	17.515	-62.166	62.5	5.3	125	37	63	-2	SrcA
2013-07-08T09:12:00.00	17.634	-61.707	25.3	4.7	155	37	63	12	SrcA
2013-10-18T04:01:56.58	16.12	-60.7352	10.0	4.0	102	76	-173	30	SrcC
2013-10-22T07:53:17.73	15.05	-60.4146	10.0	3.0	150	26	74	25	SrcC
2013-10-24T23:34:49.47	17.2	-61.0022	10.0	3.0	326	63	-96	-18	SrcC
2013-11-25T20:22:02.14	15.7	-61.31	119.0	4.0	281	34	-79	-29	SrcC
2014-01-10T03:14:02.72	16.15	-61.91	185.0	4.0	81	58	-7	18	SrcC
2014-02-09T10:54:51.05	14.56	-60.509	10.0	3.0	111	66	-78	10	SrcC
2014-02-25T09:58:15.80	16.14	-61.2614	10.0	3.0	235	44	-127	-32	SrcC
2014-05-14T23:44:10.89	14.87	-60.283	10.0	3.0	331	67	-172	32	SrcC
2014-05-16T11:40:00.00	17.0863	-60.3648	5.34	5.9	174	72	-61	4	SrcA
2014-05-16T12:30:21.00	17.14	-60.287	10.0	4.0	291	18	-154	0	SrcC
2014-05-16T12:34:54.01	17.11	-60.185	10.0	4.0	304	16	-164	-8	SrcC
2014-05-16T16:52:25.70	17.11	-60.375	10.0	5.0	287	3	-176	31	SrcC
2014-05-17T14:47:37.47	17.2	-60.297	10.0	4.0	302	16	-124	-34	SrcC
2014-06-01T06:06:33.00	15.36	-60.6919	10.0	3.0	280	41	-61	30	SrcC
2014-06-17T12:25:44.13	15.73	-61.3295	10.0	3.0	64	47	-175	12	SrcC
2014-07-10T12:54:59.83	14.98	-61.32	159.0	4.0	48	81	173	26	SrcC
2014-07-17T04:42:58.41	15.02	-60.3846	10.0	4.0	211	23	110	12	SrcC
2014-08-05T20:10:41.21	15.54	-60.7515	10.0	3.0	355	80	-161	-11	SrcC
2014-08-05T22:14:19.23	15.54	-60.7115	10.0	3.0	351	82	-167	-10	SrcC
2014-08-09T13:15:50.38	15.72	-61.514	10.0	3.0	304	73	-111	-9	SrcC
2014-08-18T20:53:14.13	15.35	-61.05	120.0	3.0	125	83	-42	-20	SrcC
2014-09-30T11:25:00.00	17.7066	-61.5032	27.82	4.1	162	40	18	-4	SrcA
2014-10-12T09:28:19.88	16.67	-60.5137	10.0	4.0	5	88	22	-64	SrcC
2014-11-25T05:33:01.00	16.74	-61.0834	10.0	3.0	9	27	-101	-4	SrcC
2014-12-19T19:30:00.00	16.1951	-61.8091	118.07	5.6	263	68	-64	3	SrcA
2015-02-14T23:00:07.41	14.73	-61.074	10.0	3.0	287	54	-94	40	SrcC
2015-02-16T21:52:21.42	15.45	-60.1326	10.0	4.0	268	43	-146	22	SrcC
2015-02-28T12:28:04.09	15.41	-61.21	137.0	4.0	183	67	-155	7	SrcC
2015-04-16T14:49:31.71	14.51	-60.3669	10.0	3.0	244	50	11	6	SrcC
2015-12-28T06:29:00.00	14.6571	-61.3454	150.0	5.6	319	34	-35	-2	SrcA
2016-03-19T11:33:00.00	17.996	-60.7019	26.0	6.0	355	50	30	0	SrcA
2016-03-22T14:09:06.17	17.308	-61.621	39.38	4.88	346	64	106	0	SrcD
2016-03-29T06:48:21.42	17.851	-60.873	21.6	3.99	184	76	-98	0	SrcD

2016-04-12T12:36:33.62	15.711	-61.483	10.91	4.49	200	45	-68	0	SrcD
2016-04-12T15:24:27.59	15.706	-61.48	6.33	4.1	326	57	-84	0	SrcD
2016-05-01T10:35:05.55	18.152	-61.521	30.48	4.81	84	49	24	0	SrcD
2016-05-08T13:47:34.53	17.705	-61.584	32.53	5.35	60	49	22	0	SrcD
2016-05-09T13:27:00.00	16.1413	-60.6692	23.94	4.4	302	48	-29	-6	SrcA
2016-05-09T13:36:27.76	16.179	-60.615	32.34	5.17	76	59	-120	0	SrcD
2016-06-12T08:56:55.92	16.858	-60.941	13.19	4.29	36	21	0	0	SrcD
2016-06-13T18:31:31.84	15.278	-61.186	145.38	4.25	34	53	-62	0	SrcD
2016-06-29T15:54:22.87	15.368	-61.119	132.18	4.48	52	59	-54	0	SrcD
2016-07-11T06:58:09.58	15.726	-61.117	21.22	4.5	70	57	-82	0	SrcD
2016-07-11T06:58:09.61	15.729	-61.118	23.81	4.5	280	39	-74	0	SrcD
2016-07-19T18:57:40.51	15.648	-60.499	36.06	4.2	210	57	58	0	SrcD
2016-08-02T07:58:32.85	15.154	-60.387	46.81	4.63	316	55	54	0	SrcD
2016-08-08T10:15:56.26	17.385	-61.917	62.15	4.91	144	61	114	0	SrcD
2016-08-19T07:21:38.12	16.026	-61.142	20.6	4.22	264	51	-120	0	SrcD
2016-08-23T01:09:49.90	14.89	-61.231	156.59	4.41	300	34	-112	0	SrcD
2016-09-05T12:12:19.98	17.285	-61.37	29.76	4.06	338	41	-62	0	SrcD
2016-09-08T21:39:51.28	15.081	-61.361	182.18	4.11	148	55	-150	0	SrcD
2016-09-19T14:33:31.06	14.985	-61.418	183.69	4.72	120	78	-16	0	SrcD
2016-10-03T15:18:58.80	15.352	-60.88	32.29	4.47	210	76	-162	0	SrcD
2016-10-14T17:24:00.00	16.7155	-60.7292	25.32	4.4	344	87	89	-1	SrcA
2016-10-14T17:25:24.00	16.723	-60.655	10.65	4.6	284	13	-166	0	SrcD
2016-10-18T22:07:43.75	15.298	-61.352	159.62	5.83	248	43	-90	0	SrcD
2016-10-18T22:14:00.00	15.223	-61.5065	146.0	5.6	84	47	-80	0	SrcA
2016-10-26T17:50:38.94	17.82	-61.019	20.27	4.66	168	66	-92	0	SrcD
2016-11-17T09:53:58.83	15.008	-61.154	165.62	4.64	336	57	52	0	SrcD
2016-11-22T04:12:25.36	12.88	-59.592	61.18	4.52	338	49	-42	0	SrcD
2016-11-26T08:07:50.43	17.716	-61.569	28.59	3.94	150	25	60	0	SrcD
2016-11-26T19:50:13.31	15.888	-60.276	46.84	4.27	58	70	8	0	SrcD
2016-12-02T22:11:59.64	15.006	-60.491	52.72	4.71	176	68	116	0	SrcD
2016-12-05T23:55:59.38	16.692	-60.678	13.0	4.07	270	45	134	0	SrcD
2017-02-03T19:22:00.00	15.0701	-60.5254	44.0	5.8	334	65	83	0	SrcA
2017-02-03T19:53:52.86	15.065	-60.457	51.14	6.23	158	36	88	0	SrcD
2017-02-11T03:46:46.20	17.824	-61.551	26.01	4.03	350	57	100	0	SrcD
2017-03-10T06:00:47.60	17.502	-62.749	102.63	4.78	30	57	-116	0	SrcD
2017-03-14T00:18:35.57	17.505	-62.755	105.29	4.44	276	49	-50	0	SrcD
2017-04-07T21:45:04.57	12.429	-60.35	60.04	4.65	156	78	-170	0	SrcD
2017-04-15T18:15:47.98	17.537	-61.047	19.09	4.73	324	70	90	0	SrcD
2017-04-15T18:48:26.36	17.531	-61.085	20.77	3.67	268	28	-104	0	SrcD
2017-04-17T04:12:41.10	17.493	-61.054	14.74	4.23	288	21	-126	0	SrcD
2017-04-17T05:15:00.00	17.4498	-61.1423	16.0	5.6	313	78	69	9	SrcA
2017-04-17T06:10:00.00	17.4793	-61.1138	18.66	4.8	133	37	-87	2	SrcA
2017-04-17T06:24:41.40	17.513	-61.025	20.59	5.13	288	28	-120	0	SrcD
2017-04-17T08:28:51.30	17.489	-61.115	14.38	3.93	238	17	-178	0	SrcD
2017-04-17T15:11:30.58	17.484	-61.038	18.25	4.03	164	70	-68	0	SrcD
2017-04-17T16:08:01.04	17.532	-61.056	14.55	3.92	34	78	12	0	SrcD
2017-04-19T20:31:33.41	17.502	-61.003	21.67	4.09	292	53	-156	0	SrcD
2017-04-21T10:16:01.46	15.044	-60.507	54.42	4.41	340	57	108	0	SrcD
2017-04-22T03:48:17.91	17.525	-61.057	17.76	3.86	254	57	158	0	SrcD
2017-04-22T09:13:53.49	17.554	-61.03	16.29	3.71	292	72	168	0	SrcD
2017-04-25T09:32:00.00	16.7696	-60.9352	38.5	4.4	336	79	82	3	SrcA
2017-04-25T09:53:31.81	16.835	-60.915	15.71	4.57	8	63	80	0	SrcD
2017-09-15T10:30:00.00	15.002	-60.5126	53.07	4.6	343	59	86	0	SrcA

2017-11-28T00:43:00.00	18.3946	-61.9281	24.52	4.8	185	79	0	-3	SrcA
2018-11-10T16:43:00.00	17.6213	-61.0678	10.0	4.5	315	74	80	1	SrcA
2018-11-10T18:38:00.00	17.5686	-61.2245	24.3	4.3	134	89	-87	8	SrcA
2019-01-04T22:47:00.00	16.8489	-61.0629	31.59	4.4	151	25	86	0	SrcA
2019-02-23T19:33:00.00	16.9186	-60.5372	25.72	4.1	13	65	-43	-2	SrcA
2019-12-19T15:39:00.00	17.8854	-61.5636	32.22	4.3	344	75	86	0	SrcA
2019-12-27T01:45:00.00	16.8394	-60.9055	30.51	4.5	146	15	31	10	SrcA
2020-01-08T14:52:00.00	15.1942	-61.3177	144.12	4.8	350	51	-54	18	SrcA



**Figure B.1:** Exemplary waveform fit with  $\sigma$ -range (if applicable) using data covariance matrix  $C_d$  (top row), model covariance matrix  $C_T$  (middle row), and combined covariance matrix  $C_D$  (bottom row). Model covariance matrix  $C_T$  in  $C_D$  adds to the  $\sigma$ -range around the rotational sensitive signal parts. Displayed example exhibits an increased sensitivity on the T-component.

# Appendix C

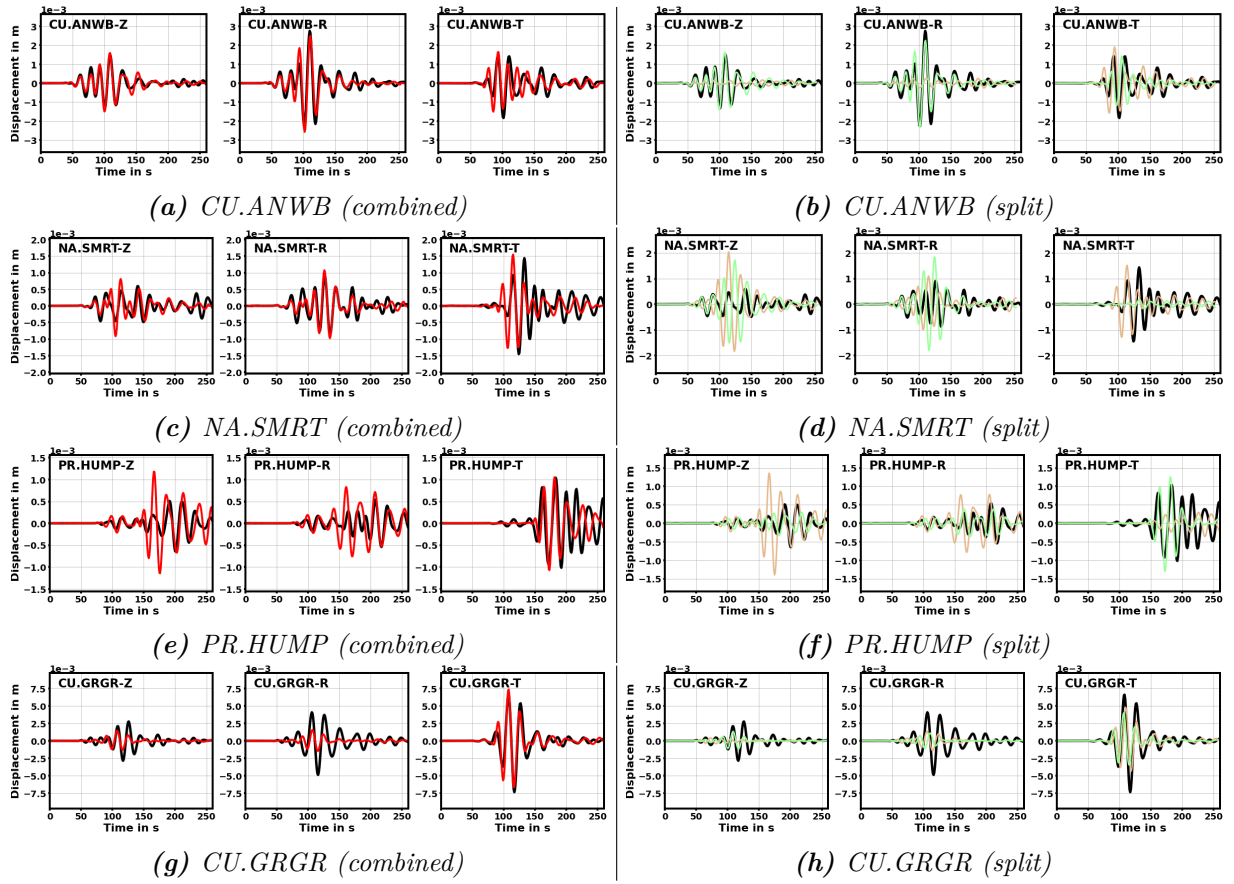
## Chapter 6

- Table C.2: Table of moment tensor solutions. The table lists the location and source information of all moment tensor solutions displayed in the introduction map (main text Figure 6.2). The list is, to our knowledge, complete for the period 1982 to February 2020 within the respective source reference (see last column).
- Table C.3: Seismic activity associated to the Martinique event. The table lists all time, location, and magnitude information and associated cluster ID of the IRIS aftershock events. Featured hypocenter locations are not updated following Figure C.2.
- Table C.4: Regional seismic network of 2007. The table lists all location, network ID, and usage information of the regional seismic network with available data per FDSN at the time of the Martinique event.
- Table C.1: Table of moment tensor modelling. The table summarized the numerical results of the main text Figure 3 of the forward/inversion simulation for the Martinique event.
- Figure 6.3: Aftershock cross-correlation analysis. Cross-correlation clustering of the fore- and aftershock seismicity associated to the 2007  $M_w$ 7.4 Martinique earthquake. We used the bandpass filtered (1-2 Hz) P and S-phase waveform data of the vertical trace at station G.FDF (Table C.4). Correlation is done for P and S separately and arranged by hand in the correlation matrix using a correlation coefficient  $cc$  of  $> 0.75$  for P and  $> 0.55$  for S. P and S correlations are then evenly weighted with  $[cc(P)+cc(S)]/2$  and plotted together. The identified groups G1 and G2 display a spatial clustering along the NS-axis. Events not belonging to either group arrange predominantly around  $15^\circ\text{N}$ .
- Figures C.1a to C.1h: Waveform fit. Waveform fit for the combined (using  $dt$  and  $dm$ ) and individual (split) source contribution of the four stations used in the doublet inversion F (Table C.1)
- Figure C.2: Hypocenter shift and origin time delay between the VoiLA database (Bie et al., 2020) and ISC catalogue (IRIS DMC, 2011). Compare methods in the main paper for detailed information.
- Figures C.3a to C.3f: Information content of the 3D cartoon.
  - Figure C.3a: Outline of the Proto-Caribbean spreading ridge model. The Proto-Caribbean fracture zone PCF proceeds with (lon, lat, depth) from (-60.805, 14.811, -89) to (-61.73, 15.15, -190). The northern ridge PCR connected to the domain boundary A-PC proceeds from (-61.06, 15.497, -93) to (-61.428, 15.039, -162) and from (-61.185, 15.556, -102) to (-61.56, 15.088, -173). The southern ridge PCR? connected to the PCF proceeds from (-60.994, 14.88, -111) to (-61.444, 14.36, -176) and from (-61.126, 14.929, -124) to (-61.571, 14.36, -195).
  - Figure C.3b: 50 well-located VoiLA events (Bie et al., 2020), 32 aftershocks, one foreshock, and about 2478 ISC events defining the heatmap with 25 km above and 75 km below the slab top.
  - Figure C.3c: Beachballs in the general lower-hemisphere projection associated with their

- location on the slab top.
- Figure C.3d: Beachballs in lower-hemisphere projection rotated relative to the slab top associated with their location on the slab top.
- Figure C.3e: Tension axis and preferred strike directions of the mechanisms in Figure C.3d.
- Figure C.3f: Rupture history of the Martinique event. The  $M_w 7.1$  strike-slip event (green beachball, lower-hemisphere) with an approximate fault length of  $\sim 57$  km (black bar below the beachball) on the Proto-Caribbean fracture zone PCF is followed, with a  $\sim 4.23$  seconds delay with the  $M_w 7.25$  dip-slip event (orange beachball, lower-hemisphere) with an approximate fault length of  $\sim 57$  km (black bar below the beachball) on the Proto-Caribbean ridge PCR. Within the next 1.5 months, at least 32 aftershocks with mechanisms similar to the two doublet components followed.
- Figure C.4: Cross-Section subplot with beachballs. Extension of main text Figure 6.5. The P- and N-axis are computed from the cross-section beachballs.
- Figure C.5a and C.5b: Doublet location grid with cross-section at  $61.25^\circ\text{W}$ . Location grid in two different view angles. The grid is built around the aftershocks and supported by the VoiLA events. Red G1 events are associated with the orange beachball and blue G2 events are associated with the green beachball. Mechanism of fault  $F1^F$  maps well with the inferred grid line while we observe differences in fault  $F2^F$  to the grid. Number and locations of G2 aftershocks made it difficult to define a location grid.
- Figure C.6: Location grid. Top view of the two location grids with the best (colors beachball) and top 30 solutions (black beachball lines) and the variance reduction (VR) heatmap in the background. The VR heatmap is computed with the best VR results (colored beachball) at the respective location.

**Table C.1:** Table of moment tensor modelling.  $dt$  represents the onset-time after 2007-11-29T19:00:20 UTC. The mechanisms are given in  $(s, d, r, C) = (\text{strike}, \text{dip}, \text{rake}, \text{CLVD})$ .  $dm$  is the moment relative to  $M_w 7.4$ .

ID	VR	Fault	Simulation	s,d,r	C	dt	dm	Lat,Lon,Z
A	0.21	single	forward	109,58,-32	89	0	1	14.944, -61.274, 150
B	0.23	single	forward	86,23,-10	95	0	1	14.944, -61.274, 150
C	0.31	single	inversion	92,30,9.5	72	0	1	14.944, -61.274, 150
D	0.34	$F1^D$	forward	86,23,-10	0	6.0	0.85	14.944, -61.274, 150
		$F2^D$		109,58,-32	0	0	0.15	14.944, -61.274, 150
		Doublet		87,26,-12	51	0	1	14.944, -61.274, 150
E	0.47	$F1^E$	inversion	76,30,10	0	1.78	0.66	14.944, -61.274, 150
		$F2^E$		116,71,-12	0	0	0.34	14.944, -61.274, 150
		Doublet		89,31,6	45	0	1	14.944, -61.274, 150
F	0.54	$F1^F$	inversion	89,17,18	0	4.23	0.7	15.0625, -61.45, 150
		$F2^F$		109,70,-10	0	0	0.3	14.95, -60.95, 170
		Doublet		94,24,13	44	0	1	$F1^F + F2^F$



**Figure C.1:** Waveform fit. Observables (black) overlaid with the combined synthetics and the synthetics of major couple F1 and minor couple F2 following the color-coding of Figure 6.4 in the main text.



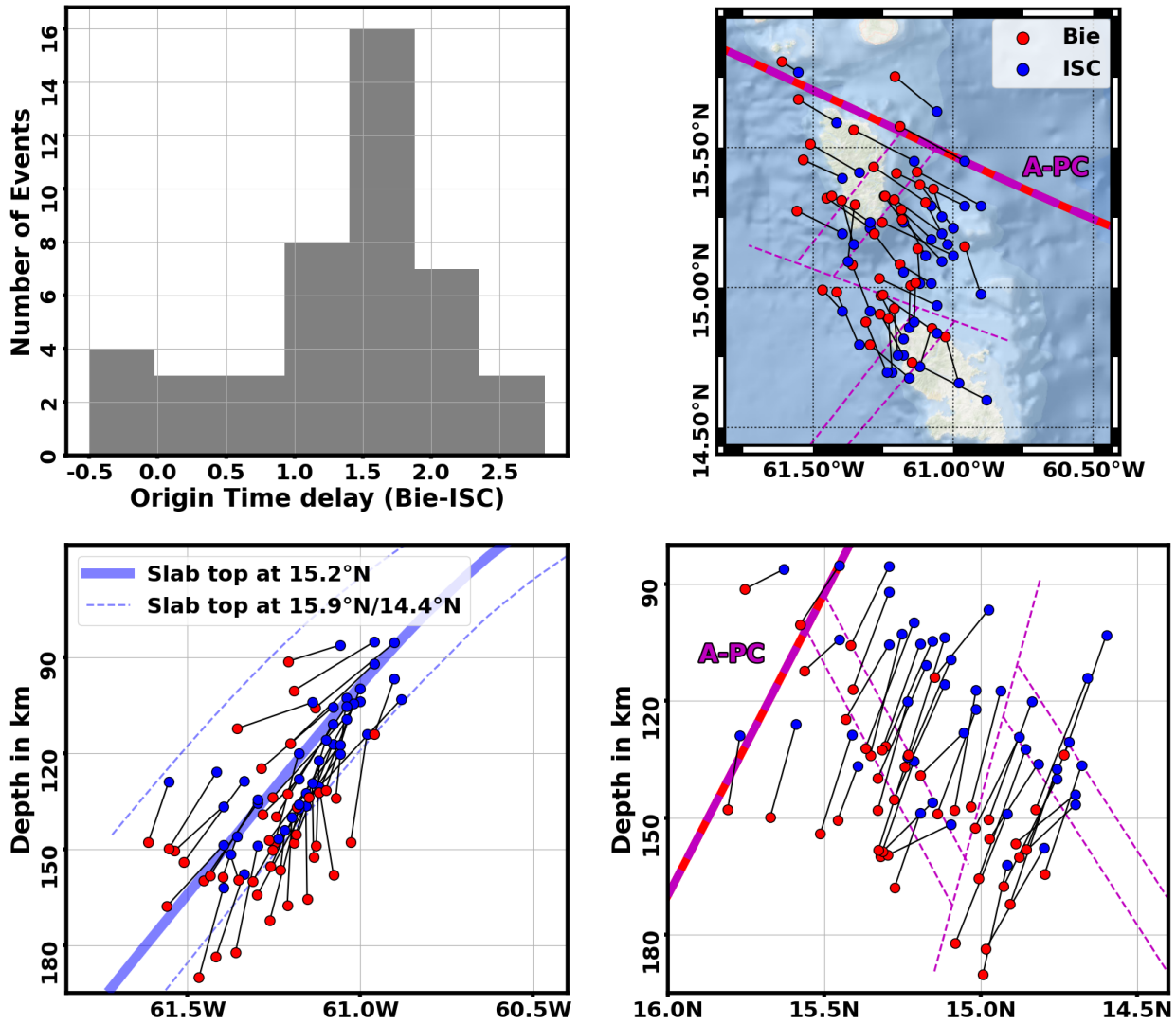


Figure C.2: Hypocenter shift and origin time delay between the VoiLA database (Bie et al., 2020) and ISC catalogue (IRIS DMC, 2011).

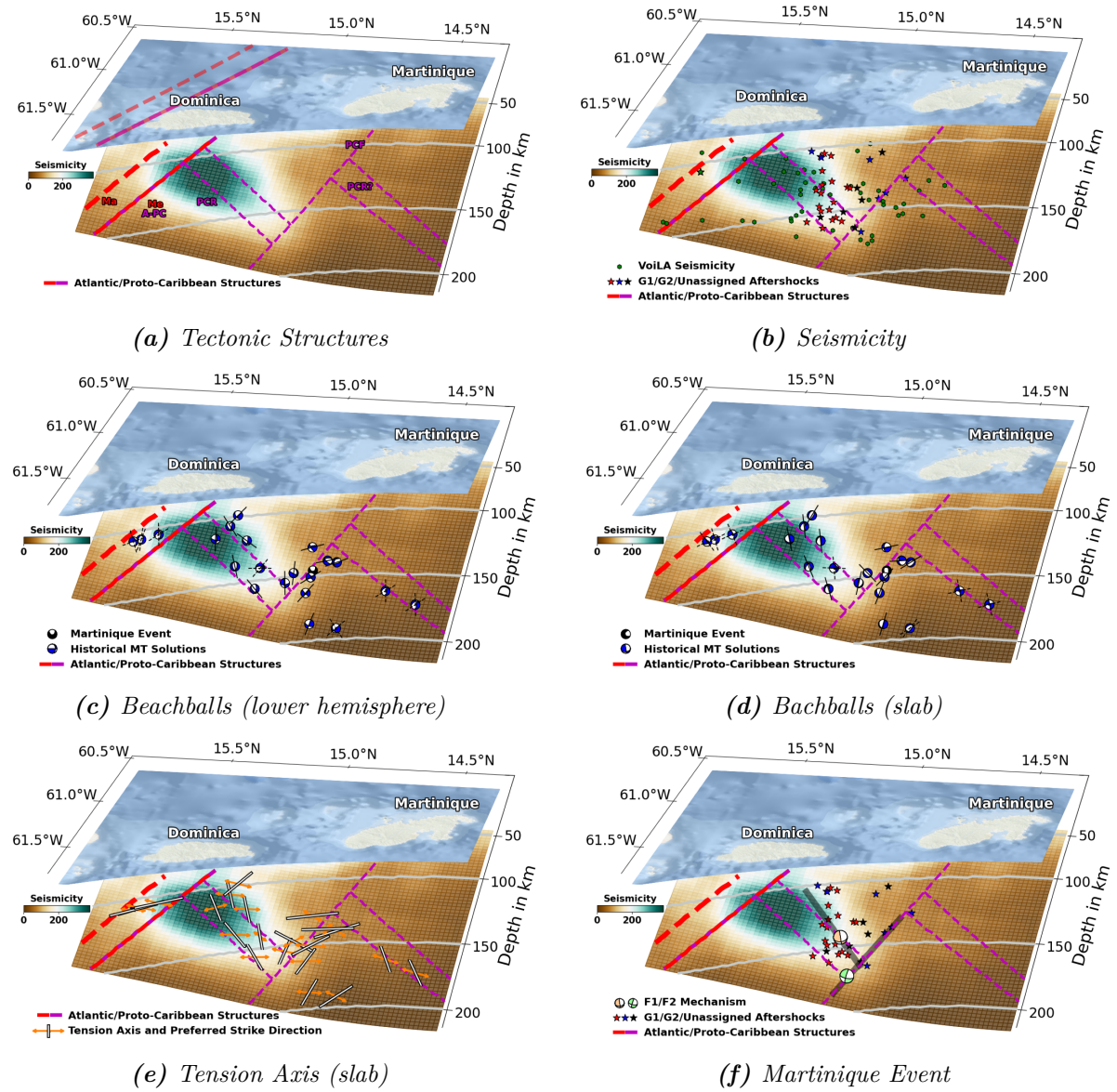


Figure C.3: Information content of the 3D cartoon.

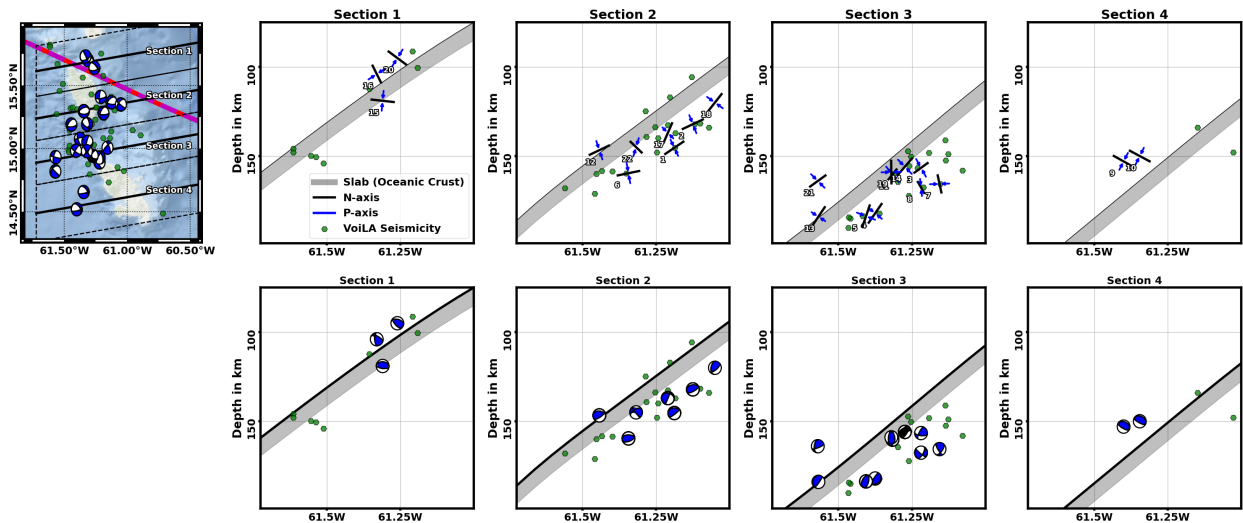
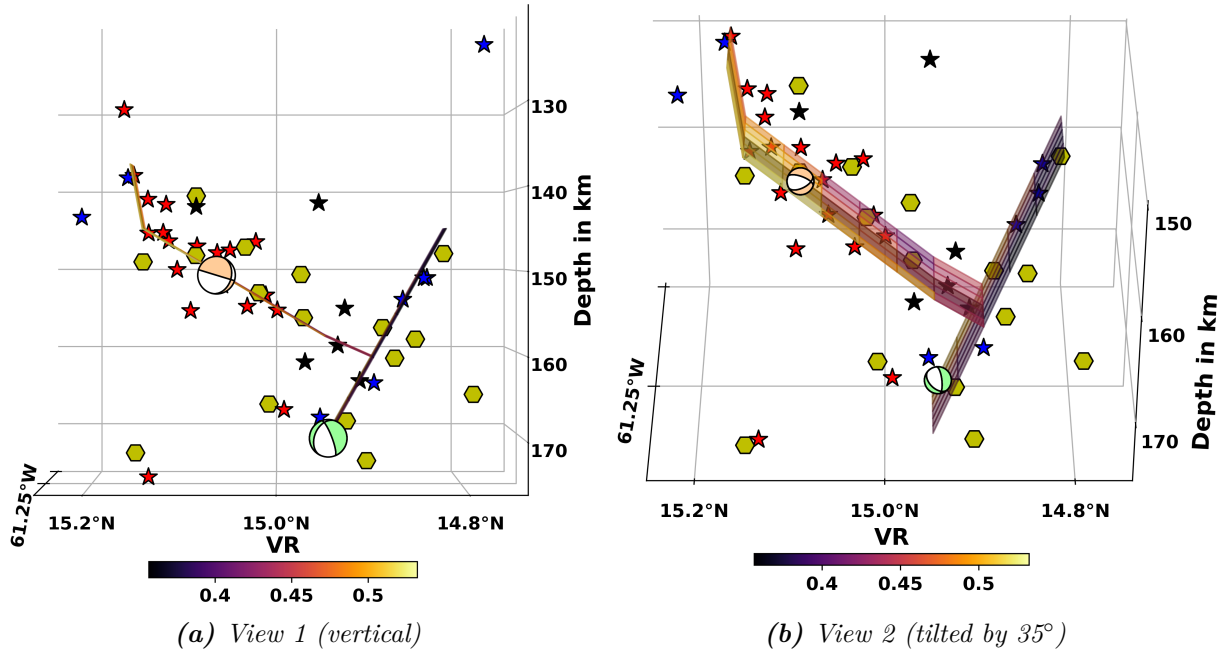


Figure C.4: Cross-Section subplot with beachballs.



**Figure C.5:** Doublet location grid with cross-section at 61.25° W. Outline of both grids are motivated by the clustered aftershock locations. Mechanism of fault F1<sup>F</sup> maps well with the inferred grid line while we observe differences in fault F2<sup>F</sup> to the grid. Number and locations of G2 aftershocks made it difficult to define a location grid.

**Table C.2:** Table of moment tensor solutions. The mechanisms are given in (s, d, r, C) = (strike, dip, rake, CLVD). The source of the MT solutions are as followed: SrcA by Lindner et al. (2023), SrcB by Quinteros et al. (2021), SrcC by U.S. Geological Survey (2022), SrcD by Gonzalez et al. (2017) and SrcE by Dziewonski et al. (1981) and Ekström et al. (2012).

ID	Time	Lat,Lon,Z	Mw	s,d,r	C	Beach.	Src
ev001	2016-06-13 18:31:31.840	15.281, -61.188, 145.375	4.25	206,40,-146 89,69,-55	0		SrcA
ev002	2016-06-29 15:54:22.870	15.367, -61.125, 132.125	4.48	227,38,-132 96,63,-62	0		SrcA
ev003	2016-08-23 01:09:49.900	14.891, -61.219, 156.625	4.41	151,66,-63 280,36,-136	0		SrcA
ev004	2016-09-08 21:39:51.280	15.078, -61.375, 182.125	4.11	160,58,-17 259,76,-147	0		SrcA
ev005	2016-09-19 14:33:31.060	14.984, -61.406, 183.75	4.72	122,73,-12 216,79,-163	0		SrcA
ev006	2016-10-18 22:08:13.750	15.297, -61.344, 159.625	5.83	248,44,-106 90,48,-75	8		SrcA
ev007	2016-11-17 09:53:58.830	15.008, -61.156, 165.625	4.64	228,63,146 335,60,32	0		SrcA
ev008	2016-12-16 19:51:56.910	14.93, -61.219, 167.625	4.17	214,64,-58 339,40,-137	0		SrcA
ev009	2015-12-19 19:49:13.000	14.52, -61.4, 153	5.6	317,37,-38 79,68,-120	-20		SrcB
ev010	2015-12-28 06:55:29.000	14.657, -61.345, 150	5.6	80,71,-119 320,34,-35	-10		SrcC
ev011	2007-12-05 12:11:23.000	15.054, -61.316, 160.3	5.2	198,79,-116 87,28,-24	7		SrcC

ev012	1996-09-24 11:42:18.000	15.191, -61.443, 146.7	5.8	86,58,-62 221,42,-127	-15		SrcC
ev013	1982-01-08 01:23:56.000	14.933, -61.568, 184	5.2	102,87,-35 194,55,-176	0		SrcC
ev014	2007-11-29 19:00:32.630	14.97, -61.26, 156	7.4	109,58,-32 217,64,-144	90		SrcE
	2007-11-29 19:00:20.000	14.944, -61.274, 150	7.4	185,86,-113 86,23,-10	95		SrcC
	2007-11-29 19:00:20.000	14.944, -61.274, 148	7.4	109,58,-31 217,64,-143	89		SrcC
ev015	2013-11-25 20:22:02.140	15.7, -61.31, 119	4.3	281,34,-79 88,57,-97	-29		SrcD
ev016	2014-06-17 12:25:44.130	15.73, -61.33, 104	3.79	64,47,-175 331,86,-43	12		SrcD
ev017	2015-02-28 12:28:04.090	15.41, -61.21, 137	4.6	183,67,-155 83,67,-25	7		SrcD
ev018	2014-08-18 20:53:14.130	15.35, -61.05, 120	3.6	125,83,-42 221,48,-171	-20		SrcD
ev019	2014-07-10 12:54:59.830	14.98, -61.32, 159	4.2	48,81,173 139,83,9	26		SrcD
ev020	2005-02-08 02:18:24.600	15.64, -61.26, 95	5.0	79,54,-134 318,54,-46	-22		SrcC
ev021	2019-09-13 16:27:18.000	14.82, -61.58, 167	4.9	129,85,-21 221,69,-175	-19		SrcB
ev022	2020-01-08 14:01:52.000	15.195, -61.322, 145	4.9	289,67,43 179,51,150	-62		SrcC

**Table C.3:** Seismic activity associated to the Martinique event. Event ev001 is a foreshock predating the main event ev002 by one day. The events ev003 to ev034 are aftershocks recognized by IRIS (IRIS DMC, 2011). The seismic events ev002 and ev021 are listed in table C.2 as ev014 and ev011, respectively. Clusters G1 and G2 relate to the clusters defined in the cross-correlation study (Figure 6.3). All events not belonging to either of these two groups are listed as G3.

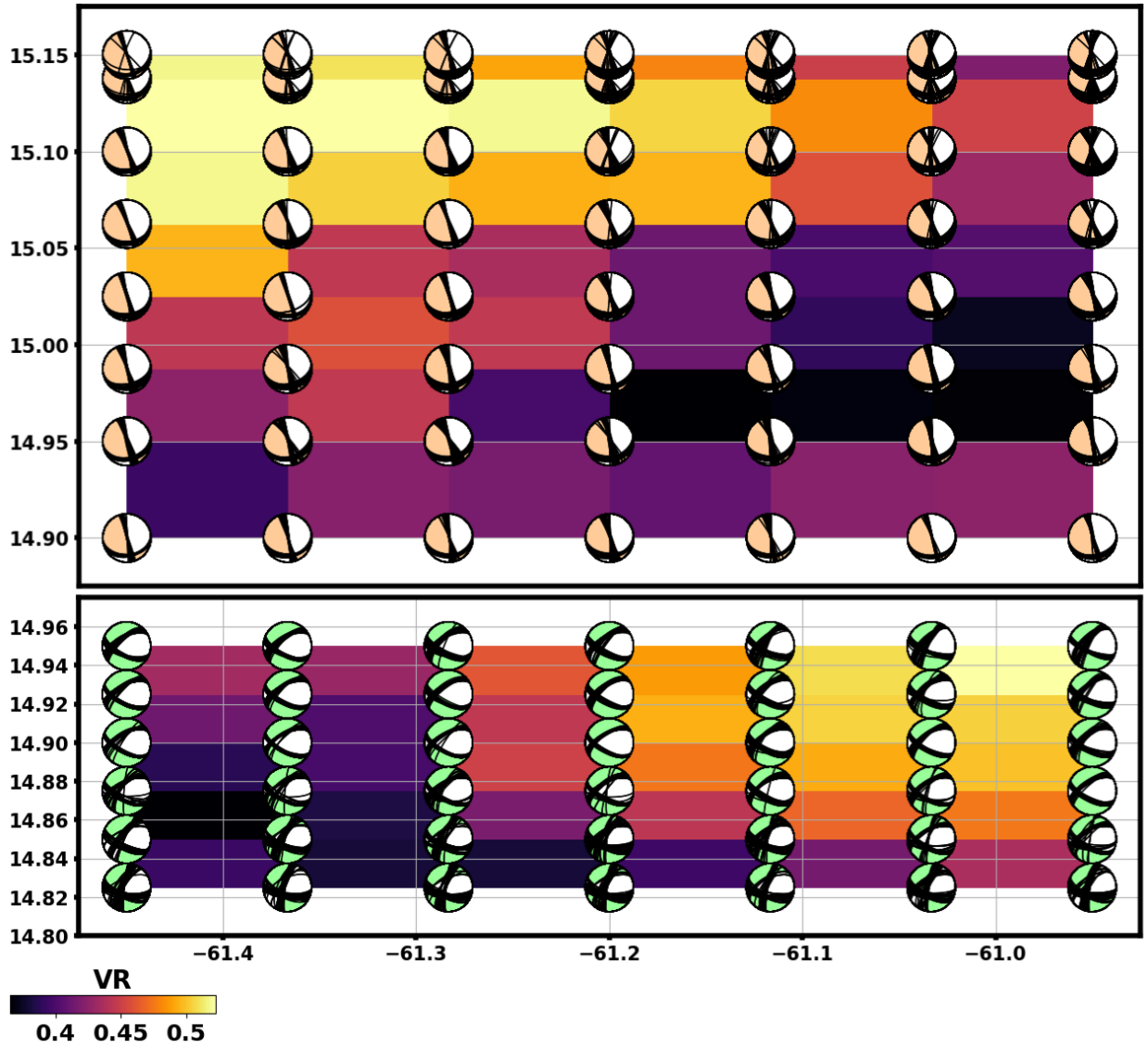
ID	Day	Time in UTC	Lat	Lon	Z in km	Mw	Cluster
ev001	2007-11-28	14:54:43.86	14.929	-61.302	154.3	3.7	G3
ev002	2007-11-29	19:00:19.96	14.995	-61.224	147.3	7.4	G3
ev003	2007-11-29	19:09:07.41	14.954	-60.892	167.4	3.2	G2
ev004	2007-11-29	19:14:41.39	15.011	-61.074	152.8	3.4	G1
ev005	2007-11-29	19:16:25.19	15.115	-61.089	142.1	3.5	G1
ev006	2007-11-29	19:34:46.69	15.132	-61.307	145.5	5.0	G1
ev007	2007-11-29	20:11:11.47	15.021	-61.256	146.5	4.5	G1
ev008	2007-11-29	20:17:07.16	15.089	-61.232	154.6	4.2	G1
ev009	2007-11-29	20:55:46.40	14.912	-60.84	163.1	3.7	G3
ev010	2007-11-29	23:00:49.06	14.955	-60.706	141.8	3.5	G3
ev011	2007-11-30	02:14:54.12	14.84	-60.72	150.8	3.8	G2
ev012	2007-11-30	02:30:41.75	14.899	-61.317	163.0	4.0	G2
ev013	2007-11-30	04:00:00.65	15.056	-61.223	151.6	4.9	G1
ev014	2007-11-30	16:22:51.87	15.134	-61.008	174.4	3.9	G1

ev015	2007-11-30	18:31:04.33	15.205	-60.893	143.6	4.0	G2
ev016	2007-12-01	14:58:52.60	14.97	-61.071	160.7	3.7	G3
ev017	2007-12-02	13:22:00.97	15.15	-60.895	138.6	3.9	G1
ev018	2007-12-03	08:14:46.81	14.782	-60.983	123.1	3.4	G2
ev019	2007-12-05	08:27:28.14	14.846	-61.079	150.8	3.4	G2
ev020	2007-12-05	09:55:10.87	15.134	-61.121	141.5	3.4	G1
ev021	2007-12-05	12:11:22.54	15.03	-61.278	154.1	5.2	G1
ev022	2007-12-06	01:55:50.87	15.083	-61.268	142.4	3.8	G3
ev023	2007-12-09	23:52:41.11	15.061	-61.328	147.8	3.8	G1
ev024	2007-12-18	16:37:26.63	15.112	-61.133	146.4	3.5	G1
ev025	2007-12-24	02:32:46.76	14.992	-61.271	166.2	4.3	G1
ev026	2007-12-25	19:03:53.91	14.868	-61.119	153.3	3.6	G2
ev027	2008-01-05	07:22:30.91	15.083	-61.051	147.0	2.7	G1
ev028	2008-01-05	09:58:14.04	14.936	-61.136	158.7	3.7	G3
ev029	2008-01-07	04:20:14.87	15.156	-60.927	138.9	3.9	G2
ev030	2008-01-08	04:37:12.10	15.16	-60.92	130.8	2.8	G1
ev031	2008-01-08	16:54:18.50	15.119	-60.905	145.4	3.9	G1
ev032	2008-01-10	18:07:31.25	15.048	-61.171	147.5	3.4	G1
ev033	2008-01-12	08:20:05.08	14.999	-61.079	154.6	3.4	G1
ev034	2008-01-13	05:56:20.27	15.103	-61.208	149.8	3.5	G1

**Table C.4:** Regional seismic network of 2007. Listed stations belong to 5 regional or global seismic networks: G - French Global Network, CU - Caribbean Network, IU - Global Seismograph Network, PR - Puerto Rico Seismic Network and NA - Caribbean Netherlands Seismic Network. <sup>1</sup>Station FDF clipped during the Martinique mainshock but recorded all aftershock events.

Station	Network	Lat	Lon	Elev in m	Island	Selected
FDF	G	14.734971	-61.146311	467.0	Martinique	No <sup>1</sup>
ANWB	CU	17.668530	-61.785570	39.0	North Barbuda	Yes
BBGH	CU	13.143400	-59.558800	180.0	Barbados	No
GRGR	CU	12.132400	-61.654000	195.0	Grenada	Yes
SJG	IU	18.109100	-66.150000	420.0	Puerto Rico	No
CDVI	PR	17.752220	-64.764720	51.0	Virgin Islands	No
HUMP	PR	18.142069	-65.848851	79.1	Puerto Rico	Yes
STVI	PR	18.353333	-64.962222	377.0	Charlotte Amalie	No
SABA	NA	17.620480	-63.243230	261.0	The Bottom	No
SEUS	NA	17.492800	-62.981400	46.0	Oranjestad	No
SMRT	NA	18.050501	-63.074600	260.0	Anquilla	Yes



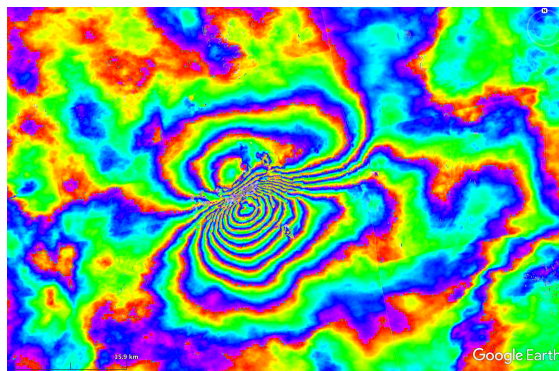


**Figure C.6:** Location grid. Top view of Figure C.5 with upper plot representing the location grid surrounding aftershock group G1 with mechanism  $F1^F$  and lower plot representing the location grid surrounding aftershock group G2 with mechanism  $F2^F$ . Best solutions are presented as red beachballs with black nodal lines highlighting the uncertainties. Solutions at locations with the highest VR show only small variations in their mechanism.

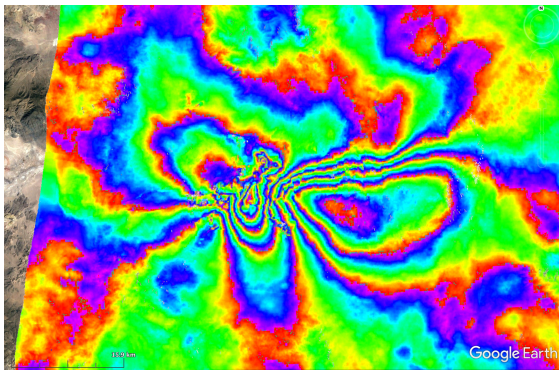


## Appendix D

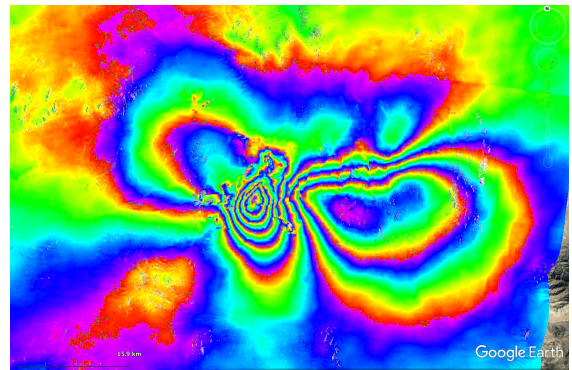
### Chapter 8



*(a) Ascending track 64.*



*(b) Descending track 71.*



*(c) Descending track 144.*

**Figure D.1:** SAR images for construction of coseismic interferograms.

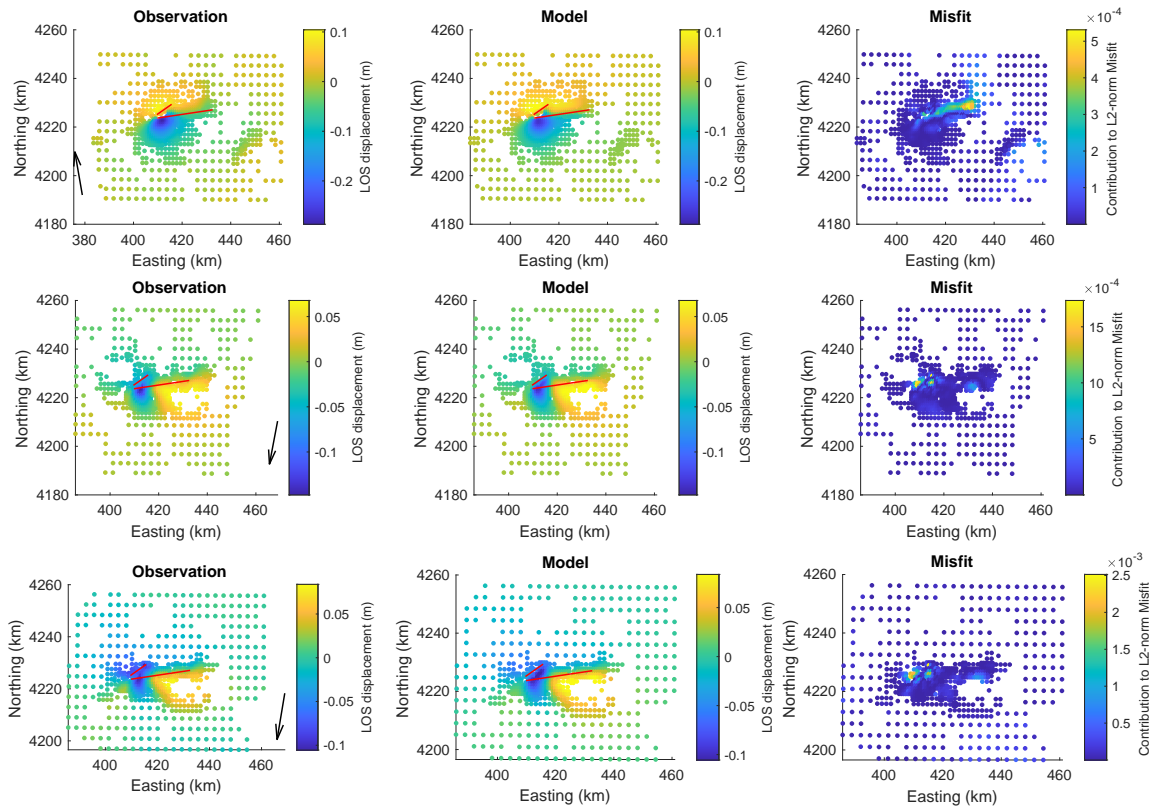


**Table D.1:** Parameter of preliminary InSAR model.

Eastern Fault		
Value	Uncertainty	Description
55.0021	10.0000	Strike (degrees)
49.7709	15.0000	Dip (degrees)
-39.9957	20.0000	Rake (degrees)
0.5978	2.0000	Slip (m)
0.0000	0.0000	Tensile component (m)
412.6496	15.0000	lon(x) projected centre
4227.2250	15.0000	lat(y) of surface break
7.4051	5.0000	length of scarp (km)
1.7162	2.0000	minimum depth of dislocation
13.5405	4.0000	maximum depth of dislocation
0.0000	0.0000	timeshift (s)
0.0000	0.0000	v - Non-DC component (s)
2.0569		Moment ( $\times 10^{18}$ N m)
6.1455		Moment magnitude $M_w$
0.3842		dip-slip dislocation (m)
-0.4580		strike-slip dislocation (m)
15.4875		fault plane width (km)
114.6872		fault plane area ( $\text{km}^2$ )
409.6166		lon(x) of 1st end of
4225.1014		lat(y) surface break
415.6827		lon(x) of 2nd end of
4229.3486		lat(y) surface break

Western Fault		
Value	Uncertainty	Description
81.5015	10.0000	Strike (degrees)
88.1649	15.0000	Dip (degrees)
-7.9587	20.0000	Rake (degrees)
1.3968	2.0000	Slip (m)
0.0000	0.0000	Tensile component (m)
421.2039	15.0000	lon(x) projected centre
4225.3859	15.0000	lat(y) of surface break
23.0011	5.0000	length of scarp (km)
3.1065	2.0000	minimum depth of dislocation
6.0798	4.0000	maximum depth of dislocation
0.0000	0.0000	timeshift (s)
0.0000	0.0000	v - Non-DC component (s)
2.8671		Moment ( $\times 10^{18}$ N m)
6.2416		Moment magnitude $M_w$
0.1934		dip-slip dislocation (m)
-1.3833		strike-slip dislocation (m)
2.9747		fault plane width (km)
68.4221		fault plane area ( $\text{km}^2$ )
409.8297		lon(x) of 1st end of
4223.6863		lat(y) surface break
432.5782		lon(x) of 2nd end of
4227.0855		lat(y) surface break



*Figure D.2: Preliminary InSAR model.*

